Contrast-ultrasound dispersion imaging for prostate cancer localization

Contrast-ultrasound dispersion imaging for prostate cancer localization

Maarten Kuenen

This research was financially supported by the Dutch Technology Foundation STW (project number 10769). Financial support for the printing of this thesis was kindly provided by Bracco Imaging Europe B.V. and by Astellas Pharma B.V.

Cover design by Paul Verspaget, Verspaget & Bruinink Grafische Vormgeving.
Printed by Ipskamp Drukkers BV.

A catalogue record is available from the Eindhoven University of Technology Library
ISBN: 978-90-386-3568-2

Contrast-ultrasound dispersion imaging for prostate cancer localization

PROEFSCHRIFT

ter verkrijging van de graad van doctor aan de Technische Universiteit Eindhoven, op gezag van de rector magnificus prof.dr.ir. C.J. van Duijn, voor een commissie aangewezen door het College voor Promoties, in het openbaar te verdedigen op maandag 10 maart 2014 om 16:00 uur

door

Maarten Petrus Joseph Kuenen

geboren te Venray

Dit proefschrift is goedgekeurd door de promotoren en de samenstelling van de promotiecommissie is als volgt:

voorzitter:	prof.dr.ir. A.C.P.M. Backx
1^{e} promotor:	prof.dr.ir. H. Wijkstra
2^{e} promotor:	prof.dr. J.J.M.C.H. de la Rosette (UvA-AMC)
copromotor:	dr.ir. M. Mischi
leden:	prof.dr.ir. N. de Jong (TUD)
	prof. P. Tortoli PhD (University of Florence)
	prof.dr.ir. F.N. van de Vosse
adviseur:	prof.dr.ir. A.P.G. Hoeks (UM)

Summary

Contrast-ultrasound dispersion imaging for prostate cancer localization

Prostate cancer is the most prevalent form of cancer in men in Western countries. Nowadays, due to a lack of reliable techniques for prostate cancer imaging, treatment options are often restricted to radical treatments, which carry significant risks of permanent side effects, such as incontinence or impotence. As a result, imaging methods could significantly benefit prostate cancer care by enabling accurate targeting of biopsies and focal therapies. In this context, an interesting marker for prostate cancer imaging is angiogenesis. This complex physiological process, which is required for cancer growth beyond 1 mm, triggers a chaotic microvascular growth that is characterized by an increase in microvascular density, tortuosity, and extravascular leakage.

In this thesis, a novel characterization of the angiogenesis-induced changes in the microvascular architecture is proposed by assessment of dispersion. While the effects of angiogenesis on microvascular perfusion are complex and contradictory, dispersion is mainly determined by multipath trajectories and is directly influenced by microvascular density and tortuosity. Dispersion assessment is pursued by modeling the transport kinetics through the microcirculation as a convective dispersion process. This process is visualized by dynamic contrast-enhanced ultrasound imaging after an intravenous injection of an ultrasound-contrast-agent bolus. Acoustic time-intensity curves are obtained at each image pixel covering the prostate and converted into indicator dilution curves representing the relative contrast-agent concentration as function of time.

In a first approach for dispersion analysis, the measured indicator dilution curves are fitted by a modified Local Density Random Walk model. This model describes the distribution of contrast-agent transit-times by an analytical solution of the convective diffusion equation. The proposed model modification allows estimation of a local, dispersion-related parameter κ at each pixel covering the prostate. Subsequently, a parametric dispersion image can be constructed by displaying the κ estimates as a color-coded value overlaid on the ultrasound

image. The parameter-estimation accuracy is increased by a maximum-likelihood algorithm, based on modeling the indicator dilution curve as the observed histogram of the underlying transit-time distribution. This algorithm may be generally applicable in indicator dilution analysis.

An alternative approach for dispersion analysis involves spatiotemporal analysis. The similarity between indicator dilution curves is shown to be inversely related to dispersion. Consequently, dispersion can be estimated indirectly as the similarity between the indicator dilution curve at each pixel and those curves measured at surrounding pixels. This local assessment does not require curve-fitting and can be normalized by choosing suitable similarity measures that are insensitive to time shift, such as the coherence of amplitude spectra. A dedicated spatial filter is proposed to prevent ultrasound speckle from affecting the spatial similarity estimation by regularization of the speckle size. In addition, time-windowing is adopted to select the most relevant time-segment of the indicator dilution curve for similarity analysis. By providing temporal realignment, time-windowing also permits similarity assessment by the correlation coefficient.

In a preliminary study, the obtained parametric images are compared to histology, obtained from patients referred for radical prostatectomy. The spatial similarity analysis provides the highest receiver-operating-characteristic curve area (0.89) to discriminate between healthy and cancerous tissue. In a more extensive clinical validation, based on 38 recordings obtained from 11 patients, the utility of the parametric images for localization of prostate cancer is compared to that of multiparametric magnetic resonance imaging. The results show that analysis of contrast-ultrasound dispersion provides a higher sensitivity and a slightly lower negative predictive value than multiparametric magnetic resonance imaging.

In conclusion, assessment of dispersion is a promising new alternative for detection of angiogenesis in prostate cancer that could enable targeting of biopsies and focal therapies. The current results motivate towards a more extensive validation. In the future, three-dimensional ultrasound imaging may further improve the method. In addition, dispersion imaging may be tested with different imaging modalities and in different forms of cancer.

Contents

Abbreviations, notation, and symbols

List of abbreviations

AT	Appearance time
ADC	Apparent diffusion coefficient
AUC	Area under the curve
CT	Computed tomography
CUDI	Contrast-ultrasound dispersion imaging, contrast-ultrasound diffusion imaging[1]
CZ	Central zone
DCE-MRI	Dynamic contrast-enhanced magnetic resonance imaging
DCE-US	Dynamic contrast-enhanced ultrasound
DICOM	Digital imaging and communications in medicine
DR	Dynamic range
DWI	Diffusion-weighted imaging
FGF	Fibroblast growth factor
FWHM	Full width at half-maximum
IDC	Indicator dilution curve
LDRW	Local density random walk
MI	Mechanical index
ML	Maximum likelihood
mpMRI	Multiparametric magnetic resonance imaging
mpUS	Multiparametric ultrasound
MRI	Magnetic resonance imaging
MRSI	Magnetic resonance spectroscopy imaging
MTT	Mean transit time
MVD	Microvascular density
NLS	Nonlinear least-squares
NPV	Negative predictive value
NSR	Noise-to-signal ratio
PDF	Probability density function
PET	Positron emission tomography
PI	Peak intensity
PPV	Positive predictive value

[1] In [J1], and therefore also in Chapter 2, the proposed method CUDI is referred to as contrast-ultrasound diffusion imaging.

PSA	Prostate-specific antigen
PT	Peak time
PZ	Peripheral zone
ROC	Receiver operating characteristic
ROI	Region of interest
SNR	Signal-to-noise ratio
SPECT	Single-photon emission computed tomography
TDC	Time-density curve
TIC	Time-intensity curve
TRUS	Transrectal ultrasound
TZ	Transition zone
UCA	Ultrasound contrast agent
VEGF	Vascular endothelial growth factor
VEGFR2	Vascular endothelial growth factor receptor 2
WIT	Wash-in time

Notation

x	Scalar
$\hat{x}_{\mathrm{ML}}$	Maximum likelihood estimate of x
$\hat{x}_{\mathrm{NLS}}$	Nonlinear least-squares estimate of x
$\mathbf{x}$	Vector
$\lvert\mathbf{x}\rvert$	Modulus of $\mathbf{x}$
$\bar{x}$	Mean value of x
$p(x)$	Probability density function over x
$p(x\lvert y)$	Conditional probability density function over x given y
$\mathbf{E}\{x\}$	Expectation of x
$\mathbf{Var}\{x\}$	Variance of x

List of symbols

α	Gamma-variate model parameter
β	Gamma-variate model parameter
γ_1	Skewness (normalized third central moment)
$\boldsymbol{\theta}$	IDC model parameter vector
κ	LDRW local dispersion parameter

λ	LDRW skewness parameter
μ	LDRW mean-transit-time parameter, lognormal model parameter (only in selected parts of Chapter 3)
ρ	Normalized spectral coherence
ρ_{prev}	Coherence as derived in Chapter 4 (used only in Chapter 5)
σ	Standard deviation, lognormal model parameter (only in selected parts of Chapter 3)
σ_1^2	Spatial variance of UCA bolus distribution at $t = t_1$ [m^2]
σ_{ax}	Gaussian image filter parameter for the axial speckle-grain size [mm]
σ_{d}	Gaussian image filter parameter for the desired speckle-grain size [mm]
σ_{lat}	Gaussian image filter parameter for the lateral speckle-grain size [mm]
τ	Substitution variable [s]
ω	Angular frequency [rad/s]
ω_{min}	Minimum angular frequency in the bandwidth of coherence analysis [rad/s]
ω_{max}	Maximum angular frequency in the bandwidth of coherence analysis [rad/s]
a_{CI}	Sensitivity of acoustic intensity to UCA concentration [a.u./(mg/L)]
a_{DR}	Dynamic-range parameter
a	Axial speckle-grain size [mm]
A	Tube cross-sectional area [m^2]
b	Lateral speckle-grain size [mm]
C	UCA concentration ([mg/L] or [mL/L]), number of indicator particles (only in Chapter 3)
d	Imaging depth [cm]
D	Diffusion or dispersion coefficient [m^2/s]
D_ℓ	Local diffusion or dispersion coefficient [m^2/s]
f_s	Sampling frequency [Hz]
$g(\cdot)$	Gray-level mapping
G	Gray level (luminance)
$H(\sigma)$	Gaussian image filter of order σ
H_{d}	Gaussian image filter characterizing the desired speckle-grain size
H_{reg}	Speckle regularization filter
I	Acoustic intensity [a.u.]
I_0	Background intensity [a.u.]
k	Number of indicator particles
K	Total number of indicator particles
$K_0(\cdot)$	Modified Bessel function of the second kind

L	Distance between injection and detection positions [m]
$\mathcal{L}(\cdot)$	Likelihood function
m	Injected UCA mass dose [kg]
m_i	Central moment of order i
M_i	Moment of order i
$M_1\|_{t_0=0}$	LDRW Moment of order i under the constraint $t_0 = 0$
n	Time sample index
n_{Tr}	Truncation index
N	Number of time samples
p	Probability
$q(\cdot)$	Dynamic-range compression function
Q	Quantization level
Q_0	Quantization level at background intensity
r	Correlation coefficient
R^2	Determination coefficient
$S(\omega)$	Magnitude spectrum of IDC $C(t)$
t	Time [s]
t_0	Injection time [s]
$\tilde{t}_0$	Theoretical injection time based on local hemodynamic parameters [s]
t_1	Time just before UCA bolus passes detection site [s]
t_{app}	Appearance time (the first time UCA microbubbles are present) [s]
t_{Tr}	Truncation time [s]
Δt	Time interval, time step [s]
v	Velocity [m/s]
v_ℓ	Local velocity [m/s]
x	Position [m]
x_0	Injection position [m]
x_1	Mean of UCA spatial distribution at $t = t_1$ [m]
x_d	Detection position [m]
Δx	Distance between x_1 and x_d [m]
y	Random variable

CHAPTER 1

Introduction

This Chapter provides a general background on prostate cancer. It is discussed how imaging techniques could support the diagnosis and treatment of prostate cancer. In addition, an overview of modern prostate cancer imaging techniques is provided.

1.1 Prostate anatomy and prostate cancer

The prostate is a small gland in the male reproductive system. It is positioned just below the bladder, surrounding the urethra. A normal human prostate is typically said to be approximately the size of a walnut. Anatomically, the prostate can be divided into several zones [1], as shown in Fig. 1.1. The peripheral zone comprises about 70% of the prostate gland (PZ) in young men. In about 70 to 80% cases, prostate cancer originates from this zone [2]. The central zone (CZ) surrounds the ejaculatory ducts; the transition zone (TZ) surrounds the urethra and grows throughout the entire life. In patients with benign prostatic hyperplasia, excessive TZ growth is responsible for various voiding problems.

Prostate cancer is the most commonly diagnosed form of cancer in men in the Western world. In the United States, 238,590 new cases of prostate cancer and 29,720 deaths due to prostate cancer are expected in 2013; this accounts for 28% of all new cancer cases and for 10% of all cancer-related deaths in men [3]. In Europe, 416,700 new prostate cancer cases and 92,200 deaths due to prostate cancer are estimated in 2012, accounting for 22.8% of all new cancer cases and 9.5% of all cancer-related deaths in men [4].

Many men have latent forms of prostate cancer that do not lead to symptoms of disease [5]. Prostate cancer is found during autopsy in a significant percentage of men who died for different reasons [6]. In fact, the prevalence of prostate cancer in men aged between 70 and 80 years is estimated at 67% [7]. The reported statistics also highlight the influence

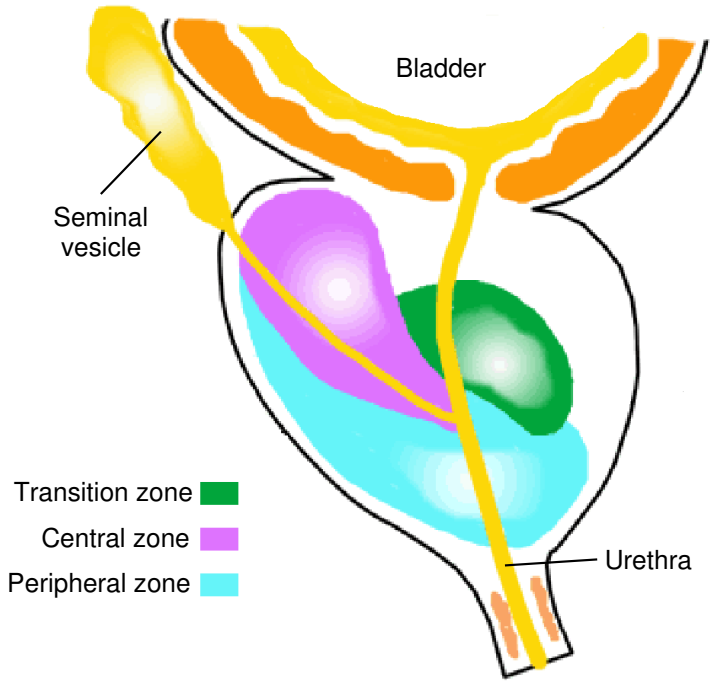

Figure 1.1 *Zonal anatomy of the prostate.*

of age on the prevalence of prostate cancer: it is widely recognized that prostate cancer is predominantly found in men of at least 50 years old [3].
Besides age, another important factor in the management of prostate cancer is its aggressiveness, defined as the risk of developing metastasis. Aggressiveness (or grade) is measured by the Gleason score, based on microscopic analysis of the level of cell differentiation in prostate tissue samples [8]. The level of cell differentiation is categorized in patterns ranging from 1 (well differentiated) to 5 (poorly differentiated). The Gleason score is then calculated by adding the grade of the most common pattern and the highest grade observed in the specimen. In practice, scores up to 5 are not considered harmful; a score of 6 is associated with a low aggressiveness. In the widely adopted D'Amico criteria, a Gleason score of 7 is associated with an intermediate risk and a score of at least 8 with a high risk [9]. These criteria highlight the importance of the Gleason score for determining the clinical significance of prostate cancer, which indicates whether treatment is required. Clinically significant cases of prostate cancer typically have a tumor volume of at least 0.5 cm^3 [10].

1.2 Current prostate cancer care

In current clinical practice, the suspicion for prostate cancer is assessed by minimally invasive tests, such as prostate-specific antigen (PSA) blood test, rectal examination, and transrectal ultrasound (TRUS).
PSA is an enzyme secreted by the prostate gland. After the discovery that the PSA concentration in the serum of men with prostate cancer is often elevated, the PSA level has been adopted on a large scale as a marker for prostate cancer [11]. Besides the PSA level, additional diagnostic information can be obtained by monitoring the evolution of the PSA level over time, e.g. by the PSA velocity or the PSA doubling time [12]. Important drawbacks of the PSA test are, however, the high false-positive rate (about 76%) [13] and the significant prevalence of prostate cancer among men with PSA levels below the common threshold of 4 ng/mL [14].
During a rectal examination, the doctor palpates the prostate by slipping his finger through the rectum. Stiff tissue areas can indicate the presence of prostate cancer. However, as only part of the prostate can be assessed by a rectal exam, many cancers are missed [15]. Moreover, this method is subject to a significant inter-observer variability [16].
TRUS is used to inspect the prostate gland for irregularities and to assess the prostate volume [2]. Fig. 1.2 shows an example of a TRUS image in which the anatomical structure of the prostate can be visualized. Prostate cancer is sometimes visible on a TRUS image as a hypoechoic region. However, TRUS cannot detect prostate cancer on a sufficiently reliable basis [17].

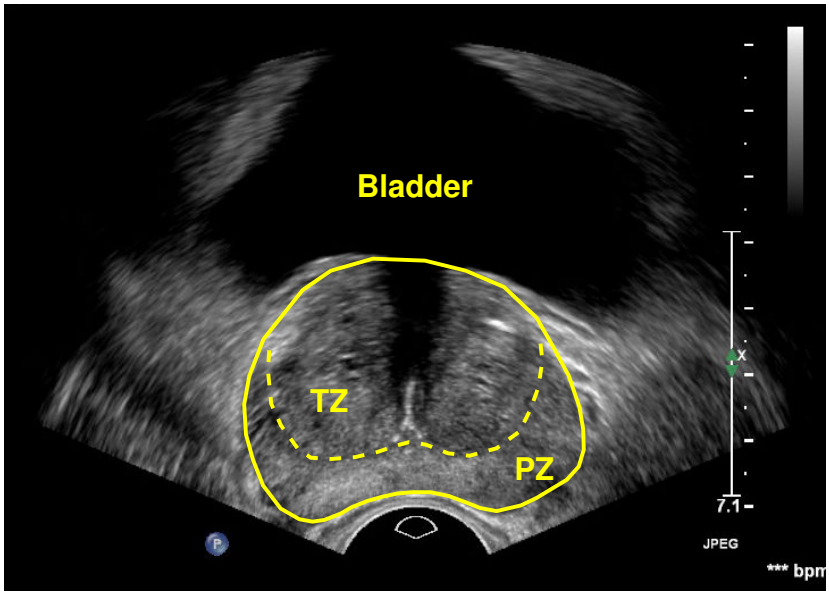

Figure 1.2 *Transversal TRUS image of the prostate. The prostate contour (solid line) and the boundary between the PZ and the TZ (dashed line) are delineated. The bladder is visible as black region in the top of the image, behind the prostate; the urethra is also visible as the bright shape in the middle of the prostate.*

Because these three methods are not sufficiently reliable to diagnose prostate cancer by themselves, they are currently used for patient stratification only [18]. If cancer is suspected, the patient undergoes systematic biopsies [19]. In this invasive investigation, between 6 and 16 prostate tissue samples are harvested using a core needle. For optimal sampling of the prostate, the samples are commonly taken based on a geometric scheme using TRUS guidance [2]. Each biopsy carries a small risk of complications such as infection [20]. Because the cancer detection sensitivity of a single set of biopsies is not sufficiently high [21], repeated biopsy investigations are often necessary. In fact, cancer is detected in 10-23% of all patients undergoing repeated biopsies [22, 23].

In case of positive biopsies, if cancer remains confined to the prostate, radical treatment, i.e., treatment of the entire prostate gland, is commonly adopted. Examples of such treatments are radiotherapy, brachytherapy, or radical prostatectomy. The risk for permanent side effects presents a significant downside to such treatments [24]. For example, one year after radical prostatectomy, incontinence and sexual function are considered a moderate-to-big problem by 14% and 52% of all patients, respectively [25].

In the current situation, many men undergo systematic biopsies, mainly due to the limited specificity of the PSA test [18]. Since the introduction of PSA testing, the number of men that are annually diagnosed with prostate cancer has risen significantly [4, 24]. However, clinically insignificant cancers, which are of no threat to the patient, are being detected in a sizeable proportion of these men [5]. As a result, the risks of overdiagnosis and overtreat-

ment have become significant issues in prostate cancer care [24]. In two large randomized trials, the potential benefits of PSA-based screening for prostate cancer did not outweigh the drawbacks associated to subsequent treatment [13, 26]. In fact, to prevent one additional prostate-cancer death by PSA-base screening, 1410 additional men would need to be screened and 48 additional men would have to be treated [13].
With the purpose of preventing overtreatment, active surveillance has been gaining interest as an alternative to invasive treatment in men with low-risk prostate cancer [27, 28]. In fact, in a randomized trial, active surveillance and radical prostatectomy resulted in similar mortality rates [29]. However, the limited accuracy of the diagnostic tools available for surveillance, together with patient anxiety, still pose significant issues for this strategy [28].
Focal therapy is another strategy to reduce the side effects of conventional radical treatments in localized prostate cancer [30]. By targeting treatment to the cancerous region and by leaving significant parts of the prostate unharmed, focal therapy aims to preserve the quality of life of the patient. Cryotherapy [31] and high-intensity focused ultrasound [32] are the most widely investigated focal treatment modalities. Additional modalities include photodynamic therapy [33], photothermal ablation [34], focal brachytherapy [35], focal radiation therapy [36], radiofrequency ablation [37] and irreversible electroporation [38]. Although many techniques show promising results, localization remains an important concern as systematic biopsies do not provide sufficient localization for a proper implementation of focal therapy [39].

1.3 The potential role of prostate cancer imaging

The current overdiagnosis and overtreatment problems in prostate cancer care result mainly from diagnostic limitations. Imaging methods have the potential to address many of these problems. By offering a better differentiation between clinically significant and latent cancers, accurate prostate cancer imaging methods may significantly improve patient stratification. With less men undergoing biopsies, imaging methods could reduce the overdiagnosis problem. In addition, imaging methods may mitigate the consequences of overdiagnosis by providing accurate prostate cancer localization. Accurate image-guided biopsy targeting may reduce the number of biopsies per patient, and, therefore, the morbidity of diagnostic methods. Accurate prostate cancer imaging would also reduce overtreatment by enabling efficient guidance for focal therapies. Furthermore, imaging methods could be used for monitoring purposes in active surveillance programs and in treatment follow-up. As a result, the morbidity of prostate cancer diagnosis and treatment could be significantly reduced by appropriate imaging methods.
This decrease in morbidity by image-guided biopsies and therapies would result from leav-

ing healthy parts of the prostate unharmed. Because failure to diagnose or treat clinically significant prostate cancer may have significant consequences for the patient, it is very important that the adopted imaging does not misclassify clinically significant cancer as healthy tissue. Therefore, the negative predictive value (NPV, i.e., the percentage of all negative observations that are correct) and the sensitivity (the percentage of all cancer cases that are detected) are, in these applications, more important than the positive predictive value (PPV, i.e., the percentage of positive observations that are correct) and the specificity (the percentage of all healthy regions classified as such).

1.4 Angiogenesis as imaging marker for cancer

Many scientists have been searching for prognostic indicators for cancer that could be assessed by minimally invasive imaging methods. In this context, the discovery of the relationship between cancer growth and angiogenesis represented a fundamental milestone [40]. Angiogenesis, which is a hallmark in the growth of a wide range of pathologies, concerns the development of a dense microvascular network [41]. The newly formed blood vessels supply oxygen and nutrients to the neoplastic tissue.

In cancer development, the role of angiogenesis is particularly crucial: without blood vessels, tumors cannot grow beyond a critical size (in the order of a millimeter) or metastasize to different organs [41]. Without this microvascular growth, tumors will remain in a dormant state. Angiogenesis is a key process also in the progression of prostate cancer [42–45]. Because angiogenesis predicts the risk of metastasis [43], it is an important prognostic indicator for prostate cancer progression.

The activation of angiogenesis in the early stages of cancer development is often referred to as the "angiogenic switch". This switch is controlled by the balance of pro- and anti-angiogenic factors: angiogenesis may be activated by promotion of pro-angiogenic factors or by inhibition of anti-angiogenic factors [46, 47]. Vascular endothelial growth factor (VEGF) and fibroblast growth factor (FGF) are examples of pro-angiogenic factors; anti-angiogenic factors include e.g. interferons, angiostatin, and thrombospondin-1 [46].

With the formation of new microvessels, angiogenesis induces a number of changes to the microvascular structure. As new microvessels are formed, the microvascular density (MVD) is increased by angiogenesis. In addition, the newly formed vessels are structurally and functionally different from normal vessels: in comparison to normal vessels, tumors vessels are often tortuous, irregular, and leaky, i.e., they feature a high permeability. Furthermore, angiogenesis causes a highly disorganized microvascular structure with shunting vessels and excessive branching [41, 48].

The structural and functional changes in the microvascular architecture may be exploited

as a marker for angiogenesis. In histological studies, MVD quantification has already been proven to provide a significant prognostic value for prostate cancer progression [43–45, 49–52]. For this reason, many scientists have pursued noninvasive assessment of microvascular features related to angiogenesis by means of quantitative imaging methods in order to achieve reliable prostate cancer imaging [53].

1.5 Emerging techniques for prostate cancer imaging

Accurate imaging of prostate cancer has been pursued by many researchers, using several different technologies. This section provides an overview of the adopted methods, their principles, as well as their value in clinical practice. Computed tomography (CT) is not discussed here, because it is not considered useful in prostate cancer detection [54].

1.5.1 Nuclear imaging

Prostate cancer features an increase in metabolism, which can be observed by a higher uptake of glucose. By adopting a radiolabeled analogue of glucose as a tracer, nuclear imaging can exploit this higher glucose uptake to identify cancer lesions. The tracer distribution is imaged by a Gamma-camera [55], either by single-photon emission computerized tomography (SPECT) or positron emission tomography (PET) [56]. The predominantly adopted tracers in prostate cancer are ^{18}F-FDG, ^{18}F- or ^{11}C-acetate, and ^{18}F- or ^{11}C-choline [57].
Due to the limited spatial resolution and the adverse effects resulting from exposure to ionizing radiation, PET and SPECT are not ideally suited for early prostate cancer imaging. Instead, research is focused on the detection of recurrent disease and metastasis [57]. With this aim, ProstaScint ® (Cytogen Corporation, Princeton, NJ), i.e., ^{111}In-capromab pendetide SPECT, was also introduced [58], but its value remains controversial [59].

1.5.2 Magnetic resonance imaging

Magnetic resonance imaging (MRI) investigates the relaxation of hydrogen protons after the application of an electromagnetic radiofrequency pulse [60]. MRI is characterized by an excellent contrast-resolution and is especially useful in soft tissues, because of the abundance of water molecules. Various relaxation properties can be measured, such as the longitudinal (T1) and transverse (T2) relaxation times. T1- and T2-weighted images provide anatomical information. In general, T1-weighted imaging is not used for prostate cancer imaging, whereas T2-weighted imaging is not considered sufficiently accurate for detection of prostate cancer [53].

Whereas conventional techniques can only assess anatomical information, functional and metabolic information can be obtained by more advanced techniques, such as diffusion-weighted imaging (DWI), MR spectroscopy imaging (MRSI), and dynamic contrast-enhanced MRI (DCE-MRI) [54]. Nowadays, a combination of these techniques, referred to as multi-parametric MRI (mpMRI), is commonly adopted. Although the value for prostate cancer localization appears to be very promising, widely different results are reported by different groups [61–63].

Diffusion-weighted imaging

The diffusion process of water molecules can be imaged by DWI [64]. Because water diffusion is constrained by obstacles, such as membranes, differences in the apparent diffusion coefficient represent structural differences. In particular, due to the high cellular density in prostate cancer, the observed apparent diffusion coefficient is typically lower than in surrounding tissues [65].

Magnetic resonance spectroscopy imaging

Similar to nuclear imaging techniques, metabolic information can be assessed by MRSI. In this technique, the relative concentration of various chemicals is estimated from the peaks in the measured spectral profiles [66]. Because prostate cancer typically features relatively low citrate levels and high choline levels, the ratio between these levels is adopted to detect prostate cancer. A high prostate cancer detection accuracy has been reported [67]. Drawbacks are the low spatial resolution (approximately 5 mm) and the long acquisition time (about 15 minutes).

Dynamic contrast-enhanced magnetic resonance imaging

DCE-MRI involves an intravenous injection of a contrast agent. Although various types of contrast media are available for clinical use, the most commonly adopted agents, based on Gadolinium (Gd), shorten the T1 relaxation time [68]. Most Gd-based contrast agents are small molecules that can traverse into the extravascular space. Blood pool agents, which remain within the circulatory system, are also available. As shown in Fig. 1.3, DCE-MRI enables dynamic measurement of the contrast-agent concentration, providing the opportunity to estimate parameters related to blood perfusion and, in case of extravasating agents, vascular wall permeability [69]. This information adds significant value for prostate cancer detection [70]. Although the adopted contrast agents are generally safer than radioactive tracers, Gd-based agents have been associated with an increased risk of developing nephrogenic systemic fibrosis [71].

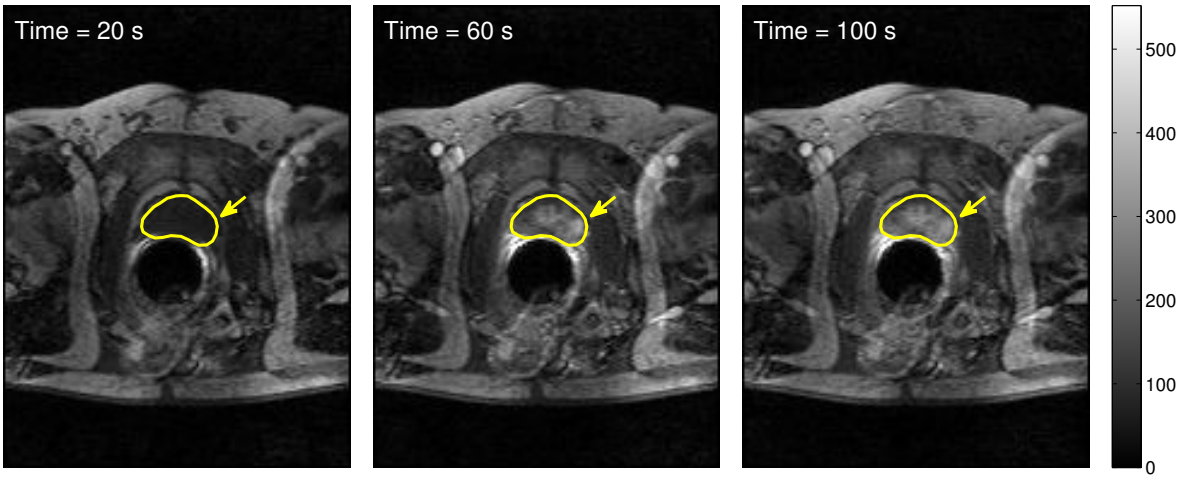

Figure 1.3 *DCE-MRI of the prostate obtained with 1.5 T at approximately 20 (left), 60 (middle) and 100 (right) seconds after injection of a Gd contrast-agent bolus. The prostate is delineated in the DCE-MR images; the lesion indicated by the arrow was confirmed to be prostate cancer after radical prostatectomy. Courtesy of the Department of Radiology, Academic Medical Center University of Amsterdam, The Netherlands.*

1.5.3 Ultrasound imaging

By measurement of the backscatter of ultrasound waves in biological tissue, important anatomical information can safely be assessed by ultrasound imaging [72]. Characterized by its cost-effectiveness, bedside availability, and high spatial resolution, TRUS imaging has been routinely adopted in the management of prostate cancer since its introduction in 1971 by Watanabe *et al.* [73]. Although TRUS cannot detect prostate cancer on a sufficiently reliable basis [17], it is used for assessment of the prostate volume, inspection of the prostate gland, and guidance of biopsies [2]. Against this background, new developments in ultrasound imaging are ideally suited for early prostate cancer imaging.

Ultrasound tissue characterization

Tissue characterization has been proposed by computerized analysis of TRUS images, initially based on B-mode images similar to those in Fig. 1.2 [74], but later also on radiofrequency signals [75]. Recently, HistoScanning^{TM} (AMD, Waterloo, Belgium) has been introduced in clinical practice for localizing prostate cancer as a computer-based analysis of radiofrequency TRUS imaging data [76]. The initial promising results have, however, yet to be confirmed in larger multicenter studies.

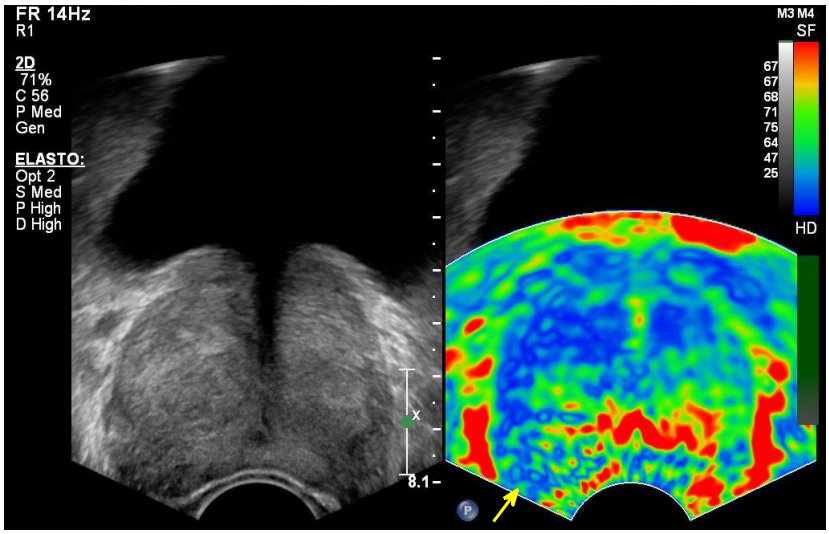

Figure 1.4 *TRUS elastography image of the prostate. The indicated lesion in the right peripheral zone (i.e., in the bottom left of the image) has a high stiffness (characterized by a blue color) and was confirmed to be prostate cancer (Gleason 7) after biopsy.*

Ultrasound elastography

With ultrasound elastography, the elastic properties of soft tissues can be assessed. After gently pushing the TRUS probe against the prostate gland, the elastic properties can be extracted from the measured compression and decompression of tissue. Due to its increased cellular density, prostate cancer typically features a higher stiffness than healthy tissue, as shown in Fig. 1.4. Ultrasound elastography shows a promising value for prostate cancer detection [77]. A major drawback of the method is its operator dependency.
Shear-wave elastography is a new technique, made possible by the development of ultrafast ultrasound imaging [78], which enables an absolute measurement of tissue stiffness. To this end, shear waves are generated by the transmitted ultrasound pulses. By ultrafast ultrasound imaging, the propagation of these shear waves through tissue can be observed, thereby allowing estimation of the Young's modulus [79]. The initial results of this method have been very promising [80].

Doppler ultrasound

Blood flow velocity can be estimated by ultrasound imaging based on the Doppler principle, i.e., from the frequency shift in backscattered ultrasound waves [81]. Color Doppler ultrasound quantifies flow velocity and direction as the mean Doppler frequency shift. However, this technique is not ideally suited for prostate cancer localization, partly due to its limited sensitivity and artifacts, such as the angle dependency [82].
Power Doppler, an alternative technique based on integration of the Doppler signal power

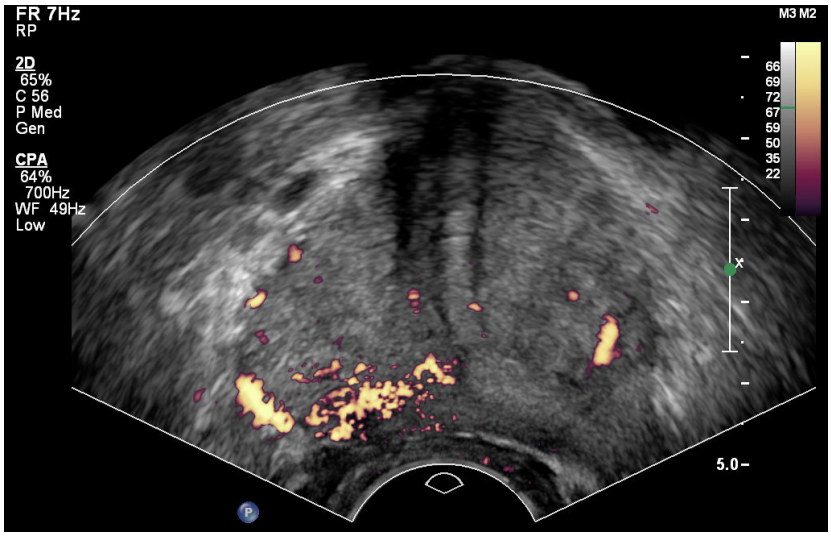

Figure 1.5 *TRUS power Doppler image of the prostate. The strong enhancement in the right peripheral zone (i.e., in the bottom left of the image) indicates a high suspicion for prostate cancer, which was confirmed by biopsy.*

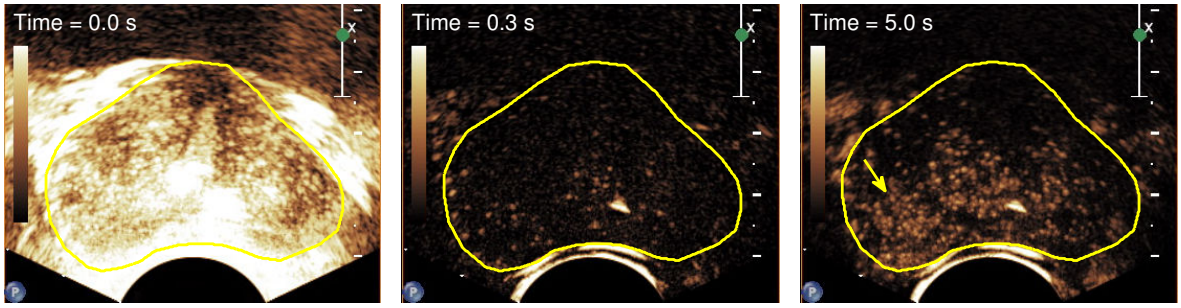

Figure 1.6 *DCE-US images of the prostate based obtained by the destruction-replenishment principle. In all DCE-US images, the prostate is delineated. On the left, a high-intensity burst is applied, causing microbubble disruption and strong backscattering. Almost no UCA microbubbles are observed immediately after this burst (middle). After 5 s, this plane of the prostate is partially reperfused (right). The indicated enhancement in the right peripheral zone (i.e., in the bottom left of the image) was confirmed to correspond to prostate cancer after radical prostatectomy.*

[83], is more sensitive to slow flow than color Doppler. A TRUS power Doppler image is shown in Fig. 1.5. Yet, these techniques have not proven sufficiently reliable for prostate cancer imaging [84], mainly because of resolution limitations: Doppler ultrasound is unable to detect flow in the smallest microvessels.

Dynamic contrast-enhanced ultrasound

Visualization of flow in the microcirculation is possible with dynamic contrast-enhanced ultrasound (DCE-US) imaging [85]. The administered ultrasound contrast agents (UCAs)

consist of encapsulated gas microbubbles with a size between 1 and 10 μm, i.e., similar to red blood cells. Different from most Gd-based MRI contrast agents, extravasation is not possible due to the microbubble size. After intravenous injection, the microbubbles remain stable in the circulation for several minutes.

UCAs were initially used with limited success for enhancement of Doppler techniques [86]. After recognizing that the commonly adopted acoustic pressures in Doppler ultrasound disrupt the UCA microbubbles, Wei *et al.* introduced the destruction-replenishment principle [87]. In this principle, which was initially implemented by intermittent imaging methods [86], tissue reperfusion is measured after disrupting all microbubbles in the imaging plane by a high-intensity burst. By lowering the acoustic pressure, UCA microbubbles can be imaged non-destructively. In this regime, the microbubble oscillation creates a strongly nonlinear acoustic backscattering. A wide variety of techniques, referred to as contrast-specific imaging techniques, have been specifically developed to isolate the nonlinear signals backscattered by microbubbles from those backscattered by blood and tissue [88]. Examples of such techniques are harmonic imaging, power modulation, and pulse inversion [88–90]. These techniques have enabled real-time imaging of the UCA concentration evolution over time, either after a destructive burst or for measurement of the passage of an intravenously injected UCA bolus through the image plane [91]. An example of DCE-US imaging of the prostate based on the destruction-replenishment technique is shown in Fig. 1.6.

Several approaches are available to quantify perfusion by DCE-US. In the initial destruction-replenishment model used in cardiology, replenishment was modeled as in a single compartment [87]. Later, this model was improved to account for the ultrasound beam profile [92] and for the lognormal flow distribution in a branching tree structure to represent the microvascular architecture [93]. For the bolus injection technique, classical indicator dilution models can be adopted to describe the UCA transport process [94–96].

Quantitative analysis is typically performed based on time-intensity curves (TICs), which measure the backscattered acoustic intensity in a region of interest (ROI) in the ultrasound image as a function of time [97, 98]. Calibration studies indicate the acoustic intensity to be approximately linearly related to the microbubble concentration [99]. Therefore, linearization of compressed DCE-US data is necessary prior to model-based analysis [94]. In practice, however, semi-quantitative TIC parameters based on amplitude and timing features are often estimated [91, 100].

For localization of prostate cancer, qualitative interpretation of the observed DCE-US patterns has shown a promising value [101, 102]. Important drawbacks of this method, such as the learning curve and the inter-observer variability [103], may be overcome by quantitative DCE-US analysis.

A new development in DCE-US imaging involves targeted microbubbles, which bind to spe-

cific receptors that are enhanced in angiogenic blood vessels. BR55 (Bracco, Milan, Italy), which consists of microbubbles that are functionalized with a heterodimer peptide targeted to vascular endothelial growth factor receptor 2 (VEGFR2) [104], is the first targeted UCA that was tested in humans [105].

1.6 Scope of this thesis

This thesis presents a new quantitative DCE-US approach that aims to detect angiogenesis, in order to achieve reliable prostate cancer imaging. As opposed to existing methods that aim to quantify perfusion, this approach is based on analysis of the UCA dispersion kinetics through the prostate.

As already described in Sec. 1.4, angiogenesis results in a highly disorganized microvascular network containing tortuous, dilated, and leaky vessels. As a result, blood flow in tumors is chaotic and variable [41]. It is, therefore, difficult to predict the effects of angiogenesis on perfusion: a higher microvascular density and the presence of arteriovenous shunts are expected to increase perfusion. However, this effect can be counterbalanced by an increased flow resistance, caused by the irregular diameter and high tortuosity of the microvessels and the increase in interstitial pressure due to extravascular leakage [48, 106].

The main hypothesis of this thesis is that angiogenesis-induced microvascular changes are better represented by UCA dispersion rather than perfusion kinetics. In this context, dispersion describes the spatiotemporal UCA spreading, which may result from several different factors.

In the classical work of Taylor [107], the dispersion of an indicator is described in an infinitely-long tube with a laminar flow regime, as schematically shown in Fig. 1.7. In this tube, the transport kinetics can be described as a convective dispersion process [108, 109]. In this scenario, dispersion results from the combination of molecular diffusion, due to the concentration gradient, and the parabolic flow profile in the tube cross-section.

Although flow in the microcirculation is generally more complex than in a relatively simple tube, the dispersion of indicator particles can be described similarly in both scenarios. By considering the microcirculation as a distributed network, similar to a porous medium, dispersion may also result from flow through the many different capillaries that create multi-path trajectories in the microvascular architecture [110]. In this characterization, dispersion is directly determined by network features, such as porosity and tortuosity [111, 112], that can be interpreted in terms of the microvascular architecture. Porosity describes the relative amount of pores, i.e., the number of pathways for the indicator to travel across the network. Dispersion is positively related to porosity, which can be viewed analogously to MVD. As a result, the increased MVD in angiogenesis may increase dispersion as a result

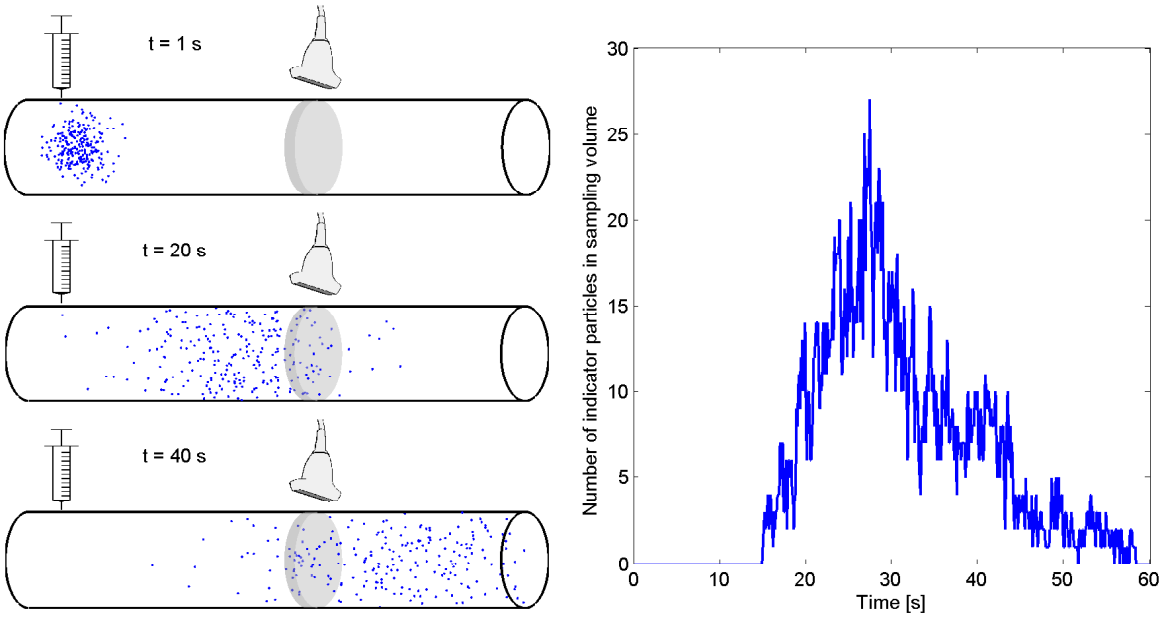

Figure 1.7 *Schematic overview of convective dispersion of indicator particles after injection in a slow, laminar flow regime in an infinitely-long tube. Three snapshots of the spatial indicator distribution, obtained at different times after injection, are shown on the left; an indicator dilution curve (IDC), showing the detected amount of indicator particles in the highlighted cross-sectional volume as function of time, is plotted on the right.*

of an increased porosity. Tortuosity describes pores not being straight, but having many twists and turns. Although tortuosity can be defined in many ways, a common definition is the ratio between length of a pore and the distance between the pore ends [113]. Tortuosity is a hallmark of the irregularly-shaped microvessels that are typically observed in angiogenesis. Because tortuosity limits dispersion, tortuous microvessels in angiogenic structures may yield a lower dispersion than regular capillaries. Therefore, microvascular features that can be physically related to the presence of angiogenesis have a direct relation to the UCA dispersion kinetics.

This thesis describes a new methodology for detection of angiogenesis by quantification of UCA dispersion, based on modeling the UCA transport process by the convective dispersion equation. The local density random walk (LDRW) model is an analytical solution of this equation. This model provides a mathematical description in terms of flow velocity and dispersion for measured indicator dilution curves (IDCs), which describe the UCA concentration at a fixed measurement site as a function of time, as shown in Fig. 1.7.

The proposed method, contrast-ultrasound dispersion imaging (CUDI), involves transrectal DCE-US imaging of the prostate after intravenous injection of an UCA bolus. The obtained image sequences visualize the transport of this UCA bolus through the microcirculation, providing acoustic TICs at all pixels. A dedicated calibration allows these TICs to

be interpreted as IDCs that are suitable for dispersion analysis by the LDRW model.

1.7 Outline of this thesis

In Chapter 2, a strategy for CUDI based on a modification of the LDRW model is introduced. This modification involves a local boundary condition based on which the IDC can be derived as a local, analytical solution of the convective dispersion equation. As a result, a local parameter, κ, which is inversely related to dispersion, can be estimated by parametric curve-fitting of acoustic TICs acquired at each image pixel. The estimated values of κ can subsequently be displayed as a color-coded value at its associated pixel in order to construct a parametric dispersion image [J1].

Because curve-fitting of acoustic TICs obtained at a single pixel poses a challenging problem, a new algorithm for estimation of hemodynamic parameters from IDCs is proposed in Chapter 3. This algorithm exploits the fact that most IDC models are probability density functions that describe the distribution of microbubble transit-times. By interpreting measured IDCs as the observed histogram of microbubble transit-times, IDC model parameters can be estimated based on maximizing the likelihood of observing this histogram. Both an *in vitro* and an *in vivo* validation of this algorithm are performed [J6].

Chapter 4 describes an alternative strategy for CUDI that does not require model fitting. As opposed to different DCE-US quantification methods, this quantification strategy involves a complete spatiotemporal analysis of UCA transport. An indirect dispersion analysis, based on observed IDC shape variations in simulations of the convective dispersion equation, is performed by assessment of the spatial similarity among TICs sampled at neighboring pixels. In this first implementation, spatial similarity is computed at each pixel as the average coherence ρ between the TIC acquired at that pixel and the TICs acquired at the surrounding pixels according to a specific spatial kernel [J2].

The formal rationale for a dispersion analysis based on assessment of TIC similarity is described in Chapter 5. A monotonic relation between the dispersion-related parameter κ and the coherence ρ between two IDCs is derived. Moreover, two methodological improvements to the spatial similarity analysis are described in Chapter 5. A dedicated spatial filter is introduced to prevent anisotropic ultrasound speckle noise from affecting the spatiotemporal analysis. This spatial filter, which involves a Wiener deconvolution, is based on measurement of the local ultrasound speckle-grain size by two-dimensional autocovariance analysis [J4]. Another methodological improvement is provided by time windowing, which makes the spatial similarity analysis less sensitive to noise and more specific to TIC shape variations.

Chapter 6 describes an alternative spatial TIC similarity assessment by the correlation coef-

ficient r in the time domain [J5]. An analytical relation between κ and r is derived for this approach, which is made possible by proper realignment of TICs by the time-windowing method described in Chapter 5.
In Chapter 7, the potential clinical benefits of CUDI are explored. The value of CUDI for localization of prostate cancer is compared to that of qualitative DCE-US imaging and to that of qualitative and semi-quantitative mpMRI [J8]. This clinical validation is based on 38 DCE-US image sequences and mpMRI investigations obtained in 11 patients. The results show that analysis of contrast-ultrasound dispersion provides a higher sensitivity and a slightly lower negative predictive value than mpMRI.
Conclusions and future directions for research are discussed in Chapter 8. Most Chapters of this thesis are based on published journal articles. In particular, Chapters 2, 3, 4, 5, and 6 are based on [J1], [J6], [J2], [J4], and [J5], respectively. Chapter 7 is in preparation as [J8] for publication in a peer-reviewed journal.

1.8 List of author's publications

Refereed journal articles

[J1] **M. P. J. Kuenen**, M. Mischi, and H. Wijkstra, "Contrast-ultrasound diffusion imaging for localization of prostate cancer," *IEEE Trans. Med. Imag.*, vol. 30, no. 8, pp. 1493–1502, 2011.

[J2] M. Mischi, **M. P. J. Kuenen**, and H. Wijkstra, "Angiogenesis imaging by spatiotemporal analysis of ultrasound-contrast-agent dispersion kinetics," *IEEE Trans. Ultrason., Ferroelectr., Freq. Control*, vol. 59, no. 4, pp. 621–629, 2012.

[J3] M. Mischi, **M. P. J. Kuenen**, J. J. M. C. H. de la Rosette, W. Scheepens, and H. Wijkstra, "Prostaatkankerlokalisatie met 'dispersion' echografie," *Tijdschrift voor Urologie*, vol. 2, pp. 67–68, 2012.

[J4] **M. P. J. Kuenen**, T. A. Saidov, H. Wijkstra, and M. Mischi, "Contrast-ultrasound dispersion imaging for prostate cancer localization by improved spatiotemporal similarity analysis," *Ultrasound Med. Biol.*, vol. 39, no. 9, pp. 1631–1641, 2013.

[J5] **M. P. J. Kuenen**, T. A. Saidov, H. Wijkstra, J. J. M. C. H. de la Rosette, and M. Mischi, "Spatiotemporal correlation of ultrasound-contrast-agent dilution curves for angiogenesis localization by dispersion imaging," *IEEE Trans. Ultrason., Ferroelectr., Freq. Control*, vol. 60, no. 12, pp. 2665–2669, 2013.

[J6] **M. P. J. Kuenen**, I. H. F. Herold, H. H. M. Korsten, J. J. M. C. H. de la Rosette, H. Wijkstra, and M. Mischi, "Maximum-likelihood estimation for indicator dilution analysis," *IEEE Trans. Biomed. Eng.*, in press, available at http://dx.doi.org/10.1109/TBME.2013.2290375.

[J7] T. A. Saidov, C. Heneweer, **M. P. J. Kuenen**, H. Wijkstra, and M. Mischi, "Fractal dimension of tumor microvasculature by DCE-US: preliminary study in mice," in preparation.

[J8] M. Smeenge, **M. P. J. Kuenen**, M. Mischi, C. Lavini, M. Engelbrecht, M. van Santen, A. W. Postema, T. M. de Reijke, M. P. Laguna Pes, J. J. M. C. H. de la Rosette, and H. Wijkstra, "Detection and localization of prostate cancer: Additional value of quantification in dynamic contrast-enhanced ultrasound and multiparametric MRI," in preparation.

[J9] M. Mischi, L. Demi, M. Smeenge, **M. P. J. Kuenen**, A. W. Postema, J. J. M. C. H. de la Rosette, and H. Wijkstra, "Transabdominal contrast-enhanced ultrasound imaging of the prostate," submitted.

International conferences

[IC1] **M. P. J. Kuenen**, H. Wijkstra, and M. Mischi, "Contrast-ultrasound diffusion imaging of the prostate," in *2nd International Workshop on Focal Therapy and Imaging in Prostate & Kidney Cancer*, Noordwijk (The Netherlands), June 10-13, 2009.

[IC2] M. Mischi, **M. P. J. Kuenen**, H. Wijkstra, A. J. M. Hendrikx, and H. H. M. Korsten, "Prostate cancer localization by contrast-ultrasound diffusion imaging," in *Proceedings of the IEEE International Ultrasonics Symposium*, Rome (Italy), September 21-23, 2009, pp. 283–286.

[IC3] M. Mischi, **M. P. J. Kuenen**, H. Wijkstra, and H. H. M. Korsten, "Prostate cancer imaging," in *24th Annual Advances in Contrast Ultrasound - ICUS Bubble Conference*, Chicago (IL), October 22-23, 2009.

[IC4] **M. P. J. Kuenen**, M. Mischi, H. Wijkstra, A. J. M. Hendrikx, and H. H. M. Korsten, "Ultrasound contrast agent diffusion imaging for localization of prostate cancer," in *15th European Symposium on Ultrasound Contrast Imaging*, Rotterdam (The Netherlands), January 21-22, 2010, pp. 37–39.

[IC5] I. H. F. Herold, **M. P. J. Kuenen**, M. Mischi, and H. H. M. Korsten, "Blood volume and ejection fraction measurements using CEUS," in *15th European Symposium on Ultrasound Contrast Imaging*, Rotterdam (The Netherlands), January 21-22, 2010, pp. 55–56.

[IC6] M. Mischi, **M. P. J. Kuenen**, and H. Wijkstra, "Imaging of angiogenesis by contrast-enhanced ultrasound," in *25th Annual meeting of the Engineering and Urology Society*, San Francisco (CA), May 29, 2010, p. 106.

[IC7] M. Mischi, **M. P. J. Kuenen**, and H. Wijkstra, "Novel method for prostate cancer detection by contrast-enhanced ultrasonography," in *28th World Congress of Endourology & SWL*, Chicago (IL), September 1-4, 2010.

[IC8] M. Mischi, **M. P. J. Kuenen**, and H. Wijkstra, "Detection of cancer microvascularization by contrast-enhanced ultrasound," in *25th Annual Advances in Contrast Ultrasound - ICUS Bubble Conference*, Chicago (IL), September 28-29, 2010.

[IC9] **M. P. J. Kuenen**, M. Mischi, and H. Wijkstra, "Coherence-based contrast-ultrasound diffusion imaging for prostate cancer detection," in *Proceedings of the IEEE International Ultrasonics Symposium*, San Diego (CA), October 11-14, 2010, pp. 1936–1939.

[IC10] **M. P. J. Kuenen**, M. Mischi, and H. Wijkstra, "Prostate cancer localization by contrast ultrasound dispersion imaging based on spatial coherence analysis," in *16th European Symposium on Ultrasound Contrast Imaging*, Rotterdam (The Netherlands), January 20-21, 2011, pp. 55–57.

[IC11] M. Mischi, **M. P. J. Kuenen**, M. P. Laguna Pes, and H. Wijkstra, "Prostate cancer localization by assessment of ultrasound-contrast-agent dispersion," in *26th Annual Meeting of the Engineering and Urology Society*, Washington (DC), May 14, 2011, p. 16.

[IC12] M. Mischi, **M. P. J. Kuenen**, T. A. Saidov, W. Scheepens, H. H. M. Korsten, and H. Wijkstra, "Prostate cancer localization by CUDI: an update," in *26th Annual Advances in Contrast Ultrasound - ICUS Bubble Conference*, Chicago (IL), September 21-22, 2011.

[IC13] M. Mischi, **M. P. J. Kuenen**, T. A. Saidov, S. G. Schalk, W. Scheepens, and H. Wijkstra, "New developments in prostate cancer localization by contrast ultrasound dispersion imaging," in *17th European Symposium on Ultrasound Contrast Imaging*, Rotterdam (The Netherlands), January 19-20, 2012, pp. 16–19.

[IC14] M. Mischi, S. G. Schalk, M. Smeenge, F. Brughi, T. A. Saidov, **M. P. J. Kuenen**, R. P. Kuipers, M. P. Laguna Pes, J. J. M. C. H. de la Rosette, and H. Wijkstra, "Registration of ultrasound and histology data for validation of emerging prostate cancer imaging techniques," in *27th Annual Meeting of the Engineering and Urology Society*, Atlanta (GA), May 19, 2012, p. 79.

[IC15] M. Mischi, **M. P. J. Kuenen**, M. Smeenge, M. P. Laguna Pes, J. J. M. C. H. de la Rosette, and H. Wijkstra, "Contrast ultrasound dispersion imaging: a new approach for prostate cancer localization," in *30th World Congress of Endourology & SWL*, Istanbul (Turkey), September 4-8, 2012.

[IC16] C. Heneweer, T. A. Saidov, T. Liesebach, T. Persigehl, **M. P. J. Kuenen**, H. Wijkstra, C.-C. Gluer, M. Heller, and M. Mischi, "Classification of different tumor types by contrast ultrasound dispersion imaging," in *World Molecular Imaging Congress*, Dublin (Ireland), September 5-8, 2012.

[IC17] M. Mischi, C. Heneweer, T. A. Saidov, **M. P. J. Kuenen**, and H. Wijkstra, "Characterization of angiogenesis in prostate cancer by DCE-US," in *27th Annual Advances in Contrast Ultrasound - ICUS Bubble Conference*, Chicago (IL), September 20-21, 2012.

[IC18] **M. P. J. Kuenen**, T. A. Saidov, H. Wijkstra, and M. Mischi, "Spatiotemporal methods for prostate cancer detection by contrast-ultrasound dispersion imaging," in *Proceedings of the IEEE International Ultrasonics Symposium*, Dresden (Germany), October 7-10, 2012, pp. 1331–1334.

[IC19] T. A. Saidov, C. Heneweer, **M. P. J. Kuenen**, T. Liesebach, H. Wijkstra, and M. Mischi, "Contrast ultrasound dispersion imaging of different tumor types," in *Proceedings of the IEEE International Ultrasonics Symposium*, Dresden (Germany), October 7-10, 2012, pp. 2149–2152.

[IC20] M. Mischi, **M. P. J. Kuenen**, M. Smeenge, M. P. Laguna Pes, J. J. M. C. H. de la Rosette, and H. Wijkstra, "Contrast ultrasound dispersion imaging: a new option for prostate cancer diagnosis and treatment," in *Proceedings of the EAU Section of Urological Imaging (ESUI)*, Berlin (Germany), October 19-20, 2012.

[IC21] H. Wijkstra, M. Mischi, and **M. P. J. Kuenen**, "Contrast ultrasound dispersion imaging (CUDI)," in *Proceedings of the British Medical Ultrasound Society's 44th Annual Scientific Meeting*, Telford (United Kingdom), December 10-12, 2012, p. 47.

[IC22] M. Mischi, **M. P. J. Kuenen**, T. A. Saidov, C. Heneweer, and H. Wijkstra, "Prostate cancer imaging by DCE-US," in *18th European Symposium on Ultrasound Contrast Imaging*, Rotterdam (The Netherlands), January 17-18, 2013, pp. 17–19.

[IC23] T. A. Saidov, C. Heneweer, **M. P. J. Kuenen**, T. Liesebach, H. Wijkstra, and M. Mischi, "Fractal dimension of tumor microvasculature by CEUS: preliminary study in mice," in *18th European Symposium on Ultrasound Contrast Imaging*, Rotterdam (The Netherlands), January 17-18, 2013, pp. 85–89.

[IC24] M. Mischi, **M. P. J. Kuenen**, M. P. Laguna Pes, J. J. M. C. H. de la Rosette, and H. Wijkstra, "Contrast ultrasound dispersion imaging in prostate cancer diagnostics," in *28th Annual Meeting of the Engineering and Urology Society*, San Diego (CA), May 4, 2013, p. 89.

[IC25] **M. P. J. Kuenen**, T. A. Saidov, C. Heneweer, H. Wijkstra, and M. Mischi, "Detection of prostate cancer by contrast-ultrasound dispersion imaging," in *6th International Symposium on Focal Therapy & Imaging in Prostate & Kidney Cancer*, Noordwijk (The Netherlands), May 29-31, 2013.

[IC26] M. Mischi, **M. P. J. Kuenen**, S. Schalk, N. Bouhouch, H. Beerlage, and H. Wijkstra, "Angiogenesis imaging in prostate cancer," in *28th Annual Advances in Contrast Ultrasound - ICUS Bubble Conference*, Chicago (IL), October 3-4, 2013.

[IC27] **M. P. J. Kuenen**, I. H. F. Herold, H. H. M. Korsten, J. J. M. C. H. de la Rosette, H. Wijkstra, and M. Mischi, "Maximum-likelihood estimation for quantitative analysis in dynamic contrast-enhanced ultrasound," in *19th European Symposium on Ultrasound Contrast Imaging*, Rotterdam (The Netherlands), January 23-24, 2014, pp. 143–147.

[IC28] N. Bouhouch, L. Demi, **M. P. J. Kuenen**, H. Wijkstra, T. J. Tjalkens, and M. Mischi, "Contrast-enhanced angiogenesis imaging by mutual information analysis," in *19th European Symposium on Ultrasound Contrast Imaging*, Rotterdam (The Netherlands), January 23-24, 2014, pp. 139–142.

[IC29] M. Mischi, **M. P. J. Kuenen**, H. P. Beerlage, J. J. M. C. H. de la Rosette, and H. Wijkstra, "Prostate cancer localization by contrast-ultrasound-dispersion imaging: results from a pilot study," to be presented at *29th Annual European Association of Urology (EAU) Congress*, Stockholm (Sweden), April 11-15, 2014.

[IC30] **M. P. J. Kuenen**, H. P. Beerlage, J. J. M. C. H. de la Rosette, H. Wijkstra, and M. Mischi, "Contrast-ultrasound dispersion imaging for prostate cancer localization: comparison between imaging and histopathology," to be presented at *EUROSON, 26th Congress of the European Federation of Societies for Ultrasound in Medicine and Biology (EFSUMB)*, Tel-Aviv (Israel), May 26-28, 2014.

Regional conferences

[RC1] **M. P. J. Kuenen**, M. Mischi, H. Wijkstra, A. J. M. Hendrikx, and H. H. M. Korsten, "Localization of prostate cancer by contrast-ultrasound diffusion imaging," in *Annual Symposium of the IEEE EMBS Benelux Chapter*, Enschede (The Netherlands), November 9-10 2009, p. 115.

[RC2] **M. P. J. Kuenen**, M. Mischi, and H. Wijkstra, "Detection of prostate cancer by contrast-ultrasound dispersion imaging," in *Biomedica*, Eindhoven (The Netherlands), April 7-8, 2011, pp. 141–142.

[RC3] **M. P. J. Kuenen**, H. Wijkstra, and M. Mischi, "Prostate cancer detection by contrast-ultrasound dispersion imaging and coherence analysis," in *10th Belgian Day on Biomedical Engineering, joint meeting with the Annual Symposium of the IEEE EMBS Benelux Chapter*, Leuven & Brussels (Belgium), December 1-2, 2011, p. 14.

[RC4] M. Mischi, **M. P. J. Kuenen**, J. J. M. C. H. de la Rosette, W. Scheepens, and H. Wijkstra, "Prostaat kanker localisatie met "dispersion" echografie," in *Voorjaarsvergadering van de Nederlandse Vereniging voor Urologie (NVU)*, Den Bosch (The Netherlands), May 10-11, 2012.

[RC5] T. A. Saidov, **M. P. J. Kuenen**, L. Demi, H. Wijkstra, and M. Mischi, "Contrast ultrasound dispersion imaging for prostate cancer localization," in *1st Jan Beneken Conference on Modeling and Simulation of Human Physiology*, Eindhoven (The Netherlands), April 25-26, 2013.

[RC6] **M. P. J. Kuenen**, T. A. Saidov, H. Wijkstra, and M. Mischi, "Prostate cancer imaging by spatiotemporal contrast-ultrasound dispersion analysis," in *Biomedica*, Aachen (Germany), June 19, 2013.

[RC7] **M. P. J. Kuenen**, H. Wijkstra, and M. Mischi, "Quantitative indicator dilution analysis based on maximum likelihood," in *Annual Symposium of the IEEE EMBS & IM Benelux Chapter*, Brussels (Belgium), December 5-6, 2013.

[RC8] N. Bouhouch, L. Demi, **M. P. J. Kuenen**, H. Wijkstra, T. J. Tjalkens, and M. Mischi, "Contrast-enhanced angiogenesis imaging by mutual information analysis," in *Annual Symposium of the IEEE EMBS & IM Benelux Chapter*, Brussels (Belgium), December 5-6, 2013.

References

[1] J. E. McNeal, "Normal histology of the prostate," *Am. J. Surg. Pathol.*, vol. 12, no. 8, pp. 619–633, 1988.

[2] A. C. Loch, A. Bannowsky, L. Baeurle *et al.*, "Technical and anatomical essentials for transrectal ultrasound of the prostate," *World J. Urol.*, vol. 25, pp. 361–366, 2007.

[3] American Cancer Society, "Cancer facts & figures 2013," Atlanta, 2013.

[4] J. Ferlay, E. Steliarova-Foucher, J. Lortet-Tieulent *et al.*, "Cancer incidence and mortality patterns in Europe: estimates for 40 countries in 2012," *Eur. J. Cancer*, vol. 49, no. 6, pp. 1374–1403, 2013.

[5] C. Gosselaar, M. J. Roobol, and F. H. Schröder, "Prevalence and characteristics of screen-detected prostate carcinomas at low prostate-specific antigen levels: aggressive or insignificant?" *BJU Int.*, vol. 95, no. 2, pp. 231–237, 2005.

[6] L. M. Franks, "Latent carcinoma," *Ann. R. Coll. Surg. Engl.*, vol. 15, no. 4, pp. 236–249, 1954.

[7] W. A. Sakr, G. P. Haas, B. J. Cassin, J. E. Pontes, and J. D. Crissman, "The frequency of carcinoma and intraepithelial neoplasia of the prostate in young male patients," *J. Urol.*, vol. 150, no. 2, pp. 379–385, 1993.

[8] D. F. Gleason, "Histologic grading of prostate cancer: a perspective," *Hum. Pathol.*, vol. 23, no. 3, pp. 273–279, 1992.

[9] A. V. D'Amico, R. Whittington, S. B. Malkowicz *et al.*, "Biochemical outcome after radical prostatectomy, external beam radiation therapy, or interstitial radiation therapy for clinically localized prostate cancer," *JAMA*, vol. 280, no. 11, pp. 969–974, 1998.

[10] T. A. Stamey, F. S. Freiha, J. E. McNeal *et al.*, "Localized prostate cancer. Relationship of tumor volume to clinical significance for treatment of prostate cancer." *Cancer*, vol. 71, no. 3 Suppl, pp. 933–938, 1993.

[11] W. J. Catalona, D. S. Smith, T. L. Ratliff *et al.*, "Measurement of prostate-specific antigen in serum as a screening test for prostate cancer," *N. Engl. J. Med.*, vol. 324, no. 17, pp. 1156–1161, 1991.

[12] A. V. D'Amico, M.-H. Chen, K. A. Roehl, and W. J. Catalona, "Preoperative PSA velocity and the risk of death from prostate cancer after radical prostatectomy," *N. Engl. J. Med.*, vol. 351, no. 2, pp. 125–135, 2004.

[13] F. H. Schröder, J. Hugosson, M. J. Roobol *et al.*, "Screening and prostate-cancer mortality in a randomized European study," *N. Engl. J. Med.*, vol. 360, no. 13, pp. 1320–1328, 2009.

[14] I. M. Thompson, D. K. Pauler, P. J. Goodman *et al.*, "Prevalence of prostate cancer among men with a prostate-specific antigen level $\geq$ 4.0 ng per milliliter," *N. Engl. J. Med.*, vol. 350, no. 22, pp. 2239–2246, 2004.

[15] W. H. Cooner, B. R. Mosley, C. L. Rutherford Jr. *et al.*, "Prostate cancer detection in a clinical urological practice by ultrasonography, digital rectal examination and prostate specific antigen," *J. Urol.*, vol. 143, no. 6, pp. 1146–1152, 1990.

[16] D. S. Smith and W. J. Catalona, "Interexaminer variability of digital rectal examination in detecting prostate cancer," *Urology*, vol. 45, no. 1, pp. 70–74, 1995.

[17] J. P. M. Sedelaar, J. G. H. van Roermund, G. L. J. H. van Leenders *et al.*, "Three-dimensional grayscale ultrasound: evaluation of prostate cancer compared with benign prostatic hyperplasia," *Urology*, vol. 57, no. 5, pp. 914–920, 2001.

[18] B. Djavan, P. Mazal, A. Zlotta *et al.*, "Pathological features of prostate cancer detected on initial and repeat prostate biopsy: results of the prospective European prostate cancer detection study," *Prostate*, vol. 47, no. 2, pp. 111–117, 2001.

[19] K. K. Hodge, J. E. McNeal, M. K. Terris, and T. A. Stamey, "Random systematic versus directed ultrasound guided transrectal core biopsies of the prostate," *J. Urol.*, vol. 142, no. 1, pp. 71–75, 1989.

[20] S. Loeb, S. van den Heuvel, X. Zhu *et al.*, "Infectious complications and hospital admissions after prostate biopsy in a European randomized trial," *Eur. Urol.*, vol. 61, no. 6, pp. 1110–1114, 2012.

[21] M. Norberg, L. Egevad, L. Holmberg *et al.*, "The sextant protocol for ultrasound-guided core biopsies of the prostate underestimates the presence of cancer," *Urology*, vol. 50, no. 4, pp. 562–566, 1997.

[22] C. G. Roehrborn, G. J. Pickens, and J. S. Sanders, "Diagnostic yield of repeated transrectal ultrasound-guided biopsies stratified by specific histopathologic diagnoses and prostate-specific antigen levels," *Urology*, vol. 47, no. 3, pp. 347–352, 1996.

[23] B. Djavan, M. Remzi, C. C. Schulman, M. Marberger, and A. R. Zlotta, "Repeat prostate biopsy: who, how and when? A review," *Eur. Urol.*, vol. 42, no. 2, pp. 93–103, 2002.

[24] C. H. Bangma, S. Roemeling, and F. H. Schröder, "Overdiagnosis and overtreatment of early detected prostate cancer," *World J. Urol.*, vol. 25, pp. 3–9, 2007.

[25] J. L. Stanford, Z. Feng, A. S. Hamilton *et al.*, "Urinary and sexual function after radical prostatectomy for clinically localized prostate cancer," *JAMA*, vol. 283, no. 3, pp. 354–360, 2000.

[26] G. L. Andriole, E. D. Crawford, R. L. Grubb III *et al.*, "Mortality results from a randomized prostate-cancer screening trial," *N. Engl. J. Med.*, vol. 360, no. 13, pp. 1310–1319, 2009.

[27] A. Bill-Axelson, L. Holmberg, M. Ruutu *et al.*, "Radical prostatectomy versus watchful waiting in early prostate cancer," *N. Engl. J. Med.*, vol. 364, no. 18, pp. 1708–1717, 2011.

[28] M. A. Dall'Era, P. C. Albertsen, C. Bangma *et al.*, "Active surveillance for prostate cancer: a systematic review of the literature," *Eur. Urol.*, vol. 62, no. 6, pp. 976–983, 2012.

[29] T. J. Wilt, M. K. Brawer, K. M. Jones *et al.*, "Radical prostatectomy versus observation for localized prostate cancer," *N. Engl. J. Med.*, vol. 367, no. 3, pp. 203–213, 2012.

[30] V. Kasivisvanathan, M. Emberton, and H. U. Ahmed, "Focal therapy for prostate cancer: rationale and treatment opportunities," *Clin. Oncol.*, vol. 25, no. 8, pp. 461–473, 2013.

[31] D. K. Bahn, P. Silverman, F. Lee, Sr. *et al.*, "Focal prostate cryoablation: initial results show cancer control and potency preservation," *J. Endourol.*, vol. 20, no. 9, pp. 688–692, 2006.

[32] H. U. Ahmed, R. G. Hindley, L. Dickinson *et al.*, "Focal therapy for localised unifocal and multifocal prostate cancer: a prospective development study," *Lancet Oncol.*, vol. 13, no. 6, pp. 622–632, 2012.

[33] T. Windahl, S.-O. Andersson, and L. Lofgren, "Photodynamic therapy of localised prostatic cancer," *Lancet*, vol. 336, no. 8723, p. 1139, 1990.

[34] U. Lindner, R. A. Weersink, M. A. Haider *et al.*, "Image guided photothermal focal therapy for localized prostate cancer: Phase I trial," *J. Urol.*, vol. 182, no. 4, pp. 1371–1377, 2009.

[35] A. V. D'Amico, C. M. Tempany, D. Schultz *et al.*, "Comparing PSA outcome after radical prostatectomy or magnetic resonance imaging-guided partial prostatic irradiation in select patients with clinically localized adenocarcinoma of the prostate," *Urology*, vol. 62, no. 6, pp. 1063–1067, 2003.

[36] D. B. Fuller, J. Naitoh, C. Lee, S. Hardy, and H. Jin, "Virtual HDRSM cyberknife treatment for localized prostatic carcinoma: dosimetry comparison with HDR brachytherapy and preliminary clinical observations," *Int. J. Radiat. Oncol. Biol. Phys.*, vol. 70, no. 5, pp. 1588–1597, 2008.

[37] S. F. Shariat, G. Raptidis, M. Masatoschi, F. Bergamaschi, and K. M. Slawin, "Pilot study of radiofrequency interstitial tumor ablation (RITA) for the treatment of radio-recurrent prostate cancer," *Prostate*, vol. 65, no. 3, pp. 260–267, 2005.

[38] W. van den Bos, B. G. Muller, and J. J. M. C. H. de la Rosette, "A randomized controlled trial on focal therapy for localized prostate carcinoma: hemiablation versus complete ablation with irreversible electroporation," *J. Endourol.*, vol. 27, no. 3, pp. 262–264, 2013.

[39] M. Tsivian, M. Kimura, L. Sun *et al.*, "Predicting unilateral prostate cancer on routine diagnostic biopsy: sextant vs extended," *BJU Int.*, vol. 105, no. 8, pp. 1089–1092, 2010.

[40] J. Folkman, "Tumor angiogenesis: therapeutic implications," *N. Engl. J. Med.*, vol. 285, no. 21, pp. 1182–1186, 1971.

[41] P. Carmeliet and R. K. Jain, "Angiogenesis in cancer and other diseases," *Nature*, vol. 407, no. 6801, pp. 249–257, 2000.

[42] Y. Li and P. J. Cozzi, "Angiogenesis as a strategic target for prostate cancer therapy," *Med. Res. Rev.*, vol. 30, no. 1, pp. 23–66, 2010.

[43] N. Weidner, P. R. Carroll, J. Flax, W. Blumenfeld, and J. Folkman, "Tumor angiogenesis correlates with metastasis in invasive prostate carcinoma," *Am. J. Pathol.*, vol. 143, no. 2, pp. 401–409, 1993.

[44] S. A. Bigler, R. E. Deering, and M. K. Brawer, "Comparison of microscopic vascularity in benign and malignant prostate tissue," *Hum. Pathol.*, vol. 24, no. 2, pp. 220–226, 1993.

[45] M. K. Brawer, "Quantitative microvessel density. A staging and prognostic marker for human prostatic carcinoma," *Cancer*, vol. 78, no. 2, pp. 345–349, 1996.

[46] D. Hanahan and J. Folkman, "Patterns and emerging mechanisms of the angiogenic switch during tumorigenesis," *Cell*, vol. 86, no. 3, pp. 353–364, 1996.

[47] S. B. Fox, G. Gasparini, and A. L. Harris, "Angiogenesis: pathological, prognostic, and growth-factor pathways and their link to trial design and anticancer drugs," *Lancet Oncol.*, vol. 2, pp. 278–289, 2001.

[48] A. Eberhard, S. Kahlert, V. Goede *et al.*, "Heterogeneity of angiogenesis and blood vessel maturation in human tumors: implications for antiangiogenic tumor therapies," *Cancer Res.*, vol. 60, no. 5, pp. 1388–1393, 2000.

[49] M. C. Hall, P. Troncoso, A. Pollack *et al.*, "Significance of tumor angiogenesis in clinically localized prostate carcinoma treated with external beam radiotherapy," *Urology*, vol. 44, no. 6, pp. 869–875, 1994.

[50] D. G. Botswick, T. M. Wheeler, M. Blute *et al.*, "Optimized microvessel density analysis improves prediction of cancer stage from prostate needle biopsies," *Urology*, vol. 48, no. 1, pp. 47–57, 1996.

[51] I. Franck Lissbrant, P. Stattin, J.-E. Damber, and A. Bergh, "Vascular density is a predictor of cancer-specific survival in prostatic carcinoma," *Prostate*, vol. 33, no. 1, pp. 38–45, 1997.

[52] M. Borre, B. V. Offersen, B. Nerstrøm, and J. Overgaard, "Microvessel density predicts survival in prostate cancer patients subjected to watchful waiting," *Br. J. Cancer*, vol. 78, no. 7, pp. 940–944, 1998.

[53] G. Russo, M. Mischi, W. Scheepens, J. de la Rosette, and H. Wijkstra, "Angiogenesis in prostate cancer: onset, progression and imaging," *BJU Int.*, vol. 110, pp. E794–E808, 2012.

[54] H. Hricak, P. L. Choyke, S. C. Eberhardt, S. A. Leibel, and P. T. Scardino, "Imaging prostate cancer: a multidisciplinary perspective," *Radiology*, vol. 243, pp. 28–53, 2007.

[55] H. O. Anger, "Scintillation camera with multichannel collimators," *J. Nucl. Med.*, vol. 5, no. 7, pp. 515–531, 1964.

[56] C. S. Levin, "Primer on molecular imaging technology," *Eur. J. Nucl. Med. Mol. Imaging*, vol. 32, no. 2, pp. S325–S345, 2005.

[57] H. Jadvar, "Prostate cancer: PET with ^{18}F-FDG, ^{18}F- or ^{11}C-acetate, and ^{18}F- or ^{11}C-choline," *J. Nucl. Med.*, vol. 52, no. 1, pp. 81–89, 2010.

[58] A.-A. A. Elgamal, M. J. Troychak, and G. P. Murphy, "ProstaScint® scan may enhance identification of prostate cancer recurrences after prostatectomy, radiation, or hormone therapy: analysis of 136 scans of 100 patients," *Prostate*, vol. 37, no. 4, pp. 261–269, 1998.

[59] V. Mouraviev, J. F. Madden, G. Broadwater *et al.*, "Use of ^{111}in-capromab pendetide immunoscintigraphy to image localized prostate cancer foci within the prostate gland," *J. Urol.*, vol. 182, no. 3, pp. 938–948, 2009.

[60] W. R. Hendee and C. J. Morgan, "Magnetic resonance imaging part I – physical principles," *West. J. Med.*, vol. 141, no. 4, pp. 491–500, 1984.

[61] A. Villers, P. Puech, D. Mouton *et al.*, "Dynamic contrast enhanced, pelvic phased array magnetic resonance imaging of localized prostate cancer for predicting tumor volume: correlation with radical prostatectomy findings," *J. Urol.*, vol. 176, no. 6, pp. 2432–2437, 2006.

[62] C. M. A. Hoeks, M. G. Schouten, J. G. R. Bomers *et al.*, "Three-Tesla magnetic resonance-guided prostate biopsy in men with increased prostate-specific antigen and repeated, negative, random, systematic, transrectal ultrasound biopsies: detection of clinically significant prostate cancers," *Eur. Urol.*, vol. 62, no. 5, pp. 902–909, 2012.

[63] S. Isebaert, L. Van den Bergh, K. Haustermans *et al.*, "Multiparametric MRI for prostate cancer localization in correlation to whole-mount histopathology," *J. Magn. Reson. Imaging*, vol. 37, no. 6, pp. 1392–1401, 2013.

[64] D. Le Bihan, E. Breton, D. Lallemand *et al.*, "MR imaging of intravoxel incoherent motions: application to diffusion and perfusion in neurologic disorders," *Radiology*, vol. 161, pp. 401–407, 1986.

[65] C. Sato, S. Naganawa, T. Nakamura *et al.*, "Differentiation of noncancerous tissue and cancer lesions by apparent diffusion coefficient values in transition and peripheral zones of the prostate," *J. Magn. Reson. Imaging*, vol. 21, no. 3, pp. 258–262, 2005.

[66] E. Casciani and G. Gualdi, "Prostate cancer: value of magnetic resonance spectroscopy 3D chemical shift imaging," *Abdom. Imaging*, vol. 31, no. 4, pp. 490–499, 2006.

[67] J. Scheidler, H. Hricak, D. B. Vigneron *et al.*, "Prostate cancer: localization with three-dimensional proton MR spectroscopic imaging clinicopathologic study," *Radiology*, vol. 213, pp. 473–480, 1999.

[68] C. F. G. C. Geraldes and S. Laurent, "Classification and basic properties of contrast agents for magnetic resonance imaging," *Contrast Media Mol. Imaging*, vol. 4, no. 1, pp. 1–23, 2009.

[69] P. S. Tofts, G. Brix, D. L. Buckley *et al.*, "Estimating kinetic parameters from dynamic contrast-enhanced T1-weighted MRI of a diffusable tracer: standardized quantities and symbols," *J. Magn. Reson. Imaging*, vol. 10, pp. 223–232, 1999.

[70] E. K. Vos, G. J. S. Litjens, T. Kobus *et al.*, "Assessment of prostate cancer aggressiveness using dynamic contrast-enhanced magnetic resonance imaging at 3 T," *Eur. Urol.*, vol. 64, no. 3, pp. 448–455, 2013.

[71] H. Thomsen, S. Morcos, and P. Dawson, "Is there a causal relation between the administration of gadolinium based contrast media and the development of nephrogenic systemic fibrosis (NSF)?" *Clin. Radiol.*, vol. 61, no. 11, pp. 905–906, 2006.

[72] T. L. Szabo, *Diagnostic ultrasound imaging: inside out*. Amsterdam: Elsevier Academic Press, 2004.

[73] H. Watanabe, H. Kaiho, M. Tanaka, and Y. Terasawa, "Diagnostic application of ultrasonotomography to the prostate," *Invest. Urol.*, vol. 8, pp. 548–559, 1971.

[74] A. L. Huynen, R. J. B. Giesen, J. J. M. C. H. de la Rosette *et al.*, "Analysis of ultrasonographic prostate images for the detection of prostatic carcinoma: the automated urologic diagnostic expert

system," *Ultrasound Med. Biol.*, vol. 20, no. 1, pp. 1–10, 1994.

[75] G. Schmitz, H. Ermert, and T. Senge, "Tissue-characterization of the prostate using radio frequency ultrasonic signals," *IEEE Trans. Ultrason., Ferroelectr., Freq. Control*, vol. 46, no. 1, pp. 126–138, 1999.

[76] J. Braeckman, P. Autier, C. Garbar *et al.*, "Computer-aided ultrasonography (HistoScanning): a novel technology for locating and characterizing prostate cancer," *BJU Int.*, vol. 101, pp. 293–298, 2007.

[77] L. Pallwein, M. Mitterberger, G. Pinggera *et al.*, "Sonoelastography of the prostate: Comparison with systematic biopsy findings in 492 patients," *Eur. J. Radiol.*, vol. 65, no. 2, pp. 304–310, 2008.

[78] L. Sandrin, M. Tanter, S. Catheline, and M. Fink, "Shear modulus imaging with 2-d transient elastography," *IEEE Trans. Ultrason., Ferroelectr., Freq. Control*, vol. 49, no. 4, pp. 426–435, 2002.

[79] J. Bercoff, M. Tanter, and M. Fink, "Supersonic shear imaging: a new technique for soft tissue elasticity mapping," *IEEE Trans. Ultrason., Ferroelectr., Freq. Control*, vol. 51, no. 4, pp. 396–409, 2004.

[80] R. G. Barr, R. Memo, and C. R. Schaub, "Shear wave ultrasound elastography of the prostate: Initial results," *Ultrasound Q.*, vol. 28, no. 1, pp. 13–20, 2012.

[81] D. N. White, "The early development of neurosonology: III. pulsatile echoencephalography and Doppler techniques," *Ultrasound Med. Biol.*, vol. 18, no. 4, pp. 323–376, 1992.

[82] J. S. Newman, R. L. Bree, and J. M. Rubin, "Prostate cancer: diagnosis with color Doppler sonography with histologic correlation of each biopsy site," *Radiology*, vol. 195, pp. 86–90, 1995.

[83] J. M. Rubin, R. O. Bude, P. L. Carson, R. L. Bree, and R. S. Adler, "Power Doppler US: a potentially useful alternative to mean frequency-based color Doppler US," *Radiology*, vol. 190, pp. 853–856, 1994.

[84] E. J. Halpern and S. E. Strup, "Using gray-scale and color and power Doppler sonography to detect prostatic cancer," *Am. J. Roentgenol.*, vol. 174, pp. 623–627, 2000.

[85] S. B. Feinstein, B. Coll, D. Staub *et al.*, "Contrast enhanced ultrasound imaging," *J. Nucl. Cardiol.*, vol. 17, no. 1, pp. 106–115, 2010.

[86] E. J. Halpern, M. Rosenberg, and L. G. Gomella, "Prostate cancer: contrast-enhanced US for detection," *Radiology*, vol. 219, no. 1, pp. 219–225, 2001.

[87] K. Wei, A. R. Jayaweera, S. Firoozan *et al.*, "Quantification of myocardial blood flow with ultrasound-induced destruction of microbubbles administered as a constant venous infusion," *Circulation*, vol. 97, pp. 473–483, 1998.

[88] P. J. A. Frinking, A. Bouakaz, J. Kirkhorn, F. J. Ten Cate, and N. de Jong, "Ultrasound contrast imaging: current and new potential methods," *Ultrasound Med. Biol.*, vol. 26, no. 6, pp. 965–975, 2000.

[89] D. Hope Simpson, C. T. Chin, and P. N. Burns, "Pulse inversion Doppler: a new method for detecting nonlinear echoes from microbubble contrast agents," *IEEE Trans. Ultrason., Ferroelectr., Freq. Control*, vol. 46, no. 2, pp. 372–382, 1999.

[90] R. J. Eckersley, C. T. Chin, and P. N. Burns, "Optimising phase and amplitude modulation schemes for imaging microbubble contrast agents at low acoustic power," *Ultrasound Med. Biol.*, vol. 31, no. 2, pp. 213–219, 2005.

[91] R. J. Eckersley, J. P. Sedelaar, M. J. K. Blomley *et al.*, "Quantitative microbubble enhanced transrectal ultrasound as a tool for monitoring hormonal treatment of prostate carcinoma," *Prostate*, vol. 51, pp. 256–267, 2002.

[92] M. Arditi, P. J. A. Frinking, X. Zhou, and N. G. Rognin, "A new formalism for the quantification of tissue perfusion by the destruction-replenishment method in contrast ultrasound imaging," *IEEE Trans. Ultrason., Ferroelectr., Freq. Control*, vol. 53, no. 6, pp. 1118–1129, 2006.

[93] J. M. Hudson, R. Karshafian, and P. N. Burns, "Quantification of flow using ultrasound and microbubbles: a disruption replenishment model based on physical principles," *Ultrasound Med. Biol.*, vol. 35, no. 12, pp. 2007–2020, 2009.

[94] M. Mischi, A. A. C. M. Kalker, and H. H. M. Korsten, "Videodensitometric methods for cardiac output measurements," *EURASIP J. Appl. Signal Processing*, vol. 5, pp. 479–489, 2003.

[95] M. Mischi, J. A. den Boer, and H. H. M. Korsten, "On the physical and stochastic representation of an indicator dilution curve as a gamma variate," *Physiol. Meas.*, vol. 29, pp. 281–294, 2008.

[96] C. Strouthos, M. Lampaskis, V. Sboros, A. McNeilly, and M. Averkiou, "Indicator dilution models for the quantification of microvascular blood flow with bolus administration of ultrasound contrast agents," *IEEE Trans. Ultrason., Ferroelectr., Freq. Control*, vol. 57, no. 6, pp. 1296–1310, 2010.

[97] D. Cosgrove and N. Lassau, "Imaging of perfusion using ultrasound," *Eur. J. Nucl. Med. Mol. Imaging*, vol. 37, pp. 65–85, 2010.

[98] M. Lamuraglia, S. L. Bridal, M. Santin *et al.*, "Clinical relevance of contrast-enhanced ultrasound in monitoring anti-angiogenic therapy of cancer: current status and perspectives," *Crit. Rev. Oncol. Hematol.*, vol. 73, no. 3, pp. 202–212, 2010.

[99] M. Lampaskis and M. Averkiou, "Investigation of the relationship of nonlinear backscattered ultrasound intensity with microbubble concentration at low MI," *Ultrasound Med. Biol.*, vol. 36, no. 2, pp. 306–312, 2010.

[100] N. Elie, A. Kaliski, P. Péronneau *et al.*, "Methodology for quantifying interactions between perfusion evaluated by DCE-US and hypoxia throughout tumor growth," *Ultrasound Med. Biol.*, vol. 33, no. 4, pp. 549–560, 2007.

[101] M. H. Wink, F. Frauscher, D. Cosgrove *et al.*, "Contrast-enhanced ultrasound and prostate cancer; a multicentre European research coordination project," *Eur. Urol.*, vol. 54, no. 5, pp. 982–993, 2008.

[102] F. Aigner, G. Schfer, E. Steiner *et al.*, "Value of enhanced transrectal ultrasound targeted biopsy for prostate cancer diagnosis: a retrospective data analysis," *World J. Urol.*, vol. 30, no. 3, pp. 341–346, 2012.

[103] M. Smeenge, M. Mischi, M. Laguna Pes, J. de la Rosette, and H. Wijkstra, "Novel contrast-enhanced ultrasound imaging in prostate cancer," *World J. Urol.*, vol. 29, pp. 581–587, 2011.

[104] S. Pochon, I. Tardy, P. Bussat *et al.*, "BR55: A lipopeptide-based VEGFR2-targeted ultrasound contrast agent for molecular imaging of angiogenesis," *Invest. Radiol.*, vol. 45, no. 2, pp. 89–95, 2010.

[105] H. Wijkstra, "BR55 in prostate cancer: an exploratory clinical trial." Available from http://clinicaltrials.gov/show/NCT01253213, 2012.

[106] S. Delorme and M. V. Knopp, "Non-invasive vascular imaging: assessing tumour vascularity," *Eur. Radiol.*, vol. 8, pp. 517–527, 1998.

[107] G. Taylor, "Dispersion of soluble matter in solvent flowing slowly through a tube," *Proc. R. Soc. A*, vol. 219, pp. 186–203, 1953.

[108] C. W. Sheppard, *Basic principles of the tracer method*. New York: John Wiley and Sons, 1962.

[109] K. H. Norwich and S. Zelin, "The dispersion of indicator in the cardio-pulmonary system," *Bull. Math. Biophys.*, vol. 32, pp. 25–43, 1970.

[110] Y.-C. Fung, *Biodynamics: circulation*, 1st ed. Berlin: Springer, 1984.

[111] R. J. M. D. de Wiest, *Flow through porous media*. London: Academic Press, 1969.

[112] J. van Brakel and P. M. Heertjes, "Analysis of diffusion in macroporous media in terms of a porosity, a tortuosity and a constrictivity factor," *Int. J. Heat Mass Tran.*, vol. 17, pp. 1093–1103, 1974.

[113] Y. S. Wu, L. J. van Vliet, H. W. Frijlink, and K. van der Voort Maarschalk, "The determination of relative path length as a measure for tortuosity in compacts using image analysis," *Eur. J. Pharm. Sci.*, vol. 28, no. 5, pp. 433–440, 2006.

CHAPTER 2

Dispersion analysis by classical indicator dilution modeling

Based on: M. P. J. Kuenen, M. Mischi, and H. Wijkstra, "Contrast-Ultrasound Diffusion Imaging[1] for Localization of Prostate Cancer," *IEEE Transactions on Medical Imaging*, vol. 30, no. 8, pp. 1496–1502,

Abstract – *Prostate cancer is the most prevalent form of cancer in western men. An accurate early localization of prostate cancer, permitting efficient use of modern focal therapies, is currently hampered by a lack of imaging methods. Several methods have aimed at detecting microvascular changes associated with prostate cancer with limited success by quantitative imaging of blood perfusion. Differently, we propose contrast-ultrasound diffusion imaging, based on the hypothesis that the complexity of microvascular changes is better reflected by diffusion than by perfusion characteristics. Quantification of local, intravascular diffusion is performed after transrectal ultrasound imaging of an intravenously injected ultrasound contrast agent bolus. Indicator dilution curves are measured with the ultrasound scanner resolution and fitted by a modified local density random walk model, which, being a solution of the convective diffusion equation, enables the estimation of a local, diffusion-related parameter. Diffusion parametric images obtained from five datasets of four patients were compared with histology data on a pixel basis. The resulting receiver operating characteristic (curve area = 0.91) was superior to that of any perfusion-related parameter proposed in the literature. Contrast-ultrasound diffusion imaging seems therefore to be a promising method for prostate cancer localization, encouraging further research to assess the clinical reliability.*

[1] In this journal article, and therefore also in this Chapter, the method is referred to as contrast-ultrasound diffusion imaging. After publication of this article, we opted to use dispersion instead of diffusion, because dispersion is a more accurate term in the present context. In addition, by adoption of the term dispersion, confusion with diffusion-weighted MRI is avoided.

2.1 Introduction

Prostate cancer is the most prevalent form of cancer in men in western countries. It accounts for 25% and 10% of all cancer diagnoses and deaths, respectively [1, 2]. Nowadays, a variety of focal therapies such as cryoablation, brachytherapy, and high-intensity focused ultrasound, are available to efficiently treat early detected and localized prostate cancer [3]. This may prevent a radical treatment as for example radical prostatectomy, with the associated risks of the patient becoming incontinent or impotent [4]. However, the limited reliability of the available noninvasive diagnostic methods hampers an efficient use of focal therapies.

The main noninvasive diagnostic method, assessing the serum prostate-specific antigen (PSA) level in blood, has a high false-positive rate (about 76%) [5]. Therefore, PSA does not enable an efficient mass screening [5] and is only used for patient stratification prior to biopsy investigation [6]. This invasive and painful investigation commonly involves taking 6 to 12 spatially distributed samples of the prostate with a core needle. Although the biopsy investigation is currently the most reliable diagnostic method, it is often repeated to achieve sufficient sensitivity [5, 6]. The limited cancer localization is another drawback. Furthermore, a considerable fraction of all detected carcinomas will not develop into a life-threatening disease [4]. Therefore, the risk of overdiagnosis and overtreatment, with a related loss in quality of life, represents a major issue in current prostate cancer care [4, 5]. These problems motivate the search for better noninvasive methods for an early detection and localization of life-threatening forms of prostate cancer. In particular, imaging methods may reduce the number of biopsies by accurate targeting and permit an efficient application of focal treatments.

Several imaging modalities are being evaluated for early prostate cancer detection. While computed tomography (CT) seems unsuitable for diagnostic prostate imaging [6], cancer detection sensitivity (on a patient basis) with magnetic resonance imaging (MRI) techniques such as diffusion weighted imaging (73-89%), dynamic contrast-enhanced MRI (69-95%), and magnetic resonance spectroscopy imaging (59-94%) is promising [7]. Transrectal ultrasound (TRUS) techniques are however equally promising, and they are more suitable than MRI in terms of cost, time, resolution, and guidance of biopsies and focal therapies [6, 8]. Therefore, TRUS improvements could be of great value for early prostate cancer localization.

For imaging purposes, a key indicator for prostate cancer is angiogenesis, i.e., the formation of a dense microvascular network characterized by an increased microvessel density (MVD) [9–12]. Angiogenesis, which is required for cancer growth beyond 1 mm^3, correlates with prostate cancer aggressiveness (i.e., risks of extracapsular growth and development of metastases) [10–12]. Therefore, imaging methods based on angiogenesis detection may

help to identify life-threatening forms of prostate cancer at an early stage.

Hypothesizing a correlation between MVD and perfusion, i.e., blood flow per tissue volume, the use of ultrasound contrast agents (UCAs) for quantitative TRUS imaging of microvascular perfusion has gained interest [6, 13, 14]. UCAs are dispersions of coated gas microbubbles that backscatter acoustic energy when hit by ultrasound waves [15, 16]. Despite an improvement in biopsy targeting, contrast-enhanced TRUS methods based on intermittent imaging and destruction-replenishment techniques have however not proven sufficiently reliable to replace systematic biopsies [17–19].

An alternative method involves dynamic contrast-enhanced ultrasound (DCE-US) imaging of the passage of an intravenously injected UCA bolus [6, 8, 14]. Up until now, only few quantitative studies have been carried out. These studies quantify perfusion by extraction of time and intensity features from the measured acoustic time-intensity curves [20–23]. However, time features do not represent the local hemodynamic characteristics since they generally depend on the entire bolus history [24], whereas intensity features are affected by scanner settings and nonlinear ultrasound propagation [25].

The reasons that the developments in quantitative perfusion imaging have not resulted in reliable prostate cancer localization may be various. In addition to limitations in the flow sensitivity, important reasons may be linked to the complex and contradictory effects of angiogenesis on perfusion [13, 22, 26, 27]. A lack of vasomotor control and the presence of arteriovenous shunts cause a low flow resistance [13, 27], but this can be counterbalanced by the small microvessel diameter and an increased interstitial pressure, due to extravascular leakage [13, 27]. MVD characterization by quantification of perfusion may therefore be unreliable.

In this paper we propose contrast-ultrasound diffusion imaging (CUDI) as an alternative noninvasive prostate cancer localization method. CUDI is based on the hypothesis that angiogenesis-induced changes in the microvascular architecture correlate better with diffusion than with perfusion. In this context, diffusion refers to the intravascular UCA spreading by apparent diffusion, due to concentration gradient and flow profile, and by convective dispersion, due to multipath trajectories through the microvasculature [28–30]. The microvascular architecture of a solid tumor can be viewed as a distributed network [31], in which flow can be modeled as flow through a porous medium [32]. Structural characteristics of porous media determine the diffusion [29, 30]. Therefore, we hypothesize intravascular UCA diffusion to be correlated with the microvascular structure and, therefore, with angiogenesis.

Based on the UCA bolus injection technique, CUDI is a new method for quantification of diffusion from time-density curves (TDCs). These curves measure the image gray level versus time at all pixels covering the prostate. By modeling the local intravascular UCA

transport by the local density random walk model, we provide a novel, theoretical framework to extract a local, diffusion-related parameter from measured TDCs. CUDI was evaluated *in vivo* by comparing five diffusion parametric images from four patients, obtained by TDC fitting at each pixel, with histology data.

2.2 Methodology

2.2.1 Data acquisition

The data acquisition was performed at the AMC University Hospital (Amsterdam, The Netherlands), after approval was granted by the local ethics committee. Written informed consent was obtained from all patients prior to their participating in this study.
A 2.4 mL SonoVue ® (Bracco, Milan, Italy) UCA bolus was injected intravenously in the patient arm. SonoVue® is a dispersion of SF_6 microbubbles coated by a phospholipid shell, whose mean diameter is 2.5 μm [33]. TRUS imaging was performed using an iU22 ultrasound scanner (Philips Healthcare, Bothell, WA) equipped with a C8-4v probe. The adopted contrast-specific imaging mode was power modulation, at a frequency of 3.5 MHz. The effective pulse length of two cycles provided an axial resolution of 0.43 mm, while a low mechanical index (MI) of 0.06 minimized microbubble disruption [15, 16]. The compression was set to C38 and the gain was adjusted to prevent truncation or saturation of the 8-bit gray level. All acquired B-mode videos were stored in DICOM (Digital Imaging and Communications in Medicine) format, which can be directly input to the analysis software that we implemented in MATLAB ® (The MathWorks, Natick, MA). Four B-mode frames recorded in power modulation mode are shown in Fig. 2.1.

2.2.2 Calibration

An accurate quantification of the UCA diffusion dynamics based on TRUS B-mode video data requires knowledge about how the measured gray level relates to the UCA concentration. To this end, we investigated the relation between UCA concentration C and the backscattered acoustic intensity I. We also studied the measurement and conversion of I into a gray level G.
For low concentrations and MI, a linear relation between C and I has been reported [34]. We performed new measurements at the Catharina hospital (Eindhoven, The Netherlands) to verify this relationship for the current equipment, settings, and UCA. The setup was similar to the static calibration setup reported in [34]. The UCA dispersions were contained in polyurethane bags that were submerged into a water-filled basin. The basin walls were covered by acoustic absorbers to minimize the acoustic reflections from the wall. To repro-

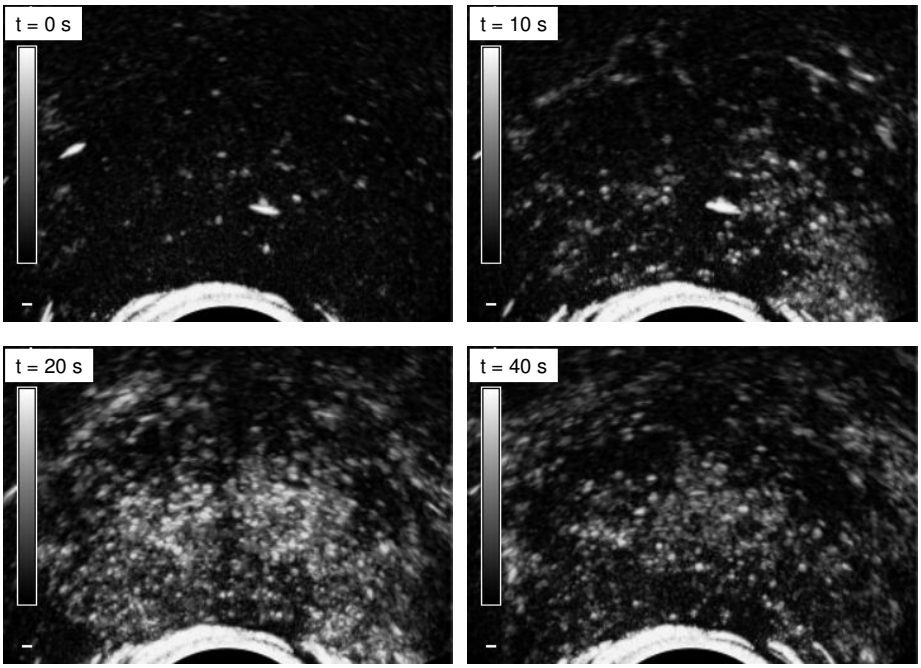

Figure 2.1 *TRUS power modulation imaging of the prostate after intravenous injection of a UCA bolus. The displayed frames are recorded before UCA appearance (top left), at initial wash-in (top right), at peak concentration (bottom left), and at wash-out (bottom right).*

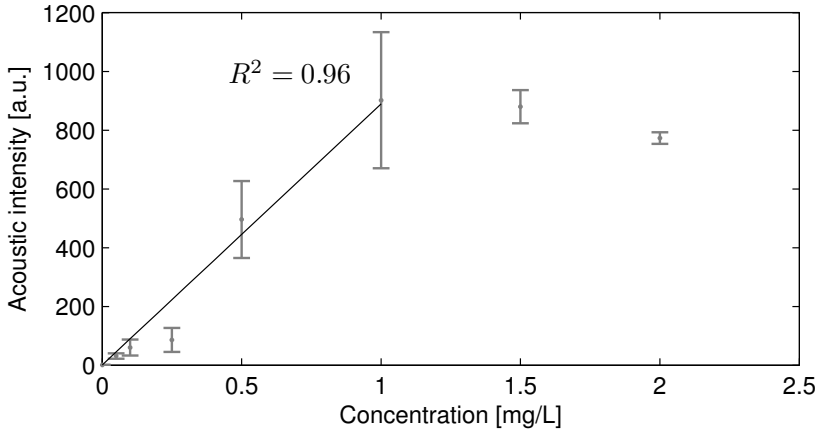

Figure 2.2 In vitro *measurement results. The gray error bars depict the acoustic intensity measured in a fixed ROI by their mean and standard deviation, whereas the black line shows the linear approximation for SonoVue ® concentrations up to 1.0 mg/L.*

duce the clinical conditions, the ultrasound probe was positioned about 1 cm away from the UCA dispersion. For each concentration, three measurements were performed, from three different SonoVue ® vials. The mean acoustic intensity was evaluated in a fixed region of interest (ROI) of the recorded B-mode images, with QLAB (Philips Healthcare, Bothell, WA) acoustic quantification software.

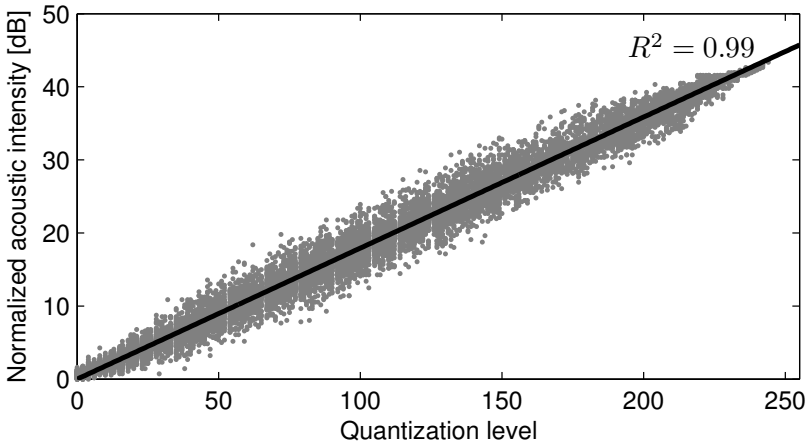

Figure 2.3 *Quantization level Q versus QLAB normalized acoustic intensity I, obtained from single-pixel ROIs. The black line represents the fitted logarithmic compression function.*

The results are shown in Fig. 2.2. For SonoVue ® concentrations up to 1.0 mg/L, C and I are linearly related ($R^2 = 0.96$) as

$$I = a_{\text{CI}} C + I_0, \tag{2.1}$$

where a_{CI} defines the sensitivity and I_0 is the background intensity due to backscatter from tissue and blood. The exact parameter values are not relevant for this study, since a linearly related measure of C is sufficient for a complete description of the UCA diffusion dynamics. With the injected dose, the *in vivo* measurements are performed within the linear calibration range that was estimated *in vitro* (Fig. 2.2). In fact, by considering a simple system of two mixing chambers representing the right and left ventricles (100 mL and 110 mL), the concentration would not overtake 0.84% of the injected concentration (5.0 g/mL) [35]. Taking into account a blood volume fraction in the prostate of 2% [36], the concentration in the prostate would remain below 0.84 mg/L, i.e., within the linear range.

The ultrasound transducer converts the backscattered ultrasound waves into an electrical voltage, proportional to $\sqrt{I}$. After amplification and demodulation, a compression of the signal dynamic range yields the quantization level $Q = q(\sqrt{I})$, and the gray mapping $g(Q)$ renders the displayed gray level G [37]. This mapping is displayed on the B-mode image and can be easily extracted and compensated for. The compression function, typically a logarithmic-like function [34, 37], is estimated by comparing QLAB acoustic quantification results to the quantization level $Q = g^{-1}(G)$ in single-pixel ROIs.

The results show a linear relationship ($R^2 = 0.99$) between $\log(I)$ and Q (Fig. 2.3). This implies a logarithmic compression function $q(\sqrt{I}) = a_{\text{DR}} \ln(I)$, in which a_{DR} is determined

by the dynamic range (DR) of the compression function as

$$a_{\mathrm{DR}} = 255 \log_{10}(e) \frac{10}{\mathrm{DR}}. \tag{2.2}$$

For the estimated dynamic range (45.73 dB), a_{DR} equals 24.22. This dynamic range is sufficiently large to enable an accurate TDC quantification [37].
Combining all relations, the function that maps UCA concentration to gray level can be written as

$$G = g\left(a_{\mathrm{DR}} \ln\left(\frac{a_{\mathrm{CI}}}{I_0} C + 1\right) + Q_0\right). \tag{2.3}$$

In (2.3), the baseline $Q_0 = a_{\mathrm{DR}} \ln(I_0)$ equals the quantization level for $C = 0$, i.e., before the UCA appearance in the prostate.

2.2.3 Diffusion modeling

Physical modeling of the intravascular UCA transport is required to analyze diffusion. Our analysis is based on the local density random walk (LDRW) model [38–40]. This model can provide a physical interpretation of the diffusion process, and it accurately fits UCA indicator dilution curves (IDCs) [23, 34]. IDCs measure the UCA concentration in a fixed sample volume as function of time and can thus be obtained from TDCs via (2.3). After a general introduction to the LDRW model, the local aspects of the diffusion process by this model are discussed.
The LDRW model characterizes the UCA transport in a straight, infinitely long tube of constant section A, in which a carrier fluid flows with a constant velocity v, as shown in Fig. 2.4. The model assumes a Brownian motion of microbubbles. The concentration dynamics $C(x,t)$ is then given by the mono-dimensional convective diffusion equation as

$$\frac{\partial C(x,t)}{\partial t} = \frac{\partial}{\partial x}\left(D \frac{\partial C(x,t)}{\partial x}\right) - v \frac{\partial C(x,t)}{\partial x}, \tag{2.4}$$

in which x and t represent the distance along the tube's main axis and the time variable, respectively. The diffusion coefficient D is assumed constant. The boundary conditions, representing a rapid bolus injection and the UCA mass conservation, are given as

$$C(x,t_0) = \frac{m}{A} \delta(x - x_0), \tag{2.5a}$$

$$\int_{-\infty}^{\infty} C(x,t)\, \mathrm{d}z = \frac{m}{A}. \tag{2.5b}$$

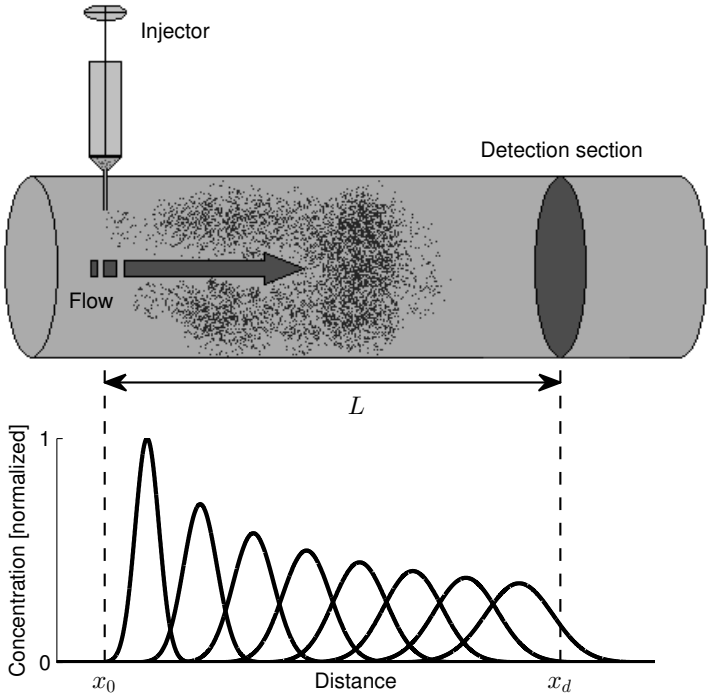

Figure 2.4 *UCA concentration dynamics by the LDRW model in an infinitely-long straight tube, with the lower curves describing the UCA concentration profile in space for increasing time.*

In (2.5), m is the total injected UCA mass dose, and t_0 and x_0 are the bolus injection time and site, respectively. The solution $C(x,t)$ is a Normal distribution in space that translates at the carrier velocity and has a variance that increases linearly with time, as shown in Fig. 2.4. The LDRW formulation for the IDC $C(t)$ is obtained by sampling $C(x,t)$ at an arbitrary detection site x_d ($x_d > x_0$) [39–41]:

$$C(t) = \mathsf{AUC}\,\frac{\exp\lambda}{\mu}\sqrt{\frac{\lambda\mu}{2\pi(t-t_0)}}\exp\left(-\frac{\lambda}{2}\left(\frac{\mu}{t-t_0}+\frac{t-t_0}{\mu}\right)\right). \tag{2.6}$$

The area under the curve (AUC) and the parameters μ and λ are defined as

$$\mathsf{AUC} = \frac{m}{vA}, \quad \mu = \frac{L}{v}, \quad \lambda = \frac{vL}{2D}, \tag{2.7}$$

where $L = x_d - x_0$ is the distance between the injection and detection sites. The parameter AUC equals the IDC integral, and μ is the mean transit time (MTT), i.e., the average time a microbubble takes to travel the distance L [39, 41]. The parameter λ is proportional to the Péclet number, which equals the ratio of the diffusive time L^2/D and the convective time μ [41]. In the Appendix (Sec. 2.5), we provide an analytical relation between λ and the statistical skewness of the IDC.

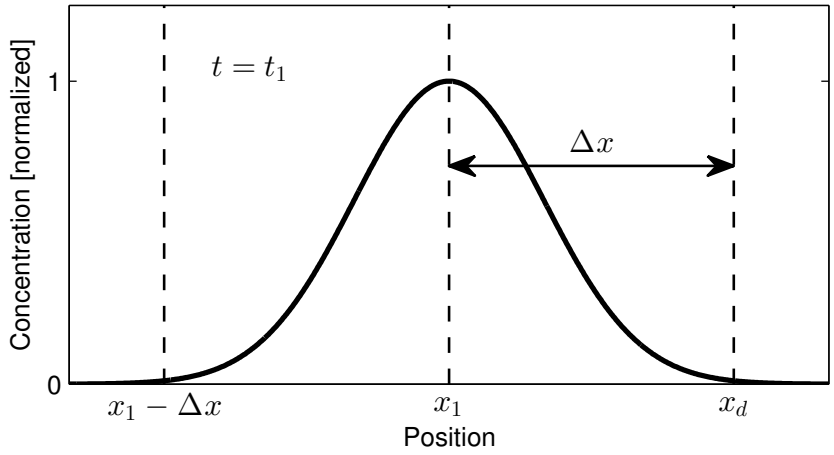

Figure 2.5 *Assumed UCA concentration profile in space at $t = t_1$, i.e., just before the bolus passage at the detection site x_d.*

By its relation to D, the parameter λ is interesting for the characterization of diffusion. However, λ also depends on the length L, which cannot be measured in our clinical application. As a consequence, λ does not characterize diffusion locally. This would require the definition of a local diffusion-related parameter that is independent of L.

To describe local aspects of the UCA diffusion process, we consider a short segment of the infinitely-long tube without making assumptions about the bolus injection. The boundary condition (2.5a) representing the bolus injection is replaced by a local boundary condition describing the spatial UCA concentration profile at time t_1, just before the bolus passage at the detection site x_d. In line with the LDRW model, we assume a Normally distributed initial spatial concentration profile given as

$$C(x, t_1) = \frac{m}{A\sqrt{2\pi\sigma_1^2}} \exp\left(-\frac{(x - x_1)^2}{2\sigma_1^2}\right), \tag{2.8}$$

with mean $x_1 = x_d - \Delta x$ and variance $\sigma_1^2 = \sigma^2(t_1)$. By adopting the boundary condition of (2.8) instead of (2.5a), we can obtain an analytical solution $C(x, t)$ for $t \geq t_1$ if we assume locally constant hemodynamic parameters, i.e., $D(x) = D_\ell$ and $v(x) = v_\ell$ for $x_1 - \Delta x \leq x \leq x_d$. This interval covers the tube segment containing the bulk of the UCA bolus at $t = t_1$ (see Fig. 2.5). For $x < x_1 - \Delta x$, D and v are not relevant and may have any value. In particular, if $D(x) = D_\ell$ for $x < x_1 - \Delta x$, the bolus injection time can be estimated as

$$\tilde{t}_0 = t_1 - \frac{\sigma_1^2}{2D_\ell}. \tag{2.9}$$

The estimate $\tilde{t}_0$ is a theoretical estimate that cannot be interpreted as the true injection time, since $D(x) = D_\ell$ only holds for $x_1 - \Delta x \leq x \leq x_d$. However, (2.9) can be used to

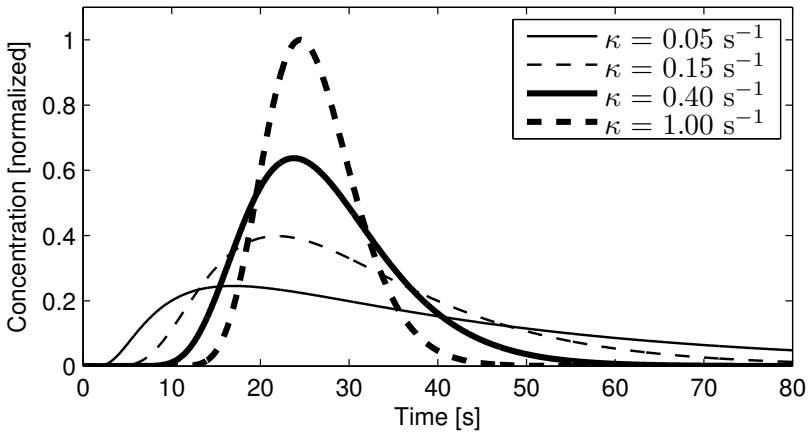

Figure 2.6 *IDC shape for various values of κ with $\mu = 25$ s.*

represent the IDC as in (2.6), although with a different parametrization:

$$t_0 = \tilde{t}_0, \tag{2.10a}$$

$$\alpha = \frac{m}{v_\ell A}, \tag{2.10b}$$

$$\mu = t_1 - \hat{t}_0 + \frac{x_d - x_1}{v_\ell}, \tag{2.10c}$$

$$\lambda = \frac{v_\ell^2}{2D_\ell}\left(t_1 - \hat{t}_0\right) + \frac{v_\ell(x_d - x_1)}{2D_\ell}. \tag{2.10d}$$

Using the parametrization in (2.10), we define a new parameter κ, dependent on D_ℓ and v_ℓ only:

$$\kappa = \frac{\lambda}{\mu} = \frac{v_\ell^2}{2D_\ell}. \tag{2.11}$$

After combining (2.11) and (2.6), the IDC can be expressed as

$$C(t) = \mathrm{AUC}\sqrt{\frac{\kappa}{2\pi\left(t - t_0\right)}}\exp\left(-\frac{\kappa\left(t - t_0 - \mu\right)^2}{2\left(t - t_0\right)}\right). \tag{2.12}$$

Being dependent on D_ℓ and v_ℓ only, κ is the local, diffusion-related parameter that we have adopted for characterization of the microvascular structure. The parameter κ can be interpreted as the local ratio between the diffusive time and the squared convective time. For low values of D_ℓ, the UCA concentration profile hardly spreads while passing x_d. This leads to a symmetric IDC, characterized by high values of κ. On the other hand, high values of D_ℓ lead to a skewed IDC, represented by small values of κ. This is shown in Fig. 2.6.

2.2.4 Parameter estimation

Local diffusion can be estimated from measured TDCs using the modified LDRW IDC formalization in (2.12) and the relation between UCA concentration and gray level in (2.3). The accuracy of the parameter estimation is determined by the temporal characteristics of IDC noise, i.e., all signals that the model function (2.6) cannot explain. Typical ultrasound noise sources such as speckle are less significant here: stationary noise affects only the IDC baseline and signals from moving linear scatterers (e.g. red blood cells) are effectively suppressed by contrast-specific imaging techniques [16]. IDC noise is therefore mainly related to microbubbles and might be caused by random microbubble movement into and out of the sample volume, represented by a pixel. Such movement produces a noise component whose variance relates directly to the microbubble concentration, satisfying the multiplicative character of IDC noise that was previously measured [34].
We evaluated the multiplicative character of IDC noise by analyzing over 50 $\times$ 10^3 curves measured *in vivo*. Signals at frequencies above 0.5 Hz were considered as noise, because the spectrum of (2.6) is restricted to frequencies lower than 0.5 Hz for a realistic range of κ (0.1-1.5 s^{-1}) and μ (10-50 s). We compared the high-frequency noise power with the low-frequency signal magnitude using a short-time Fourier transform with a Hamming window of 3.2 s. For IDCs in the real domain, the average correlation coefficient was 0.86 $\pm$ 0.07, compared with 0.52 $\pm$ 0.24 for log-domain TDCs. The relatively strong correlation in the real domain indicates multiplicative noise. Moreover, frequencies above 0.5 Hz contained 54% of the total signal power in the real domain, compared with 6% in the logarithmic domain. For these reasons, parameter estimation is performed in the logarithmic domain [42]. Although the logarithmic compression affects the error metrics for TDC fitting, the effects on the estimation of λ and μ are negligible [34].
The modified LDRW TDC formalization is obtained by combining (2.12) and (2.3). After compensating for the gray mapping, and estimating and subtracting the baseline Q_0, this expression is given as

$$Q(t) = a_{\mathrm{DR}} \ln\left(\mathrm{AUC}\sqrt{\frac{\kappa}{2\pi\,(t-t_0)}}\exp\left(-\frac{\kappa\,(t-t_0-\mu)^2}{2\,(t-t_0)}\right)+1\right). \tag{2.13}$$

In (2.13), the factor a_{CI}/I_0 is included in AUC, since only a relative measure of the UCA concentration is required.
The accuracy of the parameter estimation is improved by low-pass filtering the TDCs both in space and time (see Fig. 2.7). The spatial filter design is based on the size of the smallest microvascular networks for which local diffusion must be estimated. As angiogenesis is required for cancer to grow beyond 1 mm^3 [11], a reliable analysis of image regions with

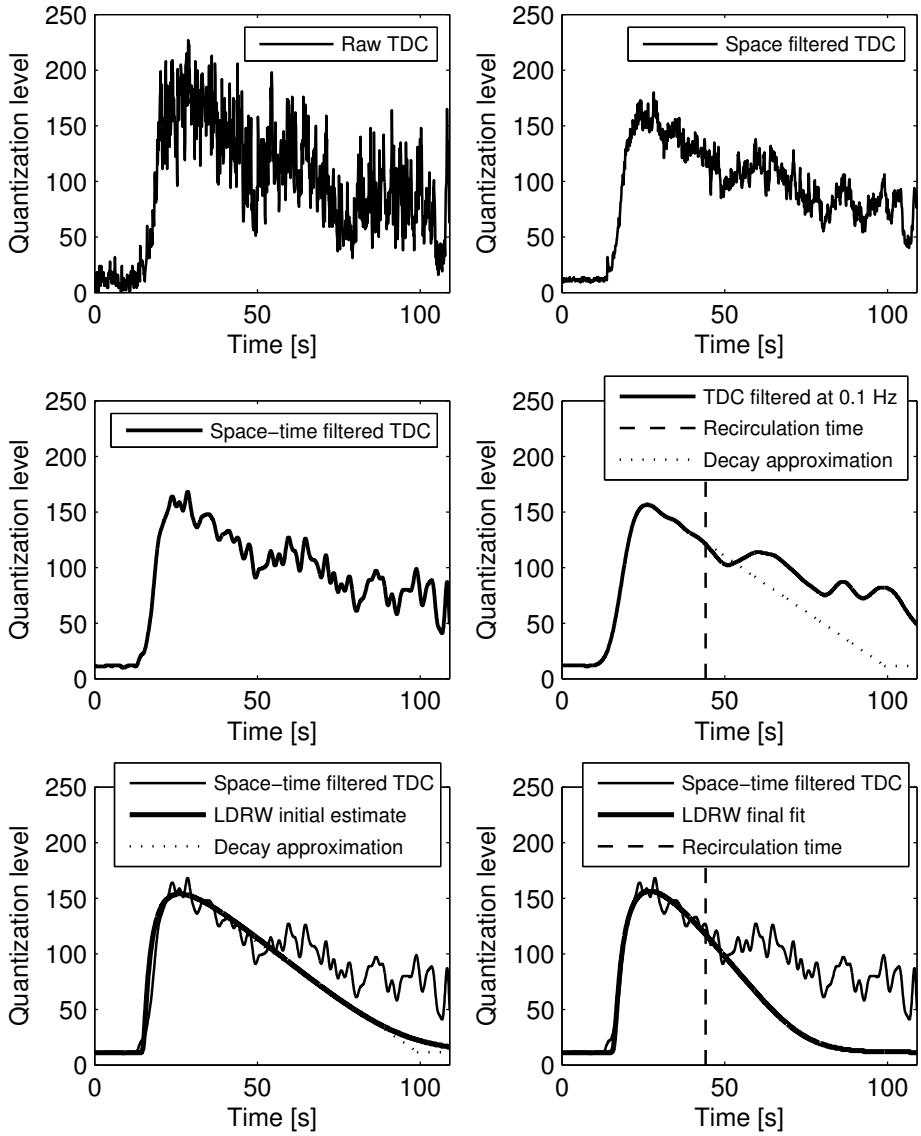

Figure 2.7 *Signal conditioning and fitting of a single-pixel TDC in the logarithmic domain.*

a radius as small as 0.62 mm is necessary. To maintain sufficient resolution for accurate characterization at this scale, we adopted a Gaussian filter with $\sigma = 0.5$ mm, whose 3-dB value is at 0.59 mm. The loss of information due to spatial filtering is limited, because the axial scanner resolution (0.43 mm) is inferior to the B-mode pixel resolution (0.15 mm). The nonuniform spatial TRUS statistics, generally due to a lower lateral resolution at larger depths, are compensated by spatial filtering; after filtering, the average correlation coefficient between neighboring pixel IDCs is independent of the scanning depth, suggesting a uniform spatial resolution. After spatial filtering, downsampling in both spatial dimensions by a factor three permits reducing the computation time by 89%.

Low-pass filtering may also be performed in time, given the scanning frame rate (about

10 Hz) as compared to the maximum TDC frequency of 0.5 Hz. We adopted a finite impulse response filter of 100 coefficients and a cut-off frequency of 0.5 Hz. A zero phase shift is obtained by filtering in both forward and backward directions.

A well-known issue in IDC analysis is recirculation, i.e., the subsequent bolus passages through a selected ROI that mask the last segment of the first-pass IDC tail [35, 39, 43]. In cardiovascular applications, IDC parameter estimation is often restricted to the interval $t \leq t_{\mathrm{Tr}}$ where recirculation does not occur. The truncation time t_{Tr} is commonly defined as the time when the IDC decays to 30% of its peak value [34, 43]. An effect similar to recirculation occurs also in the prostate, where additional UCA passages may also be due to multiple feeding arteries [44]. The effects on measured curves are, however, less evident than in cardiovascular applications (see Fig. 2.7). Therefore, we adopt a more specific approach to define t_{Tr}. The IDC decay during an interval Δt is given as

$$\frac{C(t+\Delta t)}{C(t)} = \sqrt{\frac{t}{t+\Delta t}} \exp\left(-\frac{\kappa}{2}\Delta t\left(1-\frac{\mu^2}{t(t+\Delta t)}\right)\right), \tag{2.14}$$

where $t_0 = 0$ is assumed without loss of generality. For large t, the IDC decays approximately exponentially, which corresponds to a linear TDC decay in the logarithmic domain. Therefore, t_{Tr} is determined such that the linear TDC approximation has the highest R^2 on the interval between the peak time and t_{Tr}. The choice of t_{Tr} is restricted to the interval where the IDC amplitude, in the real domain, decays to between 20% and 50% of the peak amplitude. The influence of TDC noise on the determination of t_{Tr} is reduced by additional low-pass filtering with cut-off frequency at 0.1 Hz.

LDRW model fitting can be performed with a linear regression algorithm as described in [34]. However, the computational complexity of this algorithm is high as both the parameter t_0 and the regression interval are iteratively determined. Given the large number of TDCs (about 5×10^3 for each dataset, after downsampling), we have adopted a different method, based on the statistical IDC moments [45]. We have extended this method by inclusion of the estimation of t_0 (see Appendix, Sec. 2.5), which makes the method non-iterative. However, the computation of the statistical IDC moments requires the complete first-pass IDC. For the interval $t > t_{\mathrm{Tr}}$, the IDC is approximated by an exponential decay, corresponding to the linear TDC approximation. As a final step, the obtained parameter estimates are used as initialization to fit (2.13) to the TDC for $t \leq t_{\mathrm{Tr}}$ using the Levenberg-Marquardt iteration [46], to increase the fitting accuracy. Up to five iterations were used; a higher number of iterations did not significantly improve the results. On a Windows-based workstation with an Intel Core2 Duo processor running at 3.16 GHz with 3.49 GB of RAM, one video is processed in about five minutes.

A parametric image is produced by displaying the estimates of κ for all pixels covering the

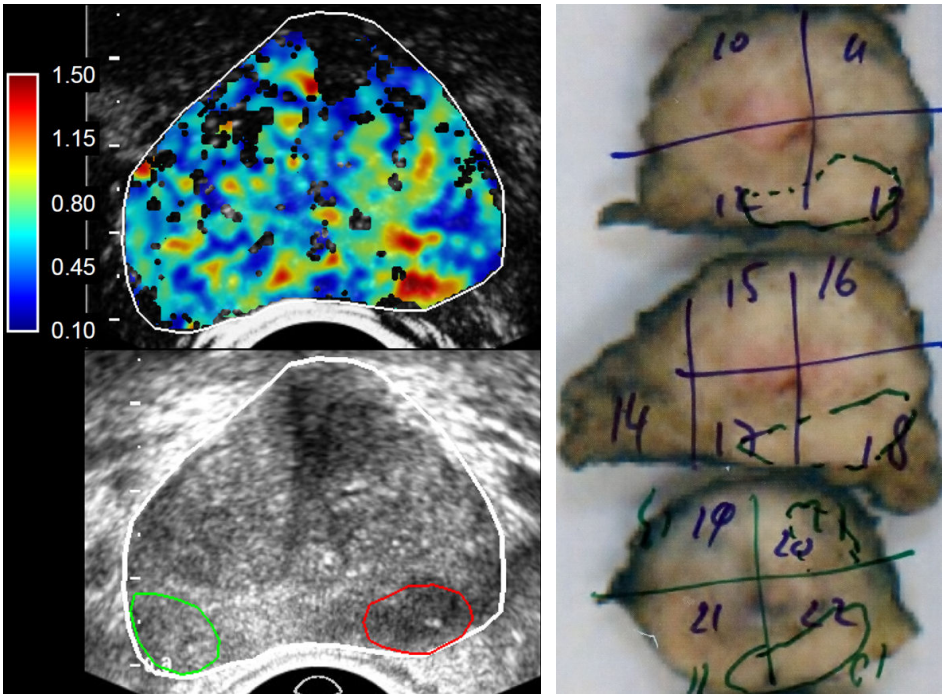

Figure 2.8 In vivo *CUDI parametric image obtained from the same data as shown in Fig. 2.1 with histology. On the top left, the diffusion parametric image is overlaid on the ultrasound power modulation image. The parameter κ is displayed as a color coding; uncolored pixels are associated with fit failure. The manually selected white contour represents the prostate boundary. The corresponding fundamental ultrasound image (bottom left) is also shown, in which the red and green polygons represent the adopted ROIs for cancerous and healthy tissue, respectively. Three corresponding histology slices, all showing cancer in the right peripheral zone, are shown on the right.*

prostate, as a color coding overlaid on the B-mode image, see Fig. 2.8. The parametric image is filtered with the same Gaussian filter ($\sigma = 0.5$ mm) as the one adopted for spatial filtering, to emphasize local diffusion at the scale where microvascular networks can be associated with the presence of cancer.

In some cases, shadowing effects or a lack of perfusion may result in fit failure. Then, the estimated parameters do not represent the UCA transport dynamics. If the determination coefficient R^2 of the TDC fit in the logarithmic domain is lower than 0.75, the fit is not accepted and no color is displayed.

2.2.5 Method validation

To validate whether the diffusion-related parameter κ can be estimated independently of the bolus history, the convective diffusion equation (2.4) was simulated by a finite difference approximation. The adopted boundary conditions were (2.5b) and (2.8). For various σ_1, a large number of IDCs were obtained for increasing L. We analyzed the dependency of the

diffusion-related parameters κ and $\lambda = \kappa\mu$ on both L and σ_1, by fitting the IDCs with the proposed algorithm.

The performance of the parameter estimation algorithm was then evaluated by fitting 40×10^3 simulated TDCs, for $\kappa \in [0.1, 1]$ and $\mu \in [10, 50]$, with additive white noise sequences. By adding these noise sequences to the TDCs, we reproduced the multiplicative noise character in the real domain [34]. The noise level was 12 dB was lower than the signal power, representing the noise level encountered *in vivo*.

A preliminary clinical validation of the method was also performed by analysis of five datasets registered from four patients referred for radical prostatectomy at the AMC University Hospital (Amsterdam, the Netherlands). After radical prostatectomy, the prostate was cut in slices of 4-mm thickness and a pathologist marked the presence of cancer by histology analysis based on the level of cell differentiation [47]. We selected the histology slice(s) corresponding to the ultrasound imaging plane and compared them with the CUDI results. Fig. 2.8 shows an example parametric diffusion image with the corresponding histology. A quantitative comparison was performed for each dataset by selecting two ROIs containing healthy and cancerous tissue, based on the histology. Because the histology analysis was not specifically aimed at a high-resolution validation, we limited the ROI selection to areas larger than 50 mm^2 that did not show significant variation across subsequent slices. We considered only the peripheral zone of the prostate [8], since about 70 to 80% of all cancers are found in this anatomical zone [8, 14]. From the histogram of κ in each ROI, the mean value and standard deviation of each specific class (healthy and cancerous tissue) were used to determine the optimal tissue-classification threshold by Bayes inference [48]. This threshold (based on all datasets) was used to derive the optimal sensitivity and specificity for pixel classification. In addition, we evaluated the receiver operating characteristic (ROC) curve on a pixel basis.

A comparison was performed with different IDC parameters proposed in the literature [14, 20–23], by repeating the same tissue classification procedure. We extracted the peak intensity (PI), the peak time (PT), the appearance time (AT, the time at which the IDC achieves 5% of PI), the full-width at half-maximum (FWHM, the time duration while the IDC exceeds PI/2 [22, 23]), the wash-in time (WIT, the time it takes for the IDC to rise from 5% to 95% of its peak value [23]), the area under the IDC (AUC), the MTT (the LDRW parameter μ) and the LDRW parameter λ. The parameters PT and AT were computed with respect to the estimated theoretical injection time t_0. All parameters were extracted from linearized fits to ensure that the comparison is not affected by differences in preprocessing.

Table 2.1 *Mean and standard deviation of IDC parameters measured in healthy and cancerous tissue.*

Parameter	Healthy tissue	Cancerous tissue
κ [s^{-1}]	0.550 $\pm$ 0.249	1.054 $\pm$ 0.283
PI [a.u.]	25.0 $\pm$ 44.0	80.0 $\pm$ 74.6
PT [s]	31.3 $\pm$ 12.0	22.1 $\pm$ 7.8
AT [s]	17.7 $\pm$ 8.5	15.5 $\pm$ 5.7
FWHM [s]	18.4 $\pm$ 5.2	10.9 $\pm$ 2.9
WIT [s]	11.3 $\pm$ 3.6	7.3 $\pm$ 2.0
MTT (μ) [s]	32.4 $\pm$ 11.9	22.7 $\pm$ 7.8
AUC [a.u.]	492 $\pm$ 1038	844 $\pm$ 757
λ	20.4 $\pm$ 10.0	24.7 $\pm$ 8.3

2.3 Results

The parameters κ and λ, estimated from IDCs obtained by simulations of the convective diffusion equation (2.4), confirmed the theoretical results of (2.10d) and (2.11) with an estimation error below 1%. This result confirms that κ, in contrast to λ, is independent of x_d and σ_1, i.e., independent of the detection site and the history of the bolus, respectively.

The parameter estimation algorithm fitted simulated TDCs with an average $R^2 = 0.999$ and $R^2 = 0.990$ in the logarithmic and real domains, respectively. If the complete TDC could be used for fitting, the mean relative error for κ was 4.33%. When the IDC tail was excluded from the fitting, as required for fitting of TDCs obtained *in vivo*, the mean relative error was 10.15%.

On the obtained B-mode image sequences that were compared with histology, the algorithm showed an average $R^2 = 0.95$ after filtering in space and time, which was by 18% higher than without filtering. In these data, 89% of the pixel IDC fits were considered sufficiently accurate ($R^2 > 0.75$ in the logarithmic domain) and 29×10^3 pixel TDC fits were included in the comparison with histology.
In all patients, we observed that the presence of cancer was associated with higher values of κ. For each parameter, the mean value and standard deviation in healthy and cancerous tissue are reported in Table 2.1. We used this information to derive the sensitivity and specificity for pixel classification, as well as the ROC curve area. For all the considered parameters, the results are reported in Table 2.2.

Table 2.2 *Sensitivity, specificity, and ROC curve area on pixel basis of several hemodynamic parameters extracted from fitted IDCs*

Parameter	Cancerous if	Sensitivity [%]	Specificity [%]	ROC curve area
κ	$\geq$ 0.804 s^{-1}	81.2	84.6	0.909
PI	$\geq$ 70.5 a.u.	56.7	84.1	0.737
PT	$\leq$ 29.5 s	82.3	56.6	0.738
AT	$\leq$ 18.7 s	79.8	48.4	0.659
FWHM	$\leq$ 14.7 s	90.1	76.2	0.895
WIT	$\leq$ 9.6 s	87.7	68.2	0.837
MTT (μ)	$\leq$ 30.0 s	82.3	58.4	0.753
AUC	$\geq$ 208 a.u.	77.1	43.4	0.608
λ	$\geq$ 19.6	72.7	47.3	0.631

2.4 Discussion and Conclusions

Contrast-ultrasound diffusion imaging (CUDI) is an innovative noninvasive imaging method for prostate cancer localization. The passage of an intravenously injected UCA bolus through the prostate is measured by dynamic TRUS imaging. The TDCs obtained from all pixels covering the prostate are analyzed and a parametric image, based on intravascular diffusion, is produced.

In a preliminary clinical validation, we have compared the cancer localization accuracy of the proposed method, CUDI, with several quantitative indicators of perfusion. More precisely, we compared the correspondence between several methods for MVD characterization and the level of cell differentiation, evaluated by a histology analysis.

The results show that the diffusion-related parameter κ has a ROC curve that is superior to that of any other IDC parameter. Although the sensitivity of some other parameters is higher, κ is the only parameter whose sensitivity and specificity both exceed 80%. While these results are obtained on a pixel basis, the clinical diagnosis would be based on a larger scale; currently, carcinomas are considered clinically significant if their size is at least 0.5 cm^3 [47]. Lesion classification is then based on large amounts of pixels. A perfect pixel-based sensitivity is therefore not strictly necessary. On the other hand, a high specificity is essential to exclude healthy areas.

Although they are less specific than κ, all IDC time parameters are smaller in the cancerous areas than in healthy areas. This is consistent with previous qualitative observations [6, 14]. Perhaps, the lower specificity of the time parameters compared to κ is related to the difficulty of interpreting these time parameters locally at the measurement site [24]. The amplitude-related parameters PI and AUC show relatively large variations, in both healthy and cancerous tissue. This may be due to their dependency on the amount of UCA entering

the prostate or to nonlinear ultrasound propagation through UCA dispersions [25].

Imaging of intravascular diffusion is a new concept, based on modeling the intravascular UCA transport by the convective diffusion equation. Whereas other researchers have taken a bottom-up approach, by analyzing flow through individual vessels and deducing the effects on vascular networks [49], we have pursued a top-down approach, aimed at macroscopic modeling of the microvascular network, similarly to [31]. In fact, we characterize the microvascular network as similar to a porous medium [32], whose structural characteristics are reflected in diffusion [30].

The parameter κ measures the ratio between diffusion and convection. High values of κ, with a relatively low diffusion with respect to convection, seem to be associated with the presence of cancer. This relative decrease in diffusion may be caused by an increased microvessel tortuosity. This is however the first study that investigates the effects of changes in the microvascular architecture on intravascular diffusion; a better understanding requires additional research.

The presented method for estimation of diffusion has the advantage that a local diffusion-related parameter κ can be estimated independently for each pixel. This parameter depends only on the local, hemodynamic parameters v_ℓ and D_ℓ and does not depend on the entire dilution history between the injection and detection site. This novel approach is based on the assumption of a Normal UCA concentration distribution in space; an assumption that is also included in the LDRW model [38]. The width of this distribution before the bolus passage through the detection site, given by σ_1, determines the resolution by which we can estimate κ (see Fig. 2.5). We have not been able to verify the use of this assumption in an experimental *in vitro* setup. However, the spatial UCA distribution in the systemic arteries is mainly determined by the transpulmonary circulation and can be well described by the LDRW model [38]. Moreover, the LDRW model is reported to be the most suitable for fitting IDCs measured in the microcirculation of animal models [23]. These results support the validity of the LDRW model assumptions.

The proposed method focuses on the temporal characteristics of the UCA diffusion dynamics. Alternative methods can be based also on spatial diffusion characteristics and will be investigated in the future. In this study, relatively simple linear filters were used to improve the robustness of parameter estimation. More advanced filtering methods can possibly provide additional improvements. In this context, coherence-enhancing diffusion filtering seems an interesting method to improve the signal quality given the anisotropy caused by the TRUS resolution and the microvascular characteristics.

An important issue concerns the validation of CUDI, as determining the position of the imaging plane with respect to the histology planes is difficult. In fact, the imaging plane often crosses several histology planes. The presented validation was therefore restricted to

patients whose histology did not show significant variation across subsequent slices. We are currently investigating new strategies to improve the comparison between imaging and histology. The validation could be improved by comparing CUDI results directly with the MVD, rather than with the level of cell differentiation. This approach, requiring the use of immunohistology [10–12], would be more accurate as CUDI aims at characterizing the microvascular structure. An additional step in the validation may also involve the zonal anatomy of the prostate. Here, the validation was restricted to the peripheral zone, where the majority of cancers are found [8, 14]. As the microvascular structure varies among different anatomical zones of the prostate, it may also be interesting to investigate the intravascular diffusion in different zones.

In the future, three-dimensional ultrasound imaging may offer great advantages for the proposed method. From a clinical perspective, the entire prostate could be studied with a single UCA bolus injection. This would resolve an important current issue, i.e., the selection of proper TRUS imaging planes such that any significant carcinoma is covered. From a technical perspective, the UCA transport could be observed in all spatial dimensions, which would open up new possibilities for spatio-temporal analysis of intravascular UCA diffusion. Moreover, the *in vivo* validation would be simplified as imaging and histology results could be compared more accurately.

In conclusion, also given the additional possibilities offered by three-dimensional ultrasound, imaging of intravascular diffusion may be a promising alternative to perfusion imaging for the localization of prostate cancer. The intravascular nature of UCA microbubbles makes contrast-enhanced ultrasound an attractive imaging modality to assess intravascular diffusion. Furthermore, the use of CUDI should not be limited to prostate cancer; the same diffusion principles also apply to many other forms of cancer, such as breast cancer. Further clinical studies are however required to evaluate the clinical reliability of CUDI.

2.5 Appendix: LDRW IDC moments and skewness

For a random variable y with probability density function (PDF) $p(y)$, the moments M_i for $i \geq 1$ are given as

$$M_i = \int_{-\infty}^{\infty} y^i p(y)\,\mathrm{d}y. \tag{2.15}$$

For $i \geq 2$, the central moments m_i are given as

$$m_i = \int_{-\infty}^{\infty} (y - M_1)^i p(y)\,\mathrm{d}y. \tag{2.16}$$

To interpret the LDRW IDC formalization in (2.6) as a PDF, we define $C(t) = 0$ for $t \leq t_0$ and divide $C(t)$ by its integral $\int_{-\infty}^{\infty} C(t)\,\mathrm{d}t = \mathsf{AUC}$ [50]. The moments M_i are then given as

$$M_i = \frac{1}{\mathsf{AUC}} \int_{t_0}^{\infty} t^i C(t)\,\mathrm{d}t. \tag{2.17}$$

The LDRW IDC moments, which for $t_0 = 0$ are denoted by $M_i|_{t_0=0}$, have been derived in [45] and [50]:

$$M_1|_{t_0=0} = \mu\left(1 + \frac{1}{\lambda}\right), \tag{2.18a}$$

$$M_2|_{t_0=0} = \left(\frac{\mu}{\lambda}\right)^2 \left(\lambda^2 + 3\lambda + 3\right), \tag{2.18b}$$

$$M_i|_{t_0=0} = (2i-1)\frac{\mu}{\lambda}\, M_{i-1}|_{t_0=0} + \mu^2\, M_{i-2}|_{t_0=0} \qquad \text{for } i \geq 3. \tag{2.18c}$$

In (2.18), $M_1|_{t_0=0}$ equals the expectation of $C(t)$. If t_0 is known, the moments $M_1|_{t_0=0}$ and $M_2|_{t_0=0}$ can be computed from measured IDCs. Therefore, solving λ and μ from (2.18a) and (2.18b) provides a non-iterative method to estimate these parameters [45].
In the current study, t_0 is however unknown so we cannot measure $M_i|_{t_0=0}$ specifically. We can only measure the moments M_i, which depend on t_0. To estimate all LDRW parameters by measuring M_i, we include t_0 in the moments analysis. The first moment M_1 for $t_0 \neq 0$ is by linearity of the expectation given as

$$M_1 = M_1|_{t_0=0} + t_0 = \mu\left(1 + \frac{1}{\lambda}\right) + t_0. \tag{2.19}$$

This result can also be derived by substitution of $t - t_0$ in the integrand of (2.17). Similarly, M_i for $i > 1$ can be derived. λ, μ and t_0 can then be solved from the obtained equations for M_1, M_2 and M_3. However, this system is very complicated and has no analytical solution. Instead, we can also measure the central moments m_i and derive expressions for m_i in terms of λ, μ and t_0. By substituting $\tau = t - t_0$, we observe that the central moments are compensated for t_0 by the time shift by $M_1 = M_1|_{t_0=0} + t_0$:

$$m_i = \frac{1}{\mathsf{AUC}} \int_{0}^{\infty} (\tau - M_1|_{t_0=0})^i C(\tau + t_0)\,\mathrm{d}\tau. \tag{2.20}$$

In fact, the argument $\tau + t_0$ ensures that the resulting function $C(\tau + t_0)$ is independent of t_0 (see (2.6)). Therefore, the moments of $C(\tau + t_0)$ are given by (2.18). By expanding $(\tau - M_1|_{t_0=0})^i$, the central moments m_i can be completely described in terms of $M_i|_{t_0=0}$.

In particular, m_2 and m_3 are given as

$$m_2 = M_2|_{t_0=0} - \left(M_1|_{t_0=0}\right)^2 = \left(\frac{\mu}{\lambda}\right)^2 (\lambda + 2)\,, \tag{2.21a}$$

$$m_3 = M_3|_{t_0=0} - 3\left(M_1|_{t_0=0}\right)\left(M_2|_{t_0=0}\right) + 2\left(M_1|_{t_0=0}\right)^3 = \left(\frac{\mu}{\lambda}\right)^3 (3\lambda + 8)\,. \tag{2.21b}$$

λ and μ can be solved from (2.21). To obtain the solution, we compute the IDC skewness γ_1, i.e., the third standardized moment of $C(t)$, which is a function of only λ:

$$\gamma_1 = \frac{m_3}{(m_2)^{3/2}} = \frac{3\lambda + 8}{(\lambda + 2)^{3/2}}. \tag{2.22}$$

This result confirms the relation between λ and the IDC skewness [39, 41, 43]. Solving λ from (2.22) provides an estimate of λ that is independent of μ and t_0. Subsequently, μ can be estimated from (2.21a) as

$$\mu = \sqrt{m_2}\frac{\lambda}{\sqrt{\lambda + 2}}. \tag{2.23}$$

Finally, we use (2.19) to estimate t_0 from M_1 as

$$t_0 = M_1 - \mu\left(1 + \frac{1}{\lambda}\right). \tag{2.24}$$

The fourth parameter AUC is given directly by the IDC integral. Since the IDC integral as well as the moments M_1, m_2 and m_3 can directly be computed from measured IDCs, all LDRW IDC parameters can be estimated by (2.22), (2.23) and (2.24).
In summary, we have obtained a method to estimate all LDRW IDC parameters, including t_0. Being non-iterative, this method has low computational requirements compared to various iterative methods.

References

[1] J. Ferlay, P. Autier *et al.*, "Estimates of the cancer incidence and mortality in Europe in 2006," *Ann. Oncol.*, vol. 18, pp. 581–592, 2007.

[2] A. Jemal, R. Siegel, E. Ward *et al.*, "Cancer statistics, 2008," *CA Cancer J. Clin.*, vol. 58, no. 2, pp. 71–96, 2008.

[3] T. J. Polascik and V. Mouraviev, "Focal therapy for prostate cancer," *Curr. Opin. Urol.*, vol. 18, pp. 269–274, 2008.

[4] C. H. Bangma, S. Roemeling, and F. H. Schröder, "Overdiagnosis and overtreatment of early detected prostate cancer," *World J. Urol.*, vol. 25, pp. 3–9, 2007.

[5] F. H. Schröder, J. Hugosson, M. J. Roobol *et al.*, "Screening and prostate-cancer mortality in a randomized European study," *N. Engl. J. Med.*, vol. 360, no. 13, pp. 1320–1328, 2009.

[6] M. H. Wink, J. J. M. C. H. de la Rosette, C. A. Grimbergen, and H. Wijkstra, "Transrectal contrast enhanced ultrasound for diagnosis of prostate cancer," *World J. Urol.*, vol. 25, pp. 367–373, 2007.

[7] M. Seitz, A. Shukla-Dave, A. Bjartell *et al.*, "Functional magnetic resonance imaging in prostate cancer," *Eur. Urol.*, vol. 55, pp. 801–814, 2009.

[8] T. Loch, "Urologic imaging for localized prostate cancer in 2007," *World J. Urol.*, vol. 25, pp. 121–129, 2007.

[9] J. Folkman, K. Watson, D. Ingber, and D. Hanahan, "Induction of angiogenesis during the transition from hyperplasia to neoplasia," *Nature*, vol. 339, no. 6219, pp. 58–61, 1989.

[10] N. Weidner, P. R. Carroll, J. Flax, W. Blumenfeld, and J. Folkman, "Tumor angiogenesis correlates with metastasis in invasive prostate carcinoma," *Am. J. Pathol.*, vol. 143, no. 2, pp. 401–409, 1993.

[11] M. K. Brawer, "Quantitative microvessel density. A staging and prognostic marker for human prostatic carcinoma," *Cancer*, vol. 78, no. 2, pp. 345–349, 1996.

[12] M. Borre, B. V. Offersen, B. Nerstrøm, and J. Overgaard, "Microvessel density predicts survival in prostate cancer patients subjected to watchful waiting," *Br. J. Cancer*, vol. 78, no. 7, pp. 940–944, 1998.

[13] D. Cosgrove, "Angiogenesis imaging - ultrasound," *Br. J. Radiol.*, vol. 76, pp. S43–S49, 2003.

[14] L. Pallwein, M. Mitterberger, A. Pelzer *et al.*, "Ultrasound of prostate cancer: recent advances," *Eur. Radiol.*, vol. 18, pp. 707–715, 2008.

[15] S. B. Feinstein, "The powerful microbubble: from bench to bedside, from intravascular indicator to therapeutic delivery system, and beyond," *Am. J. Physiol. Heart Circ. Physiol.*, vol. 287, no. 2, pp. H450–H457, 2004.

[16] N. de Jong, P. J. A. Frinking, A. Bouakaz, and F. J. ten Cate, "Detection procedures of ultrasound contrast agents," *Ultrasonics*, vol. 38, no. 1–8, pp. 87–92, 2000.

[17] A. Pelzer, J. Bektic, A. P. Berger *et al.*, "Prostate cancer detection in men with prostate specific antigen 4 to 10 ng/mL using a combined approach of contrast enhanced color Doppler targeted and systematic biopsy," *J. Urol.*, vol. 173, pp. 1926–1929, 2005.

[18] E. J. Halpern, J. R. Ramey, S. E. Strup *et al.*, "Detection of prostate carcinoma with contrast-enhanced sonography using intermittent harmonic imaging," *Cancer*, vol. 104, pp. 2373–2383, 2005.

[19] R. A. Linden, E. J. Trabulsi, F. Forsberg *et al.*, "Contrast enhanced ultrasound flash replenishment method for directed prostate biopsies," *J. Urol.*, vol. 178, pp. 2354–2358, 2007.

[20] R. J. Eckersley, D. O. Cosgrove, M. J. Blomley, and H. Hashimoto, "Functional imaging of tissue response to bolus injection of ultrasound contrast agent," in *IEEE Ultrasonics Symp. Proc.*, 1998, pp. 1779–1782.

[21] R. J. Eckersley, J. P. Sedelaar, M. J. K. Blomley *et al.*, "Quantitative microbubble enhanced transrectal ultrasound as a tool for monitoring hormonal treatment of prostate carcinoma," *Prostate*, vol. 51, pp. 256–267, 2002.

[22] N. Elie, A. Kaliski, P. Péronneau *et al.*, "Methodology for quantifying interactions between perfusion evaluated by DCE-US and hypoxia throughout tumor growth," *Ultrasound Med. Biol.*, vol. 33, no. 4, pp. 549–560, 2007.

[23] C. Strouthos, M. Lampaskis, V. Sboros, A. McNeilly, and M. Averkiou, "Indicator dilution models for the quantification of microvascular blood flow with bolus administration of ultrasound contrast agents," *IEEE Trans. Ultrason., Ferroelectr., Freq. Control*, vol. 57, no. 6, pp. 1296–1310, 2010.

[24] M. Mischi, J. A. den Boer, and H. H. M. Korsten, "On the physical and stochastic representation of an indicator dilution curve as a gamma variate," *Physiol. Meas.*, vol. 29, pp. 281–294, 2008.

[25] M.-X. Tang and R. J. Eckersley, "Nonlinear propagation of ultrasound through microbubble contrast agents and implications for imaging," *IEEE Trans. Ultrason., Ferroelectr., Freq. Control*, vol. 53, no. 12, pp. 2406–2415, 2006.

[26] R. K. Jain, "Haemodynamic and transport barriers to the treatment of solid tumours," *Int. J. Radiat. Biol.*, vol. 60, no. 1-2, pp. 85–100, 1991.

[27] S. Delorme and M. V. Knopp, "Non-invasive vascular imaging: assessing tumour vascularity," *Eur. Radiol.*, vol. 8, pp. 517–527, 1998.

[28] G. Taylor, "Dispersion of soluble matter in solvent flowing slowly through a tube," *Proc. R. Soc. A*, vol. 219, pp. 186–203, 1953.

[29] R. J. M. D. de Wiest, *Flow through porous media*. London: Academic Press, 1969.

[30] K. Vafai, Ed., *Handbook of Porous Media*, 2nd ed. Taylor & Francis Group, 2005.

[31] L. T. Baxter and R. K. Jain, "Transport of fluid and macromolecules in tumors: I. Role of interstitial pressure and convection," *Microvasc. Res.*, vol. 37, pp. 77–104, 1989.

[32] S. J. Chapman, R. J. Shipley, and R. Jawad, "Multiscale modeling of fluid transport in tumors," *Bull. Math. Biol.*, vol. 70, pp. 2334–2357, 2008.

[33] M. Schneider, "Characteristics of SonoVue^{TM}," *Echocardiography*, vol. 16, no. 7, pp. 743–746, 1999.

[34] M. Mischi, A. A. C. M. Kalker, and H. H. M. Korsten, "Videodensitometric methods for cardiac output measurements," *EURASIP J. Appl. Signal Processing*, vol. 5, pp. 479–489, 2003.

[35] X. Chen, K. Q. Schwarz, D. Phillips, S. D. Steinmetz, and R. Schlief, "A mathematical model for the assessment of hemodynamic parameters using quantitative contrast echocardiography," *IEEE Trans. Biomed. Eng.*, vol. 45, no. 6, pp. 754–765, 1998.

[36] L. Lüdemann, D. Prochnow, T. Rohlfing *et al.*, "Simultaneous quantification of perfusion and permeability in the prostate using dynamic contrast-enhanced magnetic resonance imaging with an inversion-prepared dual-contrast sequence," *Ann. Biomed. Eng.*, vol. 37, no. 4, pp. 749–762, 2009.

[37] N. G. Rognin, P. J. A. Frinking, M. Costa, and M. Arditi, "In-vivo perfusion quantification by contrast ultrasound: validation of the use of linearized video data vs. raw RF data," in *2008 IEEE Ultrasonics Symp. Proc.*, 2008, pp. 1690–1693.

[38] C. W. Sheppard, *Basic principles of the tracer method*. New York: John Wiley and Sons, 1962.

[39] M. E. Wise, "Tracer dilution curves in cardiology and random walk and lognormal distributions," *Acta Physiol. Pharmacol. Neerl.*, vol. 14, pp. 175–204, 1966.

[40] K. H. Norwich and S. Zelin, "The dispersion of indicator in the cardio-pulmonary system," *Bull. Math. Biophys.*, vol. 32, pp. 25–43, 1970.

[41] J. M. Bogaard, S. J. Smith, A. Versprille, M. E. Wise, and F. Hagemeijer, "Physiological interpretation of the skewness of indicator-dilution curves; theoretical considerations and a practical application," *Basic Res. Cardiol.*, vol. 79, pp. 479–493, 1984.

[42] A. Oppenheim, R. Schafer, and J. Stockham, T.G., "Nonlinear filtering of multiplied and convolved signals," *Proc. IEEE*, vol. 56, no. 8, pp. 1264–1291, 1968.

[43] R. K. Millard, "Indicator-dilution dispersion models and cardiac output computing methods," *Am. J. Physiol.*, vol. 272, no. Heart Circ. Physiol. 41, pp. H2004–H2012, 1997.

[44] A. Hendrikx, M. Klomp, J. Keyzer, B. Arends, and G. Zonneveld, "The role of colour velocity imaging (CVI) in prostate ultrasound," *Eur. J. Ultrasound*, vol. 3, no. 1, pp. 15–23, 1996.

[45] M. Mischi, A. A. C. M. Kalker, and H. H. M. Korsten, "Moment method for the local density random walk model interpolation of ultrasound contrast agent dilution curves," in *Proceedings on the 17th International EURASIP Conference BIOSIGNAL 2004*, Brno (Czech Rep.), 2004, pp. 33–35.

[46] G. A. F. Seber and C. J. Wild, *Nonlinear regression*. Wiley, 1989.

[47] R. Montironi, T. van der Kwast, L. Boccon-Gibod, A. V. Bono, and L. Boccon-Gibod, "Handling and pathology reporting of radical prostatectomy specimens," *Eur. Urol.*, vol. 44, pp. 626–636, 2003.

[48] C. M. Bishop, *Pattern Recognition and Machine Learning*. Springer, 2006.

[49] R. Karshafian, P. N. Burns, and M. R. Henkelman, "Transit time kinetics in ordered and disordered vascular trees," *Phys. Med. Biol.*, vol. 48, pp. 3225–3237, 2003.

[50] M. Mischi, "Contrast echocardiography for cardiac quantifications," Ph.D. dissertation, Eindhoven University of Technology, 2004, available at http://www.sps.ele.tue.nl/members/M.Mischi/.

CHAPTER 3

Maximum-likelihood estimation for indicator dilution analysis

Based on: M. P. J. Kuenen, I. H. F. Herold, H. H. M. Korsten, J. J. M. C. H. de la Rosette, H. Wijkstra, and M. Mischi, "Maximum-likelihood estimation for indicator dilution analysis," IEEE Transactions on Biomedical Engineering, in press, available at `http://dx.doi.org/10.1109/TBME.2013.2290375`.

Abstract – *Indicator-dilution methods are widely used by many medical imaging techniques and by dye-, lithium-, and thermo- dilution measurements. The measured indicator dilution curves are typically fitted by a mathematical model to estimate the hemodynamic parameters of interest. This paper presents a new maximum-likelihood algorithm for parameter estimation, where indicator dilution curves are considered as the histogram of underlying transit-time distribution. Apart from a general description of the algorithm, semi-analytical solutions are provided for three well-known indicator dilution models. An adaptation of the algorithm is also introduced to cope with indicator recirculation. In simulations as well as in experimental data obtained by dynamic contrast-enhanced ultrasound imaging, the proposed algorithm shows a superior parameter estimation accuracy over nonlinear least-squares regression. The feasibility of the algorithm for use* in vivo *is evaluated using dynamic contrast-enhanced ultrasound recordings obtained with the purpose of prostate cancer detection. The proposed algorithm shows an improved ability (increase in receiver-operating-characteristic curve area of up to 0.13) with respect to existing methods to differentiate between healthy tissue and cancer.*

3.1 Introduction

The use of indicator- or tracer-dilution methods for hemodynamic quantification in clinical applications has a long history [1]. After injection of an indicator into the bloodstream, an indicator dilution curve (IDC) can be obtained by measurement of the indicator concentration at a desired location downstream as function of time. Hemodynamic parameters of clinical interest can be extracted from IDCs.

Indicator-dilution methods are used in a wide variety of clinical applications. Many techniques were first introduced for cardiovascular quantification, mainly for assessment of cardiac output and blood volumes [1]. The original techniques for IDC measurement, such as dye- and thermodilution, have the drawback of being invasive and requiring patient catheterization [2, 3]. Nowadays, minimally-invasive imaging techniques, such as ultrasound [4], magnetic resonance imaging (MRI) [5], scintigraphy [6], and computed tomography [7], are also available. Their development has led to a wider spectrum of clinical applications, such as detection of ischemia, e.g. in the brain and the myocardium [8, 9]. In other application areas, such as oncology, indicator dilution methods are used for detection of angiogenesis [5, 10, 11].

The assessment of clinically relevant hemodynamic parameters from IDCs is based on modeling and analysis of the indicator transport kinetics. The first pass of an intravascular indicator can be represented by mathematical models that describe the distribution of indicator transit-times. Apart from providing a stochastic interpretation, several widely adopted models also offer a physiological representation of the hemodynamic phenomena. In fact, the first model proposed by Hamilton [3] describes the indicator wash-out from a single compartment. More recent models, such as the local density random walk (LDRW) model [12, 13], the lognormal model [14–16], and the gamma-variate model [17, 18], provide a physiological interpretation for the complete distribution of transit-times.

In many applications, estimation of the hemodynamic parameters of interest is performed by fitting of the IDCs to one of these models. Nonlinear least-squares (NLS) regression is typically adopted for IDC model fitting [19], as it is well-known that, in the case of additive white noise, this algorithm provides the maximum-likelihood estimates for the model parameters. However, IDC noise is not always well described by additive white noise [20–22]. As a result, NLS regression may not be the optimal method for IDC parameter estimation. This paper describes an alternative algorithm based on maximum-likelihood (ML) estimation. The stochastic nature of IDC models is exploited by considering the IDC as the observed histogram of indicator transit-times. The statistical properties of this histogram are derived. ML parameter estimation is performed by finding the parameter values that have the highest likelihood of producing the measured transit-time histogram. Apart from a general description of the algorithm, model-specific solutions for the LDRW, lognormal,

and gamma-variate models are obtained. In addition, a modification of the algorithm is proposed to cope with the common problem of indicator recirculation.
The performance of the proposed ML algorithm is compared to that of NLS regression in simulations and in IDCs measured *in vitro* by dynamic contrast-enhanced ultrasound (DCE-US) imaging. The feasibility of the algorithm *in vivo* is also shown based on DCE-US data obtained from the prostate microcirculation.

3.2 Materials and Methods

3.2.1 Statistics of indicator transit-time distributions

An IDC describes the indicator concentration as a function of time at a fixed location downstream, after injection of an indicator bolus upstream. Common models adopted to describe these IDCs, e.g., the LDRW, lognormal, and gamma-variate models, are probability distributions $p(t|\boldsymbol{\theta})$ that represent the distribution of indicator transit-times between the injection and the detection sites. The model-specific parameter vector $\boldsymbol{\theta}$ defines the IDC shape and, for these three models, offers a direct physiological interpretation of the indicator transport kinetics as well [12, 15, 18].
By interpreting an IDC as a transit-time distribution $p(t|\boldsymbol{\theta})$, indicator particles are expected to appear at the detection site at time t with probability $p(t|\boldsymbol{\theta})$. The measured transit-time of each indicator particle provides an observation of $p(t|\boldsymbol{\theta})$.
In reality, however, the transit-times of individual particles cannot be measured. Ideally, a measured IDC provides the amount of observed indicator particles C at N discrete-time samples n with time step Δt. Hence, the measured IDC $C(n)$ is the observed histogram of $p(t|\boldsymbol{\theta})$ based on a total of K transit-time observations. If these observations are independent, the probability that k particles are observed at time n is given by the binomial distribution as

$$P\{C(n)=k\} = \begin{pmatrix} K \\ k \end{pmatrix} p(n\Delta t|\boldsymbol{\theta})^k (1-p(n\Delta t|\boldsymbol{\theta}))^{K-k}. \tag{3.1}$$

An example of a simulated IDC based on (3.1) is shown in Fig. 3.1. The expectation and the variance of (3.1) are given as

$$\mathbf{E}\{C(n)\} = Kp(n\Delta t|\boldsymbol{\theta}), \tag{3.2}$$

$$\mathbf{Var}\{C(n)\} = Kp(n\Delta t|\boldsymbol{\theta})(1-p(n\Delta t|\boldsymbol{\theta})). \tag{3.3}$$

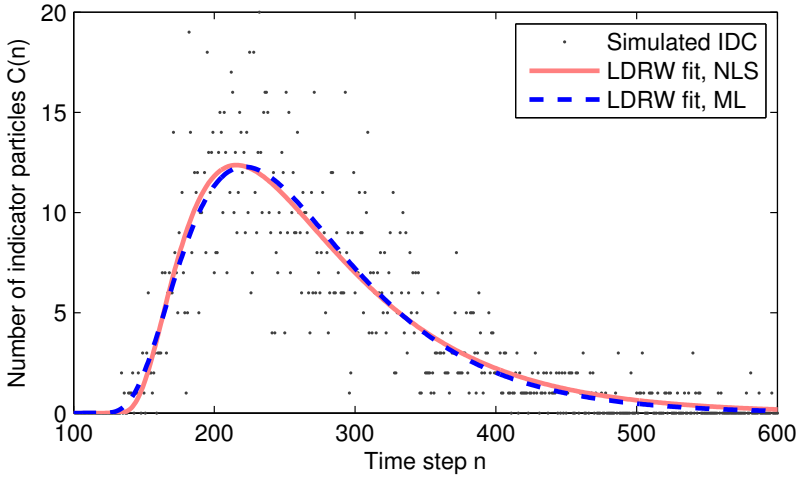

Figure 3.1 *IDC simulation obtained as histogram of 2000 randomly LDRW-distributed transit-times. The fits based on nonlinear least-squares (NLS) regression and maximum-likelihood (ML) estimation are also shown.*

The expectation $\mathbf{E}\{C(n)\}$ resembles the model IDC; the variance $\mathbf{Var}\{C(n)\}$ represents the fluctuation of the amount of indicator particles and can be considered as noise for the purpose of IDC fitting.

If the transit-time distribution is sampled by a sufficient number of time samples, such that $p(n\Delta t|\boldsymbol{\theta}) \ll 1$, the variance approximates the expectation. As a result, the noise power is proportional to the signal amplitude. This relation, which can also be appreciated in Fig. 3.1, may explain the previously observed correlation between IDC amplitude and IDC noise intensity [20], a correlation that cannot be explained by a standard additive noise model.

The instantaneous signal-to-noise ratio (SNR) of the IDC is given as

$$\mathrm{SNR}(n) = \frac{(\mathbf{E}\{C(n)\})^2}{\mathbf{Var}\{C(n)\}} = K\frac{p(n\Delta t|\boldsymbol{\theta})}{1-p(n\Delta t|\boldsymbol{\theta})}. \tag{3.4}$$

Because the SNR relates linearly to the total number of indicator particles K, K can be used to control the SNR in IDC simulations. The SNR is also influenced by the IDC shape: it is relatively high in narrow IDCs that have relatively high values of $p(n\Delta t|\boldsymbol{\theta})$ for only few samples.

3.2.2 Maximum-likelihood estimation

Based on the indicator transit-time statistics, we propose an algorithm for ML estimation of the parameter vector $\boldsymbol{\theta}$. Given the observed transit-times $t(k)$ of K observed indicator particles, we can evaluate the likelihood $\mathcal{L}(\boldsymbol{\theta})$ of the IDC model parameters. If we assume

independency of the transit-times of indicator particles, we have

$$\mathcal{L}(\boldsymbol{\theta}) = \prod_{k=1}^{K} p(t(k)|\boldsymbol{\theta}). \tag{3.5}$$

The ML solution of the parameters $\boldsymbol{\theta}$ is found by maximizing $\mathcal{L}(\boldsymbol{\theta})$. In practice, $\ln(\mathcal{L}(\boldsymbol{\theta}))$ is often maximized, because the logarithm is a monotonic function that transforms the the product into a more simple sum. A logarithmic transformation of (3.5) yields

$$\ln(\mathcal{L}(\boldsymbol{\theta})) = \sum_{k=1}^{K} \ln(p(t(k)|\boldsymbol{\theta})). \tag{3.6}$$

As already discussed, the individual transit-times $t(k)$ are unknown in reality. The transit-time histogram $C(n)$ is obtained instead. We can rewrite (3.6) in terms of $C(n)$ by grouping all particles that are sampled at the same time sample n as

$$\ln(\mathcal{L}(\boldsymbol{\theta})) = \sum_{n=1}^{N} C(n) \ln(p(n\Delta t|\boldsymbol{\theta})). \tag{3.7}$$

In (3.7), the sum acts on the time samples n rather than on the particles k. The likelihood function (3.7) equals the correlation between the measured IDC and the logarithm of the adopted IDC model. By differentiation of (3.7) with respect to $\boldsymbol{\theta}$ and equating it to zero, the ML solution for $\boldsymbol{\theta}$ can be obtained. This yields

$$\frac{\partial \ln(\mathcal{L}(\boldsymbol{\theta}))}{\partial \boldsymbol{\theta}} = \sum_{n=1}^{N} C(n) \frac{\partial p(n\Delta t|\boldsymbol{\theta})/\partial \boldsymbol{\theta}}{p(n\Delta t|\boldsymbol{\theta})} = \mathbf{0}. \tag{3.8}$$

The obtained result can be used to find the ML estimate $\hat{\boldsymbol{\theta}}_{\mathsf{ML}}$ in an iterative numerical optimization scheme.

Because $p(n\Delta t|\boldsymbol{\theta})$ is a probability distribution that integrates to 1, the area under the IDC (AUC) cannot be included in the preceding analysis. After determination of the IDC shape parameters, AUC can be estimated as the linear scale factor between the measured IDC $C(n)$ and the fit $p(n\Delta t|\hat{\boldsymbol{\theta}}_{\mathsf{ML}})$ by e.g. linear regression.

For three specific IDC models, a partially analytical solution can be derived. As an example, this derivation is provided for the LDRW model in the following section. The derivations for the lognormal and gamma-variate models, which are similar to those for the LDRW model, are reported in Appendix 3.6.

Application to the local density random walk model

The LDRW model provides both a stochastic and a physiological interpretation for the transit-time distribution. The model can be derived from a discrete one-dimensional random walk process [23] and is also an analytical solution of the convective diffusion equation for the one-dimensional case [12, 24]. The adopted boundary conditions represent a rapid injection and indicator mass conservation. Adopting a modified parametrization $\boldsymbol{\theta} = [\mu, \kappa, t_0]$ [25], the distribution of transit-times is given as

$$p(t|\boldsymbol{\theta}) = \sqrt{\frac{\kappa}{2\pi(t-t_0)}} \exp\left(-\frac{\kappa\,(t-t_0-\mu)^2}{2(t-t_0)}\right). \tag{3.9}$$

In (3.9), μ represents the mean transit time (MTT), κ is a skewness parameter related to the dispersion of the indicator bolus through the circulation, and t_0 represents the injection time. The LDRW model has been shown to accurately represent IDCs obtained by DCE-US in different applications, such as for cardiovascular quantification [13, 20] and for analysis of the microcirculation [26]. The model parameter κ has shown a promising value for detection of abnormalities in the microcirculation that are related to cancer [25].
To derive the ML solution for the LDRW model, the model in (3.9) is differentiated with respect to $\boldsymbol{\theta}$ as

$$\frac{\partial p(t|\boldsymbol{\theta})}{\partial \mu} = p(t|\boldsymbol{\theta}) \cdot \kappa \left(1 - \frac{\mu}{t-t_0}\right), \tag{3.10a}$$

$$\frac{\partial p(t|\boldsymbol{\theta})}{\partial \kappa} = p(t|\boldsymbol{\theta}) \cdot \frac{1}{2}\left(\frac{1}{\kappa} - \frac{(t-t_0-\mu)^2}{t-t_0}\right), \tag{3.10b}$$

$$\frac{\partial p(t|\boldsymbol{\theta})}{\partial t_0} = p(t|\boldsymbol{\theta}) \cdot \frac{1}{2}\left(\kappa + \frac{1}{t-t_0} - \frac{\kappa\mu^2}{(t-t_0)^2}\right). \tag{3.10c}$$

We can insert (3.10) into (3.8) to obtain the equations that satisfy the ML solution for the LDRW model as

$$\sum_{n=1}^{N} \left(1 - \frac{\mu}{n\Delta t - t_0}\right) C(n) = 0, \tag{3.11a}$$

$$\sum_{n=1}^{N} \left(\frac{1}{\kappa} - (n\Delta t - t_0) + 2\mu - \frac{\mu^2}{n\Delta t - t_0}\right) C(n) = 0, \tag{3.11b}$$

$$\sum_{n=1}^{N} \left(\kappa + \frac{1}{n\Delta t - t_0} - \frac{\kappa\mu^2}{(n\Delta t - t_0)^2}\right) C(n) = 0. \tag{3.11c}$$

In (3.11a), we have used the fact that κ is strictly positive. From (3.11a) and (3.11b) the ML estimates for μ and κ can be obtained as

$$\hat{\mu}_{\mathsf{ML}} = \frac{\sum_{n=1}^{N} C(n)}{\sum_{n=1}^{N} \frac{C(n)}{n\Delta t - t_0}}, \tag{3.12a}$$

$$\hat{\kappa}_{\mathsf{ML}} = \left[\frac{\sum_{n=1}^{N} (n\Delta t - t_0) C(n)}{\sum_{n=1}^{N} C(n)} - \hat{\mu}_{\mathsf{ML}} \right]^{-1}. \tag{3.12b}$$

We were not able to find an analytical solution for $\hat{t_{0,\,\mathsf{ML}}}$. If this parameter is already known, its value can be inserted into (3.12) to obtain a completely analytical ML solution. If t_0 is unknown, its ML estimate can be obtained by numerically solving (3.11c) after substitution of κ and μ by their ML solutions given in (3.12). As a result, the ML parameter estimation problem is significantly less complex than conventional nonlinear regression methods, because iterative optimization is only required for a single parameter.

Maximum likelihood and recirculation

A common issue in IDC analysis is recirculation, i.e., subsequent passages of the indicator bolus that overlap with the tail of the first-pass IDC. As a result, only a limited part of the tail of the transit-time distribution can be observed, as shown in Fig. 3.2.

Typically, the IDC is truncated by discarding the time segment featuring recirculation from the analysis. Parametric curve-fitting is then applied on the truncated IDC [20]. This approach cannot easily be applied for the proposed ML algorithm, because truncation affects the transit-time distribution that can be observed.

After truncating the IDC at time $t_{\mathsf{Tr}} = n_{\mathsf{Tr}}\Delta t$, the transit-time distribution $p(t|\boldsymbol{\theta})$ is no longer completely sampled: transit-times beyond the truncation time t_{Tr} cannot be observed. Instead of the original distribution, the truncated transit-time distribution is observed. This is given as

$$p_{\mathsf{Tr}}(n\Delta t|\boldsymbol{\theta}, n_{\mathsf{Tr}}) = \begin{cases} \dfrac{p(n\Delta t|\boldsymbol{\theta})}{\sum_{n=1}^{n_{\mathsf{Tr}}} p(n\Delta t|\boldsymbol{\theta})} & n \leq n_{\mathsf{Tr}} \\ 0 & n > n_{\mathsf{Tr}} \end{cases}. \tag{3.13}$$

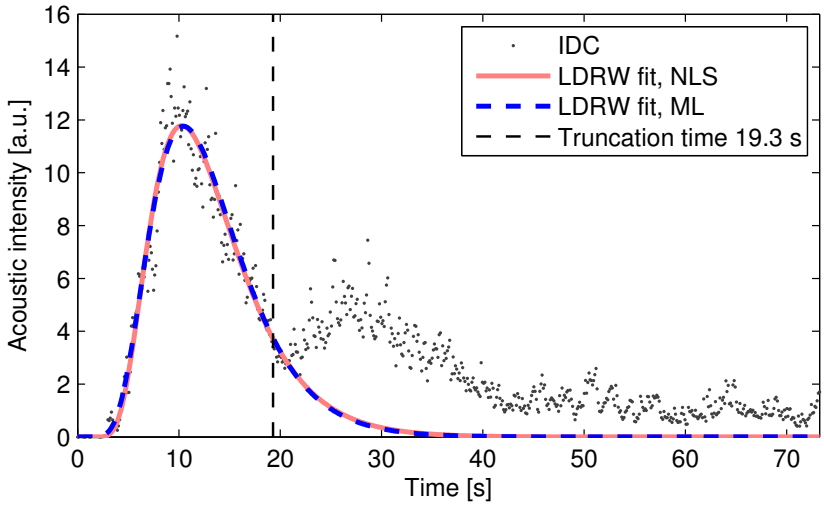

Figure 3.2 *IDC obtained* in vivo *by DCE-US, in which the tail of the transit-time distribution cannot be observed due to indicator recirculation. Also shown are LDRW model fits based on nonlinear least-squares (NLS) regression and maximum likelihood (ML), obtained after truncation of the IDC.*

In (3.13), the scaling term in the denominator ensures that $p_{\text{Tr}}(n\Delta t|\boldsymbol{\theta}, n_{\text{Tr}})$ integrates to 1, in order to properly define it as a probability distribution.
The log-likelihood based on the truncated transit-time distribution can be expressed similarly to (3.7) as

$$\ln\left(\mathcal{L}_{\text{Tr}}(\boldsymbol{\theta})\right) = \sum_{n=1}^{n_{\text{Tr}}} C(n) \ln\left(p(n\Delta t|\boldsymbol{\theta})\right) - \ln\left(\sum_{n=1}^{n_{\text{Tr}}} p(n\Delta t|\boldsymbol{\theta})\right) \sum_{n=1}^{n_{\text{Tr}}} C(n). \tag{3.14}$$

The derivative of (3.14) with respect to $\boldsymbol{\theta}$ is given as

$$\frac{\partial \ln\left(\mathcal{L}_{\text{Tr}}(\boldsymbol{\theta})\right)}{\partial \boldsymbol{\theta}} = \left(\sum_{n=1}^{n_{\text{Tr}}} C(n) \frac{\partial p(n\Delta t|\boldsymbol{\theta})/\partial \boldsymbol{\theta}}{p(n\Delta t|\boldsymbol{\theta})}\right) - \frac{\sum_{n=1}^{n_{\text{Tr}}} \partial p(n\Delta t|\boldsymbol{\theta})/\partial \boldsymbol{\theta}}{\sum_{n=1}^{n_{\text{Tr}}} p(n\Delta t|\boldsymbol{\theta})} \sum_{n=1}^{n_{\text{Tr}}} C(n). \tag{3.15}$$

The previous semi-analytical solutions for the shape parameters, as given in (3.12a) and (3.12b), do not represent the ML solution in the case of truncation. For this reason, iterative optimization is adopted to maximize (3.14). An example IDC model fit obtained by this procedure is shown in Fig. 3.2. Similarly to the original algorithm, the parameter AUC is not included in this analysis, but estimated afterward by linear regression with the fitted IDC.

Implementation

All proposed parameter estimation methods were implemented in MATLAB ® (The MathWorks, Natick, MA), with the routine `mle`. For NLS regression, the routine `lsqcurvefit` was adopted. In both cases, iterative optimization was performed with the built-in trust-region algorithm [27].
In all cases, the parameter t_0 was considered unknown. For all iterative optimization algorithms, parameter initialization was performed as follows. The parameter t_0 was initialized at 2 s before the appearance time, which represents the time at which indicator particles are first observed. The two shape parameters were then initialized using the semi-analytical ML algorithm described in Sec. 3.2.2 and Appendix 3.6. Finally, AUC was initialized by linear regression as the linear scale factor between the obtained IDC and the initialized IDC. To prevent numerical issues, a lower bound of 0.5 was adopted for the term $\sum_{n=1}^{n_{\mathrm{Tr}}} p(n\Delta t|\boldsymbol{\theta})$ in (3.14). This lower bound implies that, after truncation, the remaining time samples cover at least 50% of the complete area under the IDC.

3.2.3 Simulation study

A simulation study was performed to test the proposed ML algorithm. Simulated IDCs were derived as the observed histogram of transit-times, based on random sampling of the transit-time distribution $p(t|\boldsymbol{\theta})$ as described in Sec. 3.2.1. The adopted time step was 0.1 s. An example of a simulated IDC is shown in Fig. 3.1. Simulations were performed with both $K = 2 \times 10^3$ and $K = 5 \times 10^3$, which resulted in an SNR of 9 dB and 13 dB, respectively. These SNR values are in line with those obtained in experimental data.
In this study, simulated IDCs were generated for three models, each using 10 different values for the two IDC shape parameters within the following range:

- LDRW model: $\kappa \in$ [0.1,1], $\mu \in$ [10,40];
- lognormal model: $\mu \in$ [2,3.5], $\sigma \in$ [0.2,1];
- gamma-variate model: $\alpha \in$ [4,12], $\beta \in$ [1,4].

The parameter range was selected to represent IDCs with mean transit times ranging between approximately 10 and 40 seconds. For each parameter combination, 25 simulated IDCs were obtained. In total, 2500 IDCs were simulated for each model.
All simulated IDCs were fitted by the proposed ML algorithm, as well as by NLS regression. The performance of both parameter estimation methods was evaluated by the bias and standard deviation of the estimated parameters, relative to their true values. This choice was motivated by the wide range of adopted parameter values. In addition, we evaluated

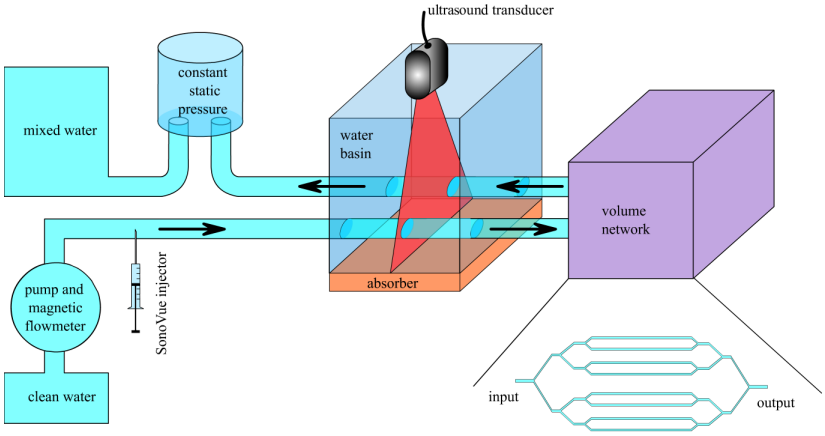

Figure 3.3 *Schematic overview of the* in vitro *set-up.*

the fitting accuracy by the determination coefficient R^2 and the required computation time for all algorithms.

The same IDCs were used to evaluate the parameter estimation performance in case of truncation. The optimal truncation time generally depends on the application. In this study, we adopted a cut-off percentage of 30%, i.e., at t_{Tr}, the model IDC has decayed to 30% of its peak value [23].

In addition, we investigated the variation in the parameter estimates with respect to the cut-off percentage by performing parameter estimation with cut-off percentages ranging between 20 and 40%. The relative standard deviation (expressed as a percentage of the mean) among the parameter estimates obtained with different cut-off percentages was evaluated to measure this variation.

3.2.4 Experimental validation

An experimental validation of the proposed algorithm was performed using DCE-US imaging. An *in vitro* set-up was constructed at the Catharina Hospital (Eindhoven, The Netherlands). The set-up, which is schematically shown in Fig. 3.3, consisted of an open network of tubes, in which flow was generated by a centrifugal pump (Medtronic 550 bio-console, Minneapolis, MN). A 0.2 mL SonoVue ® (Bracco, Milan, Italy) ultrasound-contrast-agent bolus was diluted in 20 mL of saline and subsequently injected into the flow network, which was kept open to avoid recirculation. The hydrostatic pressure was stabilized at the output. Cross-sectional ultrasound B-mode images were obtained directly before and after the tube network with an iE33 ultrasound imaging system (Philips Healthcare, Andover, MA) and a transesophageal X7-2t probe. Harmonic imaging was applied (2.7-5.4 MHz) at a mechanical index of 0.2. From the obtained image sequences, linearized acoustic time-intensity curves were obtained using acoustic quantification software QLAB (Philips Healthcare, Bothell,

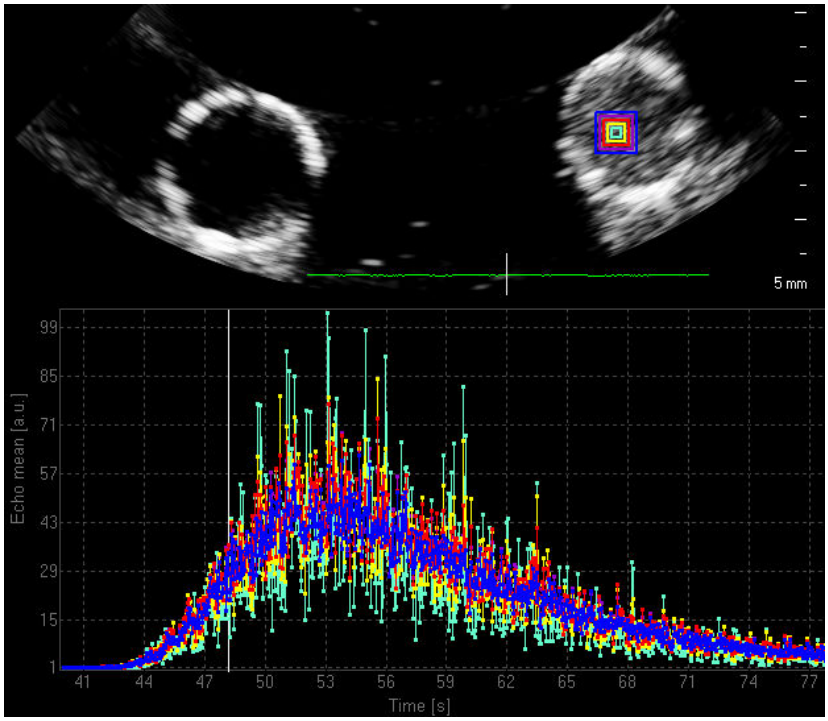

Figure 3.4 *DCE-US image (top) and acoustic time-intensity curve quantification using QLAB (bottom). In the top part, the two tubes for the inflow (left) and outflow (right) of contrast agents are visible. The curves shown in the bottom part are sampled from square ROIs in the top right of the image. The ROI size is indicative of the SNR; the blue IDC, which is least noisy, is sampled from the largest ROI, whereas the noisy teal IDC is sampled from the smallest ROI.*

WA), as shown in Fig. 3.4.

To avoid the influence of the injection function on our analysis, only the outflow curves were considered in this study. Fig. 3.4 also shows five square regions of interest (ROIs) of different sizes (from 1.81 mm^2 to 35.4 mm^2) from which the acoustic time-intensity curves were sampled. The curves in Fig. 3.4 indicate a correlation between the ROI size and the SNR of the curve. The average SNR, obtained based on the fit with the smallest mean squared error, ranged from 7 dB for the smallest ROI to 14 dB for the largest ROI. Because the number of observed indicator particles K is approximately proportional to the ROI size, this observed correlation between ROI size and SNR can be explained by (3.4).

For a direct application of indicator dilution theory on the acoustic time-intensity curves, the relation between contrast-agent concentration and measured acoustic intensity must be linear. For low concentrations and low mechanical index, a linear relation was established by several researchers [20, 25, 28]. As a result, acoustic time-intensity curves may be interpreted directly as IDCs.

Parameter estimation was performed by both ML and NLS using IDCs obtained from 79 experiments, which were performed with four different volumes between 356 and 890 mL

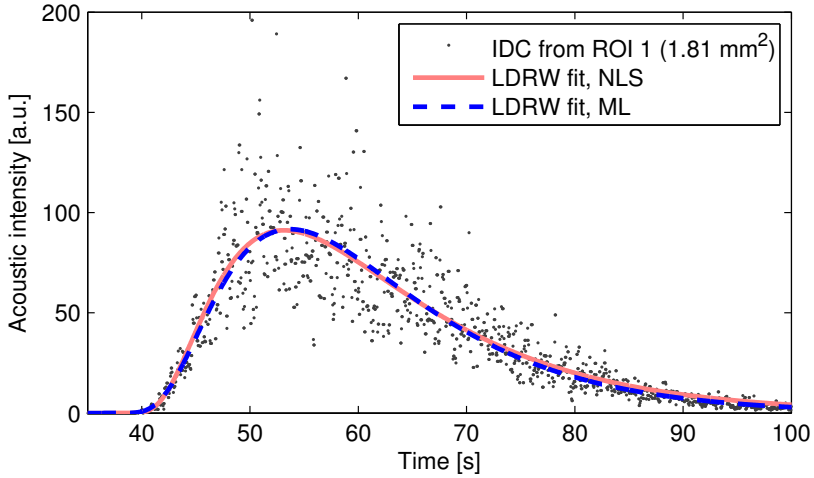

Figure 3.5 *Experimentally obtained IDC as well as LDRW model fits based on nonlinear least-squares (NLS) regression and maximum likelihood (ML).*

and at six different flow values ranging from 1 to 4 L/min. As a result, IDCs were obtained for a wide range of parameter values, as shown in Figures 3.4 and 3.5. In a few curves, the presence of air bubbles resulted in a few noisy samples. To prevent these from affecting the parameter estimation, all IDCs were median filtered with order three prior to curve-fitting. Because the true values of the parameters were not available, an indirect method was adopted to evaluate the parameter estimation performance. Since the IDCs were sampled from concentric ROIs (see Fig. 3.4), we expected the associated true parameter values to be constant across the ROIs. Consequently, we considered the variation among the parameter estimates obtained from different ROIs as an indirect error metric. The determination coefficient R^2 was adopted to evaluate the overall quality of curve-fitting. The analysis was performed using the complete IDC for fitting, and also after discarding the IDC tail ($\leq$ 30% of the peak value). Furthermore, the sensitivity of the estimated parameters with respect to the cut-off percentage was evaluated as described in Sec. 3.2.3.

3.2.5 In vivo evaluation

The feasibility of the proposed algorithm for *in vivo* use was evaluated with IDCs obtained by DCE-US imaging of the human prostate with the purpose of cancer detection. Cancer detection has been investigated using various imaging modalities, such as DCE-US and dynamic contrast-enhanced MRI [5, 10, 11, 29, 30], and is based on detection of microvascular changes related to angiogenesis and, therefore, to cancer growth.

This study was performed at the Academic Medical Center University Hospital (Amsterdam, The Netherlands) after approval was granted by the local ethics committee; written informed consent was obtained from all patients prior to this study. 17 DCE-US datasets

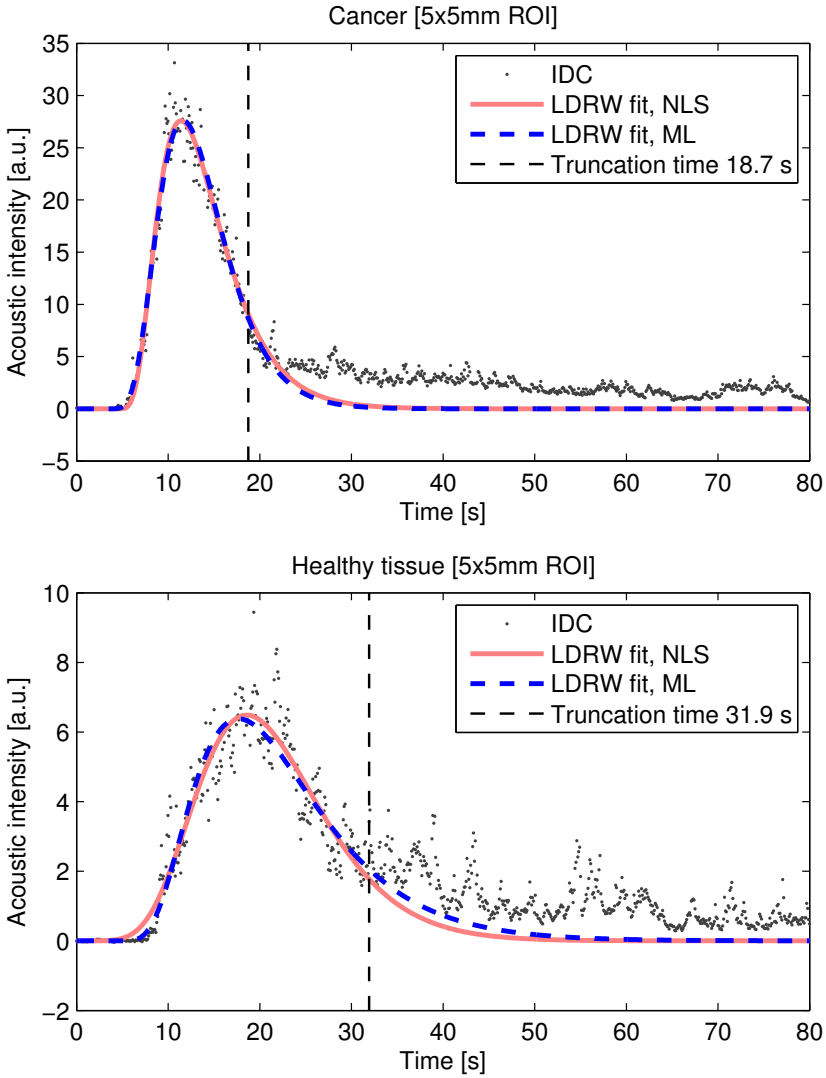

Figure 3.6 *IDCs obtained* in vivo *from cancer (top) and healthy tissue (bottom). LDRW model fits based on nonlinear least-squares (NLS) regression and maximum likelihood (ML) are also shown, as well as the truncation time.*

were obtained from 9 patients who underwent radical prostatectomy.

Data acquisition was performed using an iU22 ultrasound imaging system (Philips Healthcare, Bothell, WA) and either a C8-4v or C10-3v transrectal probe. The adopted imaging mode was power modulation, at a frequency of 3.5 MHz and a mechanical index of 0.06. In each DCE-US dataset, two IDCs were obtained by QLAB from square ROIs (5x5 mm). The ROIs were selected based on the histology ground truth to represent healthy tissue and cancer.

All obtained IDCs were fitted by the LDRW model, using both ML and NLS, as shown in Fig. 3.6. Because the optimal truncation time is generally difficult to define in these data, all IDCs were fitted using three truncation times, with recirculation cut-off percentages of

30, 40, and 50%, respectively. The optimal truncation time was selected based on the minimum mean squared error, averaged between ML and NLS, of the IDC fit. The determination coefficient R^2 was adopted to measure the quality of the obtained IDC fits.
A number of features were extracted from the fitted IDCs in order to evaluate their potential to discriminate between healthy tissue and cancer. We adopted several features that were proposed in the literature [25, 26, 31], namely, the LDRW parameter κ, the parameter AUC, the peak intensity (PI), the full-width at half maximum (FWHM, the period during which the IDC exceeds PI/2), the mean transit time (MTT $= \mu$), and the wash-in time (WIT, the time it takes for the IDC to rise from 5% to 95% of PI).
The tissue classification performance was assessed for each individual parameter using a binary decision threshold. This threshold was shifted over the observed range of parameter values in healthy tissue and cancer. At each threshold level, the sensitivity and specificity for tissue classification were evaluated to derive the receiver-operating-characteristic (ROC) curve. The area under the ROC curve was adopted to measure the tissue classification performance [32]. The optimal sensitivity and specificity were determined as the point on the ROC curve closest to ideal classification. A comparison was performed between the parameter estimates obtained by NLS and those obtained by ML.

3.3 Results

3.3.1 Simulation study

An example of curve-fitting using both NLS and ML is shown in Fig. 3.1. No significant difference in curve-fitting accuracy was observed between NLS and ML. For $K = 2 \times 10^3$, both algorithms fitted the complete IDC with $R^2 = 0.87$ and the truncated IDC (cut-off percentage 30%) with $R^2 = 0.80$. For $K = 5 \times 10^3$, these statistics were 0.94 and 0.90, respectively.
The average computation time required to fit one IDC was evaluated on a Windows-based workstation with an Intel Core2Duo processor running at 3.16 GHz with 3.49 GB of RAM. The required computation time for NLS was 0.035 s. For the ML algorithm, the average computation time was 0.032 s for estimation based on the complete IDC, as described in Sec. 3.2.2 and the Appendix (Sec. 3.6), and 0.055 s for estimation based on the truncated IDC, as described in Sec. 3.2.2.
For each parameter, the estimation accuracy was evaluated by the relative bias and standard deviation with respect to the true values. Table 3.1 reports the results for a complete as well as for a truncated IDC fitting. In general, the ML algorithm provided higher estimation accuracy than NLS.

Table 3.1 *Accuracy (relative bias ± standard deviation [%]) of parameter estimation based on 2,500 simulated IDCs per model.*

Model & parameter		Estimation based on complete IDC				Estimation based on truncated IDC (cut-off percentage 30%)			
		$K = 2 \times 10^3$		$K = 5 \times 10^3$		$K = 2 \times 10^3$		$K = 5 \times 10^3$	
		NLS	ML	NLS	ML	NLS	ML	NLS	ML
LDRW	μ	1.2 ± 13.5	0.0 ± 7.5	0.9 ± 8.5	0.1 ± 4.5	2.7 ± 18.8	0.6 ± 10.6	1.8 ± 12.4	0.2 ± 7.0
	κ	1.5 ± 14.3	0.1 ± 7.7	1.0 ± 9.1	0.2 ± 4.6	3.7 ± 25.8	1.0 ± 17.1	2.4 ± 16.9	0.4 ± 11.4
Lognormal	μ	0.2 ± 2.5	0.0 ± 1.5	0.1 ± 1.6	0.0 ± 1.0	0.5 ± 3.7	0.2 ± 2.6	0.2 ± 2.4	0.0 ± 1.6
	σ	-0.1 ± 7.7	-0.1 ± 4.0	0.0 ± 5.0	0.0 ± 2.5	0.5 ± 13.9	1.5 ± 10.2	0.1 ± 9.2	0.6 ± 6.3
Gamma-variate	α	5.7 ± 28.8	0.6 ± 13.1	2.0 ± 16.5	0.2 ± 7.8	12.7 ± 46.7	0.8 ± 21.4	4.8 ± 25.9	0.2 ± 12.9
	β	0.0 ± 13.9	0.5 ± 7.4	0.1 ± 8.9	0.2 ± 4.5	0.4 ± 21.3	2.3 ± 14.5	0.3 ± 14.2	0.9 ± 9.0

Table 3.2 *Relative standard deviation [%] among parameter estimates obtained with different recirculation cut-off percentages (20, 25, 30, 35, 40%) in 2,500 simulated IDCs per model.*

Model & parameter		$K = 2 \times 10^3$		$K = 5 \times 10^3$	
		NLS	ML	NLS	ML
LDRW	μ	4.7	2.7	3.1	1.7
	κ	8.2	6.7	5.3	4.3
Lognormal	μ	1.1	0.9	0.7	0.5
	σ	4.6	3.8	3.0	2.3
Gamma-variate	α	12.5	6.5	7.0	3.8
	β	6.5	5.1	4.2	3.1

The sensitivity of the parameter estimation with respect to the recirculation cut-off percentage is reported in Table 3.2. For all parameters, ML provided more consistent results than NLS.

3.3.2 Experimental validation

Experimental IDCs were obtained from 5 ROIs in 79 available recordings. Due to the presence of artifacts in some recordings, we considered only those recordings that could be fitted with an average determination coefficient $R^2 \geq 0.9$ (averaged across all ROIs, both algorithms, and all models). Based on this criterium, the parameter estimation precision by NLS and ML was compared using 71 recordings.

Fitting of the IDCs obtained from these recordings provided an average R^2 (across all models) of 0.94 for ML, compared to 0.95 for NLS. If the IDC was truncated at a recirculation

Table 3.3 *Relative standard deviation [%] among parameter estimates obtained from various ROIs representing the same underlying kinetic parameters in experimentally measured IDCs from 71 recordings.*

Model & parameter		Estimation based on complete IDC		Estimation based on truncated IDC (cut-off percentage 30%)	
		NLS	ML	NLS	ML
LDRW	μ	9.0	3.7	7.8	2.9
	κ	9.9	5.0	12.2	6.0
Lognormal	μ	3.7	1.6	3.4	1.3
	σ	8.7	3.7	9.3	4.2
Gamma-variate	α	14.9	6.1	11.0	4.8
	β	7.9	4.0	7.1	3.9

Table 3.4 *Relative standard deviation [%] among parameter estimates obtained with different recirculation cut-off percentages (20, 25, 30, 35, 40%) in experimentally obtained IDCs from 71 recordings.*

Model & parameter		ROI 1 (1.8 mm^2)		ROI 5 (35.4 mm^2)	
		NLS	ML	NLS	ML
LDRW	μ	7.3	2.7	6.8	2.8
	κ	16.4	13.4	15.3	12.6
Lognormal	μ	3.1	1.2	3.0	1.1
	σ	12.7	8.0	12.0	7.6
Gamma-variate	α	10.4	4.9	9.3	5.5
	β	8.4	5.4	7.7	5.6

cut-off percentage of 30%, the average R^2 was 0.92 for both algorithms.

The precision of the estimated parameters, assessed as the relative standard deviation among the parameter values estimated in different ROIs, is reported for all models in Table 3.3, both for fitting the complete IDC and for truncation of the IDC at a recirculation cut-off percentage of 30%. Similarly to the simulation results, ML showed a smaller variation in the parameter estimates than NLS for all parameters.

The sensitivity of parameter estimation to the recirculation cut-off percentage is reported for two ROIs in Table 3.4. For all models, the ML algorithm provided a smaller variation than NLS.

Table 3.5 *Sensitivity, specificity, and receiver-operating-characteristic (ROC) curve area for tissue classification*

Parameter	NLS			ML		
	Sensitivity [%]	Specificity [%]	ROC curve area	Sensitivity [%]	Specificity [%]	ROC curve area
κ	76.5	52.9	0.62	76.5	82.4	0.75
AUC	58.8	82.4	0.69	58.8	82.4	0.70
PI	70.6	70.6	0.73	70.6	70.6	0.73
FWHM	82.4	70.6	0.75	82.4	76.5	0.79
MTT	64.7	64.7	0.64	64.7	64.7	0.62
WIT	52.9	76.5	0.67	52.9	82.4	0.70

3.3.3 In vivo evaluation

The IDCs obtained *in vivo* were estimated with an average determination coefficient $R^2 = 0.92$ for both algorithms. For several IDC parameters, the classification performance obtained by ML and NLS is reported in Table 3.5.

The largest difference in classification performance between ML and NLS was found for κ: the area under the ROC curve obtained by ML was 0.13 larger than that obtained by NLS. For this parameter, the estimates obtained by the two algorithms were compared in a Bland-Altman plot [33], which is shown in Fig. 3.7. The average difference between κ estimates obtained in cancer and healthy tissue increased by 0.06 if ML was adopted instead of NLS. The parameters AUC and PI showed a very similar classification performance for NLS and ML.

3.4 Discussion

In all studies, the proposed algorithm provided accurately fitted IDCs. In fact, the obtained determination coefficient R^2, which is theoretically optimized by NLS, was approximately equal for ML and NLS in all studies.

The accuracy of the estimated parameters is, however, more important than the fitting accuracy. To this end, we assessed the bias and standard deviation. Relative statistics were adopted to accommodate for the wide range of parameter values.

The simulation results, reported in Table 3.1, indicate superior results for ML than for NLS for all three adopted models, both with and without truncation. No bias in the parameter estimation was found for either method. The required computation times were similar. Only for fitting of truncated IDCs, the ML algorithm required more computation time than NLS, perhaps because NLS was implemented using a dedicated NLS optimization routine.

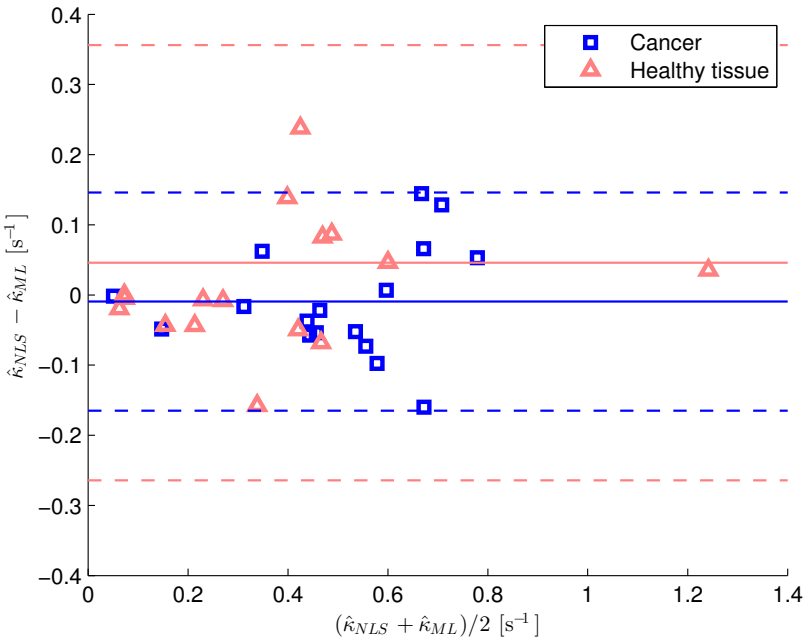

Figure 3.7 *Bland-Altman plot of the LDRW parameter κ, estimated by both NLS and ML. The solid lines represents the average difference, the dashed lines represent 95% limits of agreement.*

In the experimental data, assessment of the parameter estimation accuracy is more complicated, because the true parameter values are unknown. By assuming IDCs sampled from different ROIs (as shown in Fig. 3.4) to satisfy the same true parameter values, we assessed the precision among parameter estimates obtained from IDCs sampled from different ROIs. Table 3.3 shows the parameter estimates obtained by ML to be more consistent across the different ROIs than those obtained by NLS. This result was found for all three adopted models, both with and without IDC truncation.

In applications where indicator recirculation is significant, the definition of the optimal IDC truncation time, minimizing the effect of recirculation on the analysis, is complicated. For this reason, the sensitivity of parameter estimation to the time at which the IDC is truncated was also evaluated. As shown in Table 3.2, the simulation study showed that the ML algorithm is less dependent on the truncation time than NLS. This finding was also confirmed with our experimental data (see Table 3.4). As a result, ML is more robust with respect to the truncation time choice than NLS.

The *in vivo* evaluation shows the feasibility of the ML algorithm for use in quantitative DCE-US imaging for cancer detection. In fact, for several parameters, the classification ability based on ML is improved with respect to that based on NLS. The classification results of NLS and ML for the IDC amplitude parameters AUC and PI are very similar, probably because the parameter AUC is not included in ML estimation. Because this pa-

rameter is estimated afterward by linear regression, the optimization criterium is the same for both algorithms.

For the proposed ML algorithm, IDCs are interpreted as the observed histogram of the transit-time distribution. Although this paper focuses on the first pass of an intravascular indicator, the methodology is applicable for any transit-time distribution. The proposed approach explicitly requires transit-times of indicator particles to be independent. In fact, this assumption follows from the classical assumption in indicator dilution theory that the indicator is well-mixed with the carrier fluid [34]. Therefore, the independency assumption is merely made explicit by the proposed algorithm.

In general, the log-likelihood function to be maximized, given by (3.7), equals the correlation between the IDC and the logarithm of the model distribution. With the semi-analytical ML solutions, presented for three common indicator dilution models, iterative optimization is not required if the injection time parameter t_0 is known. This may be useful in system identification methods based on two IDCs representing the input and output of the system, where $t_0 = 0$ [13]. In this paper, as often in practice, t_0 was considered unknown. In this case, ML estimation requires iterative optimization for only a single parameter, t_0. The model-specific solutions are valid only if the complete IDC is available for parameter estimation.

Indicator recirculation, a common problem in IDC analysis, is approached by truncation of the transit-time distribution. The modified log-likelihood function, given by (3.14), contains an additional term that represents the fraction of the area under the IDC that is still observed after truncation.

In the transit-time statistics described in Sec. 3.2.1, the difference between the observed IDC and its corresponding model curve results from the limited amount of indicator particles K, which represents the sample size of the observed transit-time distribution. As shown in (3.4), the SNR scales linearly with K. It is particularly low in situations where K is relatively small, e.g., when only a small ROI can be selected to obtain the IDC. This can be observed in Fig. 3.4.

In a previous study based on DCE-US, it was observed that the IDC noise intensity is correlated with the IDC itself [20]. This correlation can also be observed for the experimental IDCs in Figures 3.4 and 3.5. This phenomenon cannot be explained by standard additive Gaussian noise statistics. It is, however, explained by the modeled transit-time statistics; as formulated in (3.3), the IDC noise intensity is linearly related to the IDC itself. Because the proposed ML algorithm is based on these statistics, it is better suited to deal with this phenomenon than standard NLS regression algorithms.

Because measurement inaccuracies are not primarily considered in this paper, the proposed algorithm is generally applicable in a variety of applications. However, if measurement inac-

curacies represent the dominant source of errors, the proposed algorithm may not provide optimal results. In this situation, ML estimation should be based on the measurement statistics rather than the transit-time statistics. For example, if the measurement errors are well represented by additive white noise, NLS will provide the most accurate results. For specific acquisition modalities, such as ultrasound and MRI, the statistics of acquisition noise are well documented [21, 22]. In general, the optimal algorithm choice should be based on the measured IDC noise statistics.
In the future, an application-specific parameter estimation method could be developed that optimally deals with both acquisition noise and transit-time statistics. Alternatively, parameter estimation can be optimized with respect to the primary sources of variability.

3.5 Conclusion

A maximum-likelihood algorithm is presented for estimation of hemodynamic parameters from indicator dilution curves. This algorithm is based on the transit-time statistics of indicator particles. Semi-analytical solutions are provided for three commonly adopted IDC models and the algorithm is extended to deal with the typical problem of indicator recirculation. A performance evaluation in simulations as well as in experimental data obtained by DCE-US shows superior results of the proposed algorithm over nonlinear least-squares regression. In addition, the feasibility of the algorithm is shown with *in vivo* data.

3.6 Appendix: Maximum-likelihood algorithm for log-normal and gamma-variate models

This appendix reports the ML algorithm for the lognormal and gamma-variate models. Only the main results are provided; the methodology is identical to that described in Sec. 3.2.2. Similar to the obtained results for the LDRW model, the solutions provided here are the ML solutions only if the complete IDC is available.

3.6.1 Lognormal model

The lognormal model describes the distribution of indicator transit-times as function of the parameters $\boldsymbol{\theta} = [\mu, \sigma, t_0]$ as

$$p(t|\boldsymbol{\theta}) = \frac{1}{\sqrt{2\pi}\sigma(t-t_0)} \exp\left(\frac{(\ln(t-t_0)-\mu)^2}{2\sigma^2}\right). \tag{3.16}$$

The derivative of $p(t|\boldsymbol{\theta})$ with respect to $\boldsymbol{\theta}$ is given as

$$\frac{\partial p(t|\boldsymbol{\theta})}{\partial \mu} = p(t|\boldsymbol{\theta}) \cdot \frac{\ln(t-t_0)-\mu}{\sigma^2}, \tag{3.17a}$$

$$\frac{\partial p(t|\boldsymbol{\theta})}{\partial \sigma} = p(t|\boldsymbol{\theta}) \cdot \frac{\mu^2-\sigma^2-2\mu\ln(t-t_0)+(\ln(t-t_0))^2}{\sigma^3}, \tag{3.17b}$$

$$\frac{\partial p(t|\boldsymbol{\theta})}{\partial t_0} = p(t|\boldsymbol{\theta}) \cdot \frac{\ln(t-t_0)-\mu+\sigma^2}{\sigma^2(t-t_0)}. \tag{3.17c}$$

Similarly to (3.12a) and (3.12b), the ML solution for the shape parameters μ and σ can be written as function of the sampled IDC $C(n)$ and t_0 as

$$\hat{\mu}_{\mathsf{ML}} = \frac{\sum_{n=1}^{N} \ln(n\Delta t - t_0) C(n)}{\sum_{n=1}^{N} C(n)}, \tag{3.18a}$$

$$\hat{\sigma}_{\mathsf{ML}} = \left(\frac{\sum_{n=1}^{N} (\ln(n\Delta t - t_0))^2 C(n)}{\sum_{n=1}^{N} C(n)} - \hat{\mu}_{\mathsf{ML}}^2 \right)^{\frac{1}{2}}. \tag{3.18b}$$

3.6.2 Gamma-variate model

The indicator transit-time distribution can also be described as a gamma-variate with parameters $\boldsymbol{\theta} = [\alpha, \beta, t_0]$ as

$$p(t|\boldsymbol{\theta}) = \frac{1}{\beta^\alpha \Gamma(\alpha)} (t-t_0)^{\alpha-1} \exp\left(-\frac{t-t_0}{\beta}\right). \tag{3.19}$$

The derivative of (3.19) with respect to $\boldsymbol{\theta}$ is

$$\frac{\partial p(t|\boldsymbol{\theta})}{\partial \alpha} = p(t|\boldsymbol{\theta}) \cdot \left(\ln(t-t_0) - \ln(\beta) - \psi(\alpha)\right), \tag{3.20a}$$

$$\frac{\partial p(t|\boldsymbol{\theta})}{\partial \beta} = p(t|\boldsymbol{\theta}) \cdot \frac{t-t_0-\alpha\beta}{\beta^2}, \tag{3.20b}$$

$$\frac{\partial p(t|\boldsymbol{\theta})}{\partial t_0} = p(t|\boldsymbol{\theta}) \cdot \left(\frac{1-\alpha}{t-t_0} + \frac{1}{\beta}\right). \tag{3.20c}$$

In (3.20a), $\psi(\alpha) = d(\ln\Gamma(\alpha))/d\alpha$ is the polygamma function of order 1. Similarly to the lognormal and LDRW models, the ML solution for the shape parameters α and β can be

derived from (3.20b) and (3.20c) in semi-analytical fashion as

$$\hat{\beta}_{\mathsf{ML}} = \frac{\sum_{n=1}^{N}(n\Delta t - t_0)C(n)}{\sum_{n=1}^{N}C(n)} - \frac{\sum_{n=1}^{N}C(n)}{\sum_{n=1}^{N}\frac{C(n)}{n\Delta t - t_0}}, \tag{3.21a}$$

$$\hat{\alpha}_{\mathsf{ML}} = \frac{\sum_{n=1}^{N}(n\Delta t - t_0)C(n)}{\hat{\beta}_{\mathsf{ML}}\sum_{n=1}^{N}C(n)}. \tag{3.21b}$$

References

[1] K. Zierler, "Indicator dilution methods for measuring blood flow, volume and other properties of biological systems: a brief history and memoir," *Ann. Biomed. Eng.*, vol. 28, pp. 836–848, 2000.

[2] G. Fegler, "Measurement of cardiac output in ansthetized animals by a thermo-dilution method," *Exp. Physiol.*, vol. 39, no. 3, pp. 153–164, 1954.

[3] W. F. Hamilton, J. W. Moore, J. M. Kinsman, and R. G. Spurling, "Simultaneous determination of the pulmonary and systemic circulation times in man and of a figure related to cardiac output," *Am. J. Physiol.*, vol. 84, pp. 338–344, 1928.

[4] S. B. Feinstein, B. Coll, D. Staub *et al.*, "Contrast enhanced ultrasound imaging," *J. Nucl. Cardiol.*, vol. 17, no. 1, pp. 106–115, 2010.

[5] P. S. Tofts, "Modeling tracer kinetics in dynamic Gd-DTPA MR imaging," *J. Magn. Reson. Imaging*, vol. 7, no. 1, pp. 91–101, 1997.

[6] H. O. Anger, "Scintillation camera with multichannel collimators," *J. Nucl. Med.*, vol. 5, no. 7, pp. 515–531, 1964.

[7] K. Miles, M. Hayball, A. Dixon *et al.*, "Colour perfusion imaging: a new application of computed tomography," *Lancet*, vol. 337, no. 8742, pp. 643–645, 1991.

[8] E. Donnemiller, J. Heilmann, G. K. Wenning *et al.*, "Brain perfusion scintigraphy with 99mTc-HMPAO or 99mTc-ECD and 123I-beta-CIT single-photon emission tomography in dementia of the Alzheimer-type and diffuse Lewy body disease," *Eur. J. Nucl. Med.*, vol. 24, no. 3, pp. 320–325, 1997.

[9] K. Wei, A. R. Jayaweera, S. Firoozan *et al.*, "Quantification of myocardial blood flow with ultrasound-induced destruction of microbubbles administered as a constant venous infusion," *Circulation*, vol. 97, pp. 473–483, 1998.

[10] N. Lassau, L. Chami, B. Benatsou, P. Peronneau, and A. Roche, "Dynamic contrast-enhanced ultrasonography (DCE-US) with quantification of tumor perfusion: a new diagnostic tool to evaluate the early effects of antiangiogenic treatment," *Eur. Radiol.*, vol. 17, no. Suppl. 6, pp. F89–F98, 2007.

[11] G. Russo, M. Mischi, W. Scheepens, J. de la Rosette, and H. Wijkstra, "Angiogenesis in prostate cancer: onset, progression and imaging," *BJU Int.*, vol. 110, pp. E794–E808, 2012.

[12] C. W. Sheppard, *Basic principles of the tracer method*. New York: John Wiley and Sons, 1962.

[13] M. Mischi, A. A. C. M. Kalker, and H. H. M. Korsten, "Contrast echocardiography for pulmonary blood volume quantification," *IEEE Trans. Ultrason., Ferroelectr., Freq. Control*, vol. 51, no. 9, pp. 1137–1147, 2004.

[14] R. W. Stow and P. S. Hetzel, "An empirical formula for indicator-dilution curves as obtained in human beings," *J. Appl. Physiol.*, vol. 7, pp. 161–167, 1954.

[15] H. Qian and J. B. Basingthwaighte, "A class of flow bifurcation models with lognormal distribution and fractal dispersion," *J. Theor. Biol.*, vol. 205, pp. 161–168, 2000.

[16] M. Mischi, H. C. M. van den Bosch, J. A. den Boer *et al.*, "Intra-thoracic blood volume measurement by contrast magnetic resonance imaging," *Magn. Reson. Med.*, vol. 61, pp. 344–353, Jan. 2009.

[17] H. K. Thompson, C. F. Starmer, R. E. Whalen, and H. D. McIntosh, "Indicator transit time considered as a gamma variate," *Circ. Res.*, vol. 14, pp. 502–515, 1964.

[18] M. Mischi, J. A. den Boer, and H. H. M. Korsten, "On the physical and stochastic representation of an indicator dilution curve as a gamma variate," *Physiol. Meas.*, vol. 29, pp. 281–294, 2008.

[19] D. W. Marquardt, "An algorithm for least-squares estimation of nonlinear parameters," *J. Soc. Ind. Appl. Math.*, vol. 11, no. 2, p. 431, 1963.

[20] M. Mischi, A. A. C. M. Kalker, and H. H. M. Korsten, "Videodensitometric methods for cardiac output measurements," *EURASIP J. Appl. Sign. Proc.*, vol. 5, pp. 479–489, 2003.

[21] R. F. Wagner, S. W. Smith, J. M. Sandrik, and H. Lopez, "Statistics of speckle in ultrasound B-scans," *IEEE Trans. Sonics Ultrason.*, vol. 30, no. 3, pp. 156–163, 1983.

[22] J. Sijbers, A. den Dekker, P. Scheunders, and D. Van Dyck, "Maximum-likelihood estimation of Rician distribution parameters," *IEEE Trans. Med. Imag.*, vol. 17, no. 3, pp. 357–361, 1998.

[23] M. Mischi, "Contrast echocardiography for cardiac quantifications," Ph.D. dissertation, Eindhoven University of Technology, 2004, available at http://www.sps.ele.tue.nl/members/M.Mischi/.

[24] K. H. Norwich and S. Zelin, "The dispersion of indicator in the cardio-pulmonary system," *Bull. Math. Biophys*, vol. 32, pp. 25–43, 1970.

[25] M. P. J. Kuenen, M. Mischi, and H. Wijkstra, "Contrast-ultrasound diffusion imaging for localization of prostate cancer," *IEEE Trans. Med. Imag.*, vol. 30, no. 8, pp. 1493–1502, 2011.

[26] C. Strouthos, M. Lampaskis, V. Sboros, A. McNeilly, and M. Averkiou, "Indicator dilution models for the quantification of microvascular blood flow with bolus administration of ultrasound contrast agents," *IEEE Trans. Ultrason., Ferroelectr., Freq. Control*, vol. 57, no. 6, pp. 1296–1310, 2010.

[27] R. H. Byrd, J. C. Gilbert, and J. Nocedal, "A trust region method based on interior point techniques for nonlinear programming," *Mathematical Programming*, vol. 89, no. 1, pp. 149–185, 2000.

[28] M. Lampaskis and M. Averkiou, "Investigation of the relationship of nonlinear backscattered ultrasound intensity with microbubble concentration at low MI," *Ultrasound Med. Biol.*, vol. 36, no. 2, pp. 306–312, 2010.

[29] M. Smeenge, J. J. M. C. H. de la Rosette, and H. Wijkstra, "Current status of transrectal ultrasound techniques in prostate cancer," *Curr. Opin. Urol.*, vol. 22, pp. 297–302, 2012.

[30] M. P. J. Kuenen, T. A. Saidov, H. Wijkstra, and M. Mischi, "Contrast-ultrasound dispersion imaging for prostate cancer localization by improved spatiotemporal similarity analysis," *Ultrasound Med. Biol.*, vol. 39, no. 9, pp. 1631–1641, 2013.

[31] N. Elie, A. Kaliski, P. Péronneau *et al.*, "Methodology for quantifying interactions between perfusion evaluated by DCE-US and hypoxia throughout tumor growth," *Ultrasound Med. Biol.*, vol. 33, no. 4, pp. 549–560, 2007.

[32] M. H. Zweig and G. Campbell, "Receiver-operating characteristic (ROC) plots: a fundamental evaluation tool in clinical medicine," *Clin. Chem.*, vol. 39, pp. 561–577, 1993.

[33] J. M. Bland and D. G. Altman, "Statistical methods for assessing agreement between two methods of clinical measurement," *Lancet*, vol. 327, no. 8476, pp. 307–310, 1986.

[34] K. L. Zierler, "Theoretical basis of indicator-dilution methods for measuring flow and volume," *Circ. Res.*, vol. 10, pp. 393–407, 1962.

CHAPTER 4

Dispersion assessment by spatiotemporal coherence analysis

Based on: M. Mischi, M. P. J. Kuenen, and H. Wijkstra, "Angiogenesis imaging by spatiotemporal analysis of ultrasound-contrast-agent dispersion kinetics," *IEEE Transactions on Ultrasonics, Ferroelectrics, and Frequency Control*, vol. 59, no. 4, pp. 621–629, © IEEE, 2012.

Abstract – *The key role of angiogenesis in cancer growth has motivated extensive research aiming at noninvasive cancer detection by blood perfusion imaging. However, the results are still limited and the diagnosis of major forms of cancer, such as prostate cancer, are currently based on systematic biopsies. The difficulty in the detection of angiogenesis partly resides in a complex relationship between angiogenesis and perfusion. This may be overcome by analysis of the dispersion kinetics of ultrasound contrast agents. Being determined by multi-path trajectories through the microvasculature, dispersion permits a better characterization of the microvascular architecture and, therefore, more accurate detection of angiogenesis. In this paper, a novel dispersion analysis method is proposed for prostate cancer localization. An ultrasound-contrast-agent bolus is injected intravenously. Spatiotemporal analysis of the concentration evolution measured at different pixels in the prostate is used to assess the local dispersion kinetics of the injected agent. In particular, based on simulations of the convective diffusion equation, the similarity between the concentration evolutions at neighbor pixels is the adopted dispersion measure. Six measurements in patients, compared with the histology, provided a receiver-operating-characteristic curve integral equal to 0.87. This result was superior to that obtained by the previous approaches reported in the literature.*

4.1 Introduction

Angiogenesis plays a fundamental role in the development of several pathologies. It consists of the formation of a dense network of microvessels, which can support the growth of neoplastic tissue. Therefore, the function of angiogenesis in cancer growth is particularly relevant [1, 2]. The assessment of the relationship between cancer growth and angiogenesis has opened new frontiers towards the definition of reliable markers for cancer aggressiveness, i.e., the risk of progression through metastases [3]. The formation of neovascular networks seems in fact an important indicator of cancer aggressiveness [3, 4], and characterization of these networks by the assessment of the microvascular density (MVD) has been reported by several authors to be highly correlated with cancer prognosis [5, 6].

Angiogenesis is a complex physiological process that can be observed at multiple levels. At the cellular level it is characterized by those expressions, such as the vascular endothelial growth factor, whose triggering action is not yet completely understood [3]. At the tissue level, angiogenesis is the formation of a dense network of microvessels, characterized by small diameters and high tortuosity and permeability (leaky walls) [5]. At the organ level, variations in organ size and shape can be observed as the result of neoplasia (abnormal growth of tissue). In addition, variations in perfusion dynamics and tissue stiffness can be observed as the result of angiogenesis and other mutations occurring at the cellular level [7, 8].

In the effort to develop an imaging technique that could detect angiogenesis and, therefore, aggressive cancer, several methods have been proposed that aim at the assessment of tissue perfusion. These methods comprise mainly the use of dynamic contrast-enhanced magnetic resonance imaging (DCE-MRI), Doppler ultrasonography, and dynamic contrast-enhanced ultrasonography (DCE-US) imaging [9–12]. Compared to MRI, the use of ultrasonography is more practical, being particularly suitable for biopsy guidance and intraoperative use.

DCE-US is especially interesting due to the nature of the adopted contrast agents and the nature of the detection process. Ultrasound contrast agents (UCAs) are micro-sized bubbles (microbubbles) of gas encapsulated in a biocompatible shell [13]. Due to their size, comparable with red blood cells, they can flow in the microvasculature while staying in the vascular pool. As a result, different from most MRI contrast agents, UCAs do not extravasate in the interstitial space and are therefore more suitable for hemodynamic quantification. The size of UCA microbubbles is much smaller than the resolution of an ultrasound scanner, which, depending on the adopted ultrasound frequency, is usually of the order of a millimeter. DCE-US imaging is in fact based on a backscatter process [14], which permits registering signals coming from scales (micron) that are smaller than the imaging scale (millimeter). This is a key feature in order to perform ultrasound characterization of the microvasculature.

Several methods have been proposed for imaging angiogenesis by DCE-US. A number of methods are based on the destruction-replenishment technique during UCA infusion, first introduced in cardiology by Wei *et al.* [15]. Although the original technique provides a measure of perfusion by using a single compartment model, alternative models have been proposed later to account for the measurement effects introduced by the ultrasound beam profile [16] and for interpreting the replenishment curve as due to a network of bifurcating vessels rather than a single compartment [17]. Assuming a Normal distribution of flow through the vessels, the UCA transit times through the vascular network was therefore represented by a lognormal probability density function, providing a measure of relative dispersion of flow through the vascular network [18]. Although more realistic than a single compartment model, a bifurcation tree does not represent the fundamental features of cancer angiogenesis, which is characterized by a chaotic vascular architecture comprising arteriovenous shunts and a higher degree of vascular tortuosity [11, 12, 19, 20]. Moreover, the model parameters depend on the history of bifurcations, lacking the ability to provide local assessments.

A number of methods for the measurement of perfusion have also been introduced that are based on the estimation of specific features of indicator dilution curves measured after an intravenous peripheral UCA bolus injection [19, 21]. Once again, all the proposed methods invariably estimate blood perfusion as an indicator for the presence of angiogenesis. However, several opposing factors influence perfusion in cancerous tissue. Low flow resistance results from a lack of vasomotor control and an increase in arteriovenous shunts, but this can be counterbalanced by an interstitial pressure increase due to extravascular leakage and by the small diameter and high degree of tortuosity of neovessels [11, 12, 19, 20]. As a result, in many applications, perfusion measurements have not led to reliable diagnostic results. In addition, the obtained measurements are always influenced by the bolus history between the UCA injection and detection sites, and a local quantification cannot be provided.

This paper focuses on a very relevant and diagnostically challenging form of cancer: prostate cancer. In the United States, prostate cancer currently accounts for 28% and 11% of all cancer diagnoses and deaths in men, respectively [22]. Similar to other forms of cancer, angiogenesis is an important indicator of prostate cancer aggressiveness [3–6]. However, current prostate cancer diagnosis still requires one or more sessions of systematic (i.e., geometrically distributed) biopsies [23, 24], and no imaging method has so far proven to be sufficiently reliable to replace this invasive procedure.

We have recently proposed a new method for the local detection of angiogenic microvasculature changes by modeling the intravascular dispersion kinetics of UCAs as a convective dispersion process [25, 26]. Modeling of UCA dispersion kinetics permits inferring the "invis-

ible" microvascular architecture for the achievement of accurate diagnostic results. Similar to previous approaches, this method is based on the analysis of acoustic time-intensity curves (TICs) in the time domain. In fact, for the low concentrations of UCA that are obtained in the prostate, the backscattered acoustic intensity is linearly correlated with the UCA concentration, and it is adopted as an indirect, linear measure of it [26, 27]. Achieving local measurements that are independent of the bolus dilution history requires making assumptions on the dilution kinetics in the spatial domain; in particular, we assumed the distribution of the UCA bolus in space to be well represented by a Gaussian probability density function.

Different from previous approaches, in this paper we present a method for the local assessment of UCA dispersion that is based on spatiotemporal analysis. Including spatial information in the analysis facilitates the estimation of local parameters representing the UCA dispersion kinetics. The assumptions on the UCA spatial distribution that are required for local measurements by the sole analysis in time domain can in fact be removed.

Simulations of the convective diffusion equation suggest the degree of similarity between neighbor TICs to be highly correlated with the degree of dispersion. Several quantitative measures of similarity are reported in the literature, especially aiming at the assessment of the connectivity between electroencephalographic biopotentials [28]. Due to the narrow bandwidth of TIC signals, we have focused on similarity measures in the frequency domain, facilitating the analysis of the relevant frequency components. This approach also enables distinguishing between signal amplitude and phase, with the phase being influenced by the UCA appearance time. In particular, the spectral coherence between neighbor curves is the adopted similarity measure.

A preliminary validation of the method was carried out with six measurements in five patients referred for a radical prostatectomy at the Academic Medical Center (AMC), University Hospital of Amsterdam, the Netherlands. The generated dispersion maps were validated by comparison with the histology results, considered as the ground truth. This validation was also extended to all the previous methods reported in the literature that are based on a UCA bolus injection.

4.2 Methodology

4.2.1 Dispersion modeling

Ultrasound imaging of one plane through the prostate is performed after an UCA intravenous injection. The evolution over time of the UCA concentration is analyzed at each pixel in the echographic video. The basis of the method we proposed in [25] and [26] consists of the

interpretation of the UCA concentration evolution as the result of a convective dispersion process [29, 30]. This process can be modeled by the convective diffusion equation, which describes the concentration-time evolution $C(\mathbf{x}, t)$ at position $\mathbf{x}$ as

$$\frac{\partial C(\mathbf{x}, t)}{\partial t} = \nabla \cdot \left[D \nabla C(\mathbf{x}, t) - \mathbf{v} C(\mathbf{x}, t) \right], \tag{4.1}$$

with D and $\mathbf{v}$ being the UCA diffusion coefficient and the UCA velocity, respectively [29, 30]. In (4.1), the diffusion coefficient D is assumed to be isotropic. Therefore, a distinction between flow ($\mathbf{v}$) and diffusion (D) is introduced in (4.1).

The local density random walk (LDRW) model [27, 29], which is a solution of the mono-dimensional convective diffusion equation with constant diffusion D and velocity v, is reported to produce accurate fits of TICs measured in cancerous tissue [31]. A fundamental parameter in the convective diffusion equation is the diffusion coefficient D, indicating the rate of diffusion of the injected agent. Although the diffusion coefficient is typically used to characterize Brownian motion, the same coefficient, better referred to as apparent diffusion [32], can also be used to characterize the dispersion process through a microvascular network [33]. The main factors influencing apparent diffusion relate to the transit-time distribution of UCA moving through multi-path trajectories determined by the microvascular architecture. Therefore, from now on, we refer to apparent diffusion as dispersion.

In our previous work, we have shown that a solution of the convective diffusion equation under simple boundary conditions provides a parameter representing the local ratio between convection and dispersion [25, 26]. Only a Gaussian spatial distribution of the UCA concentration prior to entering the measurement site (pixel) is assumed. This condition is necessary to derive a dispersion-related parameter that is local, even if the TIC analysis is limited to the time domain. In fact, the obtained parametric solution of the convective diffusion equation is a function of time t only, and is given as

$$C(t) = \mathrm{AUC} \sqrt{\frac{\kappa}{2\pi (t - t_0)}} \exp\left(\frac{-\kappa (t - t_0 - \mu)^2}{2 (t - t_0)} \right). \tag{4.2}$$

In (4.2), the TIC, $C(t)$, is a function of the theoretical injection time t_0, the area under the IDC (AUC), the mean transit time μ of the UCA bolus from the injection to the detection site, and the parameter κ, representing the local ratio between dispersive time and squared convective time. In fact, $\kappa = v^2/2D$. The scale parameter AUC represents the ratio between injected UCA dose and blood flow. In our measurements, it also includes the (linear) calibration coefficient mapping UCA concentration into backscattered acoustic intensity. By fitting the model in (4.2) to UCA TICs measured at each pixel, we can therefore generate a map of κ, i.e., a map of a dispersion-related parameter. The parameter

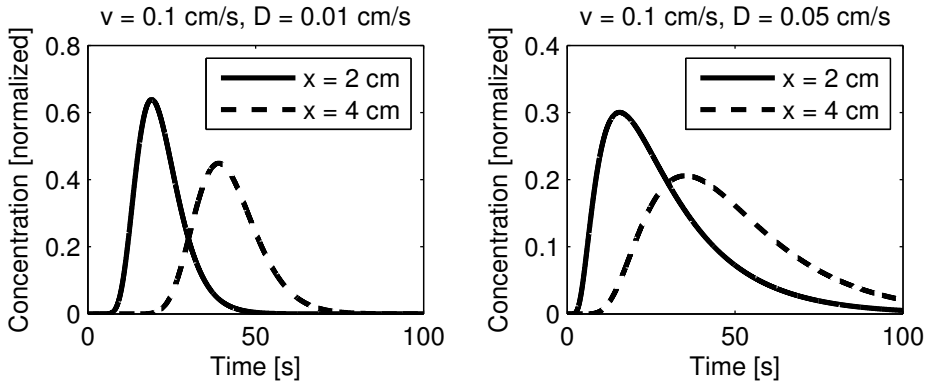

Figure 4.1 *Influence of dispersion on the similarity of TICs measured at different spatial position* x.

κ is determined by the microvascular architecture and is different from the level of flow or perfusion, estimated by all methods reported in the literature [19, 21, 31].
The model in (4.2) represents only the first pass of the injected UCA bolus. As a result, the measured TICs can only be fit prior to the arrival of subsequent passes of the injected bolus due e.g. to recirculation. This issue poses the problem of finding the optimal fitting interval, increasing the complexity of the fitting algorithm [26].

4.2.2 Spatiotemporal analysis

While the approach presented in [25] and [26] reduces to fitting TICs in the time domain, in this paper a different approach is proposed that exploits also the available spatial information by introducing a full spatiotemporal analysis. This approach originates from the observation that the shape similarity between neighbor TICs is influenced by the local degree of dispersion. Fig. 4.1 shows this phenomenon by a finite difference simulation of (4.1) in one spatial dimension, represented by the x-axis. With a fixed carrier velocity $v = 0.1$ cm/s, two TICs are derived at two different distances $x = 2$ cm (solid line) and $x = 4$ cm (dashed line) from the UCA injection site for two different diffusion coefficients $D = 0.01$ cm^2/s (left plot) and $D = 0.05$ cm^2/s (right plot). The values for the velocity and diffusion coefficient are realistic; they are chosen according to the typical blood velocity through microvessels (of the order of a millimeter per second) and the values estimated for the parameter κ in the prostate microcirculation [26].
A measure of the similarity between neighbor TICs can therefore be an indirect indicator of local dispersion without strict assumptions dictated by the adopted models and boundary conditions regulating the temporal evolution of the UCA concentration. The entire TICs can be used for the estimation of similarity without any restriction to the first pass of the injected UCA bolus. Moreover, the implementation of the proposed spatiotemporal anal-

ysis, based on similarity estimation, does not require TIC fitting, reducing signal-quality requirements and computational complexity.

Several measures of similarity can be adopted. A vast literature is in fact available, especially for the determination of connectivity between electroencephalographic biopotentials [28]. As the main scope of this paper is showing the feasibility of similarity mapping for prostate cancer localization, standard similarity measures are considered. The most common measure of similarity is the correlation coefficient. However, this is influenced by differences in UCA appearance time, causing TIC relative delays, and is therefore unsuitable for pure TIC shape comparison.

A more suitable similarity measure is represented by the spectral coherence, here indicated by the symbol ρ and calculated as the correlation coefficient of the amplitude of the TIC frequency spectra. Use of the TIC spectral coherence permits focusing on the amplitude spectra while neglecting phase information related to UCA appearance times. In addition, the frequency bandwidth representing the UCA-concentration evolution can be easily extracted, improving the signal-to-noise ratio (SNR) of the analyzed signals. The spectral coherence, ρ, is therefore the adopted similarity measure. Given the frequency amplitude spectra $S_m(\omega)$ and $S_n(\omega)$ of two TICs $C_m(t)$ and $C_n(t)$, respectively, the spectral coherence $\rho(S_m, S_n)$ is derived as

$$\rho(S_m, S_n) = \frac{\int_{\omega_{\text{min}}}^{\omega_{\text{max}}} \left[\left(S_m(\omega) - \bar{S}_m\right)\left(S_n(\omega) - \bar{S}_n\right)\right] \, \mathrm{d}\omega}{\sqrt{\int_{\omega_{\text{min}}}^{\omega_{\text{max}}} \left[S_m(\omega) - \bar{S}_m\right]^2 \, \mathrm{d}\omega \int_{\omega_{\text{min}}}^{\omega_{\text{max}}} \left[S_n(\omega) - \bar{S}_n\right]^2 \, \mathrm{d}\omega}}, \tag{4.3}$$

with $\bar{S}$ representing the mean value of $S(\omega)$ over the selected frequency interval $[\omega_{\text{min}}, \omega_{\text{max}}]$. Since the TIC bandwidth in the prostate is limited to frequencies up to 0.5 Hz [25], frequencies above 0.5 Hz are discarded and $\omega_{\text{max}} = \pi$ rad/s. The DC component, typically affected by the scanner setting, is also discarded. As a result, the frequency ω_{min} equals $2\pi f_s/N$, with f_s and N indicating the imaging frame rate (usually 10 Hz, depending on the image depth) and the number of TIC samples (about 1000 for typical 100 s TICs), respectively.

For each pixel, the TIC spectrum is compared to the spectra of the neighbor pixels. A spatial kernel determines which pixels are used for comparison. The kernel design accounts for the resolution of the scanner and the scale of the microvascular network to be imaged. The resolution of ultrasound images is anisotropic and is typically higher in the axial (longitudinal) direction. Dedicated *in vitro* experiments were performed in order to determine the scanner resolution in the adopted imaging mode. UCA microbubbles have diameters that are much smaller than the scanner resolution; therefore, ultrasound images of UCA dilutions provide an opportunity for determining point spread function and resolution of

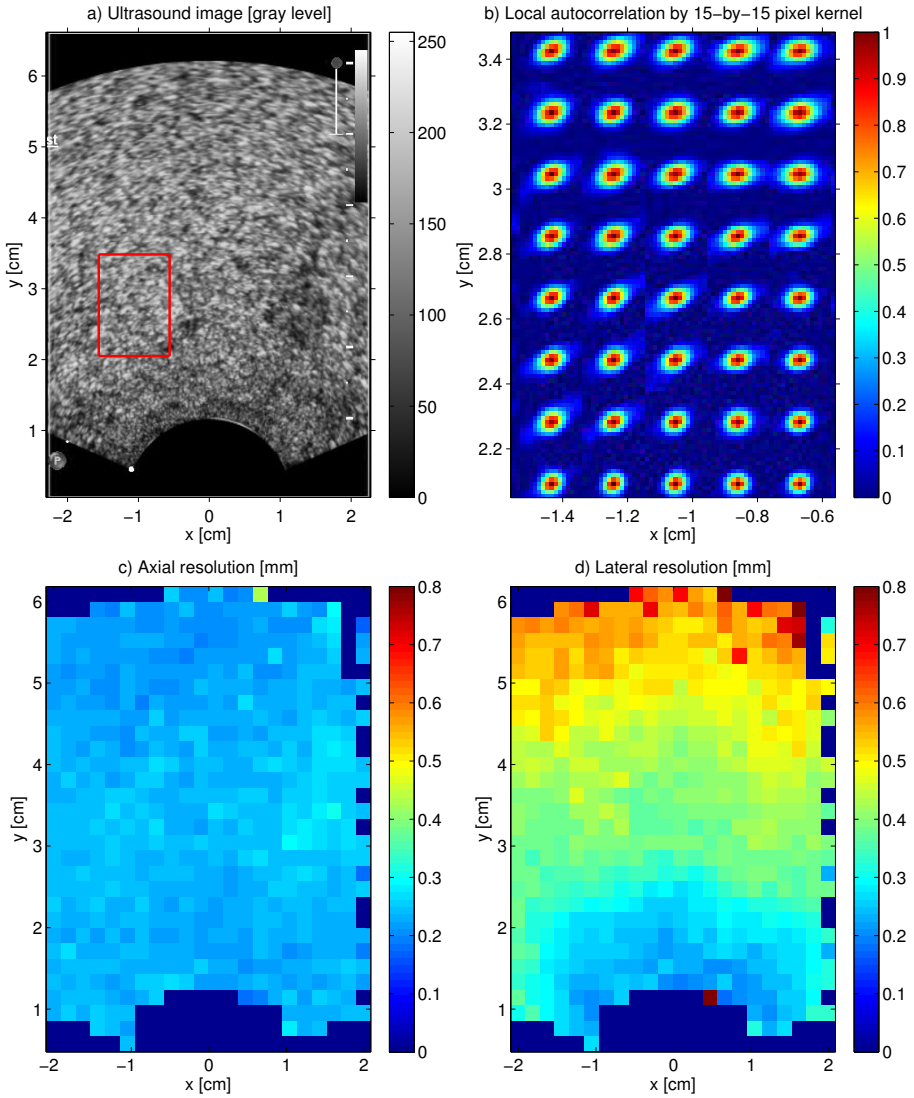

Figure 4.2 *The upper left figure (a) shows an ultrasound scan of an* in vitro *UCA dilution. Figure (b), in the upper right, shows the result of local autocorrelation analysis by a 15 x 15 pixel kernel. For visualization purposes, only a zoom of the area marked in the ultrasound scan in (a) is shown. The lower figures show the resulting maps of axial (c) and lateral (d) resolution estimated by autocorrelation analysis.*

the ultrasound imaging system. Low UCA concentrations were imaged and the scanner resolution was estimated on the basis of local autocorrelation analysis as described in [34]. The resulting ultrasound images were therefore decomposed in squared windows of 15 x 15 pixels, and the image autocorrelation function was calculated for each of these windows. According to [34], the system resolution can be estimated as the half width of the autocorrelation function at 50% of the peak amplitude. With the adopted scanner (Sec. 4.2.3) and selected imaging depth, suitable for prostate imaging, each pixel covers a surface of about 150 x 150 μm^2, smaller than the ultrasound system resolution.

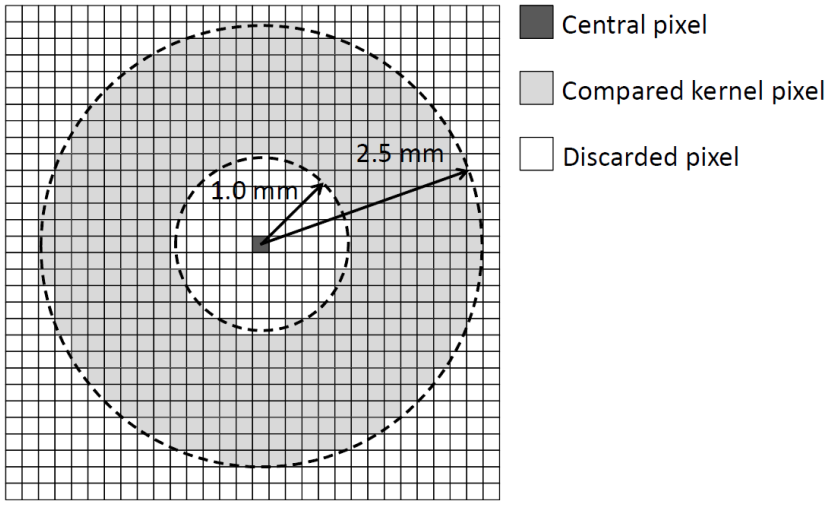

Figure 4.3 *Adopted kernel for spatial similarity analysis.*

Fig. 4.2 shows an example of image recorded *in vitro* (Fig. 4.2a), the result of the local autocorrelation analysis (Fig. 4.2b), and two maps, (Fig. 4.2c) and (Fig. 4.2d), representing the estimated lateral and axial resolution, respectively. These two resolution maps are based on the lateral and axial half width of the autocorrelation function at 50% of the peak amplitude. As expected, the far-field lateral resolution showed the lowest value, equal to 0.7 mm at a distance of 5 cm from the probe. This is the largest distance that we have encountered in transrectal prostate imaging. The resolution estimated in the axial direction was of the order of 0.3 mm, independently of the image depth. This value is in agreement with the theoretical axial resolution for the short pulses at 3.5 MHz adopted in the selected imaging mode (Sec. 4.2.3).

Given the estimated resolution, a Gaussian filter with standard deviation equal to 0.25 mm is adopted to improve the SNR of measured TICs while maintaining sufficient resolution for angiogenesis imaging. The applied low-pass Gaussian prefiltering provides also a reduction in relative resolution anisotropy and depth dependency. The resulting resolution, of the order of 1 mm in the lateral direction, also permits downsampling the image at 2 samples per millimeter. Given the original pixel size of 150 μm, a final resolution of 2 samples per millimeter corresponds to a factor three reduction in the number of processed pixels.

Angiogenesis is required for tumors to grow beyond 2-3 mm in diameter [1, 35]. Therefore, in order to detect early angiogenic processes, a resolution of at least 3 mm should be achieved. Based on the obtained image resolution (1 mm) and that necessary for early angiogenesis imaging (2-3 mm), the proposed kernel, shown in Fig. 4.3, is ring shaped, with inner and outer radii equal to 1 mm and 2.5 mm, respectively. A ring shape is adopted in order to obtain a coherence estimate that is independent of the blood perfusion direction. Coherence analysis is then performed as follows. First, the TIC amplitude spectrum is com-

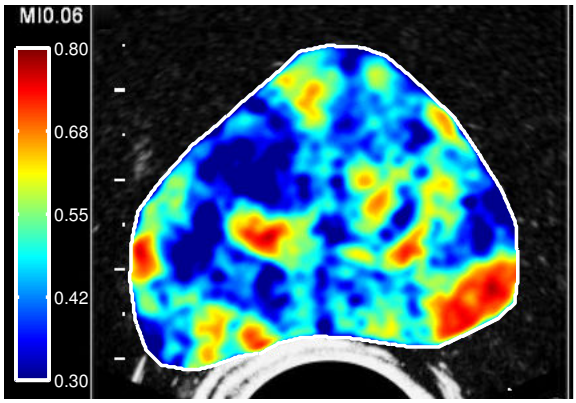

Figure 4.4 *Prostate dispersion map based on coherence analysis.*

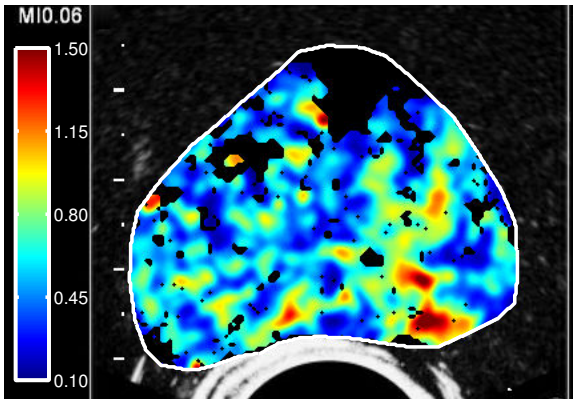

Figure 4.5 *Prostate dispersion map based on κ analysis.*

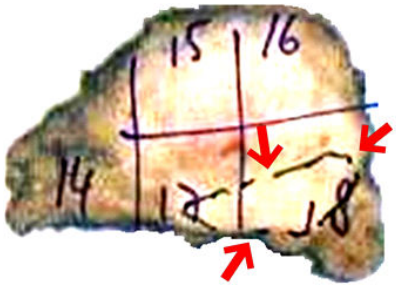

Figure 4.6 *Histology slice with marked carcinoma, indicated also by three arrows, corresponding to the dispersion map of Figures 4.4 and 4.5.*

puted for all the kernel pixels. Then the spectrum corresponding to the specified frequency range is extracted. Finally, the correlation coefficient is computed between the spectrum at the central pixel and the spectra at each pixel within the ring. These coefficients are averaged to obtain a single measure of local coherence. This procedure is repeated for all pixels covering the prostate in order to produce and display a dispersion map based on local spectral coherence. Fig. 4.4 shows an example of dispersion map. The corresponding dispersion map, based on the estimation of the parameter κ, is shown in Fig. 4.5.

4.2.3 Data acquisition

Data acquisition was performed at the AMC, University Hospital of Amsterdam (the Netherlands). An intravenous peripheral injection of a 2.4 mL SonoVue ® (Bracco, Milan, Italy) bolus was performed. SonoVue ® is a dispersion of SF_6 microbubbles with an average diameter of 3 μm encapsulated in a monolayer phospholipid shell [36]. The bolus passage through the prostate was recorded by transrectal ultrasound imaging with an iU22 ultrasound scanner (Philips Healthcare, Bothell, WA) equipped with a transrectal probe C8-4v. Exploiting the nonlinear behavior of UCA microbubble oscillations, several contrast-specific

imaging modes are nowadays available that permit enhancing the sensitivity to contrast agents while suppressing signals coming from tissue, which behaves more linearly [37]. These imaging modes are essential for UCA quantification in tissue. In this study, we used a power modulation pulse scheme at 3.5 MHz and mechanical index equal to 0.06, to avoid bubble destruction. The dynamic range was set to 45 dB, considered sufficient for accurate TIC measurements [38].
The acquired ultrasound image sequences were stored in DICOM (Digital Imaging and Communications in Medicine) format. The analysis of these files was implemented in MATLAB ® (The MathWorks, Natick, MA).
Dedicated measurements, similar to those reported in [26] and [27], were carried out in order to determine the relation between UCA concentration and backscattered acoustic intensity. Different dilutions of SonoVue ®, ranging between 0 and 0.5 mL/L, were imaged with the same equipment and the same setting adopted for the measurements in patients. The software QLAB (Philips Healthcare, Bothell, WA) was used in order to have a reference relative to the acoustic intensity backscattered by UCA dilutions. The results confirmed an approximately linear relation (correlation coefficient $r = 0.98$) for SonoVue ® concentrations up to 0.2 mL/L. This concentration range covers that encountered in prostate measurements [26]. For higher concentrations, attenuation effects become dominant and a linear approximation does no longer hold. The relation between measured acoustic intensity and stored DICOM gray levels could also be estimated by the same measurements. To this end, gray-level data and QLAB data were compared at corresponding image locations. Therefore, the relation between SonoVue ® concentration and received acoustic intensity, as well as the compression function applied by the scanner on the received signals, could be estimated and used for signal linearization. For a proper use of the indicator dilution theory [27], data linearization was applied prior to the coherence analysis.

4.2.4 Validation

The method was validated by comparing the imaging results with the histology results in six datasets obtained from five patients with prostate cancer who underwent a radical prostatectomy. After cutting the prostate in slices of 4-mm thickness, a pathologist marked the presence of prostate cancer [39]. Fig. 4.6 shows the histology results corresponding to Figures 4.4 and 4.5. Prostate cancer is associated to a decrease in cell differentiation, which is graded by the Gleason score [40].
All the marked histology slices were scanned to generate digital images of the histology results. For each prostate, one single slice was selected that was the closest to the ultrasound imaging plane, and the results were compared. The selected slice was linearly deformed in order to match the prostate contour according to the ultrasound image.

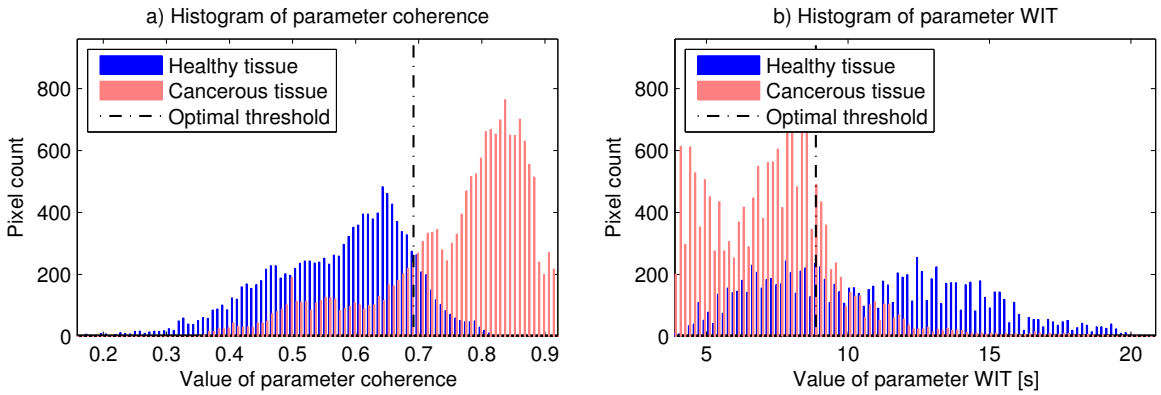

Figure 4.7 *Histograms for healthy and cancerous tissue of coherence (a) and wash-in time (b) on the full dataset.*

Two regions of interest (ROIs) larger than 0.5 cm^2, representing healthy and cancerous tissue, were then determined on the basis of the histology results and applied on the ultrasound dispersion maps. Only large regions of cancerous and healthy tissue, extending through multiple histology slices, were considered. This way, the validation results were not sensitive to unavoidable mismatches between ultrasound imaging planes and corresponding histology slices.

Each class, representing healthy and cancerous tissue, included about 12×10^3 pixels, comprising the complete dataset of 6 measurements. For each set of pixels, mean and variance of the estimated coherence was calculated. As shown in Fig. 4.7, although the class distributions of some parameters, such as the coherence parameter, were Gaussian (correlation coefficient larger than 0.8), other parameters, such as the wash-in time, did not present Gaussian distributions (correlation coefficient smaller than 0.2). Therefore, for a correct comparison of the evaluated parameters, no assumption was made on the distribution within each class. The classification threshold between healthy and cancerous tissue was therefore determined as the point on the receiver operating characteristic (ROC) curve that was the closest to the optimal classification corner (upper-left corner) [41].

Based on the determined classification threshold, each selected pixel was classified, and the method sensitivity and specificity was derived. The full ROC curve was also derived and evaluated. For comparison, the same validation procedure was also performed for the dispersion parameter κ and for all the perfusion-related parameters proposed in the literature that are estimated by TIC analysis following a UCA bolus injection [19, 21, 31]. The classification performance by perfusion-related parameters was improved by LDRW model fitting prior to the estimation. To this end, the same fitting procedure proposed in [26] was adopted. Major perfusion-related parameters, such as AUC, mean transit time (MTT), peak time (PT), and peak intensity (PI) can directly be derived from the LDRW fit parameters [42, 43]. The estimation of other perfusion parameters, such as the wash-in time

Table 4.1 *Class mean ± standard deviation for different parameters*

Parameter	Healthy	Cancerous
ρ	0.58 ± 0.11	0.76 ± 0.12
κ [s^{-1}]	0.64 ± 0.27	1.04 ± 0.29
AUC [a.u.]	364 ± 443	968 ± 1205
PI [a.u.]	23.8 ± 35.6	83.2 ± 75.6
PT [s]	30.8 ± 11.6	22.6 ± 8.0
AT [s]	17.8 ± 7.9	13.7 ± 5.7
FWHM [s]	17.2 ± 5.6	11.2 ± 3.7
WIT [s]	10.9 ± 3.6	7.4 ± 2.3
MTT [s]	22.8 ± 5.1	17.0 ± 4.1

(WIT, i.e., the time period between contrast appearance and TIC peak), appearance time (AT), and TIC full-width at half maximum (FWHM) can easily be derived from the fitted curve.

4.3 Results

The presence of cancer produced an increase in coherence. In the four analyzed prostates, an average coherence of 0.76 ± 0.12 and 0.58 ± 0.11 was estimated in ROIs representing cancerous and healthy tissue, respectively. The computation time by coherence imaging was about 99% lower than by the methods requiring TIC fitting.
Table 4.1 reports for the entire dataset the mean and standard deviations of the two classes by all the parameters considered for classification, comprising the dispersion parameters κ and ρ, as well as the TIC PI, PT, AUC, FWHM, and WIT, and the contrast AT and MTT ($\mu + t_0$) [19, 21, 26, 31]. For all these parameters, the classification performance in terms of sensitivity, specificity, and ROC curve area is reported in Table 4.2.

4.4 Discussion and conclusion

In order to overcome the limitations of perfusion imaging for prostate cancer localization, we have recently proposed the analysis of the dispersion kinetics of an UCA bolus as a better option to infer the underlying microvascular architecture and localize cancer angiogenesis [25, 26]. Our preliminary validation was promising, showing an agreement with the histology results that was superior to previous perfusion-based methods. This method is however limited to the independent analysis of multiple TICs in the time domain. In this paper, we demonstrate that by full spatiotemporal analysis of the UCA kinetics we can

Table 4.2 *Classification performance on pixel basis*

Parameter	Cancerous if	Sensitivity [%]	Specificity [%]	ROC curve area
ρ	$\geq$ 0.69	77.3	86.6	0.87
κ	$\geq$ 0.84 s^{-1}	78.5	79.5	0.84
AUC	$\geq$ 338 a.u.	78.0	70.2	0.79
PI	$\geq$ 28.2 a.u.	77.7	78.1	0.84
PT	$\leq$ 28.1 s	74.3	54.5	0.70
AT	$\leq$ 17.7 s	72.7	48.5	0.65
FWHM	$\leq$ 13.0 s	79.5	71.8	0.82
WIT	$\leq$ 8.87 s	79.7	65.0	0.78
MTT	$\leq$ 19.7 s	79.0	75.4	0.82

further improve the classification performance of the method while reducing by 99% the computational complexity, as no model fitting is required.

Based on the observation that dispersion is inversely correlated with similarity between TICs measured at different positions, spatiotemporal analysis is implemented as the estimation of the spectral coherence between neighbor TICs. Since only local, relative TIC shape variations affect the estimated coherence, the effect of attenuation and non-linear distortion of propagating ultrasound waves on the estimated coherence map is negligible as compared to other TIC parameters that are based on absolute measurements of acoustic intensity, such as PI or AUC. The proposed method was validated by comparison with the histology results after radical prostatectomy. To this end, six measurements in five patients were performed. This validation showed an improved agreement with the histology results as compared to our previous method for dispersion analysis as well as to the methods proposed in the literature that are based on perfusion imaging. In addition, no TIC fitting is required, increasing the method robustness and decreasing its complexity.

The results confirm the presence of angiogenesis to correlate with a drop in UCA dispersion [26]. This might be due to the high tortuosity of cancer neovessels [11, 12, 19, 20], which limits the dispersion distance, proportional to $\sqrt{Dt}$ [44], by confining the bolus for longer time [45]. In our future work, the link between dispersion and microvascular architecture will be investigated and determined more accurately by the realization of dedicated *in vitro* phantoms [46]. In addition, the anisotropic resolution of ultrasound images could be fully regularized by use of anisotropic low-pass prefiltering prior to the analysis.

Only a preliminary validation was carried out. An extended validation is necessary to confirm the obtained promising results. Moreover, additional similarity measures that are alternative to the spatial coherence could also be investigated.

The validation procedure should be improved by use of image registration methods that provide an accurate match between parametric ultrasound images and histology results.

Unfortunately, while a number of methods have been proposed for validation of MRI techniques [47], no such methods are available for ultrasound imaging. This is due to the limits imposed by two-dimensional imaging as well as to the poor detection of natural landmarks supporting a correct registration. In the future, if three-dimensional transrectal ultrasound imaging becomes available, new opportunities would open up for better modeling as well as for better validation by accurate image registration.

An additional issue relates to the choice for the ground truth. With the aim of angiogenesis quantification, the ground truth might be better represented by microvascular quantitative indexes, such as the MVD [5, 6], rather than by the degree of cell differentiation assessed in standard histology by the Gleason score [40].

References

[1] J. Folkman, "Tumor angiogenesis: therapeutic implications," *N. Engl. J. Med.*, vol. 285, no. 21, pp. 1182–1186, 1971.

[2] J. Folkman, K. Watson, D. Ingber, and D. Hanahan, "Induction of angiogenesis during the transition from hyperplasia to neoplasia," *Nature*, vol. 339, no. 6219, pp. 58–61, 1989.

[3] S. B. Fox, G. Gasparini, and A. L. Harris, "Angiogenesis: pathological, prognostic, and growth-factor pathways and their link to trial design and anticancer drugs," *Lancet Oncol.*, vol. 2, pp. 278–289, 2001.

[4] N. Weidner, P. R. Carroll, J. Flax, W. Blumenfeld, and J. Folkman, "Tumor angiogenesis correlates with metastasis in invasive prostate carcinoma," *Am. J. Pathol.*, vol. 143, no. 2, pp. 401–409, 1993.

[5] S. A. Bigler, R. E. Deering, and M. K. Brawer, "Comparison of microscopic vascularity in benign and malignant prostate tissue," *Hum. Pathol.*, vol. 24, no. 2, pp. 220–226, 1993.

[6] M. K. Brawer, "Quantitative microvessel density. A staging and prognostic marker for human prostatic carcinoma," *Cancer*, vol. 78, no. 2, pp. 345–349, 1996.

[7] K. W. Ferrara, C. R. Merritt, P. N. Burns *et al.*, "Evaluation of tumor angiogenesis with US: imaging, Doppler, and contrast agents," *Acad. Radiol.*, vol. 7, pp. 824–839, 2000.

[8] G. Salomon, J. KIlerman, I. Thederan *et al.*, "Evaluation of prostate cancer detection with ultrasound real-time elastography: a comparison with step section pathological analysis after radical prostatectomy," *Eur. Urol.*, vol. 54, pp. 1354–1362, 2008.

[9] P. S. Tofts, G. Brix, D. L. Buckley *et al.*, "Estimating kinetic parameters from dynamic contrast-enhanced T1-weighted MRI of a diffusable tracer: standardized quantities and symbols," *J. Magn. Reson. Imaging*, vol. 10, pp. 223–232, 1999.

[10] H. Wijkstra, M. H. Wink, and J. J. M. C. H. de la Rosette, "Contrast specific imaging in the detection and localization of prostate cancer," *World J. Urol.*, vol. 22, pp. 346–350, 2004.

[11] D. Cosgrove, "Angiogenesis imaging - ultrasound," *Br. J. Radiol.*, vol. 76, pp. S43–S49, 2003.

[12] R. Alonzi, A. R. Padhani, and C. Allen, "Dynamic contrast enhanced MRI in prostate cancer," *Eur. J. Radiol.*, vol. 63, pp. 335–350, 2007.

[13] S. B. Feinstein, "The powerful microbubble: from bench to bedside, from intravascular indicator to therapeutic delivery system, and beyond," *Am. J. Physiol. Heart Circ. Physiol.*, vol. 287, no. 2, pp. H450–H457, 2004.

[14] T. G. Leighton, *The acoustic bubble*. New York: Oxford University Press, 1995.

[15] K. Wei, A. R. Jayaweera, S. Firoozan *et al.*, "Quantification of myocardial blood flow with ultrasound-induced destruction of microbubbles administered as a constant venous infusion," *Circulation*, vol. 97, pp. 473–483, 1998.

[16] M. Arditi, P. J. A. Frinking, X. Zhou, and N. G. Rognin, "A new formalism for the quantification

of tissue perfusion by the destruction-replenishment method in contrast ultrasound imaging," *IEEE Trans. Ultrason., Ferroelectr., Freq. Control*, vol. 53, no. 6, pp. 1118–1129, 2006.

[17] J. M. Hudson, R. Karshafian, and P. N. Burns, "Quantification of flow using ultrasound and microbubbles: A disruption replenishment model based on physical principles," *Ultrasound Med. Biol.*, vol. 35, no. 12, pp. 2007–2020, 2009.

[18] H. Qian and J. B. Basingthwaighte, "A class of flow bifurcation models with lognormal distribution and fractal dispersion," *J. Theor. Biol.*, vol. 205, pp. 161–168, 2000.

[19] N. Elie, A. Kaliski, P. Péronneau *et al.*, "Methodology for quantifying interactions between perfusion evaluated by DCE-US and hypoxia throughout tumor growth," *Ultrasound Med. Biol.*, vol. 33, no. 4, pp. 549–560, 2007.

[20] S. Delorme and M. V. Knopp, "Non-invasive vascular imaging: assessing tumour vascularity," *Eur. Radiol.*, vol. 8, pp. 517–527, 1998.

[21] R. J. Eckersley, J. P. Sedelaar, M. J. K. Blomley *et al.*, "Quantitative microbubble enhanced transrectal ultrasound as a tool for monitoring hormonal treatment of prostate carcinoma," *Prostate*, vol. 51, pp. 256–267, 2002.

[22] American Cancer Society, "Cancer facts & figures 2010," Atlanta, 2010.

[23] K. K. Hodge, J. E. McNeal, M. K. Terris, and T. A. Stamey, "Random systematic versus directed ultrasound guided transrectal core biopsies of the prostate," *J. Urol.*, vol. 142, no. 1, pp. 71–75, 1989.

[24] B. Trajcevska-Boskovska, V. Georgiev, Z. Popov, B. Bogoeva, and S. Banev, "Extended 12 systematic prostate biopsy protocol can improve prostate cancer detection," *Urology*, vol. 68 Supp, no. 22, pp. 271–272, 2006.

[25] M. Mischi, M. P. J. Kuenen, H. Wijkstra, A. J. Hendrikx, and H. H. M. Korsten, "Prostate cancer localization by contrast-ultrasound diffusion imaging," in *2009 IEEE Int. Ultrasonics Symp.*, Rome, Sep. 21–23, pp. 281–294.

[26] M. P. J. Kuenen, M. Mischi, and H. Wijkstra, "Contrast-ultrasound diffusion imaging for localization of prostate cancer," *IEEE Trans. Med. Imag.*, vol. 30, no. 8, pp. 1493–1502, 2011.

[27] M. Mischi, "Contrast echocardiography for cardiac quantifications," Ph.D. dissertation, Eindhoven University of Technology, 2004, available at http://www.sps.ele.tue.nl/members/M.Mischi/.

[28] F. Wendling, K. Ansari-Asl, F. Bartolomei, and L. Senhadji, "From EEG signals to brain connectivity: a model-based evaluation of interdependence measures," *J. Neurosci. Methods*, vol. 183, no. 1, pp. 9–18, 2009.

[29] C. W. Sheppard, *Basic principles of the tracer method*. New York: John Wiley and Sons, 1962.

[30] K. H. Norwich, *Molecular dynamics in biosystems*. Oxford: Pergamon Press, 1977.

[31] C. Strouthos, M. Lampaskis, V. Sboros, A. McNeilly, and M. Averkiou, "Indicator dilution models for the quantification of microvascular blood flow with bolus administration of ultrasound contrast agents," *IEEE Trans. Ultrason., Ferroelectr., Freq. Control*, vol. 57, no. 6, pp. 1296–1310, 2010.

[32] G. Taylor, "Dispersion of soluble matter in solvent flowing slowly through a tube," *Proc. R. Soc. A*, vol. 219, pp. 186–203, 1953.

[33] Y.-C. Fung, *Biodynamics: circulation*, 1st ed. Berlin: Springer, 1984.

[34] R. F. Wagner, S. W. Smith, J. M. Sandrik, and H. Lopez, "Statistics of speckle in ultrasound B-scans," *IEEE Trans. Sonics Ultrason.*, vol. 30, no. 3, pp. 156–163, 1983.

[35] B. Nicholson and D. Theodorescu, "Angiogenesis and prostate cancer tumor growth," *J. Cell. Biochem.*, vol. 91, no. 1, pp. 125–150, 2004.

[36] J.-M. Gorce, M. Arditi, and M. Schneider, "Influence of bubble size distribution on the echogenicity of ultrasound contrast agents," *Invest. Radiol.*, vol. 35, no. 11, pp. 661–671, 2000.

[37] N. de Jong, P. J. A. Frinking, A. Bouakaz, and F. J. ten Cate, "Detection procedures of ultrasound contrast agents," *Ultrasonics*, vol. 38, no. 1–8, pp. 87–92, 2000.

[38] N. G. Rognin, P. J. A. Frinking, M. Costa, and M. Arditi, "In-vivo perfusion quantification by contrast ultrasound: validation of the use of linearized video data vs. raw RF data," in *2008 IEEE Ultrasonics Symp. Proc.*, 2008, pp. 1690–1693.

[39] R. Montironi, T. van der Kwast, L. Boccon-Gibod, A. V. Bono, and L. Boccon-Gibod, "Handling and pathology reporting of radical prostatectomy specimens," *Eur. Urol.*, vol. 44, pp. 626–636, 2003.

[40] D. F. Gleason and G. T. Mellinger, "Prediction of prognosis for prostatic adenocarcinoma by combined histological grading and clinical staging," *J. Urol.*, vol. 111, pp. 58–64, 1974.

[41] M. H. Zweig and G. Campbell, "Receiver-operating characteristic (ROC) plots: a fundamental evaluation tool in clinical medicine," *Clin. Chem.*, vol. 39, pp. 561–577, 1993.

[42] M. Mischi, A. A. C. M. Kalker, and H. H. M. Korsten, "Videodensitometric methods for cardiac output measurements," *EURASIP J. Appl. Signal Processing*, vol. 5, pp. 479–489, 2003.

[43] M. Mischi, A. A. C. M. Kalker, and H. H. M. Korsten, "Contrast echocardiography for pulmonary blood volume quantification," *IEEE Trans. Ultrason., Ferroelectr., Freq. Control*, vol. 51, no. 9, pp. 1137–1147, 2004.

[44] E. Purcell, "Life at low Reynolds number," *Am. J. Phys.*, vol. 45, pp. 3–11, 1977.

[45] P. Grathwohl, *Diffusion in natural porous media: Contaminant transport, sorption / desorption and dissolution kinetics*. Kluwer Academic Publishers, 1998.

[46] C. Demitri, A. Sannino, F. Conversano *et al.*, "Hydrogel based tissue mimicking phantom for in-vitro ultrasound contrast agents studies," *J. Biomed. Mater. Res. B Appl. Biomater.*, vol. 87, pp. 338–345, 2008.

[47] Y. Zhan, Y. Ou, M. Feldman *et al.*, "Registering histologic and MR images of prostate for image-based cancer detection," *Acad. Radiol.*, vol. 14, no. 11, pp. 1367–1381, 2007.

CHAPTER 5

Spatiotemporal coherence analysis: rationale and improvements

Based on: M. P. J. Kuenen, T. A. Saidov, H. Wijkstra, and M. Mischi, "Contrast-Ultrasound Dispersion Imaging for Prostate Cancer Localization by Improved Spatiotemporal Similarity Analysis," *Ultrasound in Medicine & Biology*, vol. 39, no. 9, pp. 1631–1641, © Elsevier, 2013.

Abstract – *Angiogenesis plays a major role in prostate cancer growth. Despite extensive research on blood perfusion imaging aimed at angiogenesis detection, the diagnosis of prostate cancer still requires systematic biopsies. This may be due to the complex relationship between angiogenesis and microvascular perfusion. Analysis of ultrasound-contrast-agent dispersion kinetics, determined by multipath trajectories in the microcirculation, may provide a better characterization of the microvascular architecture. We propose the physical rationale for dispersion estimation by an existing spatiotemporal similarity analysis. After an intravenous ultrasound-contrast-agent bolus injection, dispersion is estimated by coherence analysis among time-intensity curves measured at neighbor pixels. The method accuracy is increased by time-domain windowing and anisotropic spatial filtering for speckle regularization. The results in twelve patient datasets showed a superior agreement with histology (receiver-operating-characteristic curve area of 0.88) than those obtained by reported perfusion and dispersion analyses, providing a valuable contribution to prostate cancer localization.*

5.1 Introduction

Prostate cancer is the most common form of cancer in men in the United States, representing 29% and 9% of all cancer diagnoses and deaths, respectively [1]. Treatment often involves a radical prostatectomy, carrying the risk of severe permanent side effects like incontinence and impotence [2]. This risk could be reduced by focal therapies [3], but their use is complicated by diagnostic limitations. In fact, diagnosis requires systematic biopsies, in which the prostate is uniformly sampled up to over 16 times by a core needle. Imaging methods could significantly improve the current situation by enabling better patient stratification, biopsy targeting, and focal therapy guidance, but are not yet available.

Angiogenesis is a key prognostic indicator for prostate cancer imaging, especially due to its correlation with cancer aggressiveness and the risk of developing metastasis [4, 5]. This biochemical process leads to the formation of a dense microvascular network to support the growth of prostate cancer beyond 1 mm^3 [5]. Differences in the microvascular architecture are characterized by an increased microvascular density as well as a higher tortuosity and permeability of the vessel wall [6].

Detection of angiogenesis by assessment of tissue perfusion has been proposed using techniques such as dynamic contrast-enhanced magnetic resonance imaging (DCE-MRI), Doppler ultrasound imaging, and dynamic contrast-enhanced ultrasound (DCE-US) imaging [7–9]. Given its use in biopsy guidance and its real-time availability at the bedside, ultrasound offers a practical and cost-effective alternative to MRI for prostate imaging.

DCE-US is especially interesting because of its ability to obtain flow information from within the smallest microvessels. The adopted ultrasound contrast agents (UCAs) are coated gas microbubbles. Since their size is comparable to that of red blood cells, these microbubbles can flow into the smallest vessels while remaining in the vascular pool [10]. Ultrasound waves induce nonlinear bubble oscillations that are exploited by contrast-specific imaging techniques to suppress the signal backscattered from tissue [11].

Several DCE-US methods have been proposed for angiogenesis detection by assessment of tissue perfusion [12, 13]. Typically, quantification is performed by extracting amplitude and time features from time-intensity curves (TICs), which measure the backscattered acoustic intensity in a selected region of interest (ROI) in the ultrasound image as a function of time. When obtained by the destruction-replenishment technique [14], TICs reflect reperfusion after disruption of microbubbles in the image plane [15–17]. Alternatively, the bolus injection technique produces TICs that characterize the passage of an intravenously injected UCA bolus through the image plane [18–20].

In general, perfusion quantification has however not resulted in reliable angiogenesis detection. One reason for this may be difficult interpretation of TIC features in terms of local perfusion [21]. While amplitude-related features are strongly affected by nonlinear

attenuation and scanner settings [22], timing features generally depend on the history of the bolus transport from the injection to the detection site. Another reason for the limited results may be the complicated influence of angiogenesis on microvascular perfusion. While the presence of arteriovenous shunts and a higher microvascular density are expected to increase perfusion, these effects can be countered by an increased interstitial pressure, due to leakage, and the small diameter and high tortuosity of the newly formed microvessels [19, 23, 24].

Contrast-ultrasound dispersion imaging (CUDI) is an alternative method for detection of the angiogenesis-induced effects on the microvascular architecture [25, 26]. CUDI is based on modeling the intravascular UCA transport kinetics as a convective dispersion process. The distribution of transit times is characterized by the local UCA dispersion kinetics resulting from microvascular architectural features such as density, tortuosity and arteriovenous shunting. A dispersion-related parameter, κ, can be estimated by curve fitting of pixel TICs obtained by the bolus injection technique [25].

Recently, an indirect dispersion analysis was proposed by estimation of the spatial similarity among neighbor TICs using coherence analysis [26]. This approach is unique in the sense that it exploits the spatial information. Different from existing methods because, the estimation is inherently local and normalized. Moreover, TIC fitting and isolation of the bolus first pass are not required, resulting in increased robustness of the estimation.

Inspired by the spatiotemporal analysis proposed by [26], this paper proposes a new mathematical framework explaining the physical link between dispersion and spatial similarity. Based on a better understanding of the underlying physical processes, a number of methodological improvements are also proposed in this paper with the aim of improving the reliability and classification performance of the method. In particular, we propose a dedicated spatial filter to prevent local differences in speckle properties from affecting the similarity analysis. Additionally, TIC time windowing is incorporated to make the similarity analysis more specific to TIC shape variations.

A preliminary validation of CUDI was performed with 12 recordings in 8 patients that underwent radical prostatectomy at the Academic Medical Center (AMC) University Hospital, Amsterdam, The Netherlands. The histology results were used as ground truth to evaluate the cancer localization performance of the dispersion maps estimated by CUDI. The results were compared with those obtained by estimation of different TIC parameters described in the literature.

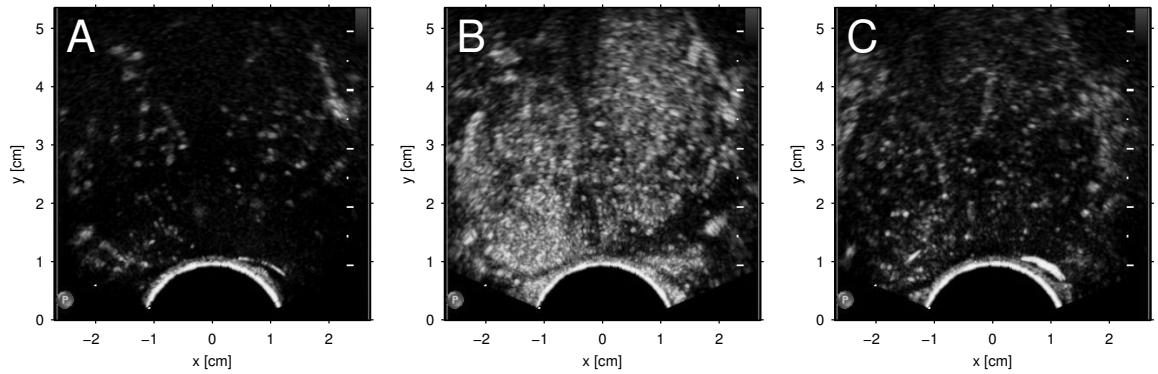

Figure 5.1 *DCE-US imaging of the prostate measured at different times after intravenous UCA bolus injection: (a) just after UCA appearance; (b) at peak intensity; (c) during UCA wash-out.*

5.2 Materials and Methods

5.2.1 Data acquisition and calibration

Acquisition of the DCE-US imaging data was performed at the AMC University Hospital in Amsterdam, The Netherlands, after the study was approved by the local ethical committee. All patients that participated in this study signed an informed consent.

After intravenous injection of a 2.4 mL SonoVue ® (Bracco, Milan, Italy) UCA bolus, DCE-US imaging of the prostate was performed with an iU22 ultrasound imaging system (Philips Healthcare, Bothell, WA) and either a C8-4v (6 recordings in 5 patients) or a C10-3v (6 recordings in 3 patients) transrectal probe. Power modulation imaging was adopted at 3.5 MHz and a low mechanical index (0.06) was used to prevent microbubble disruption. The dynamic-range setting was set to C38 for the C8-4v probe and was increased to C50 for the C10-3v probe because of an increased contrast sensitivity. In all recordings, the focus was placed in the far field and the postprocessing gain was adjusted to prevent truncation or saturation of the image color level. All acquired B-mode imaging data was stored in DICOM (Digital Imaging and Communications in Medicine) format. Fig. 5.1 shows typical frames observed in the course of DCE-US imaging after UCA bolus injection.

For quantitative analysis of DCE-US TICs, an accurate interpretation of the image color level in terms of UCA concentration is necessary. Previously performed *in vitro* measurements have confirmed a linear relationship between UCA concentration and acoustic intensity [25, 27]. The acoustic intensity is linearized by reverting the dynamic-range compression and color mapping implemented by the scanner. Based on measurements using QLAB acoustic quantification software (Philips Healthcare, Bothell, WA), we estimated a logarithmic compression function [25]. The color mapping, displayed on the B-mode image, is extracted and compensated for by inverting the luminance mapping. Although an abso-

lute TIC quantification is not possible, the proposed TIC similarity analysis only requires a relative measure of the UCA concentration.

5.2.2 Spatiotemporal dispersion modeling and similarity

The transport of UCA microbubbles through the microcirculation can be represented by a convective dispersion process [28, 29] as

$$\frac{\partial C(\mathbf{x},t)}{\partial t} = \nabla \cdot \left[D \nabla C(\mathbf{x},t) - \mathbf{v} C(\mathbf{x},t) \right]. \tag{5.1}$$

In (5.1), $C(\mathbf{x},t)$ represents the UCA concentration at position $\mathbf{x}$ and time t. The parameters $\mathbf{v}$ and D represent the convection velocity and the UCA diffusion coefficient, respectively. The diffusion coefficient D is assumed to be isotropic, by which it fundamentally differs from the flow $\mathbf{v}$. Although the diffusion coefficient D generally describes Brownian motion, this coefficient can also be interpreted as apparent diffusion [30] in order to characterize the dispersion process through the multipath trajectories across a microvascular network [31]. Apparent diffusion then reflects the distribution of UCA transit times that results from the microvascular architecture. As a result, we may refer to apparent diffusion as dispersion.
The local density random walk (LDRW) model is a solution of (5.1) in one dimension ($|\mathbf{x}| = x$) for constant parameters and boundary conditions that represent UCA mass conservation and a fast bolus injection [28]. A modified local solution for the concentration as function of time was given by [25] as

$$C(t) = \mathsf{AUC} \sqrt{\frac{\kappa}{2\pi\,(t-t_0)}} \exp\left(\frac{-\kappa\,(t-t_0-\mu)^2}{2\,(t-t_0)} \right), \tag{5.2}$$

where the local hemodynamic parameters κ and μ are given as

$$\kappa = \frac{v^2}{2D} \qquad\qquad \mu = \frac{x_0}{v}. \tag{5.3}$$

The mean transit time μ represents the time that the UCA bolus travels from the injection to the detection site. The parameter κ represents the local ratio between the dispersive time and the squared convective time. The area under the IDC (AUC) is a scale factor determined by the UCA dose and the blood flow. The purely theoretical parameters t_0 and x_0 represent the injection time and distance from the injection site, respectively.
Fitting the model in (5.2) to TICs obtained at all pixels results in a map of local estimates of the dispersion-related parameter κ that relates to the local microvascular architecture. Its relation with dispersion distinguishes κ from other proposed TIC parameters that are mainly based on perfusion [18–20].

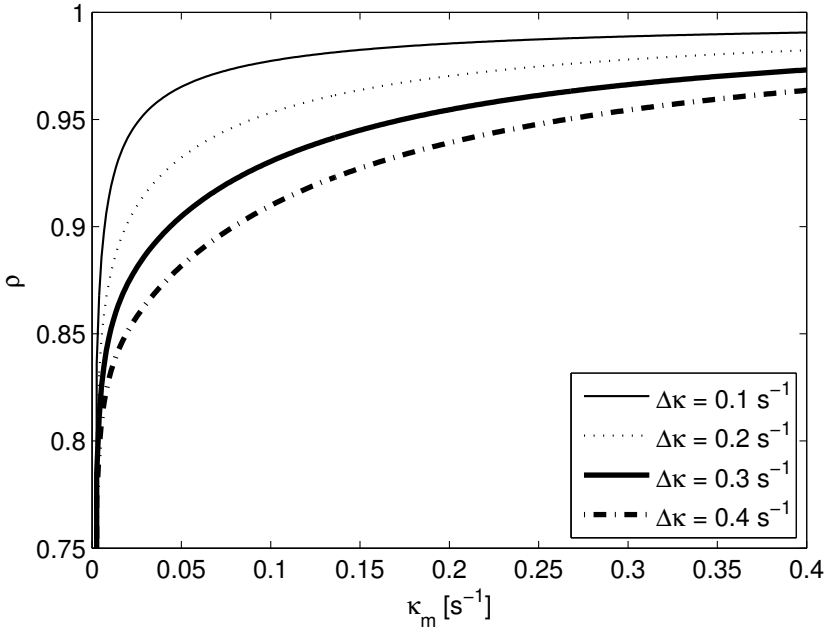

Figure 5.2 *Parametric relation between coherence $\rho(S_m, S_n)$ and κ for $\mu_m = 25$ s and $\mu_n = 20$ s. The κ parameters are related as $\kappa_n = \kappa_m + \Delta\kappa$. For similar values of κ (i.e., small $\Delta\kappa$), the coherence $\rho(S_m, S_n)$ is relatively high. For a fixed $\Delta\kappa$, the coherence increases as κ increases.*

Recently, a full spatiotemporal analysis was proposed based on assessment of spatial TIC similarity by coherence analysis [26]. This inherently local and normalized analysis provided promising results for angiogenesis detection.

In this paper, we derive the physical rationale for the spatial similarity analysis that was initially proposed in [26]. To derive the relation between dispersion and coherence, we consider two TICs $C_m(t)$ and $C_n(t)$ represented by the modified LDRW model as in (5.2). The coherence between two TICs can then be expressed in terms of the shape parameters (κ_m, μ_m) and (κ_n, μ_n). The scale factor AUC does not influence the normalized similarity analysis and we may disregard t_0, because the coherence is insensitive to phase shift.

The spectral TIC coherence is computed as the normalized correlation coefficient between two TIC magnitude spectra $S_m(\omega)$ and $S_n(\omega)$. The magnitude spectrum $S(\omega)$ of a LDRW TIC is derived as the absolute value of the Fourier transform of $C(t)$ and is given as

$$S(\omega) = \mathrm{AUC}\sqrt{\frac{2}{\pi}}\frac{\sqrt{\kappa}e^{\kappa\mu}}{\sqrt[4]{4\omega^2+\kappa^2}}\exp\left(-\mu\sqrt{\frac{\kappa}{2}}\sqrt{\kappa+\sqrt{4\omega^2+\kappa^2}}\right). \tag{5.4}$$

A solution for the coherence $\rho(S_m, S_n)$ can be found by numerical computation of the normalized correlation coefficient of (5.4) for various shape parameters κ and μ.

For values of the parameters μ and κ typically observed *in vivo*, $\rho(S_m, S_n)$ is shown in Fig. 5.2. As expected, the coherence decreases as the difference between κ_m and κ_n grows.

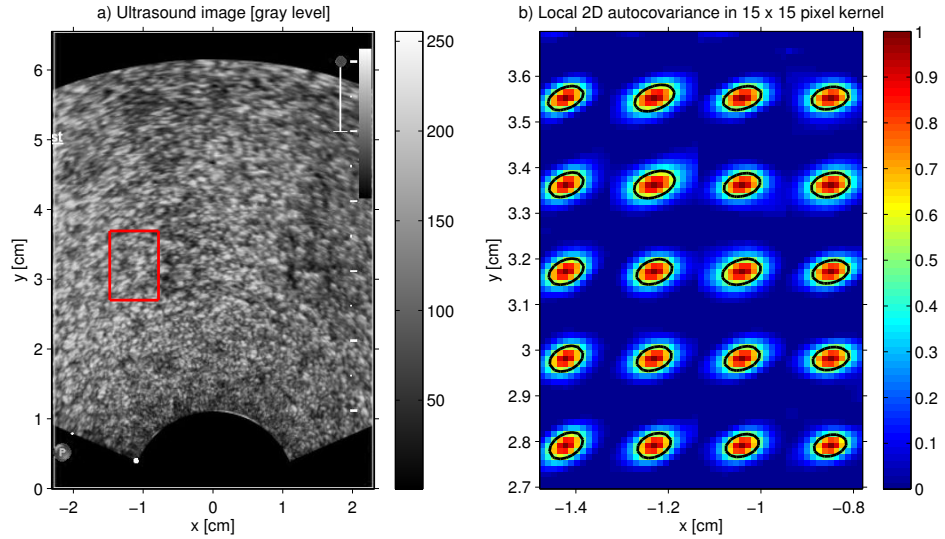

Figure 5.3 *Estimation of the axial and lateral speckle-grain size by local two-dimensional autocovariance analysis on DCE-US images of a UCA suspension in a beaker (a). From the averaged result obtained from 200 ultrasound images, contours at the half maximum level are obtained (b, zoomed in on the marked area of (a)).*

More importantly, the curves in Fig. 5.2 also demonstrate the presence of a monotonic relationship between ρ and the *average* of κ_m and κ_n. From this result, we conclude that coherence can be used as an indirect estimator of the dispersion-related parameter κ.

5.2.3 Speckle analysis and regularization

A reliable analysis of similarity among neighbor TICs requires taking the spatial resolution of the ultrasound imaging system into consideration. The axial (longitudinal) and lateral resolution are generally not equal and the lateral resolution deteriorates as the imaging depth increases [32]. As a result, the speckle-grain size is anisotropic and depth-dependent, which could affect the TIC similarity analysis. To prevent this, we propose in this paper to regularize the speckle-grain size by spatial filtering.

Commonly used ultrasound image filters improve the visual image quality using nonlinear (e.g. median filtering [33]) or adaptive techniques [32, 34, 35]. While adaptive filtering may lead to undesired effects in the subsequent analysis, most nonlinear filters are based on first-order noise statistics and not designed for speckle regularization.

To design a spatial filter for speckle regularization, we consider the ultrasound images as spatially uncorrelated images (white noise) that are low-pass filtered by a Gaussian kernel $H(\sigma_{\text{ax}}, \sigma_{\text{lat}})$. The parameters σ_{ax} and σ_{lat}, which measure the axial and lateral speckle-grain size, respectively, were estimated based on *in vitro* experiments, which were described in [26].

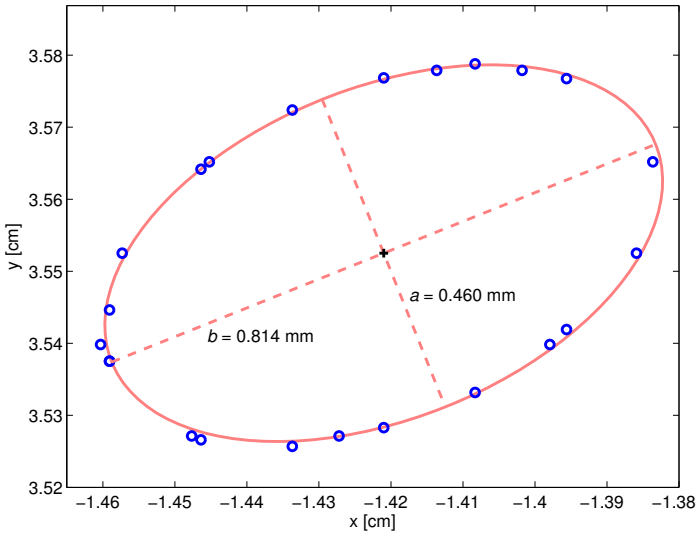

Figure 5.4 *Estimation of the local axial and lateral speckle-grain size components a and b fitting an ellipse to a local contour obtained by two-dimensional autocovariance analysis as shown in Fig. 5.3.*

For these experiments, DCE-US images were recorded from static UCA dispersions using the same settings that were used *in vivo*. An example is shown in Fig. 5.3a. These images feature fully developed speckle, because microbubbles are much smaller than the imaging wavelength and usually present in large numbers per resolution cell. In such images, the speckle-grain size can be estimated as the full-width at half maximum (FWHM) of the normalized two-dimensional autocovariance function. In fact, the spatial resolution of the ultrasound imaging system is characterized by such analysis [32, 36]. This analysis was performed for 200 DCE-US images in local image regions spanning 15 x 15 pixels (with a pixel dimension of about 0.15 mm), as shown in Fig. 5.3b. Also shown are contour points obtained at the half maximum level.

By least-squares fitting of an ellipse oriented along the axial and lateral axes to these contour points, we estimated the local axial and lateral speckle-grain size parameters a and b. This is shown in Fig. 5.4.

The parameters a and b are shown as a function of the imaging depth in Fig. 5.5. As expected, the estimated axial speckle-grain size a is independent of the depth. The obtained constant value (0.47 mm) closely resembles the theoretical value derived from the transmitted pulse length (0.43 mm). The estimated lateral speckle-grain size b increases with the imaging depth. This observation is in line with a loss in lateral resolution at larger depths, resulting from the combined effect of increased beam width and decreased line density.

The model parameters σ_{ax} and σ_{lat} are determined directly from a and b. A constant value was adopted for σ_{ax}, and a linearly increasing function of the imaging depth d was adopted for σ_{lat}, because the parameter b is accurately approximated ($R^2 = 0.95$) by such linear

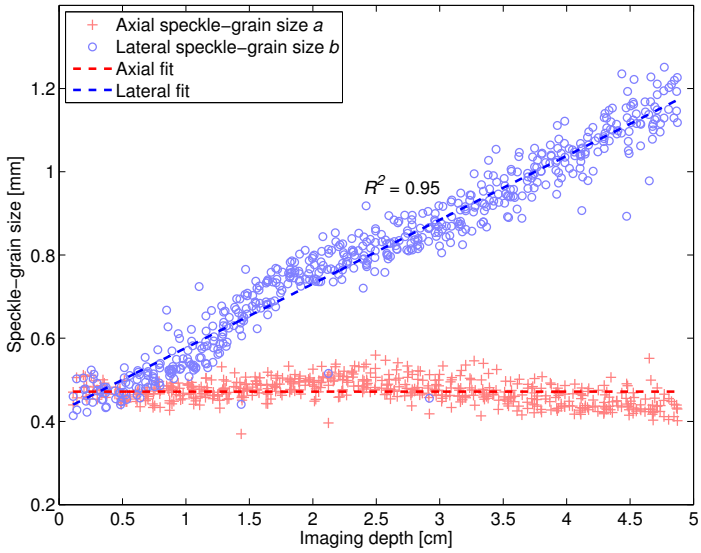

Figure 5.5 *Axial and lateral speckle-grain size a and b as a function of depth, along with a constant approximation for the axial component a and a linear approximation for the lateral component b.*

function, as shown in Fig. 5.5. The exact values of σ_{ax} and σ_{lat} are obtained by determining those values that reproduce the results of Fig. 5.5 in simulations. An optimal approximation was found for $\sigma_{\text{ax}} = 0.156$ mm and $\sigma_{\text{lat}} = 0.142 + 0.0054\ d$ mm.

The spatial filter design aims at reducing the anisotropy and the depth dependency of the speckle-grain size. To this end, we have adopted a Wiener deconvolution of $H(\sigma_{\text{ax}}, \sigma_{\text{lat}})$ [37], which theoretically reduces the speckle-grain size up to the pixel dimension. Such reduction, however, leads to a lower SNR and is in fact not necessary for the spatial similarity analysis. The SNR loss is controlled by adding a low-pass filter that is designed to replace $H(\sigma_{\text{ax}}, \sigma_{\text{lat}})$ with a known isotropic and homogeneous filter. We adopted an isotropic Gaussian filter $H_{\text{d}}(\sigma_{\text{d}})$ such that the achieved speckle-grain size will be completely determined by σ_{d}.

The complete speckle regularization filter H_{reg} is derived in the frequency domain as

$$H_{\text{reg}}(\sigma_{\text{d}}) = \frac{H_{\text{d}}(\sigma_{\text{d}}) H^*(\sigma_{\text{ax}}, \sigma_{\text{lat}})}{|H(\sigma_{\text{ax}}, \sigma_{\text{lat}})|^2 + \text{NSR}}. \tag{5.5}$$

The parameter NSR $= 1/\text{SNR}$ controls the stability of the Wiener deconvolution. Since too high NSR values can affect the speckle regularization, we selected NSR $= 10^{-3}$ as an optimal trade-off by experimental testing. To enable TIC similarity analysis at the order of a millimeter, we adopted $\sigma_{\text{d}} = 0.25$ mm. This value results in limited smoothing in areas close to the ultrasound probe and some image sharpening at larger depths, which can be seen by comparing Fig. 5.3a and Fig. 5.6a. After filtering, the axial and lateral speckle-grain sizes in the static ultrasound images are comparable and nearly constant with respect to d.

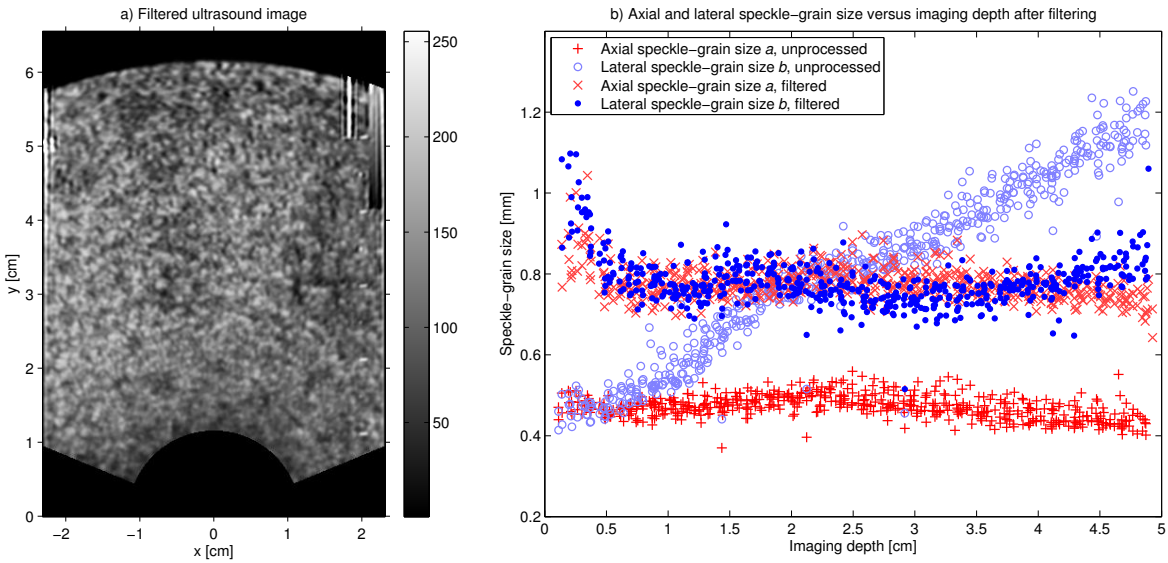

Figure 5.6 *Results of speckle regularization filtering, showing a DCE-US image of a UCA suspension in a beaker after filtering (a) and the obtained axial and lateral speckle-grain size a and b as a function of depth (b).*

This is shown in Fig. 5.6b.

To investigate how the proposed spatial filter influences the similarity analysis, we compared the results of the TIC similarity analysis with those obtained by using standard Gaussian filtering, as adopted by [26]. In particular, we evaluated the influence of filtering on coherence as function of the imaging depth. All parametric images obtained for ρ were analyzed by dividing all pixel values into 10 subgroups, each covering a range of 0.5 cm. In each subgroup, we evaluated the mean and standard deviation of the difference between the similarity obtained by both filters.

5.2.4 Windowing for similarity analysis

Before applying the spatial TIC similarity analysis, a window, i.e., time segment, is first selected for each TIC. The purpose of windowing is to make the analysis more specific to TIC shape variations by capturing the period representing the UCA bolus passage. In addition, windowing adds standardization to the method.

The adopted time window has a length of 35 s and starts at the TIC appearance time, t_{app}, that is, the first time microbubbles are present locally. At each pixel, t_{app} is estimated as the first time at which the log-compressed TIC achieves 10% of its peak value, as shown in Fig. 5.7.

The robustness of appearance time detection is improved by median filtering of each TIC in time. The blocksize is equivalent to five seconds in order to remove noise spikes, due to e.g. microbubbles from a previous UCA injection. Remaining errors are further reduced by

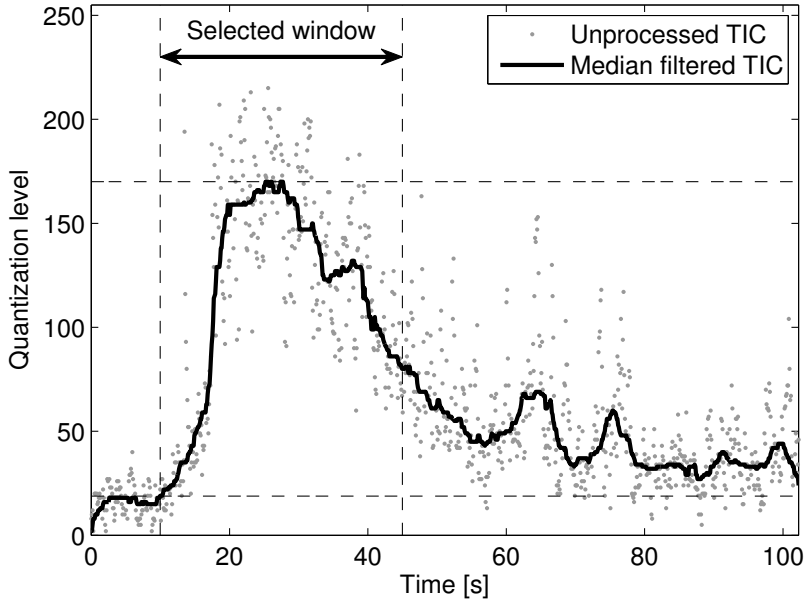

Figure 5.7 *Wash-in and wash-out kinetics and time-window selection in a TIC observed* in vivo.

two-dimensional spatial median filtering of the detected appearance time with a blocksize of 5 x 5 pixels.

Because optimizing the time-domain window is not straightforward, we determined the optimal window by comparing the cancer detection performance for various window lengths and starting times, relative to the appearance time. To investigate the overall effect of windowing on the similarity analysis, we also compared the coherence results to those obtained in [26], i.e., without windowing. The results of both comparisons are reported in the Results section.

5.2.5 Spatial TIC similarity analysis

After spatial filtering, time windowing, and data linearization, a local spatial TIC similarity analysis is performed for all pixels covering the prostate. At each pixel, the average coherence is computed between the local TIC and all TICs in a ring-shaped kernel that contains surrounding pixels at distances between 1.0 and 2.5 mm [26]. By choosing an isotropic kernel, we exploit the isotropic nature of the dispersive process with respect to the convective process in (5.1), such that the analysis becomes independent of any possible dominant perfusion direction. The kernel dimensions are based on the obtained speckle-grain size ($4\sigma_d = 1.0$ mm) and the scale at which early angiogenesis occurs [5], respectively.

Prior to the analysis, the prostate boundary is determined by a manual ROI selection. By displaying the coherence at each pixel as a color-code value overlaid on the ultrasound image, we obtain a parametric dispersion image. As a postprocessing step, this image is

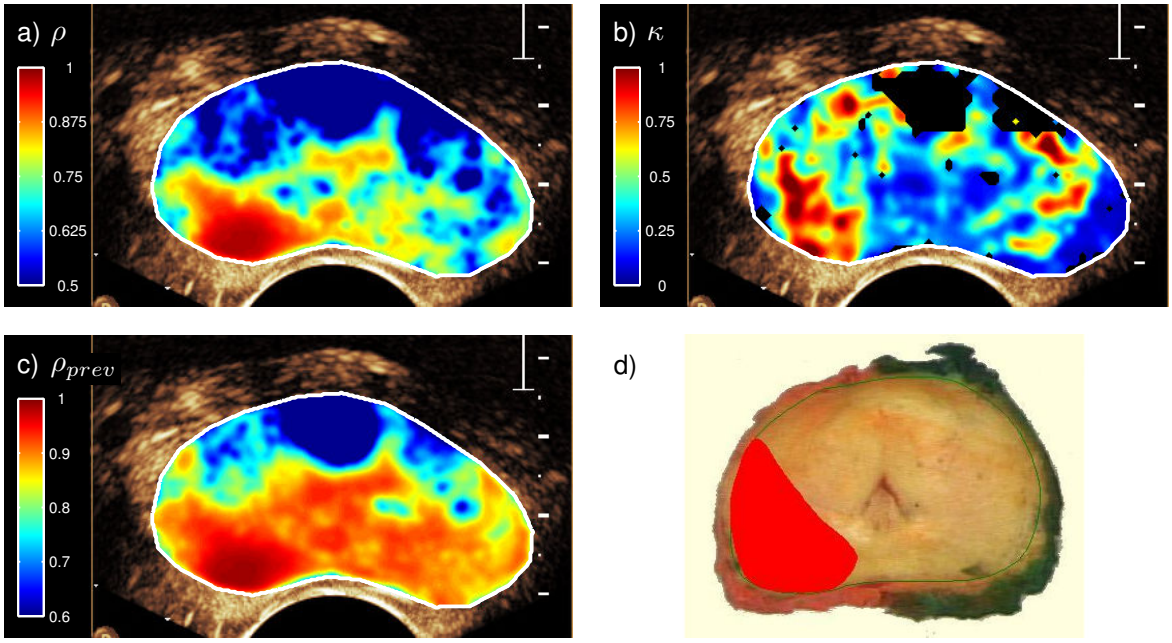

Figure 5.8 *Parametric dispersion images of the prostate based on coherence analysis as described in this paper (ρ, a), the dispersion-related TIC parameter κ (b) [25], and coherence analysis as described by [26] (ρ_{prev}, c). The corresponding histology slice (d) with carcinoma marked in red is also shown.*

filtered with a Gaussian kernel ($\sigma = 0.5$ mm). Because only tumors larger than 1 mm^3 require angiogenesis for growth [5], details at smaller scales are removed. A parametric dispersion image based on coherence is shown in Fig. 5.8a. For comparison, the corresponding parametric images based on the dispersion-related parameter κ and coherence ρ_{prev} obtained by the methodology of [26] are shown in Figures 5.8b and 5.8c, respectively.
Because the pixel size (about 0.15 mm) is smaller than the parameter σ_{d} that characterizes the speckle-grain size, spatial downsampling can be adopted to reduce the computation time. To prevent spatial aliasing, downsampling is constrained by a maximum pixel size $2\sigma_{\text{d}} = 0.5$ mm. In most datasets, this results in a downsampling factor of three. The complete analysis is implemented in MATLAB ® (The MathWorks, Natick, MA). On a 64-bits Windows 7 workstation with an Intel® Core2Duo processor running at 3.16 GHz with 8 GB of RAM, processing of one DCE-US dataset (usually containing about 1000 frames) takes about four minutes, of which about 50% is required for spatial filtering.

5.2.6 Preliminary clinical validation

To evaluate the cancer localization potential of the proposed analysis, the imaging results were compared with histology results for 12 datasets recorded from 8 patients that underwent radical prostatectomy at the AMC Unversity Hospital, Amsterdam, The Netherlands.

After radical prostatectomy, the prostate was fixed and divided into slices with a thickness of 4 mm. In each slice, the presence of cancer was evaluated by a pathologist as described by [38]. In Fig. 5.8d, the histology section corresponding to the parametric dispersion images of Figures 5.8a-c is shown.
Based on the histology results, we selected two regions of interest (ROIs) of about 0.5 cm^2 in each parametric dispersion image to represent healthy and cancerous tissue. Because clinically significant tumors have a volume of at least 0.5 cm^3 [38], we only considered relatively large regions of either cancerous or healthy tissue in the peripheral zone of the prostate that extended through several histology slices. By this procedure, the validation results are less sensitive to any mismatches between the ultrasound plane and the histology slices. The ROIs of all patients were combined to create two datasets, representing healthy and cancerous tissue, containing a total of about 60×10^3 pixels.
With these data, a statistical analysis was performed to evaluate the pixel classification ability of CUDI. From the datasets representing cancerous and healthy tissue, histograms of coherence were computed for each tissue class and the receiver operating characteristic (ROC) curve was derived based on the histology ground truth [39]. The optimal classification threshold was then obtained by finding the point on the ROC curve with the smallest Euclidian distance to the optimum, representing 100% sensitivity and specificity. With this threshold, we determined the optimal sensitivity and specificity for pixel classification.
Using this statistical analysis, we compared the performance for the coherence ρ with that obtained by the coherence ρ_{prev} as described by [26], by the local, dispersion-related LDRW parameter κ [25] and by a number of perfusion-related parameters proposed in the literature [18–20]. These included AUC, mean transit time (MTT), peak time (PT), peak intensity (PI), wash-in time (WIT, i.e., the time period between UCA appearance and peak intensity), appearance time (AT), and FWHM of the TIC.

5.3 Results

5.3.1 Effects of spatial filtering and windowing

The influence of the speckle regularization filter on the similarity analysis was evaluated by comparing the obtained coherence ρ with that obtained by Mischi *et al.* [26], i.e., after standard Gaussian filtering with $\sigma = 0.25$ mm. We observed an average decrease in coherence when the speckle regularization filter was applied, as compared the use of standard Gaussian filtering. This decrease was generally stronger for larger depths, as shown in Fig. 5.9.
The effect of time windowing on the coherence analysis is also shown in Fig. 5.9. For

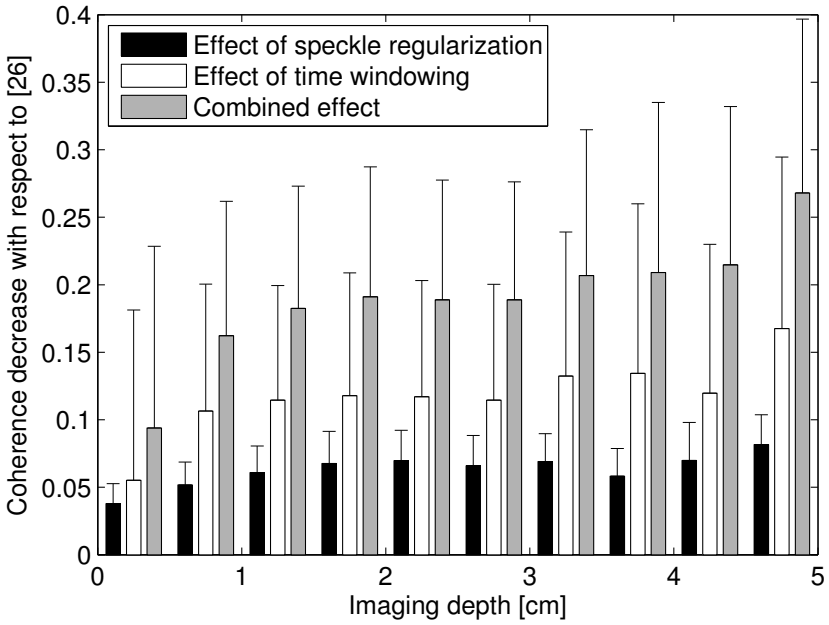

Figure 5.9 *Effect of speckle regularization and time windowing on the obtained coherence level as a function of depth, based on all parametric dispersion images. The mean coherence decrease resulting from speckle regularization (black), time windowing (white) and both techniques (gray) are shown as function of depth, with respect to the coherence level ρ_{prev} obtained with Gaussian filtering ($\sigma = 0.25$ mm) and without time windowing [26]. Errorbars represent the standard deviation.*

Table 5.1 *Area under ROC curve for pixel classification obtained by coherence analysis for various window lengths and starting times with respect to the local TIC appearance time t_{app}.*

Window length [s]	Window starting time [s]			
	t_{app}	$t_{\text{app}} - 2$	$t_{\text{app}} - 5$	$t_{\text{app}} - 10$
30	0.875	0.861	0.830	0.783
35	0.880	0.869	0.855	0.792
40	0.874	0.864	0.851	0.808
45	0.862	0.856	0.853	0.816
50	0.855	0.853	0.847	0.819
60	0.840	0.840	0.839	0.823

all imaging depths, we observed an average decrease in ρ when the time window was incorporated into the analysis.

The combined effect of spatial filtering and time windowing is also shown in Fig. 5.9. In addition, it can be observed by comparing Figures 5.8a and 5.8c. The analysis result of Fig. 5.8c was obtained using the methodology of [26], i.e., without time windowing and by spatial filtering with a Gaussian kernel ($\sigma = 0.25$ mm) instead of speckle regularization.

The effect of different windowing settings on the achieved pixel classification performance is

Table 5.2 *Classification performance of different TIC parameters on a pixel basis.*

Parameter	Sensitivity [%]	Specificity [%]	ROC curve area
ρ	78.1	81.6	0.88
ρ_{prev}	67.2	79.1	0.82
κ	66.6	68.7	0.70
AUC	44.0	70.9	0.61
PI	43.7	79.2	0.65
PT	53.0	79.6	0.70
AT	52.8	64.4	0.60
FWHM	74.4	70.7	0.76
WIT	66.7	65.0	0.72
MTT	53.2	82.1	0.70

reported in Table 5.1. The average area under the ROC curve achieved by the coherence ρ is reported for several window lengths and starting times. Optimal classification (ROC curve area of 0.880) was achieved with a 35-s window starting at the TIC appearance time t_{app}. In comparison, the obtained ROC curve area was 0.818 if windowing was not performed, i.e., if the entire TIC was used for coherence analysis.

5.3.2 Preliminary clinical validation

In all patient datasets, we observed an increased coherence in the presence of cancer. The mean coherence ρ measured in ROIs representing cancerous and healthy tissue was 0.78 ± 0.13 and 0.56 ± 0.14, respectively. Table 5.2 lists the optimal classification threshold, sensitivity, specificity and ROC curve area for all parameters. In addition, the ROC curves are shown in Fig. 5.10.

5.4 Discussion

The current diagnostic limitations that hamper prostate cancer care could be overcome by reliable angiogenesis detection, but the associated microvascular changes are complex and difficult to detect by imaging of perfusion. Recently, we have proposed an alternative characterization of the microvascular architecture based on analysis of the UCA dispersion kinetics. Dispersion estimation was performed either by curve-fitting of TICs [25] or by analysis of the spatial TIC similarity [26].

This paper focuses on the analysis of spatial TIC similarity, since it offers several advantages with respect to most methods that perform TIC parameter estimation in the time domain. A fundamental advantage is the analysis of UCA kinetics in both space and time.

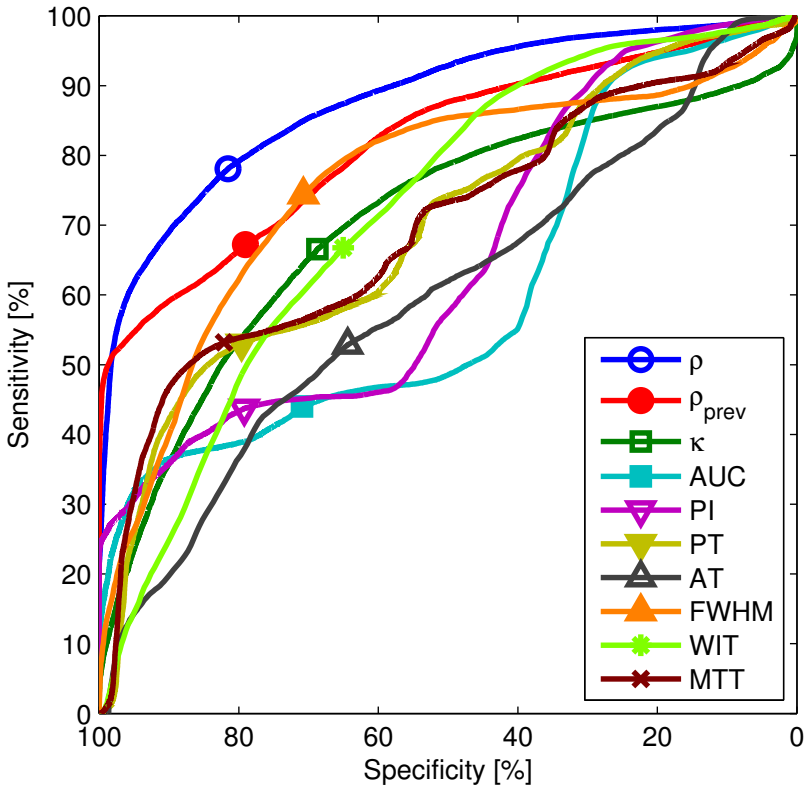

Figure 5.10 *Receiver-operating-characteristic curves for pixel classification for the coherence ρ, the coherence ρ_{prev} as described by [26], the dispersion-related TIC parameter κ, and several perfusion-related TIC parameters. On each curve, a marker is placed at the point representing optimal sensitivity and specificity.*

In fact, whereas most TIC parameters are influenced by the entire path from UCA injection to the detection site, the spatial similarity analysis provides a local assessment. By using normalized similarity measures, the analysis is also inherently normalized and, therefore, more robust to distortions, such as nonlinear attenuation, than TIC amplitude features. In addition, curve-fitting and isolation of the bolus first pass are not required.

In this work, we present the physical rationale for a dispersion analysis by assessment of spatial TIC similarity. To derive the relation between dispersion and TIC similarity, we have considered two TICs represented by the LDRW model. TIC similarity, as given by the coherence ρ, is investigated as a function of the dispersion-related LDRW model parameter κ. By confirming that higher values of κ lead to a higher coherence, the results shown in Fig. 5.2 provide the formal basis for the characterization of dispersion by assessment of TIC similarity. The coherence levels measured *in vivo* are generally lower than those in Fig. 5.2. This is likely due to the limited SNR of TICs measured *in vivo*. The similarity analysis could be extended by the use of alternative similarity measures in a future study.

The results of the preliminary validation are in agreement with the obtained monotonic

relationship between κ and ρ, since both parameters show an increase in cancer tissue relative to healthy tissue. This can also be observed by comparing Figures 5.8a and 5.8b. This increase in κ and ρ is in line with our previous finding of a lower dispersion, relative to convection, in the presence of angiogenesis. The lower dispersion might be caused by a higher tortuosity of the newly formed microvessels [23, 24]. In future work, the relation between dispersion and microvascular architecture will be studied in more detail by *in vitro* phantom studies.

In this paper, we also describe two methodological improvements that are designed to make the spatial similarity analysis more specific to TIC shape variations. By incorporating spatial filtering for speckle regularization and TIC time windowing, the spatial TIC similarity analysis provides a better estimation of contrast-agent dispersion.

The analysis of spatial similarity in ultrasound images is generally affected by ultrasound speckle noise. We have addressed this issue by prefiltering the DCE-US images with a dedicated speckle regularization filter. As an alternative to filtering, the dimensions of the spatial similarity kernel could have been locally adapted to the local speckle parameters a and b to reduce the sensitivity to the local speckle characteristics. This approach would however lead to an anisotropic kernel, which is less suited for a similarity analysis that focuses on isotropic dispersion rather than anisotropic convection.

The spatial filter design methodology, which is based on local estimation of the speckle-grain size, is also applicable for different transducers. It is, however, not optimized for spatial resolution enhancement, which is typically performed by deconvolution in the radiofrequency domain [40]. By balancing between sharpening and smoothing, the adopted filter is achieves an approximately constant and isotropic speckle-grain size that is sufficiently small for the subsequent similarity analysis. Filtering also increases the SNR, although the improvement is not homogeneous; it is larger in areas where more smoothing is performed, i.e., close to the probe.

The results shown in Fig. 5.9 indicate that the speckle regularization filter has only a limited influence on the coherence estimation. A significant part of the decrease is due to the lower filter order: the effective axial filter order was decreased from 0.25 mm to $\sqrt{\sigma_{\mathrm{d}}^2 - \sigma_{\mathrm{ax}}^2} = 0.195$ mm. The lateral speckle-grain size reduction causes an additional coherence decrease as the depth increases.

Spatial filtering does not have a significant impact on the tissue classification results. This is mainly because the validation was limited to peripheral zone of the prostate, where the majority of cancer is found [7]. This zone is very close to the probe, i.e., where the effect of filtering on coherence is small.

TIC time windowing is applied to make the analysis more specific to the underlying hemodynamic parameters that govern the UCA kinetics. By isolating relevant TIC segments,

the sensitivity of the similarity analysis to TIC noise is decreased. As a result, windowing enables a better estimation of TIC shape variations, and therefore, dispersion. Because optimization of the window settings is not straightforward, we adopted those settings that optimized the pixel classification performance. The main effect of time windowing, explaining most differences between Figures 5.8a and 5.8c, is a reduction in the coherence level in image regions where a high level was not caused by similarity of the underlying hemodynamics.

Overall, spatial filtering and TIC time windowing result in a lower average coherence ρ compared to ρ_{prev} in both tissue types, as shown in Fig. 5.9. In a preliminary validation, the area under the ROC curve for the pixel classification was increased from 0.82 to 0.88. This improvement was almost exclusively the result of TIC time windowing.

The preliminary validation was limited to the peripheral zone of the prostate. Given its fundamentally local nature, the proposed spatial similarity analysis might perhaps also be useful for analysis of other anatomical zones of the prostate, such as the transition zone, that have different microvascular characteristics.

In the future, the clinical validation could be extended and the use of dedicated image registration methods could reduce the positional discrepancy between ultrasound and histology slices. In this regard, significant improvements could possibly also be provided by three-dimensional DCE-US imaging, which would also enable new alternatives for modeling and analysis of the UCA kinetics.

A more accurate validation may also comprise the use of immunohistology. With such a validation, dispersion can possibly be compared directly with the microvascular characteristics, rather than the level of cell differentiation measured by the Gleason score in regular histology analysis [41].

5.5 Conclusions

Characterization of ultrasound-contrast-agent dispersion by analysis of the similarity among neighbor time-intensity curves shows promising preliminary results for prostate cancer localization. In this work, we investigated the relation between dispersion and TIC similarity by analysis of the coherence ρ between LDRW TICs. The resulting positive correlation between the dispersion-related TIC parameter κ and TIC similarity was confirmed in the preliminary validation. Dedicated spatial filtering and TIC time windowing are proposed to increase the robustness of the similarity analysis, by making it less sensitive to anisotropic ultrasound speckle and TIC noise, respectively.

References

[1] American Cancer Society, "Cancer facts & figures," Atlanta, 2012.

[2] C. H. Bangma, S. Roemeling, and F. H. Schröder, "Overdiagnosis and overtreatment of early detected prostate cancer," *World J. Urol.*, vol. 25, pp. 3–9, 2007.

[3] T. J. Polascik and V. Mouraviev, "Focal therapy for prostate cancer," *Curr. Opin. Urol.*, vol. 18, pp. 269–274, 2008.

[4] N. Weidner, P. R. Carroll, J. Flax, W. Blumenfeld, and J. Folkman, "Tumor angiogenesis correlates with metastasis in invasive prostate carcinoma," *Am. J. Pathol.*, vol. 143, no. 2, pp. 401–409, 1993.

[5] M. K. Brawer, "Quantitative microvessel density. A staging and prognostic marker for human prostatic carcinoma," *Cancer*, vol. 78, no. 2, pp. 345–349, 1996.

[6] S. A. Bigler, R. E. Deering, and M. K. Brawer, "Comparison of microscopic vascularity in benign and malignant prostate tissue," *Hum. Pathol.*, vol. 24, no. 2, pp. 220–226, 1993.

[7] M. Seitz, A. Shukla-Dave, A. Bjartell *et al.*, "Functional magnetic resonance imaging in prostate cancer," *Eur. Urol.*, vol. 55, pp. 801–814, 2009.

[8] M. Smeenge, M. Mischi, M. Laguna Pes, J. de la Rosette, and H. Wijkstra, "Novel contrast-enhanced ultrasound imaging in prostate cancer," *World J. Urol.*, vol. 29, pp. 581–587, 2011.

[9] G. Russo, M. Mischi, W. Scheepens, J. de la Rosette, and H. Wijkstra, "Angiogenesis in prostate cancer: onset, progression and imaging," *BJU Int.*, vol. 110, pp. E794–E808, 2012.

[10] S. B. Feinstein, "The powerful microbubble: from bench to bedside, from intravascular indicator to therapeutic delivery system, and beyond," *Am. J. Physiol. Heart Circ. Physiol.*, vol. 287, no. 2, pp. H450–H457, 2004.

[11] N. de Jong, P. J. A. Frinking, A. Bouakaz, and F. J. ten Cate, "Detection procedures of ultrasound contrast agents," *Ultrasonics*, vol. 38, no. 1–8, pp. 87–92, 2000.

[12] M. Lamuraglia, S. L. Bridal, M. Santin *et al.*, "Clinical relevance of contrast-enhanced ultrasound in monitoring anti-angiogenic therapy of cancer: current status and perspectives," *Crit. Rev. Oncol. Hematol.*, vol. 73, no. 3, pp. 202–212, 2010.

[13] D. Cosgrove and N. Lassau, "Imaging of perfusion using ultrasound," *Eur. J. Nucl. Med. Mol. Imaging*, vol. 37, pp. 65–85, 2010.

[14] K. Wei, A. R. Jayaweera, S. Firoozan *et al.*, "Quantification of myocardial blood flow with ultrasound-induced destruction of microbubbles administered as a constant venous infusion," *Circulation*, vol. 97, pp. 473–483, 1998.

[15] M. Krix, F. Kiessling, N. Farhan *et al.*, "A multivessel model describing replenishment kinetics of ultrasonics contrast agent for quantification of tissue perfusion," *Ultrasound Med. Biol.*, vol. 29, no. 10, pp. 1421–1430, 2003.

[16] M. Arditi, P. J. A. Frinking, X. Zhou, and N. G. Rognin, "A new formalism for the quantification of tissue perfusion by the destruction-replenishment method in contrast ultrasound imaging," *IEEE Trans. Ultrason., Ferroelectr., Freq. Control*, vol. 53, no. 6, pp. 1118–1129, 2006.

[17] J. M. Hudson, R. Karshafian, and P. N. Burns, "Quantification of flow using ultrasound and microbubbles: a disruption replenishment model based on physical principles," *Ultrasound Med. Biol.*, vol. 35, no. 12, pp. 2007–2020, 2009.

[18] R. J. Eckersley, J. P. Sedelaar, M. J. K. Blomley *et al.*, "Quantitative microbubble enhanced transrectal ultrasound as a tool for monitoring hormonal treatment of prostate carcinoma," *Prostate*, vol. 51, pp. 256–267, 2002.

[19] N. Elie, A. Kaliski, P. Péronneau *et al.*, "Methodology for quantifying interactions between perfusion evaluated by DCE-US and hypoxia throughout tumor growth," *Ultrasound Med. Biol.*, vol. 33, no. 4, pp. 549–560, 2007.

[20] C. Strouthos, M. Lampaskis, V. Sboros, A. McNeilly, and M. Averkiou, "Indicator dilution models for the quantification of microvascular blood flow with bolus administration of ultrasound contrast agents," *IEEE Trans. Ultrason., Ferroelectr., Freq. Control*, vol. 57, no. 6, pp. 1296–1310, 2010.

[21] M.-X. Tang, H. Mulvana, T. Gauthier *et al.*, "Quantitative contrast-enhanced ultrasound imaging: a review of sources of variability," *Interface Focus*, vol. 1, no. 4, pp. 520–539, 2011.

[22] M.-X. Tang and R. J. Eckersley, "Nonlinear propagation of ultrasound through microbubble contrast agents and implications for imaging," *IEEE Trans. Ultrason., Ferroelectr., Freq. Control*, vol. 53, no. 12, pp. 2406–2415, 2006.

[23] S. Delorme and M. V. Knopp, "Non-invasive vascular imaging: assessing tumour vascularity," *Eur. Radiol.*, vol. 8, pp. 517–527, 1998.

[24] A. Eberhard, S. Kahlert, V. Goede *et al.*, "Heterogeneity of angiogenesis and blood vessel maturation in human tumors: implications for antiangiogenic tumor therapies," *Cancer Res.*, vol. 60, no. 5, pp. 1388–1393, 2000.

[25] M. P. J. Kuenen, M. Mischi, and H. Wijkstra, "Contrast-ultrasound diffusion imaging for localization of prostate cancer," *IEEE Trans. Med. Imag.*, vol. 30, no. 8, pp. 1493–1502, 2011.

[26] M. Mischi, M. P. J. Kuenen, and H. Wijkstra, "Angiogenesis imaging by spatiotemporal analysis of ultrasound-contrast-agent dispersion kinetics," *IEEE Trans. Ultrason., Ferroelectr., Freq. Control*, vol. 59, no. 4, pp. 621–629, Apr. 2012.

[27] M. Mischi, A. H. M. Jansen, and H. H. M. Korsten, "Identification of cardiovascular dilution systems by contrast ultrasound," *Ultrasound Med. Biol.*, vol. 33, no. 3, pp. 439–451, 2007.

[28] C. W. Sheppard, *Basic principles of the tracer method*. New York: John Wiley and Sons, 1962.

[29] K. H. Norwich and S. Zelin, "The dispersion of indicator in the cardio-pulmonary system," *Bull. Math. Biophys.*, vol. 32, pp. 25–43, 1970.

[30] G. Taylor, "Dispersion of soluble matter in solvent flowing slowly through a tube," *Proc. R. Soc. A*, vol. 219, pp. 186–203, 1953.

[31] Y.-C. Fung, *Biodynamics: circulation*, 1st ed. Berlin: Springer, 1984.

[32] R. S. C. Cobbold, *Foundations of biomedical ultrasound*. Oxford: Oxford University Press, 2007.

[33] T. Huang, G. Yang, and G. Tang, "A fast two-dimensional median filtering algorithm," *IEEE Trans. Acoust., Speech, Signal Process.*, vol. 27, no. 1, pp. 13–18, feb 1979.

[34] J. Bamber and C. Daft, "Adaptive filtering for reduction of speckle in ultrasonic pulse-echo images," *Ultrasonics*, vol. 24, no. 1, pp. 41–44, 1986.

[35] O. V. Michailovic and A. Tannenbaum, "Despeckling of medical ultrasound images," *IEEE Trans. Ultrason., Ferroelectr., Freq. Control*, vol. 53, no. 1, pp. 64–78, 2006.

[36] R. F. Wagner, S. W. Smith, J. M. Sandrik, and H. Lopez, "Statistics of speckle in ultrasound B-scans," *IEEE Trans. Sonics Ultrason.*, vol. 30, no. 3, pp. 156–163, 1983.

[37] A. K. Jain, *Fundamentals of digital image processing*. Englewood Cliffs, NJ: Prentice Hall, 1989.

[38] R. Montironi, T. van der Kwast, L. Boccon-Gibod, A. V. Bono, and L. Boccon-Gibod, "Handling and pathology reporting of radical prostatectomy specimens," *Eur. Urol.*, vol. 44, pp. 626–636, 2003.

[39] M. H. Zweig and G. Campbell, "Receiver-operating characteristic (ROC) plots: a fundamental evaluation tool in clinical medicine," *Clin. Chem.*, vol. 39, pp. 561–577, 1993.

[40] R. Jirik and T. Taxt, "Two-dimensional blind bayesian deconvolution of medical ultrasound images," *IEEE Trans. Ultrason., Ferroelectr., Freq. Control*, vol. 55, no. 10, pp. 2140–2153, october 2008.

[41] D. F. Gleason, "Classification of prostatic carcinoma," *Cancer Chemother. Rep.*, vol. 50, pp. 125–128, 1966.

CHAPTER 6

Spatiotemporal correlation analysis for dispersion assessment

Based on: M. P. J. Kuenen, T. A. Saidov, H. Wijkstra, and M. Mischi, "Spatiotemporal correlation of ultrasound-contrast-agent dilution curves for angiogenesis localization by dispersion imaging," *IEEE Transactions on Ultrasonics, Ferroelectrics, and Frequency Control*, vol. 60, no. 12, pp. 2665–2669, © IEEE, 2013.

Abstract – *The major role of angiogenesis in cancer development has driven many researchers to investigate the prospects of noninvasive cancer imaging based on assessment of microvascular perfusion. The limited results so far may be caused by the complex and contradictory effects of angiogenesis on perfusion. Alternatively, assessment of ultrasound-contrast-agent dispersion kinetics, resulting from features such as density and tortuosity, has shown a promising potential to characterize angiogenic effects on the microvascular structure. This method, referred to as contrast-ultrasound dispersion imaging (CUDI), is based on contrast-enhanced ultrasound imaging after an intravenous contrast-agent bolus injection. In this paper, we propose a new spatiotemporal correlation analysis to perform CUDI. We provide the rationale for indirect estimation of local dispersion by deriving the analytical relation between dispersion and the correlation coefficient among neighboring time-intensity curves obtained at each pixel. This robust analysis is inherently normalized and does not require curve-fitting. In a preliminary validation of the method for localization of prostate cancer, the results of this analysis show superior cancer localization performance (receiver-operating-characteristic curve area of 0.89) than those of previously reported CUDI implementations and perfusion estimation methods.*

6.1 Introduction

Angiogenesis is a complex physiological process involved in the development of various pathologies. Angiogenesis supports the growth of neoplastic tissue by forming a dense microvascular network. Particularly relevant is its fundamental role in cancer growth [1]. The microvascular structure resulting from angiogenesis is characterized by a high density of small-diameter vessels with a high tortuosity and permeability, producing extravascular leakage [2]. In histological studies, the assessment of microvascular density (MVD) has been reported to correlate with cancer prognosis [2].

Angiogenesis imaging with the objective of cancer detection has been pursued in many studies [3]. In this context, dynamic contrast-enhanced ultrasound (DCE-US) is an attractive imaging modality because of its ability to measure signals backscattered from within the smallest vessels [4]. The adopted ultrasound contrast agents (UCAs) are coated gas microbubbles. The strongly nonlinear interaction between ultrasound waves and microbubbles can be exploited to suppress the mostly linear backscattering from tissue [5]. The obtained contrast-specific imaging techniques enable dynamic measurement of the passage of an intravenously injected UCA bolus through the image plane. Alternatively, with the destruction-replenishment technique, reperfusion can be measured after disrupting all microbubbles in the imaging plane with a high-intensity burst [6, 7].

Several researchers have reported the assessment of microvascular perfusion by DCE-US imaging for detection of angiogenesis [8–10]. Perfusion is typically estimated from time-intensity curves (TICs) that measure the backscattered acoustic intensity in a region of interest (ROI) in the ultrasound image as a function of time.

Up until now, quantitative DCE-US imaging of perfusion has however not led to reliable cancer detection. This may be due to the difficulty in the interpretation of local microvascular perfusion from the estimated parameters [11]. Nonlinear attenuation and scanner settings may affect TIC amplitude features; timing parameters generally depend on the entire history of the bolus transport and are, therefore, difficult to interpret locally. A more fundamental issue concerns the complex effects of angiogenic microvascular changes on perfusion: although an increased MVD may lead to increased perfusion, this increase can be counteracted by the increased interstitial pressure and vessel tortuosity [12].

Contrast-ultrasound dispersion imaging (CUDI) has been proposed as an alternative characterization of the microvascular changes caused by angiogenesis [13]. CUDI models the UCA transport kinetics as a convective dispersion process, in which UCA dispersion results directly from structural features, such as density and tortuosity. In the original method, dispersion was estimated by parametric curve-fitting of TICs obtained at each pixel after an intravenous UCA bolus injection [13].

A more recent, spatiotemporal dispersion analysis involved the assessment of the similarity

among TICs measured at neighboring pixels by coherence analysis in the frequency domain [14]. Different from existing quantification methods, this spatial similarity analysis inherently provides a local and normalized assessment. Moreover, it does not require curve-fitting and isolation of the first passage of the UCA bolus.

This paper builds upon the spatiotemporal analysis described in [14]. Alternative to the previous coherence analysis, TIC similarity is estimated in the time domain by the TIC correlation coefficient. The physical rationale for this spatiotemporal correlation analysis is provided by an analytical relation between dispersion and the correlation coefficient between TICs.

The proposed method was validated by evaluating its performance for prostate cancer localization. Prostate cancer is the most common form of cancer in western men [15]. The diagnosis is currently based on systematic biopsies, as the development of diagnostic imaging methods for prostate cancer has proven highly challenging [16]. In the present validation, parametric dispersion images obtained from 12 DCE-US datasets of 8 patients were compared with histology, obtained after radical prostatectomy. A statistical analysis was performed to compare the cancer localization ability of different implementations of CUDI with that of previously reported perfusion analysis methods.

6.2 Materials and Methods

6.2.1 Dispersion and TIC correlation

The theoretical basis for analysis of UCA dispersion kinetics is provided by modeling the UCA transport through the microcirculation as a convective dispersion process [17, 18], as

$$\frac{\partial C(\mathbf{x},t)}{\partial t} = \nabla \cdot \left[D(\mathbf{x}) \nabla C(\mathbf{x},t) - \mathbf{v}(\mathbf{x}) C(\mathbf{x},t) \right]. \tag{6.1}$$

The UCA concentration dynamics $C(\mathbf{x},t)$ is represented in (6.1) in space $\mathbf{x}$ and time t, as function of the convection velocity $\mathbf{v}(\mathbf{x})$ and the UCA dispersion coefficient $D(\mathbf{x})$.

The modified local density random walk (LDRW) model is a solution of the one-dimensional case of (6.1) for locally constant parameters [13]. The UCA concentration $C(t)$ at a fixed detection site downstream after an intravenous UCA bolus injection is modeled as a function of time as

$$C(t) = \mathsf{AUC} \sqrt{\frac{\kappa}{2\pi\,(t-t_0)}} \exp\left(\frac{-\kappa\,(t-t_0-\mu)^2}{2\,(t-t_0)} \right). \tag{6.2}$$

The shape of $C(t)$ is governed by the local, dispersion-related skewness parameter $\kappa = v^2/2D$ and the mean transit time μ. The parameters AUC and t_0 represent the area under $C(t)$ and the theoretical injection time, respectively.

Similarly to common perfusion analysis techniques [8], dispersion analysis can be performed by parametric curve-fitting of (6.2) to TICs measured at each pixel [13].

As an alternative to these time-domain analysis techniques, we recently suggested a complete spatiotemporal analysis [14], in which dispersion is estimated indirectly as the spatial similarity among neighboring TICs. The similarity between TICs was estimated by their coherence, which was calculated as the normalized correlation coefficient between TIC amplitude spectra. This similarity measure is insensitive to arrival time differences and can be effectively targeted to the relatively small frequency range that is most relevant in TIC analysis.

In this paper, we propose the correlation coefficient r in the time domain as an alternative TIC similarity measure to the coherence ρ. Suitable alignment based on the UCA appearance time is provided together with dedicated TIC windowing (see Sec. 6.2.2). As a result, the subsequent similarity analysis is not affected by arrival time differences. Moreover, as opposed to coherence, the correlation coefficient includes TIC phase components that also contribute to the TIC shape, and, therefore, to the assessment of dispersion.

To enable a dispersion analysis by assessment of spatial TIC correlation, we have investigated the correlation coefficient $r(C_m, C_n)$ between two TICs $C_m(t)$ and $C_n(t)$ represented as in (6.2). The subscripts m and n refer to two close locations at which the TICs are sampled. Because of TIC alignment, $t_0 = 0$ is adopted for both $C_m(t)$ and $C_n(t)$. An analytical solution for $r(C_m, C_n)$ is given as

$$r(C_m, C_n) = \frac{\int_0^\infty \left[(C_m(t) - \bar{C}_m)(C_n(t) - \bar{C}_n)\right]\,\mathrm{d}t}{\sqrt{\int_0^\infty \left[C_m(t) - \bar{C}_m\right]^2\,\mathrm{d}t \int_0^\infty \left[C_n(t) - \bar{C}_n\right]^2\,\mathrm{d}t}} \tag{6.3}$$

$$= \frac{K_0\left(\sqrt{\kappa_m + \kappa_n}\sqrt{\kappa_m\mu_m^2 + \kappa_n\mu_n^2}\right)}{\sqrt{K_0(2\kappa_m\mu_m)K_0(2\kappa_n\mu_n)}}. \tag{6.4}$$

In (6.3), $\bar{C}$ is the mean value of $C(t)$ over the time-interval $[0, \infty]$. In (6.4), the function $K_0(\cdot)$ represents the modified Bessel function of the second kind.

As expected, the resulting analytical relation depends only on the shape parameters κ and μ. It is independent of α due to normalization. For values of κ and μ typically observed *in vivo* [13], the correlation coefficient r is plotted in Fig. 6.1. These plots demonstrate that r increases as the difference between κ_m and κ_n decreases. More importantly, these

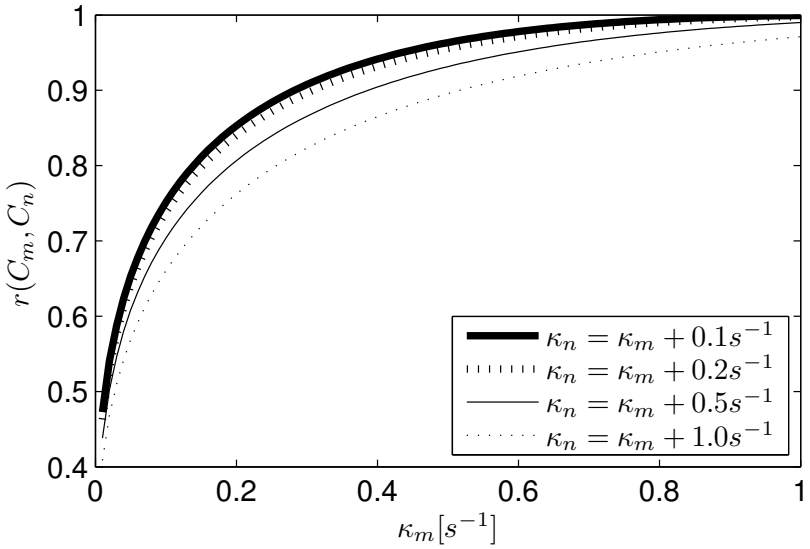

Figure 6.1 *Correlation function $r(C_m, C_n)$ as a function of κ_m and κ_n for $\mu_m = \mu_n = 20$ s.*

plots also show a monotonic increase in r as both κ_m and κ_n increase. As a result, the correlation coefficient r between two TICs can be interpreted as an indirect estimate of the dispersion-related parameter κ. This result provides the formal basis for a spatiotemporal dispersion analysis by assessment of the correlation coefficient among TICs.

6.2.2 Spatiotemporal correlation analysis

A spatiotemporal analysis is performed by local estimation of the TIC correlation coefficient. Prior to this analysis, spatial filtering and TIC windowing are performed to increase the robustness of the correlation analysis.

In the observed DCE-US images, the spatial speckle characteristics are anisotropic and depth-dependent [14]. To prevent speckle from affecting the TIC correlation analysis, the speckle size is regularized to about 0.8 mm by dedicated spatial filtering [19].

The robustness of the analysis is increased by windowing, i.e., selection of the most relevant TIC time segment [19]. Windowing provides temporal TIC alignment and increases the sensitivity of the proposed correlation analysis to TIC shape variations, by removing TIC noise outside the adopted window. The adopted window starts at the local TIC appearance time, which is defined as the first time at which the TIC achieves 10% of its peak level. Detection of the TIC appearance time is made robust by median filtering in time (on TICs with a blocksize of 5 s) and in space (on the detected appearance times with a blocksize of 5 x 5 pixels). Based on optimization of the pixel classification results, we adopted a window length of 40 s. Given the typical frame rate of 10 Hz, this length is equivalent to about 400 samples.

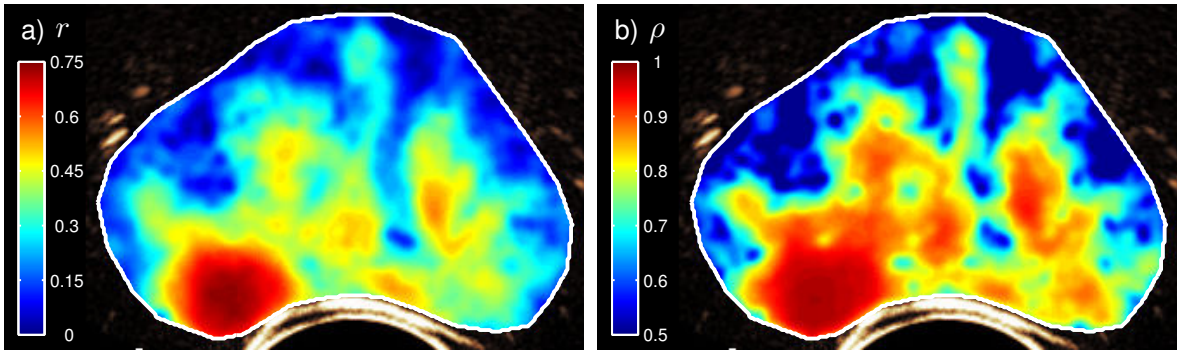

Figure 6.2 *Parametric dispersion images with histology based on correlation r (a) and coherence ρ (b).*

Figure 6.3 *The histology slice with carcinoma marked in red, corresponding to the parametric dispersion images of Fig. 6.2.*

At each pixel, the TIC correlation r is estimated by a local spatial TIC correlation analysis. Using direct calculation of (6.3), r is evaluated as the average correlation coefficient between the local pixel TIC and the surrounding pixel TICs in a ring-shaped kernel [14]. The inner radius of 1.0 mm is based on the speckle size obtained after filtering [19]; the outer radius of 2.5 mm is based on the scale of angiogenic networks. After computation, r is displayed as a color-coded value at each pixel, overlaid on the DCE-US image, as shown in Fig. 6.2a. The adopted color scale is based on the average observed range of r. For comparison, the same approach was applied to estimate the coherence ρ [14]. For ρ, the optimal results were achieved using a window length of 35 s. In Fig. 6.2b, the parametric dispersion image based on coherence corresponding to Fig. 6.2a is shown.

6.2.3 Data acquisition and validation

Acquisition of the data was performed at the Academic Medical Center University Hospital (Amsterdam, The Netherlands). After written informed consent was obtained, a 2.4 mL SonoVue ® (Bracco, Milan, Italy) UCA bolus was injected intravenously. DCE-US imaging of the prostate was performed with an iU22 ultrasound imaging system (Philips Healthcare, Bothell, WA) and either a C8-4v (6 recordings in 5 patients) or C10-3v (6 recordings in 3

patients) probe. Power modulation imaging was performed at a frequency of 3.5 MHz and a mechanical index of 0.06.

The acquired B-mode image sequences were linearized by reverting the color mapping and the estimated logarithmic compression function [13]. Based on the linear relationship between microbubble concentration and acoustic intensity for low concentrations [13], the analysis was performed using the linearized acoustic intensity.

To validate the performance of the obtained parametric images for prostate cancer localization, they were compared with histology, obtained after radical prostatectomy. The histology slice corresponding to the parametric dispersion images of Fig. 6.2 is shown in Fig. 6.3.

In each dataset, two ROIs of at least 0.5 cm^2 were selected based on the histology ground truth to represent healthy tissue and cancer. In total, the validation dataset contained about 60×10^3 pixels. Based on the histograms of r for both tissue classes, the receiver operating characteristic (ROC) curve was evaluated. The optimal sensitivity and specificity for pixel classification were determined as the point on the ROC curve closest to ideal classification.

The classification performance of the correlation r was compared to that of the coherence ρ, the dispersion-related TIC parameter κ, and several perfusion-related TIC parameters. These included the area under the curve (AUC), peak intensity (PI), peak time (PT), appearance time (AT), full-width at half maximum (FWHM), wash-in time (WIT) and mean transit time (MTT) [9, 10]. The parameter κ and the perfusion parameters were estimated by LDRW model fitting of pixel TICs. Spatial (Gaussian kernel, $\sigma = 0.5$ cm) and temporal (100-taps low-pass filter, cut-off frequency of 0.5 Hz) filtering were performed prior to fitting [13].

6.3 Results

An increased spatial TIC similarity was observed in the presence of cancer by both parameters r and ρ. The average correlation coefficient r was 0.18 ± 0.09 in healthy tissue and 0.39 ± 0.15 in cancer. For the coherence ρ, these values were 0.56 ± 0.14 and 0.78 ± 0.13, respectively. For all parameters, the optimal sensitivity, specificity, and area under the ROC curve are reported in Table 6.1. The spatial similarity parameters r and ρ provided the highest area under the ROC curve.

Table 6.1 *Classification statistics*

Parameter	Sensitivity [%]	Specificity [%]	ROC curve area
r	77.3	86.0	0.89
ρ	78.1	81.6	0.88
κ	66.6	68.7	0.70
AUC	44.0	70.9	0.61
PI	43.7	79.2	0.65
PT	53.0	79.6	0.70
AT	52.8	64.4	0.60
FWHM	74.4	70.7	0.76
WIT	66.7	65.0	0.72
MTT	53.2	82.1	0.70

6.4 Discussion and Conclusions

In this paper, we propose an implementation of contrast-ultrasound dispersion imaging based on spatial TIC correlation analysis. By deriving the analytical relation between the TIC correlation coefficient r and the dispersion-related TIC parameter κ, the formal basis for dispersion estimation by spatial TIC correlation analysis is provided.

The high tissue classification accuracy for correlation r and coherence ρ is probably due to the robust nature of the spatial TIC similarity analysis. Because the analysis is performed by direct calculation of (6.3), it is inherently normalized and provides a local assessment. Therefore, it may be relatively robust to nonlinear artifacts resulting from e.g. nonlinear attenuation and microbubble gas diffusion phenomena, which affect the acoustic microbubble behaviour [11, 20]: if all TICs within the kernel, i.e., within 0.5 cm^2, will be similarly affected, the effect on the TIC similarity estimate will be relatively limited compared to that on fitted TIC parameters.

Tissue motion, although negligible in the observed data, may also affect the reliability of TIC quantification. Motion artifacts, which affect all TICs, may significantly hamper the accuracy of TIC fitting. In the proposed analysis, motion artifacts may cause a positive bias resulting from the similarity of TIC motion artifacts.

An alternative TIC correlation assessment could be obtained by computation of (6.4) after estimation of κ and μ. This approach would require curve fitting and isolation of the bolus first pass. Moreover, high-frequency fluctuations, which would be considered noise in the context of TIC fitting, may in fact represent local transport of microbubbles. This information could be highly relevant for the proposed spatiotemporal analysis.

Overall, the observed values of the correlation r are lower than those of the coherence ρ. This can be explained by the fact that r, as opposed to ρ, is influenced by high-frequency

TIC components, which have a lower spatial similarity. Given the limited bandwidth of coherence analysis between 0 and 0.5 Hz, ρ is based on about 18 samples. In comparison, r is based on about 400 samples, possibly explaining the slight classification improvement by r as compared to ρ. This improvement may also be due to inclusion of TIC phase information, which also contributes to the TIC shape, into the similarity estimation.
In the future, the proposed method may be evaluated and further improved in experimental phantom studies [21]. Up until now, however, the development of microvascular phantoms, in which angiogenesis-related features such as density and tortuosity can be controlled, remains highly challenging.
In conclusion, localization of cancer by analysis of the spatial TIC correlation coefficient provides encouraging results. The validation should however be extended in future work.

References

[1] J. Folkman, K. Watson, D. Ingber, and D. Hanahan, "Induction of angiogenesis during the transition from hyperplasia to neoplasia," *Nature*, vol. 339, no. 6219, pp. 58–61, 1989.

[2] S. A. Bigler, R. E. Deering, and M. K. Brawer, "Comparison of microscopic vascularity in benign and malignant prostate tissue," *Hum. Pathol.*, vol. 24, no. 2, pp. 220–226, 1993.

[3] G. Russo, M. Mischi, W. Scheepens, J. de la Rosette, and H. Wijkstra, "Angiogenesis in prostate cancer: onset, progression and imaging," *BJU Int.*, vol. 110, pp. E794–E808, 2012.

[4] S. B. Feinstein, B. Coll, D. Staub *et al.*, "Contrast enhanced ultrasound imaging," *J. Nucl. Cardiol.*, vol. 17, no. 1, pp. 106–115, 2010.

[5] N. de Jong, P. J. A. Frinking, A. Bouakaz, and F. J. ten Cate, "Detection procedures of ultrasound contrast agents," *Ultrasonics*, vol. 38, no. 1–8, pp. 87–92, 2000.

[6] K. Wei, A. R. Jayaweera, S. Firoozan *et al.*, "Quantification of myocardial blood flow with ultrasound-induced destruction of microbubbles administered as a constant venous infusion," *Circulation*, vol. 97, pp. 473–483, 1998.

[7] M. Arditi, P. J. A. Frinking, X. Zhou, and N. G. Rognin, "A new formalism for the quantification of tissue perfusion by the destruction-replenishment method in contrast ultrasound imaging," *IEEE Trans. Ultrason., Ferroelectr., Freq. Control*, vol. 53, no. 6, pp. 1118–1129, 2006.

[8] D. Cosgrove and N. Lassau, "Imaging of perfusion using ultrasound," *Eur. J. Nucl. Med. Mol. Imaging*, vol. 37, pp. 65–85, 2010.

[9] R. J. Eckersley, J. P. Sedelaar, M. J. K. Blomley *et al.*, "Quantitative microbubble enhanced transrectal ultrasound as a tool for monitoring hormonal treatment of prostate carcinoma," *Prostate*, vol. 51, pp. 256–267, 2002.

[10] N. Elie, A. Kaliski, P. Péronneau *et al.*, "Methodology for quantifying interactions between perfusion evaluated by DCE-US and hypoxia throughout tumor growth," *Ultrasound Med. Biol.*, vol. 33, no. 4, pp. 549–560, 2007.

[11] M.-X. Tang, H. Mulvana, T. Gauthier *et al.*, "Quantitative contrast-enhanced ultrasound imaging: a review of sources of variability," *Interface Focus*, vol. 1, no. 4, pp. 520–539, 2011.

[12] A. Eberhard, S. Kahlert, V. Goede *et al.*, "Heterogeneity of angiogenesis and blood vessel maturation in human tumors: implications for antiangiogenic tumor therapies," *Cancer Res.*, vol. 60, no. 5, pp. 1388–1393, 2000.

[13] M. P. J. Kuenen, M. Mischi, and H. Wijkstra, "Contrast-ultrasound diffusion imaging for localization of prostate cancer," *IEEE Trans. Med. Imag.*, vol. 30, no. 8, pp. 1493–1502, 2011.

[14] M. Mischi, M. P. J. Kuenen, and H. Wijkstra, "Angiogenesis imaging by spatiotemporal analysis of

ultrasound-contrast-agent dispersion kinetics," *IEEE Trans. Ultrason., Ferroelectr., Freq. Control*, vol. 59, no. 4, pp. 621–629, Apr. 2012.

[15] American Cancer Society, "Cancer facts & figures," Atlanta, 2012.

[16] M. Smeenge, J. J. M. C. H. de la Rosette, and H. Wijkstra, "Current status of transrectal ultrasound techniques in prostate cancer," *Curr. Opin. Urol.*, vol. 22, pp. 297–302, 2012.

[17] C. W. Sheppard, *Basic principles of the tracer method*. New York: John Wiley and Sons, 1962.

[18] K. H. Norwich and S. Zelin, "The dispersion of indicator in the cardio-pulmonary system," *Bull. Math. Biophys.*, vol. 32, pp. 25–43, 1970.

[19] M. P. J. Kuenen, T. A. Saidov, H. Wijkstra, and M. Mischi, "Contrast-ultrasound dispersion imaging for prostate cancer localization by improved spatiotemporal similarity analysis," *Ultrasound Med. Biol.*, vol. 39, no. 9, pp. 1631–1641, 2013.

[20] S. Casciaro, R. Palmizio Errico, F. Conversano, C. Demitri, and A. Distante, "Experimental investigations of nonlinearities and destruction mechanisms of an experimental phospholipid-based ultrasound contrast agent," *Invest. Radiol.*, vol. 42, pp. 95–104, 2007.

[21] C. Demitri, A. Sannino, F. Conversano *et al.*, "Hydrogel based tissue mimicking phantom for in-vitro ultrasound contrast agents studies," *J. Biomed. Mater. Res. B Appl. Biomater.*, vol. 87, pp. 338–345, 2008.

CHAPTER 7

Prostate cancer localization by CUDI and mpMRI

In preparation for submission as: M. Smeenge, M. Kuenen, M. Mischi, M. Engelbrecht, C. Lavini, M. van Santen, A. Postema, T. de Reijke, M. P. Laguna Pes, J. de la Rosette, and H. Wijkstra, "Detection and localization of prostate cancer: Additional value of quantification in Dynamic Contrast-Enhanced Ultrasound and Multiparametric MRI."

Abstract – *The aim was to assess the additional value of semi-quantitative analysis of dynamic contrast-enhanced ultrasound (DCE-US) and dynamic contrast-enhanced MRI (DCE-MRI) when used together with qualitative image interpretation for the localization of prostate cancer in the same patients, using radical prostatectomy specimens as reference standard. 11 consecutive patients underwent both DCE-US and multiparametric MRI (mpMRI) before radical prostatectomy. Per patient, 2-4 DCE-US image planes were recorded. Every image plane was divided into 4 quadrants, resulting in 152 regions of interest (ROIs). For each imaging modality, a qualitative interpretation was performed first, followed by a combined interpretation of qualitative and semi-quantitative parameters. Prostate cancer suspicion was scored for each ROI and correlated with histopathology. Using a stringent assessment (all tumors), DCE-US showed a statistically significant increase between qualitative and combined analysis for sensitivity, 46% vs. 58% ($p = 0.04$), and a significant decrease in specificity, 75% vs. 64% ($p = 0.02$). For mpMRI a significant increase was seen between qualitative and combined analysis for sensitivity 31% vs. 47% ($p = 0.01$), the difference in specificity, 94% vs. 85% ($p = 0.10$), was not significant. Using a clinical assessment (tumors larger than 0.5 cm^3), DCE-US showed an increase between qualitative and combined analysis for sensitivity, 73% vs. 86%, and a decrease in specificity, 89% vs. 82%. For mpMRI an increase was seen between qualitative and combined analysis for sensitivity 56% vs. 81%, and a decrease in specificity, 97% vs. 92%. In conclusion, in both DCE-US and mpMRI, semi-quantitative interpretation is a useful addition to qualitative interpretation for the detection and localization of prostate cancer. For both modalities, a statistically significant increase in sensitivity and a decrease in specificity (significant only for DCE-US) were seen.*

7.1 Introduction

In developed countries, prostate cancer is the most common neoplasm in men, accounting for one in four new cancer cases. In the US, the incidence rate is 165 per 100.000 males and in the UK, the incidence rate is 105 per 100.000 males [1, 2]. Advanced, high-grade prostate cancer is likely to be detected using the currently available diagnostic tools like prostate-specific antigen (PSA) testing, digital rectal examination and transrectal ultrasonography (TRUS). However, at this time detection may be to late to perform a curative treatment. When diagnosed being organ confined and in early stage, the chances of curing prostate cancer are higher and comorbidity after treatment is lower.

Unfortunately, PSA, rectal examination, and TRUS perform poorly in detecting organ confined, early stage prostate cancer [3]. Therefore, when suspicion of prostate cancer arises, systematic prostate biopsies are taken in every patient, with associated discomfort and comorbidity [4, 5]. Reliable imaging that can properly visualize prostate cancer is greatly needed for comorbidity reduction and improvement of screening, diagnosis, and treatment. Nowadays, multiparametric magnetic resonance imaging (mpMRI) and dynamic contrast-enhanced ultrasound (DCE-US) are two promising image modalities for prostate cancer visualization [6–14].

Malignant growth induces angiogenesis and neovascularization, which is expected to result in a difference in blood flow and perfusion between benign and malignant tissue [15, 16]. The diagnostic accuracy in prostate cancer detection may possibly increase when these differences could be visualized, for example with DCE-US or dynamic contrast-enhanced MRI (DCE-MRI) [12, 17].

Recently, we conducted a study comparing DCE-US and mpMRI with histology after radical prostatectomy for the localization of prostate cancer, demonstrating that under the same conditions, DCE-US and mpMRI are comparable in detection and localization of prostate cancer. Correlation of lesions larger than 0.5 cm^3 resulted in a sensitivity of 59% with a specificity of 91% for DCE-US and a sensitivity of 65% with a specificity of 91% for mpMRI. In this study, imaging was assessed by subjective, qualitative interpretation, which is known to have a high inter- and intraobserver variability and a steep learning curve [7].

To allow an objective analysis of hemodynamic differences and reduce user dependency, different quantification methods, based on the extraction of functional parameters, have been investigated. Recent publications show promising results using semi-quantitative and pharmacokinetic model parameters in both DCE-US and mpMRI for discrimination between malignant and benign prostate tissue [18–28]. In these publications, quantification is based on comparing contrast hemodynamic parameters in regions of interest (ROIs) with known malignant and benign tissue. However, it would be very interesting to evaluate the benefit of these quantitative models in clinical practice. In this regard, mpMRI is one step ahead

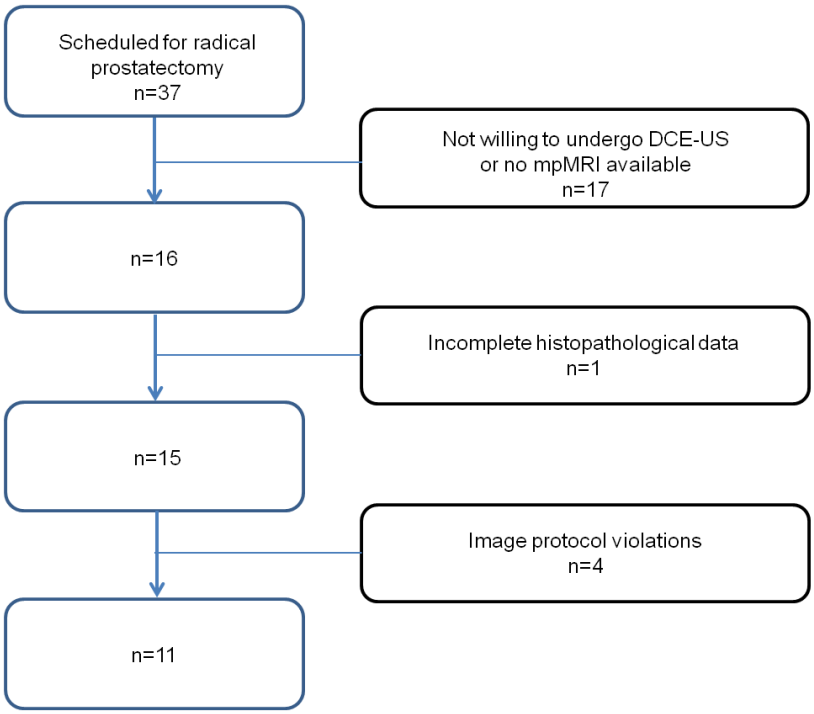

Figure 7.1 *Flow diagram presenting selection criteria for inclusion.*

of DCE-US and studies on localization of prostate cancer using dynamic contrast-enhanced MRI (DCE-MRI) have already shown the potential additional value of quantitative analysis using hemodynamic parameters [27, 29, 30].
In this study we investigated the additional value of semi-quantitative analysis of DCE-US and mpMRI when used together with qualitative interpretation in the same patients for the localization of prostate cancer.

7.2 Materials and Methods

Between January 2012 and July 2013, 11 consecutive patients with biopsy proven prostate cancer, scheduled for radical prostatectomy in the AMC (Academic Medical Center, Amsterdam, The Netherlands) were included in this study. The inclusion diagram is presented in Fig. 7.1 and the patient characteristics are presented in Table 7.1.
The DCE-US study was approved by the institutional review board and the mpMRI investigations were performed on clinical basis before undergoing radical prostatectomy. All patients signed an informed consent, allowing use of their DCE-US, mpMRI and histological data for comparison.
All examiners (DCE-US, mpMRI and pathology) received scoring sheets on which the prostate was divided in 5 transverse planes. Every plane was subdivided in 4 quadrants

Table 7.1 *Patient characteristics.*

Number of patients included		11
Mean age (range) [years]		62 (55-69)
Mean PSA (range) [ng/mL]		7.6 (3.2-12.6)
Clinical T-stage	cT1	6
	cT2	4
	cT3	1
Pathological T-stage	pT2a	1
	pT2b	0
	pT2c	3
	pT3a	6
	pT3b	1
Pathological Gleason score frequency	6	4
	7	4
	8	1
	9	2

or ROIs, resulting in a total of 20 ROIs per prostate, and a total of 220 ROIs. However, for logistical reasons, between 2 and 4 planes were visualized per patient by DCE-US. A total of 38 imaging planes were obtained in these 11 patients. Every image plane was divided in 4 ROIs, resulting in 152 ROIs used for analysis. This division in planes and ROIs was derived from a study on standardized interpretation and reporting of mpMRI results by Dickinson *et al.* [31]. The examiners were asked to delineate areas suspect for prostate cancer presence and score the likelihood of tumor presence for each ROI on a 5 point Likert-scale [31, 32] to obtain clear and standardized reporting.

The DCE-US investigations were performed using a Philips iU22 ultrasound system (Philips Healthcare, Bothell, WA) with a C10-3v transrectal endfiring probe. Every plane was visualized in the contrast-specific imaging mode and a low mechanical index of 0.06 was used to minimize contrast microbubble destruction. After intravenous injection of a contrast-agent bolus (SonoVue ®, Bracco, Milan, Italy), DCE-US imaging was performed for 120 seconds to record the in-and outflow. A DCE-US image, obtained at approximately the time of peak enhancement, is shown in Fig. 7.2b.

Qualitative interpretation of DCE-US images was done by a trained US examiner with 200-300 imaging sessions of experience in performing and reading prostate DCE-US imaging. The examiner was blinded for all clinical and histological patient data. The US examiner then combined qualitative DCE-US reading with semi-quantitative interpretation.

For DCE-US semi-quantification, three parameters, based on the spreading (dispersion)

of the contrast agent bolus within the microvascular architecture, were adopted for quantitative interpretation. Structural differences in the microvascular architecture, caused by angiogenesis and, therefore, correlated to aggressive prostate cancer, are believed to be well-characterized by dispersion [15]. The analysis is based on recorded time-intensity curves (TICs) obtained at every DCE-US image pixel. The parameter kappa [18] measures the TIC skewness, which can be interpreted as the ratio between the wash-in and wash-out slopes. The parameters coherence and correlation [23, 24, 28] measure the local similarity among TICs measured at neighboring DCE-US image pixels. All dispersion-related parameters were evaluated using parametric maps, as for example shown in Fig. 7.2c.

The mpMRI investigations were performed at 1.5 T (AVANTO, Siemens Healthcare, Erlagen, Germany) with an endorectal coil following European Society of Urogenital Radiology (ESUR) guidelines [14]. The image protocol consisted of T2-weighted turbospin-echo sequences, diffusion-weighted imaging (DWI), and DCE-MRI, as shown in Fig. 7.2d-f. DWI was performed using B-values of 0, 100 and 800. Apparent diffusion coefficient (ADC) maps were automatically calculated afterwards. DCE-MRI images were acquired in the transverse plane after an intravenous bolus injection of 0.1 mmol of MRI contrast medium (Gadovist ®, Bayer AG, Leverkusen, Germany) per kilogram of body weight. A three-dimensional volume covering the entire prostate with identical positioning as the T2-weighted sequence was acquired every 2.5 seconds during 210 seconds.

Qualitative interpretation of mpMRI images was performed by an uro-radiologist with experience between 200 and 300 prostate mpMRI interpretations. He was blinded for all clinical and histological patient data. Qualitative mpMRI reading was then combined with semi-quantitative interpretation of the DCE-MRI images by the same uro-radiologist.

For semi-quantitative DCE-MRI analysis, the TIC-derived parameters, maximal (peak) enhancement, time-to-peak, slope (wash-in) and curve shape [19, 29, 33] were used and visualized by parametric maps. For example, Fig. 7.2g shows the result of semi-quantitative DCE-MRI analysis based on peak enhancement.

For histopathological analysis the prostate specimen was formalin-fixed, dissected in 4-mm-thick transversal slices, paraffin-embedded and stained with haematoxylin/eosin. Tumor location, stage and Gleason score were determined by a pathologist in training and subsequently revised by an experienced uro-pathologist. Both were blinded for DCE-US and mpMRI results. Cancer lesions were delineated on the slides and transferred to photographs of the original transverse slices and on the pathology-scoring sheet, as for example shown in Fig. 7.3.

Due to prostate deformation after radical prostatectomy and plane mismatch caused by angle differences in slicing and imaging plane, correlation between imaging and histology is challenging. First, a "one-to-one" comparison was performed in which imaging ROI scores

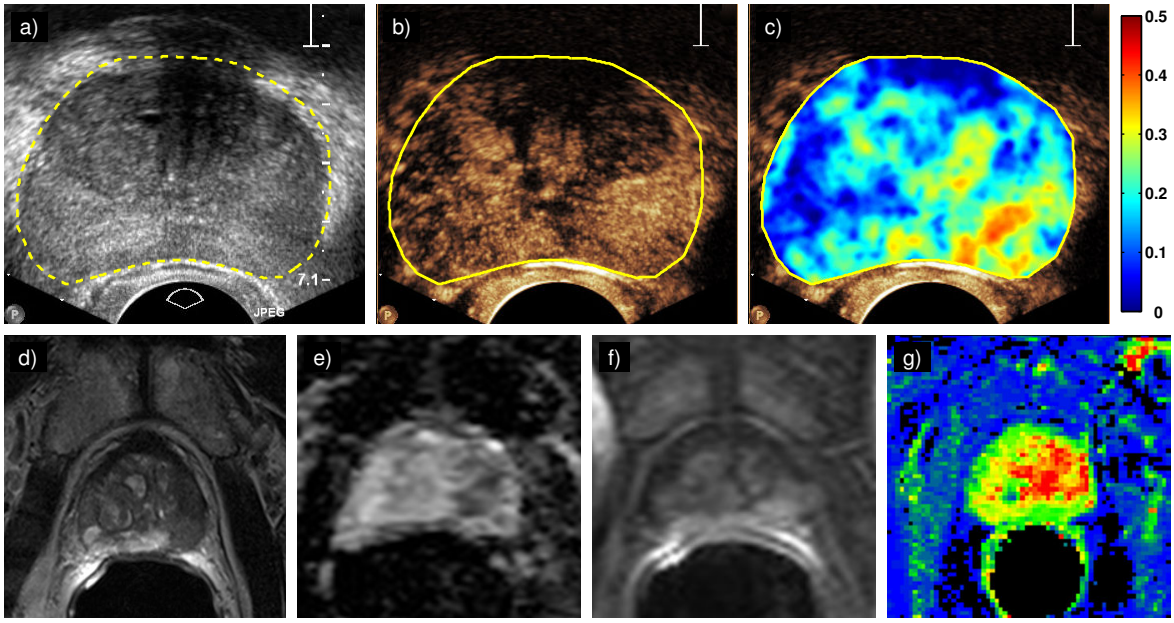

Figure 7.2 *DCE-US (a-c) and mpMRI (d-g) imaging of the prostate. For ultrasound, a fundamental TRUS image (a), a DCE-US image obtained approximately during peak enhancement (b), and a quantitative DCE-US parametric dispersion map (c), based on correlation analysis [28], are shown. The mpMRI images show the results of T2-weighted imaging (d), the apparent diffusion coefficient (ADC) map (e), DCE-MRI at approximately the time of peak enhancement (f), and semi-quantitative DCE-MRI (g) based on peak enhancement [33]. In images (b-g), a suspicious lesion is observed in the left peripheral zone (i.e., in the bottom right of the images), which was confirmed by histology analysis after radical prostatectomy (see Fig. 7.3).*

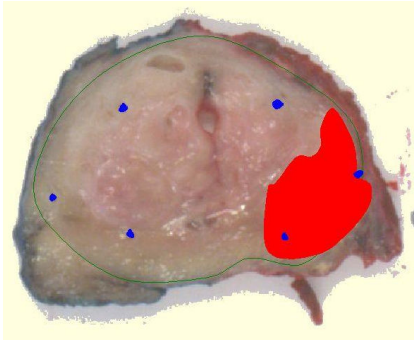

Figure 7.3 *Histology slice corresponding to the DCE-US and mpMRI images shown in Fig. 7.2.*

were compared with the single corresponding pathology ROI (Fig. 7.4, solid arrow). In this approach, no correction is provided for possible plane and angle mismatches. Therefore, a second, "neighboring-included" analysis, was performed in which the imaging ROI was not only compared to the corresponding pathology ROI, but also to the same ROI in directly adjacent pathology slices, as shown in Fig. 7.4 by the dashed arrows. We believe this analysis, based on similar correlations by Turkbey *et al.* and Isebaert *et al.* [12, 13], is more

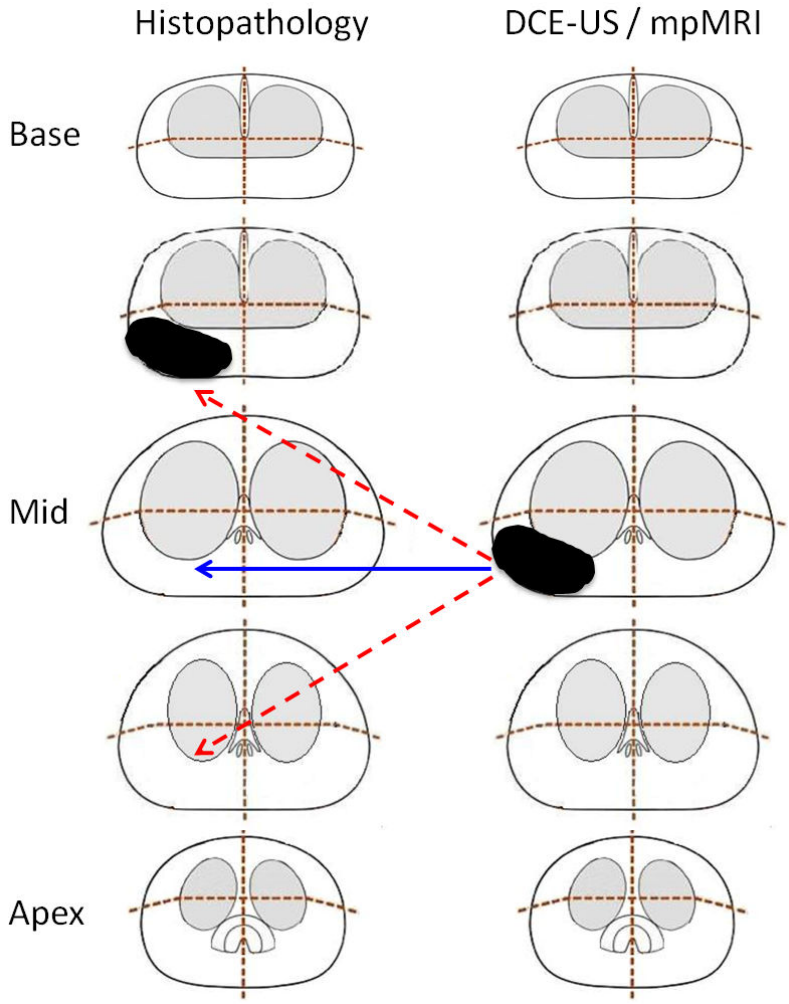

Figure 7.4 *Correlation of histopathology and imaging. The tumor is located in the lower-right quadrant of the base/mid plane (black area). On imaging however, the tumor is seen one plane lower, in the mid plane. The solid arrow depicts the "one-to-one" correlation, in this case "false positive." In the "neighboring-included" correlation, the quadrant is also compared with the same quadrant one plane above and below (solid and dashed arrows). Since one plane above contains tumor, it is scored "true positive."*

robust to possible deformation and misalignment in planes.

The reference standard, based on histopathological analysis, was determined twice per ROI. For the first analysis, using a stringent method, all ROIs containing any amount of prostate cancer were marked positive. In a second, clinical analysis all prostate cancer lesions smaller than 0.5 cm^3 were excluded when tumor was missed in the corresponding imaging ROI. Measurement of the tumor volume was performed using the formula length $\times$ height $\times$ width $\times$ 0.52. The rationale for the clinical approach is that small lesions represent little clinical significance [34, 35]. Only planes in which both DCE-US

Table 7.2 *Decision matrix tables for all analyses for Likert-scale level 3, 4, and 5.*

			Histopathology							
			"One-to-one"				"Neighboring-included"			
			Stringent		Clinical		Stringent		Clinical	
			+	-	+	-	+	-	+	-
DCE-US	Qualitative	+	33	20	33	20	43	10	43	10
		-	39	60	20	79	25	74	16	83
	Qualitative and semi-quantitative	+	42	29	42	29	55	16	55	16
		-	30	51	12	69	18	63	9	72
mpMRI	Qualitative	+	22	5	22	5	24	3	24	3
		-	50	75	25	100	30	95	19	106
	Qualitative and semi-quantitative	+	34	12	34	12	38	8	38	8
		-	38	68	13	93	18	88	9	97

and mpMRI imaging was performed were included for analysis. Depending on the number of planes visualized with DCE-US, 8-16 ROIs were analyzed per prostate. Decision matrix tables were constructed for each analysis of DCE-US and mpMRI, and sensitivity, specificity, positive predictive value (PPV) and negative predictive value (NPV) were calculated. Simultaneous comparison of sensitivity and specificity between the different DCE-US and mpMRI methods was performed using matched sample tables and the extended McNemar's test [36]. The test is only usable for the stringent "one-to-one" correlation since the clinical and neighboring analyses have no fixed amount of tumor-positive results for both DCE-US and mpMRI, qualitative and semi-quantitative analyses.

7.3 Results

Prostate cancer was confirmed in all 11 patients by histopathological examination. Of the 152 ROIs, 72 contained tumor.

The radiologist assessed image quality for every mpMRI session on a 3-point scale, good, moderate and poor. 9 of the 11 recordings were reported as good, and two were reported as moderate image quality. For DCE-US, all recordings were reported as good quality.

Table 2 presents the decision matrix tables for Likert-scale level 3, 4 and 5 suspicions for all four assessments and Table 3 shows the sensitivity, specificity, PPV and NPV.

For qualitative interpretation alone, stringently assessed using the "one-to-one" correlation, a sensitivity of 46% and a specificity of 75% were seen for DCE-US. For mpMRI, these

Table 7.3 *Sensitivity, specificity, PPV and NPV values, expressed as probability, for all analyses for Likert-scale level 3, 4, and 5. Numbers in parentheses represent the 95% confidence intervals.*

			"One-to-one"		"Neighboring-included"	
			Stringent	Clinical	Stringent	Clinical
DCE-US	Qualitative	Sensitivity	0.46 (0.35-0.57)	0.62 (0.49-0.74)	0.63 (0.51-0.74)	0.73 (0.60-0.83)
		Specificity	0.75 (0.65-0.83)	0.80 (0.71-0.87)	0.88 (0.79-0.93)	0.89 (0.81-0.94)
		PPV	0.62 (0.49-0.74)	0.62 (0.49-0.74)	0.81 (0.69-0.89)	0.81 (0.69-0.89)
		NPV	0.61 (0.51-0.70)	0.80 (0.71-0.87)	0.75 (0.65-0.82)	0.84 (0.75-0.90)
	Qualitative and semi-quantitative	Sensitivity	0.58 (0.47-0.69)	0.78 (0.65-0.87)	0.75 (0.64-0.84)	0.86 (0.75-0.92)
		Specificity	0.64 (0.53-0.73)	0.70 (0.61-0.79)	0.80 (0.70-0.87)	0.82 (0.72-0.88)
		PPV	0.59 (0.48-0.70)	0.59 (0.48-0.70)	0.77 (0.66-0.86)	0.77 (0.66-0.86)
		NPV	0.63 (0.52-0.73)	0.85 (0.76-0.91)	0.78 (0.68-0.85)	0.89 (0.80-0.94)
mpMRI	Qualitative	Sensitivity	0.31 (0.21-0.42)	0.47 (0.33-0.60)	0.44 (0.32-0.58)	0.56 (0.41-0.70)
		Specificity	0.94 (0.86-0.97)	0.95 (0.89-0.98)	0.97 (0.91-0.99)	0.97 (0.92-0.99)
		PPV	0.81 (0.63-0.92)	0.81 (0.63-0.92)	0.89 (0.72-0.96)	0.89 (0.72-0.96)
		NPV	0.60 (0.51-0.68)	0.80 (0.72-0.86)	0.76 (0.68-0.83)	0.85 (0.77-0.90)
	Qualitative and semi-quantitative	Sensitivity	0.47 (0.36-0.59)	0.72 (0.58-0.83)	0.68 (0.55-0.79)	0.81 (0.67-0.90)
		Specificity	0.85 (0.76-0.91)	0.89 (0.81-0.93)	0.92 (0.84-0.96)	0.92 (0.86-0.96)
		PPV	0.74 (0.60-0.84)	0.74 (0.60-0.84)	0.83 (0.69-0.90)	0.83 (0.69-0.91)
		NPV	0.64 (0.55-0.73)	0.88 (0.80-0.93)	0.83 (0.75-0.89)	0.92 (0.85-0.95)

statistics were 31% and 94%, respectively. Combined interpretation, stringently assessed using the "one-to-one" correlation, resulted in a sensitivity and a specificity of 58% and 64% for DCE-US, respectively, and 47% and 85% for mpMRI, respectively. For DCE-US, further analysis showed a statistically significant increase between qualitative and combined analysis for sensitivity, 46% vs. 58% ($p = 0.04$), and a significant decrease in specificity, 75% vs. 64% ($p = 0.02$). For mpMRI, a significant increase was seen between qualitative and combined analysis for sensitivity 31% vs. 47% ($p = 0.01$). The difference in specificity, 94% vs. 85%, was not significant ($p = 0.10$). When comparing combined qualitative and semi-quantitative analysis of DCE-US and mpMRI, a significant difference was seen for specificity, 63% vs. 85% ($p < 0.01$), in favor of the mpMRI analyses. The difference in sensitivity, 59% vs. 47%, was not significant ($p = 0.12$).

Looking at the clinical, "neighboring-included" assessment, sensitivity and specificity rose for all interpretations when compared to the stringent "one-to-one" assessment. For qualitative interpretation, a sensitivity of 73% and a specificity of 89% were seen for DCE-US. These statistics were 56% and 97%, respectively, for mpMRI. Using the combined interpretation, a sensitivity and a specificity of 86% and 82% were seen for DCE-US, respectively, and 81% and 92% for mpMRI, respectively.

7.4 Discussion

In this study, the additional value of semi-quantitative analysis over qualitative analysis in DCE-US and mpMRI was evaluated in the detection and localization of prostate cancer in the same patients with radical prostatectomy as reference standard.

The results demonstrate that for both DCE-US and mpMRI, semi-quantitative interpretation is a useful addition to qualitative interpretation. A statistically significant increase in sensitivity was seen for both imaging modalities. The specificity decreased significantly ($p = 0.02$) for the DCE-US analysis only; for mpMRI, this decrease was not significant ($p = 0.10$). Although no statistical analysis was performed on the clinically assessed, "neighboring-included" results, these numbers show an even higher increase in sensitivity and lower decrease in specificity when qualitative interpretation only, and combined interpretations are compared.

In all analyses, the absolute increase in sensitivity was higher than the decrease in specificity. Not missing tumors is most important when considering these imaging modalities as future screening tools for prostate cancer and, therefore, the increase in sensitivity is more important than the decrease in specificity. Moreover, the NPV increases for both modalities when semi-quantitative analysis was added to the qualitative analysis.

At the moment, most quantitative DCE-US methods are based on assessment of perfusion. These methods assume a causal relation between angiogenic microvascular changes and microvascular perfusion [21, 22, 37, 38]. However, angiogenesis has complex and possibly opposing effects on perfusion [18, 21]. Kuenen *et al.* introduced an alternative quantification method based on the diffusion or dispersion of contrast agents in the microcirculation. In preliminary studies, three different approaches for dispersion assessment were compared on a pixel basis to histology data, obtained after radical prostatectomy. All dispersion parameters provided a superior area under the receiver-operating-characteristic curve for tissue classification than perfusion-related parameters [23, 24, 28].

Since a large amount of results were generated using a 1-5 point Likert-scale, only a selection is presented. The results of suspicion levels 3, 4 and 5 were considered to be the most important since, in our opinion, not missing tumors is more important than an increased specificity. Therefore, suspicion level 3 was labeled as possibly tumor and analyzed as "positive" on imaging together with level 4 and 5 suspicion. Suspicion level scores of 1 and 2 were considered as (highly) likely not malignant and therefore analyzed as "negative."

A limitation in this study was the small, single-center patient group used for the analyses. Another limitation is the interpretation by a single observer per imaging modality. However, all DCE-US and mpMRI analyses were performed in the same patient group. All patients were known to have prostate cancer, which could have influenced scoring by the examiners. A limitation for transrectal DCE-US was that visualization could only be performed in one

2D-plane for 120 seconds per contrast bolus injection. For every additional plane, a new bolus injection had to be administered. In practice, 2 to 4 planes were visualized per image session. The tumor might be located in between visualized planes, and consequently missed. A solution to this problem is 3D/4D imaging, enabling whole prostate quantification analysis after one single bolus injection.

The correlation of DCE-US and mpMRI images with histology is challenging in many ways. One challenge is the mismatch between DCE-US, mpMRI, and pathology planes, which all are acquired at different angles. Due to endfiring probe usage, DCE-US planes fan out from the posterior side of the prostate. Histopathology planes, however, fan out from the anterior side of the prostate due to urethra stretching and fixation during workup. mpMRI planes are all in transverse plane. Using the "neighboring-included" correlation, adapted from Turkbey *et al.* and Isebaert *et al.*, we aimed to compensate for this plane mismatch by including the adjacent histology planes to the comparison with imaging [12, 13]. However, this could result in a more favorable picture than the actual situation. If multiple tumors are present in one prostate, an imaging ROI that was falsely scored positive might be marked "true-positive" due to presence of a second tumor in the neighboring ROI in one of the adjacent planes.

For the clinical approach, the gold standard, being the number of tumor-positive ROIs in histology, was dynamic, due to visibility of tumors smaller than 0.5 cm^3 on imaging. Since some tumors smaller than 0.5 cm^3 are correctly seen on imaging, it would not be correct in our opinion to score the corresponding ROIs as "false positive." Therefore, for the clinical analyses, tumors smaller than 0.5 cm^3 were scored negative only when on imaging the corresponding ROI was scored negative. As a result, the clinical interpretation is only applied to the negatively scored ROIs, shifting score from "false positive" to "true negative" while maintaining the same "true positive" scores.

An attempt to solve histology and imaging correlation problems has been described by Turkbey *et al.* [30]. After surgical removal, the prostate was fixed in a specific 3D mold based on the MRI prostate contours, before sectioning into slices for histopathological examination using the exact same planes as acquired on the transversal MRI images. This method solves mentioned plane angulation difficulties. However, correlation with multiple imaging methods, such as US and MRI in this study, will be very difficult since all imaging has to be acquired in the exact same planes.

Another solution for the mismatch between imaging and histology would involve the use of 3D models. Using reconstructions of the imaging and histology into overlapping 3D prostate models, cross-reference of suspicious lesions and histology slices in exact the same ROI is possible. However, 3D reconstruction is difficult due to prostate deformation by ultrasound probe, endorectal-coil usage, surgical removal and pathological preparation.

During the last decade, single-modality MRI interpretation changed to multi-modality (multiparametric) interpretation, combining the best of anatomical and functional imaging. Nowadays, anatomical and functional imaging of the prostate, using different US modalities like greyscale, Doppler, (shear-wave) elastography and DCE-US, is possible. However, literature on multiparametric US (mpUS) interpretation is scarce [39]. If the change from single modality US to mpUS is made, this could potentially further improve detection and localization of prostate cancer.

Many studies have been evaluating semi-quantitative and pharmacokinetic model parameters in both DCE-US and mpMRI for discrimination between known malignant and benign prostate regions [18–28]. This comparison is vital in identifying the most suitable parameters for discriminating malignant from benign tissue. However, testing of these parameters in the clinical workflow is essential to demonstrate their value for prostate cancer detection and localization. This has only been evaluated by a few mpMRI studies, showing the potential additional value of quantitative analysis using hemodynamic parameters [27, 29, 30].

We show that semi-quantitative analysis can improve prostate cancer detection and localization, for both DCE-US and mpMRI, when used together with qualitative interpretation. However, in our experience (semi-)quantitative analyses have to undergo further development before use without qualitative interpretations is useful.

7.5 Conclusion

In both DCE-US and mpMRI, semi-quantitative interpretation is a useful addition to qualitative interpretation for the detection and localization of prostate cancer. A significant increase in sensitivity was seen for both imaging modalities, specificity decreases significantly for the DCE-US analysis only.

References

[1] American Cancer Society, "Cancer facts and statistics." [Online]. Available: http://www.cancer.org/research/cancerfactsstatistics/

[2] Cancer Research UK, "Cancer incidence for common cancers." [Online]. Available: http://www.cancerresearchuk.org/cancer-info/cancerstats/incidence/commoncancers/

[3] A. M. D. Wolf, R. C. Wender, R. B. Etzioni *et al.*, "American cancer society guideline for the early detection of prostate cancer: update 2010," *CA Cancer J. Clin.*, vol. 60, no. 2, pp. 70–98, 2010.

[4] A. Heidenreich, P. J. Bastian, J. Bellmunt *et al.*, "EAU guidelines on prostate cancer. Part 1: screening, diagnosis, and local treatment with curative intent - update 2013," *Eur. Urol.*, vol. 65, no. 1, pp. 124–137, 2014.

[5] M. Smeenge, J. J. M. C. H. de la Rosette, and H. Wijkstra, "Current status of transrectal ultrasound techniques in prostate cancer," *Curr. Opin. Urol.*, vol. 22, pp. 297–302, 2012.

[6] F. Pinto, A. Totaro, A. Calarco *et al.*, "Imaging in prostate cancer diagnosis: present role and future perspectives," *Urol. Int.*, vol. 86, no. 4, pp. 373–382, 2011.

[7] M. Smeenge, M. Mischi, M. Laguna Pes, J. de la Rosette, and H. Wijkstra, "Novel contrast-enhanced ultrasound imaging in prostate cancer," *World J. Urol.*, vol. 29, pp. 581–587, 2011.

[8] B. Turkbey, P. S. Albert, K. Kurdziel, and P. L. Choyke, "Imaging localized prostate cancer: current approaches and new developments," *Am. J. Roentgenol.*, vol. 192, no. 6, pp. 1471–1480, 2009.

[9] Y. F. Guo, F. H. Li, S. W. Xie *et al.*, "Value of contrast-enhanced sonographic micro flow imaging for prostate cancer detection with t-PSA level of 4-10 ng/mL," *Eur. J. Radiol.*, vol. 81, no. 11, pp. 3067–3071, 2012.

[10] H. Uemura, F. Sano, A. Nomiya *et al.*, "Usefulness of perflubutane microbubble-enhanced ultrasound in imaging and detection of prostate cancer: phase II multicenter clinical trial," *World J. Urol.*, vol. 31, no. 5, pp. 1123–1128, 2013.

[11] F. Sano, H. Terao, T. Kawahara *et al.*, "Contrast-enhanced ultrasonography of the prostate: various imaging findings that indicate prostate cancer," *BJU Int.*, vol. 107, no. 9, pp. 1404–1410, 2011.

[12] S. Isebaert, L. Van den Bergh, K. Haustermans *et al.*, "Multiparametric MRI for prostate cancer localization in correlation to whole-mount histopathology," *J. Magn. Reson. Imaging*, vol. 37, no. 6, pp. 1392–1401, 2013.

[13] B. Turkbey, P. A. Pinto, H. Mani *et al.*, "Prostate cancer: value of multiparametric MR imaging at 3 T for detection - histopathologic correlation," *Radiology*, vol. 255, no. 1, pp. 89–99, 2010.

[14] J. O. Barentsz, J. Richenberg, R. Clements *et al.*, "ESUR prostate MR guidelines 2012," *Eur. Radiol.*, vol. 22, no. 4, pp. 746–757, 2012.

[15] G. Russo, M. Mischi, W. Scheepens, J. de la Rosette, and H. Wijkstra, "Angiogenesis in prostate cancer: onset, progression and imaging," *BJU Int.*, vol. 110, pp. E794–E808, 2012.

[16] J. P. Sedelaar, G. J. van Leenders, C. A. Hulsbergen-van de Kaa *et al.*, "Microvessel density: correlation between contrast ultrasonography and histology of prostate cancer," *Eur. Urol.*, vol. 40, no. 3, pp. 285–293, 2001.

[17] M. H. Wink, F. Frauscher, D. Cosgrove *et al.*, "Contrast-enhanced ultrasound and prostate cancer; a multicentre European research coordination project," *Eur. Urol.*, vol. 54, no. 5, pp. 982–993, 2008.

[18] M. P. J. Kuenen, M. Mischi, and H. Wijkstra, "Contrast-ultrasound diffusion imaging for localization of prostate cancer," *IEEE Trans. Med. Imag.*, vol. 30, no. 8, pp. 1493–1502, 2011.

[19] S. Isebaert, F. D. Keyzer, K. Haustermans *et al.*, "Evaluation of semi-quantitative dynamic contrast-enhanced MRI parameters for prostate cancer in correlation to whole-mount histopathology," *Eur. J. Radiol.*, vol. 81, no. 3, pp. E217–e222, 2012.

[20] E. K. Vos, G. J. S. Litjens, T. Kobus *et al.*, "Assessment of prostate cancer aggressiveness using dynamic contrast-enhanced magnetic resonance imaging at 3 T," *Eur. Urol.*, vol. 64, no. 3, pp. 448–455, 2013.

[21] N. Elie, A. Kaliski, P. Péronneau *et al.*, "Methodology for quantifying interactions between perfusion evaluated by DCE-US and hypoxia throughout tumor growth," *Ultrasound Med. Biol.*, vol. 33, no. 4, pp. 549–560, 2007.

[22] Y. Zhu, Y. Chen, J. Jiang *et al.*, "Contrast-enhanced harmonic ultrasonography for the assessment of prostate cancer aggressiveness: a preliminary study," *Korean J. Radiol.*, vol. 11, no. 1, pp. 75–83, 2010.

[23] M. P. J. Kuenen, T. A. Saidov, H. Wijkstra, and M. Mischi, "Contrast-ultrasound dispersion imaging for prostate cancer localization by improved spatiotemporal similarity analysis," *Ultrasound Med. Biol.*, vol. 39, no. 9, pp. 1631–1641, 2013.

[24] M. Mischi, M. P. J. Kuenen, and H. Wijkstra, "Angiogenesis imaging by spatiotemporal analysis of ultrasound-contrast-agent dispersion kinetics," *IEEE Trans. Ultrason., Ferroelectr., Freq. Control*, vol. 59, no. 4, pp. 621–629, Apr. 2012.

[25] Y. S. Sung, H.-J. Kwon, B.-W. Park *et al.*, "Prostate cancer detection on dynamic contrast-enhanced MRI: computer-aided diagnosis versus single perfusion parameter maps," *Am. J. Roentgenol.*, vol. 197, no. 5, pp. 1122–1129, 2011.

[26] E. Niaf, O. Rouvière, F. Mège-Lechevallier, F. Bratan, and C. Lartizien, "Computer-aided diagnosis of prostate cancer in the peripheral zone using multiparametric MRI," *Phys. Med. and Biol.*, vol. 57, no. 12, pp. 3833–3851, 2012.

[27] A. B. Rosenkrantz, A. Sabach, J. S. Babb *et al.*, "Prostate cancer: Comparison of dynamic contrast-enhanced MRI techniques for localization of peripheral zone tumor," *Am. J. Roentgenol.*, vol. 201, no. 3, pp. W471–W478, 2013.

[28] M. P. J. Kuenen, T. A. Saidov, H. Wijkstra, J. J. M. C. H. de la Rosette, and M. Mischi, "Spatiotemporal correlation of ultrasound-contrast-agent dilution curves for angiogenesis localization by dispersion imaging," *IEEE Trans. Ultrason., Ferroelectr., Freq. Control*, vol. 60, no. 12, pp. 2665–2669, 2013.

[29] S. Verma, B. Turkbey, N. Muradyan *et al.*, "Overview of dynamic contrast-enhanced MRI in prostate cancer diagnosis and management," *Am. J. Roentgenol.*, vol. 198, no. 6, pp. 1277–1288, 2012.

[30] B. Turkbey, H. Mani, V. Shah *et al.*, "Multiparametric 3T prostate magnetic resonance imaging to detect cancer: histopathological correlation using prostatectomy specimens processed in customized magnetic resonance imaging based molds," *J. Urol.*, vol. 186, no. 5, pp. 1818–1824, 2011.

[31] L. Dickinson, H. U. Ahmed, C. Allen *et al.*, "Scoring systems used for the interpretation and reporting of multiparametric MRI for prostate cancer detection, localization, and characterization: could standardization lead to improved utilization of imaging within the diagnostic pathway?" *J. Magn. Reson. Imaging*, vol. 37, no. 1, pp. 48–58, 2013.

[32] A. B. Rosenkrantz, S. Kim, R. P. Lim *et al.*, "Prostate cancer localization using multiparametric MR imaging: comparison of prostate imaging reporting and data system (PI-RADS) and Likert scales," *Radiology*, vol. 269, no. 2, pp. 482–492, 2013.

[33] C. Lavini, J. J. C. Verhoeff, C. B. Majoie *et al.*, "Model-based, semiquantitative and time intensity curve shape analysis of dynamic contrast-enhanced MRI: a comparison in patients undergoing antiangiogenic treatment for recurrent glioma," *J. Magn. Reson. Imaging*, vol. 34, no. 6, pp. 1303–1312, 2011.

[34] A. S. Duffield, T. K. Lee, H. Miyamoto, H. B. Carter, and J. I. Epstein, "Radical prostatectomy findings in patients in whom active surveillance of prostate cancer fails," *J. Urol.*, vol. 182, no. 5, pp. 2274–2279, 2009.

[35] A. Shukla-Dave, H. Hricak, O. Akin *et al.*, "Preoperative nomograms incorporating magnetic resonance imaging and spectroscopy for prediction of insignificant prostate cancer," *BJU Int.*, vol. 109, no. 9, pp. 1315–1322, 2012.

[36] N. E. Hawass, "Comparing the sensitivities and specificities of two diagnostic procedures performed on the same group of patients," *Br. J. Radiol.*, vol. 70, no. 832, pp. 360–366, 1997.

[37] R. J. Eckersley, J. P. Sedelaar, M. J. K. Blomley *et al.*, "Quantitative microbubble enhanced transrectal ultrasound as a tool for monitoring hormonal treatment of prostate carcinoma," *Prostate*, vol. 51, pp. 256–267, 2002.

[38] E. Quaia, "Assessment of tissue perfusion by contrast-enhanced ultrasound," *Eur. Radiol.*, vol. 21, no. 3, pp. 604–615, 2011.

[39] M. Brock, T. Eggert, R. J. Palisaar *et al.*, "Multiparametric ultrasound of the prostate: adding contrast enhanced ultrasound to real-time elastography to detect histopathologically confirmed cancer," *J. Urol.*, vol. 189, no. 1, pp. 93–98, 2013.

CHAPTER 8

Discussion and future prospects

In this Chapter, the results of this thesis are discussed, focusing both on the technical and on the clinical aspects of the developed methods. Potential future developments in this field are also discussed.

Nowadays, efficient care for prostate cancer, the most common form of cancer in Western men [1, 2], is hampered by diagnostic limitations. In the current situation, many men undergo systematic biopsies. This invasive and potentially painful procedure is often unnecessary in retrospect [3, 4]. Moreover, because accurate cancer localization is currently not feasible, treatment choices are often limited to radical treatments, such as a radical prostatectomy, that carry significant risks of permanent side effects, such as impotence and incontinence [5].

In this thesis, contrast-ultrasound dispersion imaging (CUDI) is proposed as a novel quantitative imaging method to overcome the diagnostic limitations in prostate cancer care. This method aims at detecting angiogenesis, in an effort to localize aggressive cases of prostate cancer. Because the method is based on transrectal ultrasound (TRUS), it can potentially be adopted at an early stage and it can possibly be applicable for accurate targeting of biopsies and therapies.

Characterization of the ultrasound-contrast-agent (UCA) dispersion kinetics in the microcirculation is proposed to infer the underlying microvascular structure. To this end, the microvascular architecture is considered as a distributed network, similar to a porous medium. Using this characterization, typical features observed in angiogenic microvascular structures, such as an increased microvascular density (MVD) and tortuosity, can be interpreted in terms of the dispersion kinetics.

In all our studies, the presence of prostate cancer was associated with a relative decrease in dispersion. More precisely, the observed ratio between perfusion and dispersion was higher in cancer than in healthy tissue. This relative decrease in dispersion may perhaps result from an increase in the microvessel tortuosity, which limits the dispersion distance in the microvascular network. Alternatively, arteriovenous shunts may cause a relative increase in perfusion with respect to dispersion. The precise effects of angiogenesis on the prostate microcirculation were, however, not directly evaluated in the current work. It is recommended that the effects of angiogenesis on UCA dispersion are investigated in more detail in the future. For instance, a future validation could involve immunohistological analysis of prostate cancer tissue, which would provide evidence regarding the microvascular architecture. In this context, animal models could also play an important role. Preliminary results of an ongoing animal study suggest angiogenic microvascular growth to be correlated with dispersion [6]. In addition, dedicated *in vitro* experiments could be helpful for validation of the effects of structural changes on UCA dispersion as observed by dynamic contrast-enhanced (DCE-US) imaging [7, 8]. By measuring UCA dispersion in various microvascular phantoms with known differences in characteristics, such as porosity or tortuosity, changes in UCA dispersion could be better correlated with microvascular changes.

A calibration study was performed to enable analysis of the UCA transport kinetics by

quantitative DCE-US imaging. In general, DCE-US image artifacts, which may for instance result from nonlinear attenuation and microbubble disruption, may affect the reliability of quantitative analysis [9–12]. As shown in Chapter 2, these artifacts are mitigated by using low UCA concentrations and a low mechanical index (MI): within these constraints, the observed backscattered acoustic intensity is approximately linearly related to the UCA concentration. Taking into account also the postprocessing implemented on the ultrasound imaging system, the DCE-US image intensity can be interpreted in terms of the relative UCA concentration after data linearization. As a result, time-intensity curves (TICs) obtained by DCE-US imaging can be converted into indicator dilution curves (IDCs) that are suitable for quantitative analysis of the UCA transport kinetics.

In the first dispersion analysis method, described in Chapter 2, IDCs obtained at all DCE-US image pixels are analyzed individually. The local density random walk (LDRW) model, which is an analytical solution of the convective dispersion equation, is adopted to describe the first passage of an intravenously injected bolus through the prostate microcirculation. A model modification is proposed to describe local UCA dispersion. The modification involves a local boundary condition, in which the local spatial distribution of the UCA bolus is approximated by a Normal distribution. As a result of this modification, a local, dispersion-related parameter, κ, can be estimated by IDC curve-fitting. More precisely, κ represents the local ratio between the squared convection velocity and the UCA dispersion coefficient. By parametric curve-fitting of IDCs obtained at all DCE-US image pixels covering the prostate, a parametric dispersion image based on κ can be obtained. A practical limitation of the method concerns recirculation, i.e., subsequent passages of the UCA bolus through the prostate. The effects of UCA recirculation are not described by the LDRW model, as it only describes the first bolus passage. To prevent these effects from influencing the dispersion analysis, the IDC time segment featuring recirculation effects is identified and discarded from the analysis. The initial prostate cancer localization results obtained by κ were superior to those obtained by semi-quantitative parameters based on IDC amplitude and time features.

The generally low signal-to-noise ratio (SNR) in DCE-US image sequences poses another challenge to the quantitative analysis from IDCs obtained at spatial scales close to the pixel resolution. In order to deal with the multiplicative noise encountered in IDC analysis, a dedicated parameter estimation algorithm is proposed in Chapter 3. This algorithm is generally applicable in indicator dilution analysis for all models, such as the LDRW model, that can be interpreted as the distribution of transit-times. The algorithm is based on the interpretation of an IDC as the observed histogram of microbubble transit-times. Parameter estimation is then performed by maximizing the likelihood of observing this histogram, which can be solved partially analytically for several IDC models. A dedicated adaptation of

this algorithm is developed to deal with recirculation. The parameter estimation precision of this algorithm was superior to that obtained by standard nonlinear least-squares (NLS) methods, both in simulations and in experimental data.

An alternative method for dispersion quantification is described in Chapters 4, 5, and 6. In this method, which circumvents many of the methodological limitations of the first method, a complete spatiotemporal analysis is proposed. The spatial similarity among IDCs obtained at neighboring pixels is considered as an indirect estimate for dispersion. This approach is not restricted to the first passage of the bolus and is, therefore, less sensitive to artifacts due to recirculation. Furthermore, contrary to commonly adopted semi-quantitative TIC parameters based on amplitude and time features, the analysis of spatial similarity is inherently local and normalized.

In a first implementation of this method, described in Chapter 4, the spectral coherence ρ is adopted as a measure of IDC similarity. The resulting coherence analysis is independent of UCA appearance time differences as the IDC phase information is discarded. At each pixel, the average coherence is evaluated between the local pixel IDC and all surrounding IDCs defined by a spatial kernel. An isotropic kernel, independent of the blood flow direction, is adopted. The kernel size is based on the size of angiogenic microvascular structures. Furthermore, IDCs at directly neighboring pixels, which would provide a high similarity due to limitations in the spatial ultrasound image resolution, are excluded from the kernel. The resulting kernel has a ring shape and contains all pixels at distances between 1.0 and 2.5 mm.

In Chapter 5, the relation between dispersion and coherence is evaluated in more detail. To this end, the coherence between two IDCs represented by the LDRW model is investigated. By showing that ρ is monotonically related to the average parameter κ, the formal rationale for the spatial IDC coherence analysis is provided. In this chapter, several methodological improvements are also described. A dedicated spatial filter, based on Wiener deconvolution, is proposed for regularization of the anisotropic DCE-US speckle-grain size. By applying this filter, the spatial similarity analysis is made insensitive to the intrinsic anisotropy in DCE-US images. Additionally, the similarity analysis is restricted to the most informative IDC time segment by time-windowing. As a result, IDC noise outside this segment can no longer affect the similarity analysis.

The introduction of time-windowing provides temporal realignment, such that differences in the IDC appearance times are compensated. As a result, a wider range of similarity measures become available for the proposed spatiotemporal analysis. In Chapter 6, the IDC correlation coefficient r is proposed as an alternative to the coherence for spatial IDC similarity analysis. To this end, an analytical relation between κ and r is derived. In the future, the use of alternative similarity measures could be investigated. For instance, non-

linear measures based on the concept of information entropy, such as mutual information, could be considered.

Overall, the best cancer localization results were obtained with the spatial similarity analysis. This may be due to a number of reasons. A major factor could be the fact that the spatial information is explicitly included in the spatial IDC similarity analysis. This information is not exploited by the curve-fitting analysis or by conventional semi-quantitative approaches. In addition, the spatial similarity analysis is less sensitive to UCA recirculation than the curve-fitting analysis and it does not require curve-fitting. Furthermore, no assumptions are required for the spatial similarity analysis in order to provide a local assessment. The similarity analysis is also inherently normalized, facilitating the comparison of different parametric images.

To determine the clinical value of CUDI, the method is compared to multiparametric magnetic resonance imaging (mpMRI) in the clinical validation described in Chapter 7. Although limited in its sample size, this is the first study in which the clinical utility of quantitative DCE-US and mpMRI for prostate cancer localization is compared. For DCE-US, addition of the quantification results by CUDI to the qualitative interpretation provided a significant increase in sensitivity. The associated decrease in specificity was lower than the increase in sensitivity in all comparisons. As compared to mpMRI, CUDI provided a higher sensitivity and a slightly lower negative predictive value (NPV). These results establish the value of CUDI for prostate cancer localization. More importantly, the value of CUDI is placed in the context of several previously reported studies that were performed for mpMRI [13–15]. In subgroups of patients, mpMRI and CUDI may be combined to exploit both the high specificity of mpMRI and the high sensitivity of CUDI.

The comparison between CUDI and histology is hampered by mismatches between the DCE-US and histology planes. For this reason, the technical validation in Chapters 2 through 6 is restricted to large prostate cancers that were found across several histology planes. The clinical validation described in Chapter 7 includes a less stringent comparison between DCE-US and histology planes. In future research, more advanced methods are required to increase the accuracy of the validation procedure. To this end, a dedicated registration algorithm has been developed [16].

A limitation of the current CUDI implementation resides in the need for an expert to interpret the obtained parametric images. A dedicated classification method for lesion characterization would significantly simplify the adoption of CUDI into clinical practice. An advanced classifier could, for instance, be based on different CUDI implementations and also on patient characteristics, such as age and prostate-specific antigen (PSA) level.

In the future, a more extensive clinical validation is necessary before CUDI can be adopted in clinical practice. To this end, a multi-center study has been initiated. Fig. 8.1 shows an

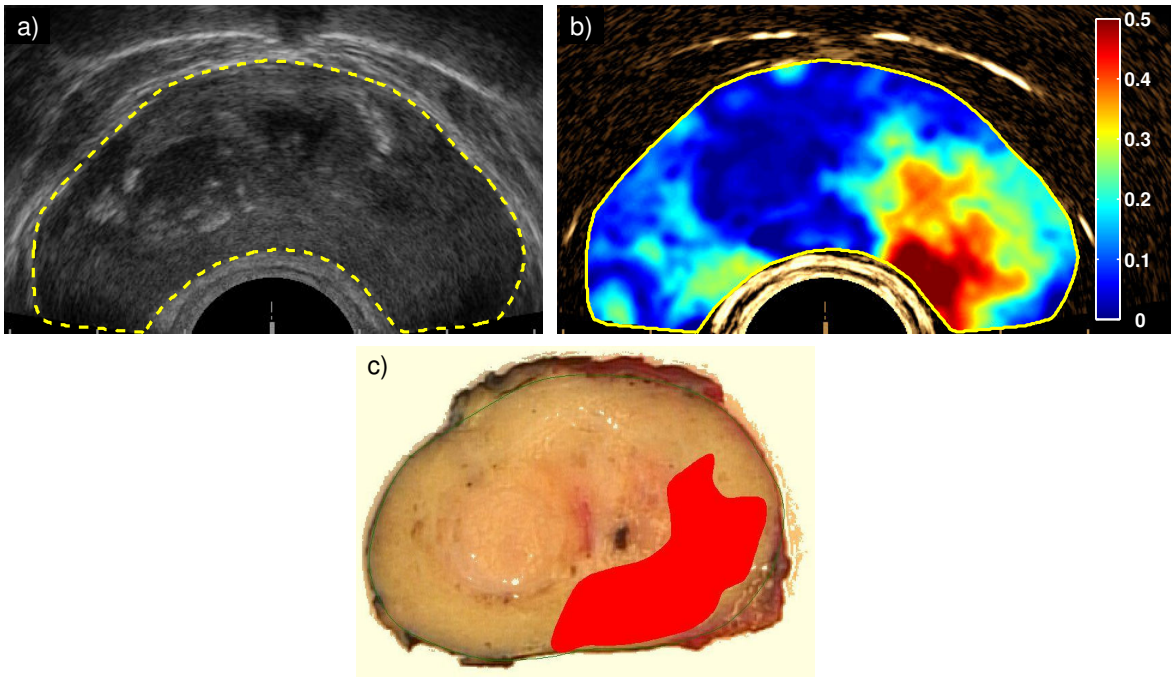

Figure 8.1 *CUDI result obtained at the Jeroen Bosch Hospital ('s-Hertogenbosch, The Netherlands) with an UltraView 800 imaging system (BK Medical, Herlev, Denmark). A fundamental ultrasound image (a) is shown, as well as the corresponding CUDI image (b), based on spatiotemporal correlation analysis as described in Chapter 6. Also shown is the corresponding histology slice (c), obtained after radical prostatectomy.*

example of a CUDI parametric image with histology, obtained at the Jeroen Bosch Hospital in 's-Hertogenbosch, The Netherlands, with an UltraView 800 imaging system (BK Medical, Herlev, Denmark). In this multi-center study, the parametric images obtained by CUDI are compared to the corresponding histology, obtained after radical prostatectomy. The sensitivity and specificity for cancer localization can be evaluated on a larger scale.

A more prospective evaluation of CUDI is necessary to determine the clinical benefit. The main potential of prostate imaging methods, such as CUDI, is a significant reduction in the morbidity of diagnostic and therapeutic methods. Diagnostic improvements could involve better patient stratification and image-guided biopsies. To determine the additional value of CUDI in these applications, patients referred for radical prostatectomy do not represent the ideal study population. All of these patients are already known to have prostate cancer. In diagnostic applications, however, CUDI would also be performed in healthy men. A more suitable patient population could, for instance, be based on patients scheduled for systematic biopsies. The results obtained by CUDI may be compared with the pathology results obtained from the systematic biopsies. If CUDI would provide a sufficiently high NPV for cancer detection in this patient population, the method may be useful for additional patient stratification prior to biopsies. In addition, the diagnostic yield of CUDI-targeted biopsies

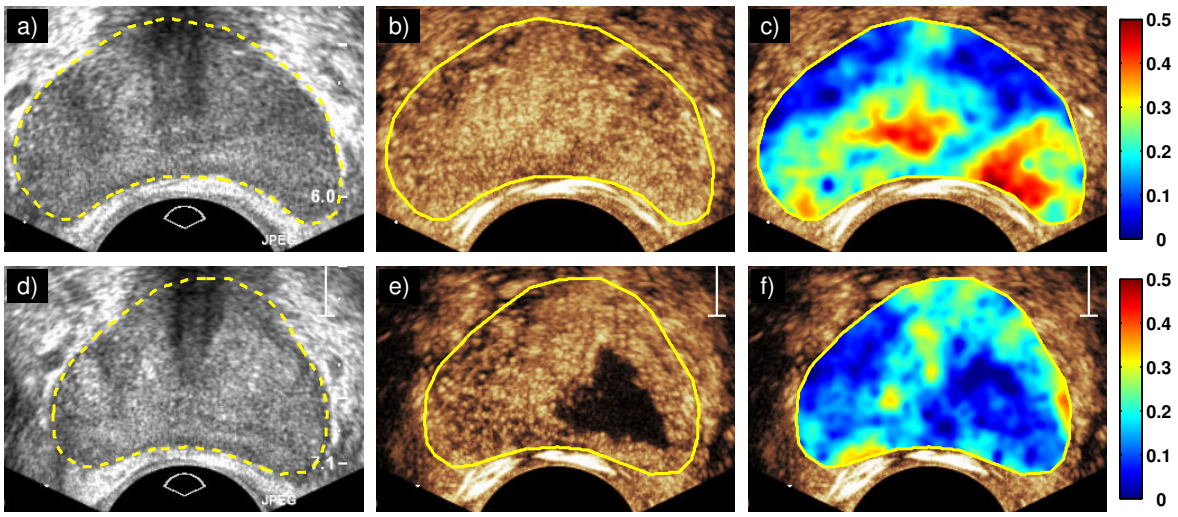

Figure 8.2 *Prostate images obtained before (a-c) and approximately four weeks after focal irreversible electroporation (d-f). On the left (a,d), fundamental ultrasound images are shown. The middle images (b,e) are DCE-US images obtained at approximately the time of peak enhancement. On the right (c,f), CUDI images based on spatiotemporal correlation analysis as described in Chapter 6 are shown. Whereas conventional TRUS imaging does not show any effect of this treatment, the DCE-US image clearly shows a lack of UCA microbubbles that is likely indicative of necrosis. On the CUDI image, the observed correlation coefficient is approximately zero.*

could be evaluated. Efficient biopsy targeting by CUDI would benefit from a direct implementation of the methodology on the ultrasound imaging system, which would make CUDI available in quasi-real-time.

Imaging methods, such as CUDI, could also open up alternative treatment options, such as focal therapy [17], which are currently not feasible due to diagnostic limitations [18]. For example, the value of CUDI for monitoring focal therapies, such as cryotherapy, high-intensity focused ultrasound, or irreversible electroporation [19–21], could be investigated. In a pilot study, the effects of irreversible electroporation therapy on the prostate have been evaluated by CUDI, as shown in Fig. 8.2.

In the future, the introduction of three-dimensional DCE-US imaging may offer great advantages to CUDI. One of the major clinical limitations of the current method, i.e., the image plane selection, would be resolved. Moreover, the entire prostate could be studied with only a single bolus injection. This would speed up data acquisition protocols. Coupled with dedicated registration methods, three-dimensional CUDI could improve targeting of biopsies and therapies. On the technical side, three-dimensional dispersion analysis methods could be developed by extending the existing spatial similarity analysis to three dimensions. Additionally, three-dimensional DCE-US imaging would open up new possibilities for three-dimensional analysis of UCA dispersion.

The optimal clinical use of CUDI may involve a combination with alternative TRUS-based imaging methods, such as elastography [22, 23]. By shear-wave elastograhpy (SWE), the tissue stiffness can be quantified objectively and noninvasively [24]. Similar to mpMRI, a combination of different physical quantities, such as dispersion and elasticity, may increase the diagnostic reliability for prostate cancer localization. Since TRUS is routinely used for prostate volume measurement and for systematic biopsy guidance, multiparametric ultrasound is better suited for prostate cancer localization than mpMRI if the diagnostic results are comparable.

Another interesting development, which is expected to play an important role in this context, concerns the introduction of targeted microbubbles for DCE-US imaging [25]. These microbubbles are attracted to specific receptors that are typically observed in angiogenesis. As a result, some of the microbubbles will attach to these receptors and stop flowing through the vascular architecture, which can be detected by available DCE-US imaging techniques. In this field, ongoing research is focused on increasing the binding efficiency using the acoustic radiation force [26] and on investigating the acoustic behavior of bound microbubbles, potentially leading to specialized pulse schemes for detection of bound microbubbles [27].

In conclusion, contrast-ultrasound dispersion imaging is proposed and developed using several different implementations. The promising results obtained for prostate cancer localization motivate towards a more extensive validation. Future applications of CUDI could potentially involve patient stratification, biopsy targeting, focal therapy guidance and therapy monitoring. Furthermore, three-dimensional CUDI could be developed and the use of CUDI in different imaging modalities and different forms of cancer could be evaluated.

References

[1] American Cancer Society, "Cancer facts & figures 2013," Atlanta, 2013.

[2] J. Ferlay, E. Steliarova-Foucher, J. Lortet-Tieulent *et al.*, "Cancer incidence and mortality patterns in Europe: Estimates for 40 countries in 2012," *Eur. J. Cancer*, vol. 49, no. 6, pp. 1374–1403, 2013.

[3] F. H. Schröder, J. Hugosson, M. J. Roobol *et al.*, "Screening and prostate-cancer mortality in a randomized European study," *N. Engl. J. Med.*, vol. 360, no. 13, pp. 1320–1328, 2009.

[4] G. L. Andriole, E. D. Crawford, R. L. Grubb III *et al.*, "Mortality results from a randomized prostate-cancer screening trial," *N. Engl. J. Med.*, vol. 360, no. 13, pp. 1310–1319, 2009.

[5] J. L. Stanford, Z. Feng, A. S. Hamilton *et al.*, "Urinary and sexual function after radical prostatectomy for clinically localized prostate cancer," *JAMA*, vol. 283, no. 3, pp. 354–360, 2000.

[6] T. Saidov, C. Heneweer, M. Kuenen *et al.*, "Contrast ultrasound dispersion imaging of different tumor types," in *Proc. IEEE International Ultrasonics Symposium (IUS)*, Dresden, Germany, 2012, pp. 2149–2152.

[7] C. Veltmann, S. Lohmaier, T. Schlosser *et al.*, "On the design of a capillary flow phantom for the evaluation of ultrasound contrast agents at very low flow velocities," *Ultrasound Med. Biol.*, vol. 28, no. 5, pp. 625–634, 2002.

[8] C. Demitri, A. Sannino, F. Conversano *et al.*, "Hydrogel based tissue mimicking phantom for in-

vitro ultrasound contrast agents studies," *J. Biomed. Mater. Res. B Appl. Biomater.*, vol. 87, pp. 338–345, 2008.

[9] E. Stride and N. Saffari, "Investigating the significance of multiple scattering in ultrasound contrast agent particle populations," *IEEE Trans. Ultrason., Ferroelectr., Freq. Control*, vol. 52, no. 12, pp. 2332–2345, 2005.

[10] M.-X. Tang and R. J. Eckersley, "Nonlinear propagation of ultrasound through microbubble contrast agents and implications for imaging," *IEEE Trans. Ultrason., Ferroelectr., Freq. Control*, vol. 53, no. 12, pp. 2406–2415, 2006.

[11] J. J. F. A. H. Grootens, M. Mischi, M. Böhmer, H. H. M. Korsten, and R. M. Aarts, "Modeling of ultrasound propagation through contrast agents," in *Proc. 4th European Congress for Medical and Biomedical Engineering*, Antwerp, Belgium, 2008, pp. 440–443.

[12] L. Demi, G. Russo, H. Wijkstra, and M. Mischi, "Observed cumulative time delay between second harmonic and fundamental component of pressure wave fields propagating through ultrasound contrast agents," in *J. Acoust. Soc. Am.*, vol. 134, no. 5, San Francisco (CA), 2013, p. 3977. [Online]. Available: http://dx.doi.org/10.1121/1.4830491

[13] A. Villers, P. Puech, D. Mouton *et al.*, "Dynamic contrast enhanced, pelvic phased array magnetic resonance imaging of localized prostate cancer for predicting tumor volume: Correlation with radical prostatectomy findings," *J. Urol.*, vol. 176, no. 6, pp. 2432–2437, 2006.

[14] E. K. Vos, G. J. S. Litjens, T. Kobus *et al.*, "Assessment of prostate cancer aggressiveness using dynamic contrast-enhanced magnetic resonance imaging at 3 T," *Eur. Urol.*, vol. 64, no. 3, pp. 448–455, 2013.

[15] S. Isebaert, L. Van den Bergh, K. Haustermans *et al.*, "Multiparametric MRI for prostate cancer localization in correlation to whole-mount histopathology," *J. Magn. Reson. Imaging*, vol. 37, no. 6, pp. 1392–1401, 2013.

[16] S. G. Schalk, T. A. Saidov, H. Wijkstra, and M. Mischi, "3D registration of histology and ultrasound data for validation of prostate cancer imaging," in *Proc. SPIE Medical Imaging*, Lake Buena Vista (FL), 2013, pp. 86 692T–86 692T–10.

[17] V. Kasivisvanathan, M. Emberton, and H. U. Ahmed, "Focal therapy for prostate cancer: Rationale and treatment opportunities," *Clin. Oncol.*, vol. 25, no. 8, pp. 461–473, 2013.

[18] M. Tsivian, M. Kimura, L. Sun *et al.*, "Predicting unilateral prostate cancer on routine diagnostic biopsy: sextant vs extended," *BJU Int.*, vol. 105, no. 8, pp. 1089–1092, 2010.

[19] D. K. Bahn, P. Silverman, F. Lee, Sr. *et al.*, "Focal prostate cryoablation: Initial results show cancer control and potency preservation," *J. Endourol.*, vol. 20, no. 9, pp. 688–692, 2006.

[20] H. U. Ahmed, R. G. Hindley, L. Dickinson *et al.*, "Focal therapy for localised unifocal and multifocal prostate cancer: a prospective development study," *Lancet Oncol.*, vol. 13, no. 6, pp. 622–632, 2012.

[21] W. van den Bos, B. G. Muller, and J. J. M. C. H. de la Rosette, "A randomized controlled trial on focal therapy for localized prostate carcinoma: hemiablation versus complete ablation with irreversible electroporation," *J. Endourol.*, vol. 27, no. 3, pp. 262–264, 2013.

[22] L. Pallwein, M. Mitterberger, G. Pinggera *et al.*, "Sonoelastography of the prostate: Comparison with systematic biopsy findings in 492 patients," *Eur. J. Radiol.*, vol. 65, no. 2, pp. 304–310, 2008.

[23] R. G. Barr, R. Memo, and C. R. Schaub, "Shear wave ultrasound elastography of the prostate: Initial results," *Ultrasound Q.*, vol. 28, no. 1, pp. 13–20, 2012.

[24] J. Bercoff, M. Tanter, and M. Fink, "Supersonic shear imaging: a new technique for soft tissue elasticity mapping," *IEEE Trans. Ultrason., Ferroelectr., Freq. Control*, vol. 51, no. 4, pp. 396–409, 2004.

[25] S. Pochon, I. Tardy, P. Bussat *et al.*, "BR55: A lipopeptide-based VEGFR2-targeted ultrasound contrast agent for molecular imaging of angiogenesis," *Invest. Radiol.*, vol. 45, no. 2, pp. 89–95, 2010.

[26] P. J. A. Frinking, I. Tardy, M. Théraulaz *et al.*, "Effects of acoustic radiation force on the binding efficiency of BR55, a VEGFR2-specific ultrasound contrast agent," *Ultrasound Med. Biol.*, vol. 38, no. 8, pp. 1460–1469, 2012.

[27] O. Couture, M. R. Sprague, E. Cherin, P. N. Burns, and F. S. Foster, "Reflection from bound

microbubbles at high ultrasound frequencies," *IEEE Trans. Ultrason., Ferroelectr., Freq. Control*, vol. 56, no. 3, pp. 536–545, 2009.

Dankwoord

Hoewel het misschien niet zo lijkt als je naar de kaft kijkt, maak je een proefschrift niet alleen. Zonder hulp van een aantal mensen om mij heen zou dit proefschrift er immers nooit gekomen zijn. Ik wil dan ook graag een aantal mensen enorm veel bedanken voor alle steun, zowel inhoudelijk als persoonlijk, die ik heb mogen ontvangen.

First and foremost, I would like to express lots of thanks to my co-promotor dr. ir. Massimo Mischi. When we met about seven years ago to discuss an internship abroad, I would have never imagined that both a Master thesis project and a PhD study would follow. Looking back, I have been very fortunate with you as my supervisor, as you have given me a very productive and pleasant atmosphere in which I had the opportunity to grow as a scientist and as a person. Even though you had to correct my initial manuscripts a seemingly infinite amount of times, you always remained confident in me. Massimo, thanks a lot for your support!

Mijn eerste promotor, prof. dr. ir. Hessel Wijkstra, wil ik graag bedanken voor de unieke kans om mee te draaien in de dagelijkse praktijk bij het AMC, waar ik de beperkingen van de huidige prostaatkankerdiagnostiek met eigen ogen heb kunnen zien. Daardoor ben ik overtuigd geraakt van de noodzaak van nieuwe beeldvormingstechnieken. Voor mij was deze noodzaak een extra motivatie om in ons onderzoek het onderste uit de kan te halen. Ik waardeer het zeer dat prof. dr. Jean de la Rosette mijn tweede promotor is. Het is immers erg belangrijk dat nieuwe medische technologie ook wordt gedragen door de medische professionals die deze technologie gaan toepassen. Het feit dat u promotor bent, bevestigt de klinische toegevoegde waarde van dit onderzoek.

In addition, I would like to thank the committee members, prof. dr. ir. Nico de Jong, prof. dr. ir. Frans van de Vosse, prof. dr. ir. Arnold Hoeks en prof. dr. ir. Ton Backx, for reading and reviewing this thesis. In this regard, I would also like to thank prof. Piero Tortoli whom I met as an outstanding professor, but also as a very warm person, during my internship in Florence. The wonderful time I spent at the MSD lab is a period that I

will always remember.
This research was part of the STW-project "Prostate cancer detection by contrast ultrasound diffusion imaging." I would like to thank all members of the user committee for their input and feedback during the progress meetings.
In de afgelopen jaren heb ik gemerkt hoe belangrijk het is dat technische en klinische onderzoekers elkaar aanvullen om tot een optimaal resultaat te komen. De samenwerking in het AMC, met name met drs. Martijn Smeenge en drs. Arnoud Postema, heb ik als heel prettig ervaren. Martijn en Arnoud, voor de vele uren die jullie aan ons klinisch artikel geschreven hebben, wil ik jullie in het bijzonder bedanken. Ook wil ik graag drs. Ingeborg Herold en prof. dr. Erik Korsten bedanken voor alle hulp en samenwerking bij de vele calibratiemetingen die we hebben gedaan in het Catharina Ziekenhuis. Daarnaast wil ik graag dr. Wout Scheepens (Catharina Ziekenhuis) en dr. Harrie Beerlage (Jeroen Bosch Ziekenhuis) bedanken voor de fijne samenwerking.
Er is een groep mensen die ik zeker een woord van dank verschuldigd ben: dat zijn alle patienten die vrijwillig hebben meegewerkt aan ons onderzoek. Voor deze patienten die, vaak ondanks hun eigen prostaatkankerbehandeling, bereid waren om een steentje bij te dragen aan de toekomst van anderen, heb ik veel bewondering.
Over the years, Gianna, Tamerlan, Stefan, Simona, and Libe have joined the prostate cancer imaging project. I have really enjoyed working together with each of you and I'll remember the fun times at conferences. I would also like to thank the students Francesco and Nabil for their significant contributions.
In the past years, I have been able to do research in the very nice environment of the Signal Processing Systems group of prof. dr. ir. Jan Bergmans at TU/e. I would like to thank all staff members and colleagues for this pleasant time. Thanks to my initial roommates Brian, Joep, Hooman, and Iman, and to Diana, Michiel, Aline, Chiara, Hans, Federica, and many others for the nice discussions during coffee and lunch breaks.
Buiten het onderzoek om ben ik geregeld op stap geweest met mijn vrienden. Bedankt voor de leuke avondjes stappen en voor het jaarlijkse vriendenweekend, dat iedere keer weer voor voldoende gezelligheid en ontspanning zorgt.
Pap, mam, Jeroen en Marjolein, bij jullie ben ik al mijn hele leven thuis en door jullie ben ik geworden wie ik nu ben. Ik waardeer het enorm dat jullie altijd voor me klaar staan. Gerrit, Jeanne, Frank, Roel en Ron, bedankt dat ik ook bij jullie al jarenlang een tweede thuis kan vinden.
Een speciaal woord van dank is dan nog weggelegd voor een bijzonder iemand. Loes, met jou heb ik alle mooie, maar ook alle mindere mooie momenten van het promoveren gedeeld. Altijd was jij er voor mij, ook op mindere dagen. Daar ben ik je heel dankbaar voor en ik heb ontzettend veel zin om samen verder aan onze toekomst te bouwen!

About the author

Maarten Kuenen was born on October 22, 1985 in Venray, The Netherlands. After finishing pre-university secondary education in 2003 at Dendron College in Horst, The Netherlands, he studied Electrical Engineering at Eindhoven University of Technology in Eindhoven, The Netherlands. During his study, he completed two internships, which involved software optimization for an open platform for ultrasound research, at the University of Florence, Italy, and electromagnetic detection of cracks in metal surfaces, at TNO in Eindhoven, The Netherlands, respectively. In 2009, he graduated with honors within the Signal Processing Systems group on the development of quantitative techniques for prostate cancer detection based on contrast-enhanced ultrasound imaging. Subsequently, he worked at the AMC as a researcher for three months on the validation of imaging techniques for prostate cancer localization, in preparation for a PhD project at Eindhoven University of Technology, Eindhoven, The Netherlands. This project was part of the STW VIDI project granted to dr. ir. Massimo Mischi, titled "Prostate cancer detection by contrast-ultrasound diffusion imaging." The results of this project are presented in this dissertation. They have also been published in several international academic journals and presented at various international conferences. In particular, for the article "Maximum-likelihood estimation for indicator dilution analysis," Maarten received the IEEE-EMBS Best Paper Award in 2013 from the IEEE-EMBS Benelux Chapter. Since January 2014, he is employed at Philips Research in Eindhoven, The Netherlands.